TESLA - COLLABORATION

Contributions to the 4th European Particle Accelerator Conference, London, 27 June to 1 July, 1994 and to the 17th LINAC Conference, LINAC 94, Tsukuba, Japan, August 22 to 26, 1994

September 1994, TESLA 94-24

Contents TESLA Report 94-24

Contributions to the 4th European Particle Accelerator Conference, London, 27 June to 1 July, 1994

Contributions to the 17th LINAC Conference, LINAC 94, Tsukuba, Japan, August 22 to 26, 1994

[1] Presented at the 1994 21st International Power Modulator Symposium, June 27 - 30, 1994, Costa Mesa, CA., USA

The TESLA Test Facility Linac Injector

M. Bernard, J.C. Bourdon, R. Chehab, T. Garvey, B. Jacquemard, B. Mouton, M. Omeich, J. Rodier, P. Roudier, Y. Thiery,
Laboratoire de l'Accélérateur Linéaire, IN2P3 - CNRS, Orsay, France.

B. Aune, M. Desmons, J. Fusellier, J.F. Gournay, M. Jablonka, J.M. Joly, M. Juillard, A. Mosnier,
DAPNIA / SEA-CE, Saclay, France.

S. Buhler, T. Junquera,
Institut de Physique Nucléaire, IN2P3 - CNRS, Orsay, France.

Abstract

The TESLA Test Facility (TTF) Linac is a 500 MeV, 1.3 GHz superconducting accelerator under construction at DESY (Hamburg) by an international collaboration. The linac is being built to demonstrate the viability of the superconducting RF approach to a future e^+e^- linear collider. Within the collaboration three participating French laboratories (LAL, IPN and DAPNIA) have undertaken the task of designing and constructing a phase 1 injector for TTF. We describe the studies towards the realisation of this 7 - 14 MeV, 8 mA high duty cycle (800 μs pulse, 10 Hz repetition rate) injector. The front end of the injector will consist of a 250 keV electron gun, a 216.7 MHz sub-harmonic bunching cavity and a superconducting capture cavity at the main linac frequency. This is followed by a beam analysis line and a transport section to match the beam from the capture cavity to the first cryomodule of the main linac.

1. INTRODUCTION

The TTF linac will essentially consist of an injector, four 12 m long cryomodules each containing eight 9 cell superconducting (SC) 1.3 GHz cavities of length 1.04 m, and a beam analysis line to measure the properties of the accelerated beam. To properly test such issues as HOM dissipation and wakefield excitation requires an injector capable of delivering a train of bunches with the characteristics of the TESLA proposal itself, i.e. 5×10^{10} electrons per pulse at 1 MHz intervals during an 800 μs macro-pulse[1]. In contrast, the problems of operating high gradient (15 to 25 MV/m) SC cavities under high beam loading can be investigated using an injector capable of delivering the same average current albeit at reduced bunch charge and increased repetition rate. With this goal in mind we are constructing a 'phase 1' injector for TTF for which the specification is given in table 1.

Table 1
Specification of TTF phase 1 injector

beam energy	> 5 MeV
average current	8 mA
pulse length	800 μs
bunch length	1 mm (rms)
energy spread	< 1% (rms)
RMS emittance	5 - 10 mm-mrad (normalised)
repetition rate	10 Hz

2. DESCRIPTION OF THE INJECTOR

The principal components of the injector consist of, (i) a triode electron gun capable of delivering micro-bunches with a variable frequency, (ii) a sub-harmonic bunching (SHB) cavity to provide longitudinal pre-bunching of the electron pulses, (iii) a superconducting 'capture cavity' to further bunch the electrons and to provide some pre-acceleration before injection into the linac, (iv) an analysis line to verify the correct adjustment of the beam parameters and (v) a transport section, consisting of two triplet magnets, to match the correctly adjusted beam to the main linac.

The bunch repetition frequency will be controlled by the application of fast (<1 ns) pulses to the gun cathode at the desired rate. The maximum rate of repetition is equal to the frequency of the SHB (216.7 MHz). At this frequency the 8 mA average current corresponds to bunch charges of 37 pC (2.31×10^8 e's per pulse). For good pre-bunching the initial pulse-width should be sufficiently short in comparison with the period of the SHB and we set this to be 640 ps (± 25° of RF phase at 216.7 MHz) which corresponds to gun currents of 115 mA for 'triangular' pulses.

The choice of a superconducting structure (identical to those used in the cryomodules) for the capture cavity is influenced by the long macro-pulse width and consequent high average power that would be required of a copper structure to provide significant pre-acceleration of the beam coming from the gun. On the other hand, the leakage field of the SC cavity and the fact that it is not β-graded, necessitates the use of a gun producing electrons of energy superior to 200 keV.

2.1 *The Electron Gun*

The electron gun will be a modified triode gun, built by Hermosa Electronics (California), and originally employed on the ALS linac at Saclay[2]. After reduction of the anode-cathode spacing we have measured currents in excess of 500 mA at 30 kV. This is largely sufficient to provide the possibility of operating the injector at frequencies lower than 216.7 MHz. The additional energy of the beam will be provided by an electrostatic accelerating column capable of sustaining 300 kV in air, as is employed on the S-DALINAC at the TH Darmstadt[3]. Simulations of the injector using the PARMELA code indicate that we need to maintain the gun voltage to better than 0.1% during the 800 μs pulse if we wish to keep

the final beam parameters within the required specification. In order to do this we power the column via a 33 nF capacitor fed by a 300 kV - 1 mA power supply. The risk of electrical breakdown and the consequent release of stored energy in the system presents a major concern for the succesful operation of the injector. Simulations using the EGUN[4] code indicate that not all of the current available from the gun can be reasonably transported through the electrostatic column and so initial operation of the injector will be restricted to 216.7 MHz. However the installation of an 'Einzel' focusing lens at the input to the column holds the promise of increased bunch charge operation at a later date[5].

2.2 *The Sub-harmonic Buncher*

The frequency of the SHB cavity is chosen to be 1/6 of the frequency of the main accelerating cavities in order that its period is sufficiently larger than the gun pulse widths. This is required to ensure good pre-bunching of the beam and to avoid as much as possible the loss of electrons on the SC walls of the capture cavity. The SHB cavity consists of a single re-entrant cell and is fabricated from stainless steel. To provide the cavity with a high quality factor (Q = 24300) the inner walls of the cell will be coated with a thin (20 μm) deposition of copper. SUPERFISH calculations indicate that the cavity will have a transit-time corrected shunt impedance ($R_S = V^2/2P$) of 3.11 MΩ. The peak cavity Volts required to provide the necessary pre-bunching is calculated to be 50 keV leading to a modest peak power dissipation of 400 W. In order to provide some margin for safety the cavity will be powered using an RFTS (Bordeaux) amplifier, capable of delivering 2 kW pulses for up to 5 ms at 10 Hz. The amplifier is rated to have a phase stability of ± 0.5° and amplitude stability of ± 0.5% during a 1 ms pulse.

2.3 *The Capture Cavity*

The role of this cavity is twofold; (i) to terminate the bunching initiated upstream. The bunches will have a duration of < 100 ps at the entrance to the cavity and will be compressed by a further factor of 10, (ii) in addition this cavity will provide the necessary energy (7 - 14 MeV) for injection into the first cryomodule, the energy depending on the field at which the strucure is operated. The capture cavity is a standard TESLA cavity (9 cell, 1.3 GHz) identical to the 32 cavities of which the TTF linac is composed. It incorporates all of the new concepts developed for the TESLA project, i.e. the helium vessel integrated to the body of the cavity with a reduced LHe volume (25 liters), and with both the main and HOM couplers located in the cryostat vacuum. This cavity is installed in a special cryostat connected to the cryogenic distribution lines of the linac and is operated at 1.8 K. Although there is sufficient reserve power in the 4.5 MW klystrons which power the main linac cavities (1 klystron per 16 cavities) the capture cavity will be powered with its own individual 300 kW klystron. This will permit improved control of the klystron phase and amplitude thus simplifying the operation of the injector. It should be noted that, as for the main linac cavities, this structure will be operated in pulsed mode in contrast to other SC RF systems which accelerate continuous beams and are constantly powered with RF.

2.4 *Beam Diagnostics*

To verify that the beam has the required characteristics it is necessary to install appropriate instrumentation along the linac. A capacitive pick-up monitor will be used at the exit of the column to monitor the beam pulse from the gun. Current measurements elsewhere will be made with toroidal monitors, in particular, differential measurements of the current before and after the capture cavity will detect the presence of any beam losses and provide a signal to "trip-off" the gun. Beam position monitors (BPM) will be "button electrode" devices as employed at the ESRF[6]. An additional electrode on one BPM will allow a measurement of the RF phase of the beam with respect to the master-oscillator phase.

The transverse profile of the beam will be measured using retractable aluminium-oxide screens. Quantitative information on the horizontal beam profile will be obtained for the 250 keV beam using a secondary electron-emission monitor (SEM-grid). The low range of 250 keV electrons in suitable grid materials make the design of this monitor particularly delicate. A non-rotating magnetic lens upstream of the SEM-grid will enable the calculation of the beam emittance from measured profiles using the '3-gradient' technique.

The transverse profile of the beam after acceleration in the capture cavity will be measured using optical transition radiation (OTR) from a thin metallic foil placed in the beam path. As above, profile measurements for different settings of the first of the triplets will allow calculation of the emittance of the accelerated beam. In particular, the use of an image intensifier coupled to a CCD camera may permit time resolved emittance measurements of a small window (>100 ns) within the macro-pulse. Streak camera measurements of the OTR signal will permit measurement of the bunch length with 2 ps resolution. A second SEM-grid, placed at the focal plane of the bending magnet of the beam analysis line will measure the horizontal profile of the deviated beam thus allowing measurement of the energy dispersion. The SEM-grid will have forty tungsten wires of 0.1 mm diameter placed 2 mm apart and will provide an energy resolution of 0.1%. The vertical profile of the deviated beam will be measured using OTR.

Faraday cups, placed before the capture cavity and the first cryomodule, will be used during commisioning of the linac which will start cautiously with reduced pulse-widths of 10 μs, gradually building up to the full 800 μs pulse-width. X-ray monitors placed in the neighbourhood of beam collimators will provide an alarm in the event of beam scraping.

3. INJECTOR SIMULATIONS

We have performed extensive modelling of the injector beam dynamics from the exit of the electrostatic column to the entrance of the first cryomodule using the simulation code PARMELA[7]. Initial runs were used to optimise the distance from the SHB to the capture cavity for reasonable SHB field

amplitudes. The distance between the gun and the SHB is set to a minimum while still allowing space for appropriate elements (pumping, focusing, steering, diagnostics...). The simulation uses the electromagnetic fields of the capture cavity and SHB as calculated from their geometries using SUPERFISH. In the case of the capture cavity the important contribution of the leakage field is taken into account. The final layout of the injector is shown in figure 1. To maintain reasonable transverse beam sizes four magnetic lenses are employed between the gun exit and the entrance to the capture cavity cryostat, their positions and field strengths being optimised in the simulation.

At the time of writing the largest uncertainty among the beam parameters is the size and divergence of the beam which will emerge from the electrostatic column. We assume for the moment therefore, as reference input parameters to the code, a maximum beam radius of 2.5 mm, a maximum divergence of 6 mrad (edge emittance = 15 mm-mrad), an energy of 250 keV, a pulse-width of ± 150° at 1.3 GHz and a bunch population of 2.31×10^8. Initially we have used a capture cavity field corresponding to a maximum energy gain of 15 MV/m but our simulations show that equally good beam characteristics can be found for energy gains as low as 7MV/m. A lower RF field offers the advantage that the RF focusing effect of the cavity is reduced leading to a less divergent beam exiting the structure. This in turn makes the matching of the beam to the linac less sensitive to the setting of the triplets[8]. In addition the required performance of the capture cavity is easier to achieve. The simulations show that de-bunching of the beam in the long (6.36 m) transport section between the capture cavity and the linac is negligible for energy gains of 10 MV/m and we now take this value as our 'reference case'. The final beam characteristics at the exit of the capture cavity are shown in table 2 and can be seen to be compatible with the injector specification.

Table 2
Injector beam characteristics as calculated by PARMELA
(for capture cavity energy gain of 10 MV/m)

Energy	9.9 MeV
RMS phase width	0.77°
Total phase width	3.2°
RMS bunch length	0.49 mm
RMS energy spread	78 keV
Total energy spread	300 keV
Relative energy spread (rms)	0.8%
Norm. rms emittance (both planes)	4.2 mm-mrad

4. ACKNOWLEDGEMENTS

We are indebted to many of our fellow TESLA collaborators for discussions regarding the injector in the course of numerous TTF workshops and meetings.

5. REFERENCES

[1] B. Dunham and M. Jablonka, "Modelling of a High Charge Injector for the TESLA Test Facility", these proceedings.
[2] B. Aune et. al., "Improvement of the Electron Injection for the ALS Electron Linac", Proc. of the Linear Accelerator Conference, California, USA, SLAC report 303, 1986.
[3] H. Genz et. al., "Operational Experience and Results from the S-DALINAC, Proceedings of EPAC 92, Berlin, FRG, March 1992, pp 49-51.
[4] W.B. Herrmansfeldt, "EGUN - An Electron Optics and Gun Design Program", SLAC report 331, 1988.
[5] J. Chaumont, private communication.
[6] K.Scheidt and F. Loyer, "Synchrotron Injector Beam Position Monitor System", Proceedings of EPAC 92, Berlin, FRG, March 1992, pp 1121-1123.
[7] We use a version of the original PARMELA code which has undergone some revision. See B. Mouton, LAL/SERA 93-455, September 1993.
[8] H. Weise, private communication.

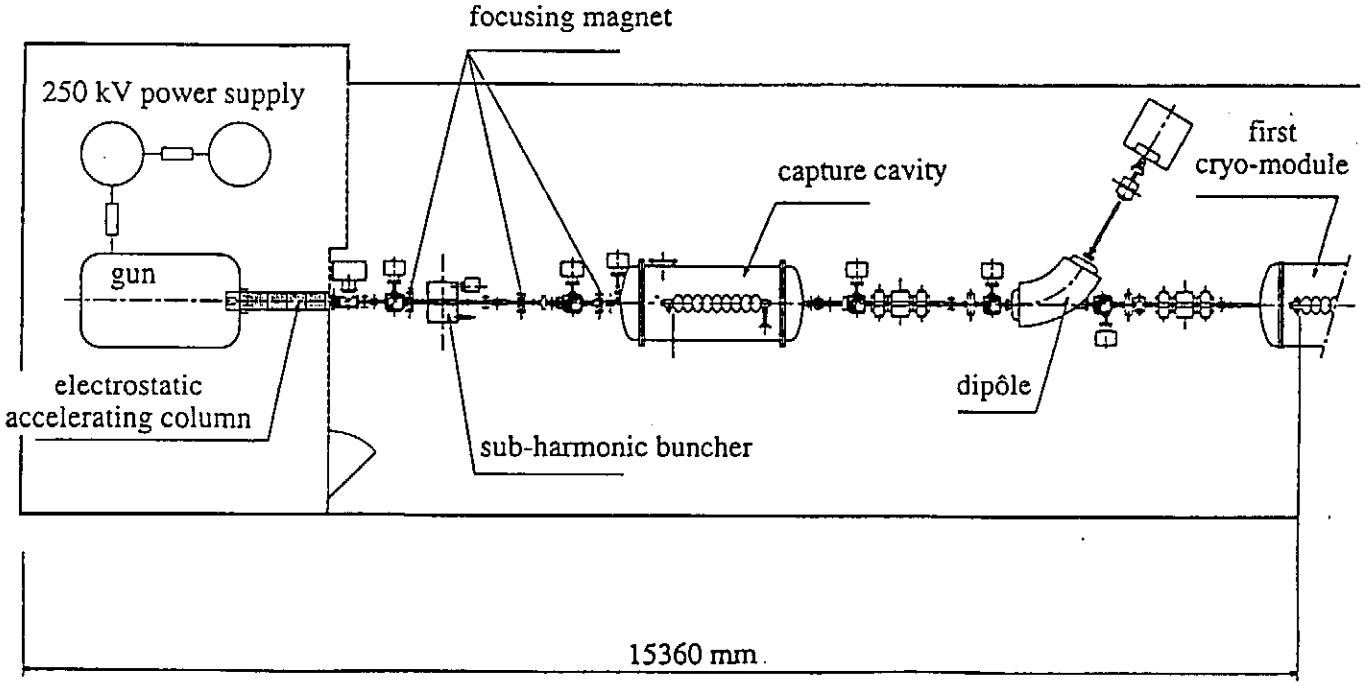

Figure 1. Schematic Layout of TTF Injector.

Quadrupolar Wakefield Induced Single-Bunch Emittance Growth in Linear Colliders

Stéphane FARTOUKH, Olivier NAPOLY
CEA, DSM/DAPNIA/Service d'Etudes des Accélérateurs
CE-Saclay, F-91191 Gif-sur-Yvette CEDEX, France

Abstract

Emittance dilution can be induced in linear colliders by the short range quadrupolar wakefields generated, even in perfectly aligned accelerating structures, by the charge distribution of flat beams. We consider a linac with a constant phase-advance FODO lattice and we calculate, for different energy scaling laws of the beta functions along the linac, the single-bunch transverse emittance growths for a two-particle model where the bunch is represented by a head and a tail centered beam ellipse. We analyze the implication of this effect for the linar collider designs.

1 INTRODUCTION

Preserving the beam transverse emittances from being degraded along the linacs in order to reach the design luminosity at the interaction point is a major challenge of the future linear collider design. Many years ago, quadrupole wakefields were recognized as a possible source of emittance dilution [1] along the linac of the SLAC linear collider. Quadrupole wakefields are induced by the beating of the horizontal and vertical beta-functions which, even for round beams, generates a non-zero transverse charge quadrupole moment proportional to the beam averaged $\langle x^2 \rangle - \langle y^2 \rangle$. They in turn create a quadrupole gradient focusing error along the beam, which modifies the designed beam transport optics of the linac. However, it was soon realized that dipole wakefields are the dominant source of emittance growth. This is essentially due to the facts that, first the dipole transverse wake potential grows more rapidly with respect to the transverse coordinates (that is linearly rather than quadratically for the quadrupole one) and, second the quadrupole moment of round beams rapidly averages to zero along the linac.

In the next linear collider the obligation, related to beamstrahlung, to accelerate flat beams with a large horizontal to vertical emittance ratio reinforces the expected effect of quadrupole wakefields because the quadrupole moment, dominated by the horizontal average $\langle x^2 \rangle$, remains positive along the linac. Moreover, unlike the dipole one, the quadrupole wake of a centered beam accelerated along a perfectly aligned linac does not vanish. Since the single-bunch emittance growth is a collective effect proportional to N^2, where N is the bunch population, depending in an essential way on the injection energy and on the focalisation along the linac, it is important to know what is the maximum bunch charge which can be accelerated without degrading the transverse emittance for given injection energy and focalisation optics. This is the question we want to answer in this paper by calculating the single-bunch emittance growth induced by quadrupole wakefields in the framework of the "2 particle model" where the bunch is modeled by 2 beam ellipses representing the head and the tail of the bunch. We will consider a bunch injected on-axis in a perfectly aligned linac. We will assume FODO lattice with a *constant* phase-advance and a scaling of the FODO-lengths and beta-functions as E^α, where E is the energy along the linac.

2 CALCULATION OF THE EMITTANCE GROWTH

2.1 The 2-particle model

We consider a bunch formed by 2 slices separated by Δz. The two slices have identical beam matrix Σ_0 at injection. While the first slice obeys the design focalisation along the linac, the second one is affected by the quadrupole gradient induced by the quadrupole wake of the first slice in the accelerating structures. Their beam matrices Σ_1 and Σ_2 therefore differ at the linac exit, although their emittances stay equal. Parametrizing a beam matrix as

$$\Sigma = \epsilon \begin{pmatrix} \beta & -\alpha \\ -\alpha & \gamma \end{pmatrix}$$

with $\epsilon = \sqrt{\det \Sigma}$ the emittance, the total emittance of the bunch is given by

$$\epsilon_b = \sqrt{\det\left(\frac{\Sigma_1 + \Sigma_2}{2}\right)} = \epsilon_1 \sqrt{1 + \frac{1}{4}(\delta\alpha^2 - \delta\beta\,\delta\gamma)}$$

where $\delta\alpha$, $\delta\beta$ and $\delta\gamma$ are the differences of the α, β and γ parameters between the two slices. At the lowest order, the emittance growth is then given by

$$\frac{\delta\epsilon}{\epsilon} = \frac{1}{8}(\delta\alpha^2 - \delta\beta\delta\gamma)$$

2.2 Transverse motion with focusing error

The transverse motion of the first slice in the linac is governed by the Hill equation with an acceleration term

$$x'' + E'/E\,x' + K\,x = 0$$

where x represents either transverse coordinate, E' is the energy gradient and K the focusing gradient along the linac. We assume that the tail slice feels a focusing gradient δK due to the quadrupole wake from the head slice

in the accelerating structures [1]. Denoting by $R(s,s')$ the transfer matrix from position s' to s along the linac associated with the gradient K, and by $(R+\delta R)(s,s')$ the one associated with $K+\delta K$, one has

$$\delta\Sigma = \Sigma_2 - \Sigma_1 = \delta Q \cdot \Sigma_1 + \Sigma_1 \cdot \delta Q^{\mathsf{T}}$$

to first order in δR, with δQ the following matrix

$$\delta Q = \delta R(s_1,s_0) \cdot R^{-1}(s_1,s_0) \ ,$$

δQ^{T} its transpose, and s_0 and s_1 the beginning and end positions in the linac. The transfer matrix obeys the following differential equation

$$\partial_s R(s,s') = A(s) \cdot R(s,s')$$

with the matrix $A(s)$, deduced from Hill's equation, given by

$$A(s) = \begin{pmatrix} 0 & 1 \\ -K(s) & -(E'/E)(s) \end{pmatrix} .$$

The matrix δQ can be calculated by integrating the equation for the difference δR. Neglecting the difference $\delta(E'/E)$ in the accelerating gradient between the slices which originates from the RF-phase and the longitudinal wakefield, one gets at first order in δK

$$\delta Q = \int_{s_0}^{s_1} ds\, R(s_1,s) \cdot \delta A(s) \cdot R(s_1,s)^{-1} \ ,$$

with

$$\delta A(s) = \begin{pmatrix} 0 & 0 \\ -\delta K(s) & 0 \end{pmatrix} .$$

The above expression of δQ only involves the R_{12} and R_{22} matrix elements of $R(s_1,s)$, which can be written as

$$R_{12}(s_1,s) = \sqrt{\frac{E}{E_1}}\sqrt{\beta\beta_1}\sin(\Delta\psi)$$
$$R_{22}(s_1,s) = \sqrt{\frac{E}{E_1}}\sqrt{\frac{\beta}{\beta_1}}(\cos(\Delta\psi) - \alpha_1\sin(\Delta\psi))$$

where $\Delta\psi$ is the phase advance from s to s_1. This leads to the following expression of the difference between the head and tail beam matrices

$$\delta\Sigma = \epsilon_1 \int_{s_0}^{s_1} ds\, \delta K(s)\,\beta(s) \begin{pmatrix} -\beta_1 \sin & \alpha_1 \sin - \cos \\ \alpha_1 \sin - \cos & \frac{\sin}{\beta_1}(1+2\alpha_1 \tan - \alpha_1^2) \end{pmatrix}$$

where the argument of the trigonometric functions is $2\Delta\psi$. The emittance growth at the lowest order in the gradient error δK is then simply given by

$$\frac{\delta\epsilon}{\epsilon} = \frac{1}{8}\left|\int_{s_0}^{s_1} ds\, \delta K(s)\,\beta(s)\, \exp(2i\Delta\psi)\right|^2 .$$

2.3 The quadrupole wake induced focusing error

As first discussed in [1], the quadrupole wakefields created by the first slice and averaged over a long accelerating section induce a transverse Laplace force given by

$$e(\vec{E} + \vec{v}\times\vec{B}) = N e^2\, w_2(\Delta z)\, Q_1\, (x\hat{x} - y\hat{y})$$

with N the bunch population, $Q_1 = \langle x^2\rangle - \langle y^2\rangle$ the transverse quadrupole moment of the head slice, $\hat{x}$ and $\hat{y}$ the unit vectors in the x and y directions, and w_2 the average quadrupolar wake potential [2] of the accelerating structure, assumed axisymmetric, per unit length and unit charge. As in [1], we assume that there is no source of xy-coupling in the linac and we neglect the effect of the skew-quadrupolar wakefields proportional to $\langle xy\rangle$. For flat beams, the large horizontal over vertical emittance ratio allows the following approximation

$$Q_1(s) = \epsilon_x(s)\,\beta_x(s) - \epsilon_y(s)\,\beta_y(s) \simeq \epsilon_x(s)\,\beta_x(s)$$

Translated in the equation of motion, the above Laplace force gives rise to the following focusing gradient

$$\delta K(s) = -\frac{N e^2}{E(s)}\, w_2(\Delta z)\, \epsilon_x(s)\,\beta_x(s)$$

which we parametrize as $\delta K(s) = -A(s)\,\beta_x(s)$ for later convenience. Notice that the coefficient $A(s)$ scales like the inverse of the energy squared along the linac.

2.4 Emittance Growth after one FODO cell

The emittance growth after one FODO cell can be easily calculated by assuming that the energy is constant over the cell and that the beam is matched. In fact, we consider a cell with μ phase-advance starting by either half a focusing quadrupole F/2 or half a defocusing one D/2. The horizontal and vertical emittance growths are then given by

$$\frac{\delta\epsilon_{x,y}}{\epsilon_{x,y}} = c_{x,y}^2\,\frac{A^2\,L^6}{2}$$

where L is the distance between two quadrupoles. The coefficients c_x and c_y depend on the phase advance and on the cell type. As shown in Table 1 for 60° and 90° phase advances, they are always of the order of one.

Table 1: Coefficients $c_{x,y}$ for the single cell emittance growth.

μ	c_x at F/2	c_y at F/2	c_x at D/2	c_y at D/2
60°	3.37	-1.73	4.63	-1.25
90°	0.727	-1.66	3.27	-1.00

2.5 Emittance Growth over the linac

To calculate the emittance growth over the linac, we assume that the phase advance per cell μ is constant along the linac while the length L scales as $L_0(E/E_0)^\alpha$, E_0 being the injection energy and L_0 the distance between two quadrupoles in the first cell. To simplify the calculation, we also assume that the linear rise of the energy along the linac is slow compared to the beta-wavelength

$$E'/E \ll 1/2L \ .$$

The energy can then be approximated by a step function such that it is constant and the beam is assumed to

Table 2: 500 GeV c.m. energy linear collider parameters and characteristic length L_c for $E_0 = 5$ GeV.

	CLIC	VLEPP	NLC	SBLC	TESLA
f_{RF} [GHz]	30	14	11.4	3	1.3
N [10^9]	6	200	6.5	29	50
$\gamma\epsilon_x$ [10^{-6}m]	1.8	20	5	10	20
σ_z [μm]	170	750	100	500	1000
$W(2\sigma_z)$ [cm^{-5}]	4×10^4	560	200	0.3	
$w_2(2\sigma_z)$ [V/C m]	3.6×10^{24}	5.0×10^{22}	1.8×10^{22}	2.7×10^{19}	5.0×10^{16}
L_c [m]	20	12	81	340	1830

be matched in every cell. Since the beta functions scale like the length L, the gradient error δK then scales as $\delta K_0 (E/E_0)^{\alpha-2}$ where δK_0 is the gradient error in the first cell. The integral over the linac entering in the expression of the emittance growth can then be replaced by a sum over the N FODO cells composing the linac, leading to

$$\frac{\delta\epsilon}{\epsilon} = \frac{1}{8}\left|\sum_{n=1}^{N} e^{2in\mu}\left(\frac{E_n}{E_0}\right)^{3\alpha-2}\int_{s_0}^{s_0+2L_0} ds\, \delta K_0(s)\,\beta_0(s)\, e^{2i\Delta\psi}\right|^2 .$$

The emittance growth over the linac is therefore equal to the emittance growth after the first cell $(\delta\epsilon/\epsilon)_0$ times a correction factor as given by

$$\frac{\delta\epsilon}{\epsilon} = \left(\frac{\delta\epsilon}{\epsilon}\right)_0 \left|\sum_{n=1}^{N} e^{2in\mu}\left(\frac{E_n}{E_0}\right)^{3\alpha-2}\right|^2 .$$

For an infinite number of cells, the above alternating sum diverges when $\alpha > 2/3$, oscillates when $\alpha = 2/3$, and converges when $\alpha < 2/3$. This clearly shows the special role of the $\alpha = 2/3$ scaling, independently of the value of the phase advance μ. For finite N, the sum can be easily evaluated when μ is a submultiple of 2π. In particular, for 90° phase advance, writing

$$\left(\frac{E_{n+1}}{E_0}\right)^{3\alpha-2} - \left(\frac{E_n}{E_0}\right)^{3\alpha-2} \simeq (3\alpha-2)\frac{2L_n E'}{E_0}\left(\frac{E_n}{E_0}\right)^{3\alpha-3}$$

and then replacing the sum over the cells back to an integral over the linac, leads to

$$\frac{\delta\epsilon_{x,y}}{\epsilon_{x,y}} = c_{x,y}^2 \frac{A_0^2 L_0^6}{8}\begin{cases} \left(\left(\frac{E_1}{E_0}\right)^{3\alpha-2} - 1\right)^2 & \text{if } \alpha \neq \frac{2}{3} \\ (1-(-1)^N)^2 & \text{if } \alpha = \frac{2}{3} \end{cases}$$

where E_1 is the beam energy at the end of the linac. When $E_1 \gg E_0$, the emittance growth scales like $(E_1/E_0)^{6\alpha-4}$ if $\alpha > 2/3$, and is independent of E_1 if $\alpha \leq 2/3$. From the above discussion on the $N \to \infty$ convergence, the critical exponent 2/3 does not depend on the value of the phase advance. In fact the emittance growth for 60° phase advance is given by the 90° result divided by $\sin^2(\pi/3)$.

3 IMPLICATION FOR LINEAR COLLIDER DESIGNS

To evaluate the magnitude of this effect for the linear collider designs, we introduce the characteristic length L_c as

$$L_c = A_0^{-1/3} = \left(\frac{N r_e^2 w_2(\Delta z)\,\epsilon_x(s_0)}{E_0}\right)^{-1/3} .$$

The emittance growth induced by quadrupole wakefields then reads

$$\frac{\delta\epsilon_{x,y}}{\epsilon_{x,y}} = \frac{c_{x,y}^2}{8}\left(\frac{L_0}{L_c}\right)^6 \begin{cases} \left(\left(\frac{E_1}{E_0}\right)^{3\alpha-2} - 1\right)^2 & \text{if } \alpha \neq \frac{2}{3} \\ (1-(-1)^N)^2 & \text{if } \alpha = \frac{2}{3} \end{cases}$$

so that it is small only when $L_0 \ll L_c$. The length L_c is given in Table 2 for all linear colliders (except JLC for which the RF frequency is not yet known) assuming an injection energy $E_0 = 5$ GeV. The wake potential w_2, evaluated for $\Delta z = 2\sigma_z$, has been calculated with TBCI [2] for TESLA and, for the other designs, derived from the wake function $W = 4\pi\epsilon_0 w_2$ given in [1] for the SLC 3 GHz cavities down to a distance of 3 mm. For RF frequencies f_{RF} higher than 3 GHz, we used the following scaling formula

$$W^{(f_{RF})}(2\sigma_z) = \lambda^5\, W^{(3\,\mathrm{GHz})}(2\,\lambda\,\sigma_z)$$

with $\lambda = f_{RF}/3\,\mathrm{GHz}$.

As shown by Table 2, the emittance growth can be sizeable for the designs with the highest RF frequency. This is even more true if the linac optics scales linearly with energy ($\alpha = 1$) due to the correction factor $(E_1/E_0)^2$.

4 CONCLUSION

Using a simple "2 slice model", we have estimated at the lowest order in the wake potential the emittance growth induced by the transverse quadrupole wakefields for a flat bunch accelerated in a perfectly aligned linac. The emittance growth increases quadratically with the population and the horizontal emittance of the bunch. It depends also strongly on the injection energy E_0 and the linac focalisation optics. Assuming that the half beta-wavelength is given by $L_0(E/E_0)^\alpha$ as a function of the energy E along the linac, the emittance growth is proportional to $(L_0/L_c)^6$ with a correction factor $(E_1/E_0)^{6\alpha-4}$ when $\alpha > 2/3$. The characteristic length L_c sets a lower limit on the beta-wavelength close to 20 meters, and even below for $\alpha = 1$, for the highest RF-frequency linear collider designs.

5 REFERENCES

[1] A.W. Chao and R.K. Cooper, "Transverse Quadrupole Wake Field Effects in High Intensity Linacs", Particle Accelerators, vol. 13, pp. 1-12, 1983

[2] T. Weiland, "Comment on Wake Field Computation in Time Domain", NIM,vol. 216, pp. 31-34, 1983

Field Stabilization in a Superconducting Cavity Powered in Pulsed Mode

Alban Mosnier, Jean-Michel Tessier
CEA, DSM/DAPNIA/Service d'Etudes d'Accélérateurs
CE-SACLAY,F-91191 Gif/Yvette Cedex, France

Abstract

The Lorentz forces (also called "radiation pressure") and microphonics, by shifting the cavity frequency, are the main bunch-to-bunch energy spread sources. With superconducting cavities operating in pulsed mode, the Lorentz Forces problem arises from the wall deformation response time [1] . The cavity frequency goes on to shift after the field rise time, whereas the beam is passing through the cavity. After a brieve review of the two methods [2,3] coping with the Lorentz forces detuning when one cavity only is fed by one klystron, the effect of parameters spreads is studied when several cavities are fed by one klystron. External feedback loops to minimize the residual amplitude and phase errors are then added and the loop gains are determined. The influence of a spread in external Qs (from coupler tolerances or on purpose for having different fields from cavity to cavity) is analysed and the extra power needed to stabilize the total accelerating voltage is given after an optimization of the beam injection time. Finally, microphonics effects, which can increase dramatically the field errors, are considered and a remedy, allowing to alleviate the problem, is proposed [4].

1. INTRODUCTION

The beam energy spread at the exit the TESLA linac must be below the energy acceptance of the final focus but also small enough to limit the emittance dilution due to chromatic and dispersive effects. The intra-bunch energy spread, resulting from the rf sinusoidal wave and the induced bunch wake potential, can be reduced to about 5.10^{-4}, by running properly the bunch off the crest of the accelerating wave [5]. Any cavity field fluctuation, in phase and in amplitude, during the beam pulse will generate some bunch-to-bunch energy spread. It would be desirable to keep this energy spread below the intra-bunch energy spread in order to assure that the bunch-to-bunch chromatic effects will be no worse than the single bunch ones.

2. DESCRIPTION OF METHODS

During the field rise time, the generator frequency must be locked in any case on the cavity frequency which is shifting because of the Lorentz forces. The phase lock can be provided by a voltage controlled oscillator (VCO) or a self-excited loop. In the first method the generator frequency is then suddenly switched to the reference frequeny (1300 MHz) as soon as the beam is injected into the cavity, leading to a frequency jump at the beam injection time. The secong method uses the self-exciting loop principle during the field rise time and during the beam pulse, without any frequency jump. To minimize the phase shift for both methods during the beam traversal, the cavity frequency must be higher at the beginning (positive phase slope) and lower (negative phase slope) at the end than the reference frequency. The figure 1 gives the cavity frequency shifts (relative to the reference frequency) and the phase errors evolutions for the TESLA cavity parameters when the initial phase and the initial cavity frequency have been adjusted to cancel the phase deviation when the beam is injected and to minimize the phase error during the beam pulse.

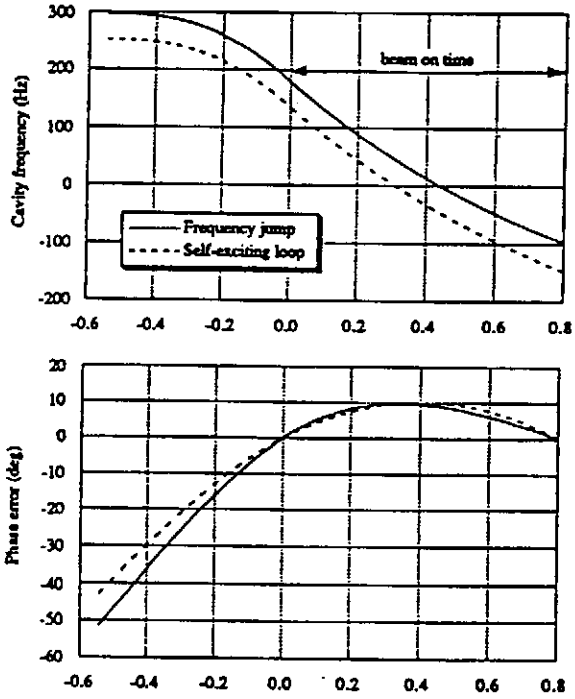

Figure 1 : Relative cavity frequency and phase error for both methods

The TESLA and TTF parameters and the resulting amplitude and phase errors, assuming one cavity driven by one generator, are listed in the table below for comparison.

	TESLA	TTF
Accelerating Gradient	25 MV/m	15 MV/m
Beam current	8 mA	8 mA
electric time constant τ_e	0.78 ms	0.78 ms
mechan. time constant τ_m	1 ms	1 ms
beam injection time $\tau_e \ln 2$	0.54 ms	0.54 ms
beam pulse duration	0.8 ms	0.8 ms
detuning parameter K	1 Hz/(MV/m)^2	1 Hz/(MV/m)^2
Amplitude error	$5\text{-}6\ 10^{-3}$	$0.7\ 10^{-3}$
Phase error	10 deg	3.5 deg

Without stiffening system, the static Lorentz forces detuning has been estimated to be slightly higher than 1000 Hz for a field gradient of 25 MV/m. With the stiffening system, the detuning reduces to 400 or 600 Hz according to the rigidity of the tuning system. A detuning parameter of 1 $Hz/(MV/m)^2$ has been conservatively retained. The mechanical time constant, which parametrizes the dynamic wall deformation response, has been measured on a 5-cell cavity at 1.5 GHz, and is assumed to be of the same order of magnitude.

3. MEASUREMENTS ON A 1.5 GHZ CAVITY

In order to prove the validity of the methods, they were tested on existing 5-cell cavities at Saclay. Since the Lorentz forces detuning is much stronger on these non-stiffened cavities (a factor 3.6 higher), the same static detuning of about 230 Hz was obtained with a lower accelerating gradient (8 MV/m instead of 15 MV/m). In addition, the beam current was simulated by injecting a rf signal in phase with the beam. The plots 2 show the amplitude and phase errors for the self-exciting loop arrangement during the field rise time and the beam pulse with different initial tunings of the cavity. The phase error was set to zero at the beginning of the beam pulse by readjusting the initial phase for each tuning value. For optimal initial tuning (200 Hz higher than the reference frequency), the amplitude and phase fluctuations are minimum, whereas the amplitude is growing with the time when the cavity is not correctly tuned and the phase slope is positive (negative) just after the field rise time when the tuning frequency is too high (low).

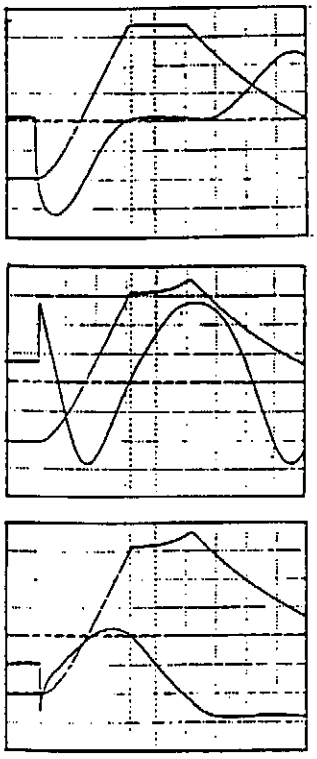

Figure 2 : Measured field amplitude and phase error for optimal (top) too high (center) and too low tunings (bottom) for the self-exciting loop arrangement

4. EFFECTS OF PARAMETERS SPREADS

In the aim to reduce the cost of the power sources, two 8-cavity modules are powered by one 5 MW klystron. Since the rf and mechanical parameters of the cavities are expected to be not identical, the effects of a spread in the different parameters have been studied. During the field rise time, the generator frequency has to be locked on the varying cavity frequency. Since the cavities cannot be initially perfectly tuned, the frequency tracking must be carried out by using the phase signal from the vectorial sum of all cavity voltages and not from a single cavity voltage. With this arrangement, there is no dramatic performance degradation when a spread in the initial cavity tuning or a spread in the detuning parameter K and mechanical time constant are introduced. The figure 3 shows the histograms of the errors for a gradient of 15 MV/m and with 1000 different simulations, where the initial tuning of the 16 cavities has been randomly varied between ± 40 Hz (corresponding to a tuning angle error of 10°).

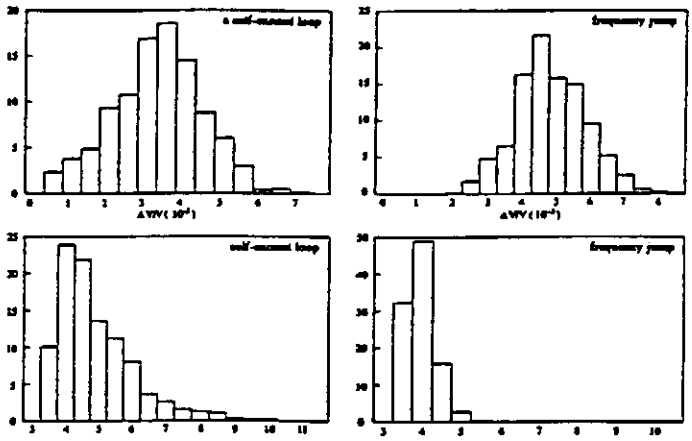

Figure 3 : amplitude (top) and phase (bottom) histograms with static cavity tuning errors for self-excited loop (left) and frequency jump (right) methods

In the same way, the histograms of the errors for a simultaneous spread of 20 % in the detuning parameter K and the mechanical time constant, are showed on the figure 4, for 1000 simulations.

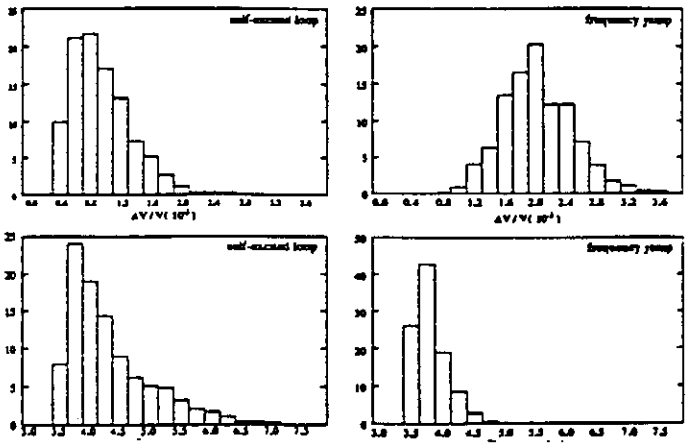

Figure 4: amplitude (top) and phase (bottom) histograms with K and τ_m spreads for self-excited loop (left) and frequency jump (right) methods

5. FEEDBACK LOOPS

Feedback loops have to stabilize the field fluctuations, which are induced mainly either by Lorentz forces or by microphonics detunings, while keeping the needed extra rf power (peak and average) within a reasonable level. In order to reduce the coupling between amplitude and phase feedback, the feedback loops must use a vectoriel modulator, in which an in phase signal, proportional to the amplitude error and an out of phase signal, proportional to the phase error are added to the main drive signal. Loop gains of 50 for the phase and 100 for the amplitude are a good compromise between the extra needed rf power and the resulting amplitude and phase errors. Taking into account the perturbation due to the Lorentz forces only, the resulting energy spread is of the order of 10^{-5} for an increase of the rf powers of about 10% peak and 4 % average.

6. Q-SPREAD EFFECTS

In order to make the best possible use of the SC gradient capability, it would be advantageous to operate each cavity at its maximum field. Since the cavity tuning is not allowed to play with (see previous study), the easiest way of varying the cavity gradients in a chain fed by one klystron, is to change the external Qs from cavity to cavity. Even without Lorentz forces detuning however, a spread in external Qs, resulting from coupler tolerances or on purpose for having different cavity fields, will affect dramatically the amplitude error of the total voltage, because the source is not any more matched to the beam loads. This error must therefore be minimized first by means of the incident power (P_g) and of the beam injection time (t_0), before attempting to close the feedback loops, which would result to a huge extra rf power. Assuming for example a uniform spread in accelerating field around 25 MV/m of a string of 16 cavities, the figure 5 gives the required source power in kW as a function of the total voltage fluctuation for different widths of the gradient spread (10, 15 and 20 %). About 230 kW per cavity (instead of 200 kW) are needed to reach amplitude errors of the order of 10^{-4} for a gradient spread of ± 20 %.

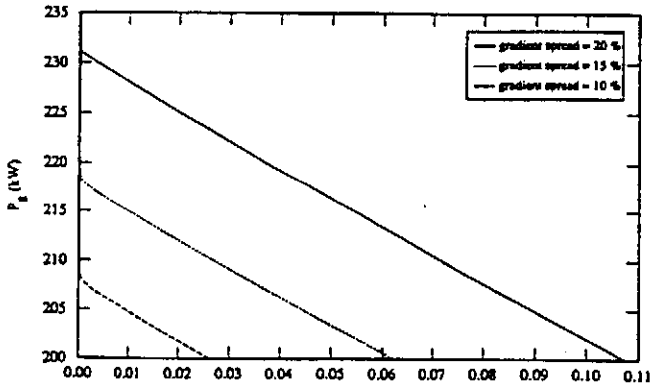

Figure 5: Needed source power (in kW) vs. the fluctuation level of the total voltage

If the Lorentz forces effects are included, the final energy spread is of the order of 2 10^{-4} with the gains of 100 and 50 for the amplitude and phase loops. The net additional powers to be delivered by the source are finally 30 % peak and and 20 % average with a Q-spread of ± 20 %.

7. MICROPHONICS EFFECTS

The main effect of microphonics, because they change the cavity frequency, is to displace the rf phase with respect to the beam, assuming that the initial phase is fixed. The demand of rf power from the feedback loops would then be huge. Instead of having a fixed initial phase, we could think of a feedback system acting on this initial phase to recover a vanishing phase shift when the beam is coming. Unfortunately the frequencies of mechanical vibrations are expected to be around and above the TESLA repetition rate of 10 Hz, making a direct feedback unefficient. Instead of having fixed phase and amplitude references of the feedback loops, floating references following the actual phase and amplitude at the beginning of the beam pulse (by means of a tracking-and-hold circuits), can solve the microphonics problem in case of too large mechanical vibrations. The beam energy is then constant within a beam pulse but could slightly fluctuate from pulse to pulse. This is not harmful for a long machine like TESLA because the errors coming from the Lorentz forces detuning are correlated whereas the errors coming from the microphonics detuning (jitter) are essentially uncorrelated. The figure 6 shows for example the phase error curves during the beam pulse for 3 cavity tunings, including the Lorentz forces effects : the optimal one and with a shift of ± 50 Hz around due to microphonics, giving moderate extra powers (20% peak and 6% average), with amplitude and phase loop gains of 100 and 50.

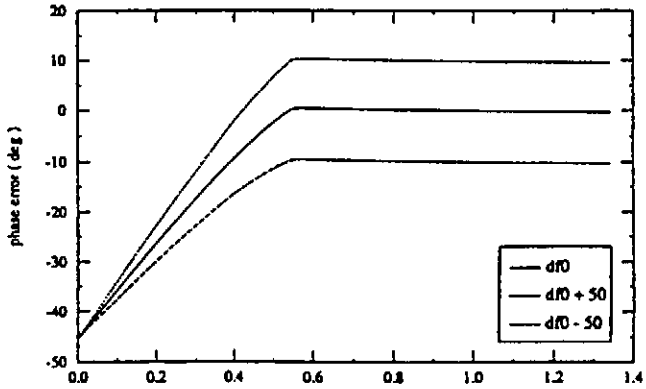

Figure 6: Phase profiles for the optimal initial tuning and ± 50 Hz around

8. REFERENCES

[1] A. Mosnier, "Dynamic measurements of the Lorentz Forces on a MACSE cavity", TESLA Report 93-09

[2] H. Henke, B. Littmann, "Mechanical Parameter Influence on the TESLA Cavity under Lorentz Forces", TESLA Report 93-12

[3] A. Mosnier, "Field Stabilization with Lorentz Forces", DAPNIA/SEA Note 93-03

[4] A. Mosnier and J.-M. Tessier, "Field Stabilization Study for TESLA", DAPNIA/SEA 94-07

[5] A. Mosnier and O. Napoly, "Energy spread Induced in the TESLA Linac", TESLA Report 93-07

FFADA
Computer Design of Final Focus Systems for Linear Colliders

Olivier NAPOLY, Bruce DUNHAM
CEA, DSM/DAPNIA/Service d'Etudes des Accélérateurs
CE-Saclay, F-91191 Gif-sur-Yvette CEDEX, France

Abstract

FFADA, for Final Focus Automatic Design and Analysis, is a program which allows the user to automatically design a generic final focus system corresponding to a set of a few basic beam and machine parameters for linear colliders. It also derives the main properties of the designed system in terms of momentum acceptance, tracking, collimation requirements and Oide effect. Finally, the program analyzes the effect of magnet misalignment and field errors on the beam parameters and luminosity at the interaction point.

1 INTRODUCTION

Final focus systems (FFS) must reduce the colliding beam to nanometer spot sizes at the interaction point (IP) of future linear colliders. With the transverse emittances foreseen, the corresponding β^* are in the range of 0.1–1mm. The main difficulty is then to correct the chromatic aberrations which dominate the linear optics as soon as the energy spread is larger than β^*/l^*, where l^* is the distance separating the IP from the last focusing quadrupole. A generic system, adapted from the SLC final focus optics [1] has been derived [2, 3] which is free from 2nd and 3rd order aberrations. This solution is highly symmetric, provides several image points of the IP to monitor the beam, and contains the minimal number of four sextupoles (two non-interleaved pairs) for the chromatic correction. It is well adapted to designs where the beam energy spread is below 1% and, with additional sextupoles [4, 5], it can provide a larger energy acceptance.

The generic system is a telescopic transfer line which includes: a matching telescopic transformer (MT) with π–phase advance, achieving the first demagnification of the beam with two quadrupole doublets; a chromatic correction section (CCS); that is, a +1–transformer with 4π–phase advance including two sextupole pairs to cancel the second order chromatic aberrations generated mainly by the last focusing doublet; a final telescopic transformer (FT) achieving the final demagnification of the beam to the desired spot size at the IP, with π–phase advance again and two quadrupole doublets.

In this paper we describe the computer program FFADA which automatizes the operations needed to design and analyze such a generic final focus system. In this way, a FFS can be rapidly optimized for a set of basic beam and machine parameters, and adapted to later changes of these parameters. After generating the telescopic transfer line matched to second order, FFADA analyzes the following properties:

1) the energy acceptance of the system, both analytically and by tracking;
2) the beta-functions and beam envelopes in the last doublet down to the IP;
3) the effect of the synchrotron radiation in the last doublet on the beam spot size [6] and the beam collimation requirements;
4) the sensitivity of the luminosity to beam transverse offset and dispersion at the IP;
5) the tolerances to misalignment and field errors of the magnets of the system.

FFADA runs under UNIX SystemV with FORTRAN and the optics code MAD [7] available. Its structure is modular so that new functions can be easily included. The results are presented in a few output files associated with each modules, and in a series of output files for graphics presentation. An extended presentation of the program FFADA can be found in [8].

2 INPUT PARAMETERS

For the sake of the presentation, we consider an hypothetical design for a "future linear collider", abbreviated to `flc`. The final focus sytem derived by FFADA and its properties are essentially determined by two input data files. The final focus optics depends on the optics and hardware parameters defined in the file `flc.ffs`, while the properties of the system, such as the bandwidth, the beam envelopes or the tolerances, are determined by the beam parameters given in the `flc.beam`.

```
                        FLC BEAM
Energy                                  [GeV]     : 250.

Horizontal RMS at the IP                [nm]      : 100.
Vertical   RMS at the IP                [nm]      :  10.

Horizontal normalized emittance         [m]       : 1.0e-6
Vertical   normalized emittance         [m]       : 1.0e-8

Longitudinal RMS                        [mm]      : 0.1
Relative energy RMS                               : 1.e-3
Energy profile case   [-1=linear, 0=zero]         : 1

Bunch population                                  : 1.0e+10
Repetition rate                         [Hz]      : 1.0e+2
```

Table 1 : Beam parameter definitions at the IP

2.1 Beam parameters

The desired beam parameters at the IP are defined in `flc.beam` (see Table 1). The transverse and longitudinal distributions are assumed Gaussian. The energy distribution is the superposition of an incoherent Gaussian distribution and a coherent energy profile $\delta(z)$ along the bunch which describes the combined effect of the RF accelerating phase and longitudinal wakefield. If not zero, the energy profile $\delta(z)$ can be selected among several options including linear or user defined profiles.

```
                Input parameters for FFS

Total length of the FFS                          [m] : 600.
Total horizontal demagnification                     : 50.
Total vertical   demagnification                     : 100.

              Parameters of Final Telescope
Horizontal FT demagnification        XM = -R22 :  10.
Vertical   FT demagnification        YM = -R44 :  20.
Length of last drift                     [m] :   3.0
Length of last but one drift             [m] :   0.35
Polarity of last quadrupole                  :   D
Length of last quadrupole                [m] :   1.1
Pole-tip field of last doublet quads     [T] :   6.
Aperture diameter of last doublet quads [mm] :  48.
Length of first drift                    [m] :   1.
Length of first doublet quads            [m] :   0.3

             Parameters of Matching Telescope
Polarity of last quadrupole                  :   D
Maximum pole-tip field                   [T] :   1.4
Aperture diameter of last quad          [mm] :   4.
Length of first drift                    [m] :   0.5

             Parameters of Microvertex Detector
Aperture diameter                       [mm] :  30.
```

Table 2 : Optics and hardware parameters of the FFS

2.2 Optics and hardware parameters

The optics, layout and hardware parameters of the final focus sytem which can be freely set are defined in `flc.ffs` (see Table 2). However, some parameters will differ in the final focus system derived by FFADA, namely: the total length of the FFS and the length of the first drift of the 2 telescopes which are the values for the thin lens solution first derived by FFADA, and are modified in the process of matching it to a thick lens one; and, the length of the last quadrupole of the final telescope which is used as a starting value for the optimization of the final telescope [2]. This length l_Q can be initially set from the condition $1/l_Q \simeq K_1(Q)l^*$ that the focal length of the last quadrupole is equal to the length of the last drift l^*. If the starting value is too far from l_Q, a thin lens solution might not be reached for the final telescope.

The aperture of the vertex detector is only used to evaluate the beam collimation requirements from the constraint that the beam-generated synchrotron radiation must not impact on it.

3 DESCRIPTION OF THE PROGRAM

FFADA is composed of several modules which are executed sequentially. Each one is dedicated to a different function and generates output and graphics files displaying the main results. Some modules needs extra auxiliary input parameters. We now describe these modules in the order in which they are executed. A detailed description of the output and graphics files is given in [8].

3.1 TELE4: analytic derivation of a thin lens solution

This module generates an analytic solution for the 2 telescopes where the last quadrupole of each telescope is a thick lens as fixed by `flc.ffs`, and the first 3 are thin lenses. This solution is obtained by solving, for the given demagnifications, the 6 dimensional system obtained by expressing the 6 independent elements of the horizontal and vertical transfer matrices as functions of the strength of the 3 thin lenses and the length of the 3 following drifts, using the solution given in [9]. Once the total length of the telescopes is known, the CCS optics is scaled to match the total length of the FFS given in `flc.ffs`.

Starting from an analytic solution for 2-doublet telescopes where the last quadrupole is already a thick lens, allows the program to automatically find a solution with 4 thick lenses.

3.2 MAD: 2nd order matching of the FFS and bandwidth calculation

This module calls the MAD program [7] in order to perform the following operations:

1. read the thin lens telescope optics generated above and the MAD input file `ccs.mad` describing the optics of the CCS;
2. match the optics of the line (MT , CCS , FT) to first and second order, with thick elements;
3. plot layout, beta-functions and dispersion;
4. plot the energy dependent beta-functions at the IP;
5. store the matched FFS optics in a MAD file.

The MAD file `ccs.mad` describing the generic CCS optics is provided with the program. With some restrictions as to the coherence of the program, it can be modified and even replaced by the user to describe another correction system.

3.3 TRACK: tracking simulations

This module calls MAD to perform tracking simulations of the FFS. A first simulation is made for 2 bunches of typically 10,000 particles distributed as defined in `flc.beam`. The beam spot sizes and the luminosity from the 2 colliding bunches are calculated from the resulting distributions. A second set of simulations is made to analyze the energy acceptance of the system. The spot sizes and luminosity are calculated for beams with Gaussian energy spread varying typically from 0 and 1%. In all cases the beam-beam forces are neglected.

This tracking module can also be activated with the program DIMAD [10]. However, this requires using a modified version of the DIMAD code in which beam energy profiles $\delta(z)$ can be generated and tracked. With the latest MAD versions (8.14 or later) as well as with DIMAD, the stochastic effect of synchrotron radiation in the magnets is taken into account.

3.4 *DBLT: beam envelopes in the last doublet, collimation and Oide effect*

This module calculates and plots various quantities relevant to the last doublet optics and to the interaction region, namely:

1) the Twiss β and α functions and the beam envelopes from the last doublet down to the IP;
2) the beam collimation requirement arising from clearing the synchrotron radiation generated by the beam in the last doublet, through a vertex detector located at the IP, and through the opposing doublet with hyperbolic or circular aperture. The requirement which minimizes the population of collimated particles, for a uniform distribution of halo, is given and used in the graphics output;
3) the Oide limit [6] for the horizontal and vertical spot sizes at the IP. The calculation is done both analytically and by tracking with MAD (or DIMAD).

3.5 *DIFFLUM: luminosity loss versus beam offset and dispersion at the IP*

For head-on collision, the luminosity is at a maximum with respect to the beam offset, dispersion and coupling at the IP. This module calculates the nominal luminosity expected for head-on collisions and the second order derivatives [11] of the luminosity with respect to the transverse position and angular offsets and dispersions of the *two beams* at the IP. In the calculations, the"hour-glass" effect is taken into account while the pinch effect is not.

3.6 *ERROR: magnet misalignment and field errors, tolerances*

After summarizing the number and types of the magnets included in the system, this module performs a detailed analysis of the effect of small 3d-displacements, 3d-rotations and field errors of the quadrupole and sextupole magnets. These effects are translated to the beam centroid and beam matrix at the IP and analyzed in terms of relative beam offset, dispersion, spot size growth, waist shift and xy-coupling at the IP.

Then, restricting to the 2d-transverse misalignments, the loss of luminosity resulting from uncorrelated random motion of all magnets of the two FFS (except the last doublet) on the one hand, and fixed displacement of the quadrupoles of the two opposing doublets on the other hand, is calculated using the 2nd order derivatives derived in DIFFLUM. This analysis is repeated with the assumption of a perfect steering correction of the beams at the IP. In the case of no steering, i.e. for uncorrected vibrations, the luminosity reduction arises mainly from the relative beam position offset. In the case where the offset is corrected, the reduction arises from the remaining dispersion, including that introduced by the two opposing steering kickers which are located at the first doublet of the last telescope.

4 FUTURE DEVELOPMENTS

We have presented the first version of the program FFADA. This computer program has been written to facilitate the design, optimization and evolution of final focus systems for linear colliders. It also performs the analysis of the most important properties of the system, such as bandwidth, collimation or tolerances, and then launches tracking simulations of the line. The needed input parameters are meant to be as few and basic as possible. The further developments envisaged are as follows:

1) analyze the effect of misalignment and field errors of the dipole magnets;
2) implement the dependence of the luminosity on the 4×4 transverse phase-space submatrix of the FFS transfer matrix (e.g. include waist-shifts and xy-coupling);
3) derive tolerances on the second and higher order field errors (sextupole and higher multipoles);
4) extend the program to non-zero crossing angle;
5) interface the program with standard or widely distributed graphics software (GKS, HIGZ, TopDraw).

5 REFERENCES

[1] J.J. Murray, K.L. Brown and T. Fieguth, Proc.of Part. Acc. Conf., Washington, D.C., March 1987 & SLAC-PUB-4219 (Feb.1987).

[2] O. Napoly, T.M. Taylor and B. Zotter, Proc.of XIVth HEACC, Tsukuba, Japan (Aug.1989). See also O. Napoly and B. Zotter, CLIC Note 107 (Jan.1990).

[3] R. Helm and J. Irwin, Proc.of 1992 Linear Acc. Conf., Ottawa, Canada (Aug.1992).

[4] R. Brinkmann, "Optimization of a Final Focus System for Large Momentum Bandwidth", DESY-M-90/14 (Nov.1990).

[5] A. A. Sery, "VLEPP Final Focus System", INP Preprint 91-113 (1991).

[6] K. Oide, Phys.Rev.Letters 61,1713 (1988).

[7] H. Grote and F.C. Iselin, "The MAD Program", CERN/SL/90-13 (AP) Rev.3 (Jan.1993).

[8] B.Dunham and O.Napoly, Saclay preprint CEA/DAPNIA/SEA 94-06.

[9] Y-C Chao and J. Irwin, "Solution of a three-thin-lens system with arbitrary transfer properties", SLAC-PUB-5834 (Oct.1992)

[10] R.V. Servranckx, K.L. Brown, L. Schachinger and D. Douglas, "Users Guide to the Program DIMAD", SLAC Report 285 UC-28 (A) (May 1985).

[11] O. Napoly, Part. Acc. 40/4, 181 (1993)

Low Frequency Linear Colliders

R. Brinkmann, DESY,
Notkestr. 85, D-22603 Hamburg
for the S-Band and TESLA collaborations

Abstract

The various approaches towards a future linear collider with a center-of-mass energy of 300...500 GeV and a luminosity of $10^{33}...10^{34}$ cm^{-2} s^{-1} currently under investigation cover a frequency range from 1.3 GHz to 30 GHz for the accelerating rf. This paper reports on the status of the design for the two approaches at the lower end of this frequency scale, namely the TESLA superconducting L-band (1.3 GHz) accelerator and the approach using conventional S-band (3 GHz) structures. Common to both designs are a high AC-to-beam power transfer efficiency and relaxed tolerances relative to high frequency machines. The general layout, accelerator physic issues, and the potential for energy and luminosity upgrade for the TESLA and S-band linear colliders are discussed.

1. INTRODUCTION

Among the different design studies for a next generation e^+/e^- linear collider, the SBLC and the TESLA approaches both follow the concept of a rather low rf-frequency ω_{rf} and a moderate accelerating gradient g, which allows for a high overall efficiency and relaxed tolerances in combination with reduced wakefield effects in the linac (the wakefields scale approximately as $W_{\parallel} \propto \omega_{rf}^2$, $W_{\perp} \propto \omega_{rf}^3$). In case of the SBLC, it is proposed to use conventional travelling wave accelerating structures at 3 GHz (S-Band) and g=17 MV/m. It is to a certain extend an extrapolation of the existing SLC machine [1] operating at the same frequency, therefore likely being of all designs the one closest to existing technology and able to profit most directly from the experience gathered at the SLC. The TESLA approach uses superconducting Nb accelerating structures operating at 1.3 GHz (L-Band) and is aiming for an accelerating gradient of g=25 MV/m with a quality factor (unloaded) of $Q_0=5\times10^9$ at T=2K. The choice of 1.3 Ghz is mainly a compromise between surface resistance ($\propto\omega_{rf}^2$) on one and R/Q (favoring a high frequency) on the other side. Another argument is the availability of klystrons at this operating frequency. Whereas the advantages of very low wakefields and high acceleration efficiency are obvious, the challenge of TESLA is clearly to demonstrate that stable operation with a gradient of g=25 MV/m can be achieved not only within a laboratory experiment but on a large scale. In addition, the costs of the s.c. structures have to be drastically reduced.

The SBLC and TESLA linear collider studies are pursued at DESY in international collaborations with institutes in China, France, Germany, Italy, Japan, Netherlands, Russia and USA contributing to the technical R&D and/or the design of the 500 GeV collider. In the following, the present status of design is described. After a discussion of general parameters, the layouts of the collider interaction region, the main linac and the injection system are presented. In section 6, the upgrade potential of SBLC and TESLA is discussed. A brief summary of the R&D status is given in section 7.

2. PARAMETERS

The achievable luminosity of a linear collider is determined by the following basic parameters:

- the average power per beam P_b, which is limited by a reasonable AC-power limit and the overall AC-to-beam transfer efficiency η
- the normalized vertical emittance ε_y, limited by tolerances
- the maximum tolerable beamstrahlung energy loss $<\Delta E/E>_{rad}$, limited by background considerations and the energy resolution required by the high energy physics experiment.

Using basic relations for the luminosity and the beamstrahlung and assuming an optimum beta-function β_y^* at the interaction point (IP) equal to the bunchlength σ_z, the luminosity is in good approximation given by:

$$L = const. \times \frac{P_b}{\gamma} \times \frac{< \Delta E / E >_{rad}^{1/2}}{\varepsilon_y^{1/2}}$$

With P_b in MW, $<\Delta E/E>_{rad}$ in % and ε_y in 10^{-6}m, we find $const./\gamma \sim 2.8\times10^{32} cm^{-2}s^{-1}$ at E_{cm}=500 GeV. SBLC and TESLA achieve a high efficiency $\eta_{AC\text{-}to\text{-}beam}$ by accelerating long bunchtrains per linac pulse allowing for high P_b, at the same time keeping beamstrahlung at a low level. The required emittances and beam sizes at the IP are close to what has been achieved at the FFTB experiment [2]. A list of the main SBLC and TESLA parameters is given in table 1.

3. INTERACTION REGION, FINAL FOCUS, COLLIMATION

Keeping beamstrahlung at a low level is an essential prerequisite for acceptable background conditions and good energy resolution for the high energy physics experiment. The most important parameters concerning beam-beam effects are summarized in table 2. With the relatively large spacing between bunches (especially for TESLA with Δt_b=1μs), only the background produced per bunch crossing is relevant. Thus the small numbers of e^+e^- pairs N_{pair} outside a mask with 5cm radius and 100mrad opening angle as well as the hadronic background (N_{hadr}) are handable.

Table1: main parameters of the S-band and TESLA 500 GeV (c.m.) linear colliders

	SBLC	TESLA	
active length	29.4	20	km
t_{pulse}	2	800	μs
n_b/pulse	125	800	
Δt_b	16	1000	ns
f_{rep}	50	10	Hz
N_e/bunch	2.9	5.1	10^{10}
$\varepsilon_x/\varepsilon_y$	10/0.5	20/1	10^{-6} m
β_x^*/β_y^*	22/0.8	25/2	mm
σ_x^*/σ_y^*	670/28	1000/64	nm
σ_z	0.5	1	mm
$<\Delta E/E>_{rad}$	3.2	3.0	%
P_b	7.2	16.5	MW
P_{AC} (2 linacs)	113	137	MW
$\eta_{AC\text{-}to\text{-}beam}$	13	24	%
L (incl H_D)	3.6	6.5	$10^{33}cm^{-2}s^{-1}$

In case of the SBLC, beams have to cross at an angle (θ_c=3 mrad) in order to avoid the multibunch kink-instability [3] due to parasitic interactions. A reduction of luminosity caused by an effective increase of the hor. beamsize is avoided by employing a simple crab-crossing scheme with finite dispersion at the IP, making use of a coherent energy spread within the bunch of about σ_E=0.5 % [4]. For TESLA a head-on collision design with electrostatic separation of the beams after the final doublet is possible [5], see fig.1. This allows TESLA to use s.c. quadrupoles which provide a large aperture (a_Q=20 mm) for the exiting disrupted beam and the beamstrahlung γ's emitted at the IP with large angles (SBLC uses conventional quadrupoles with a_Q=4mm).

The magnet lattice between the IR and the main linac consists of the final focus system (FFS) for beamsize demagnification and chromatic corrections, a collimation section to protect the IR quads from large amplitude particles and bending sections for creating a sufficient separation between two beamlines if the collider is to serve two experiments. The bend between collimation and the FFS also helps to reduce background due to muons originating at the collimators.

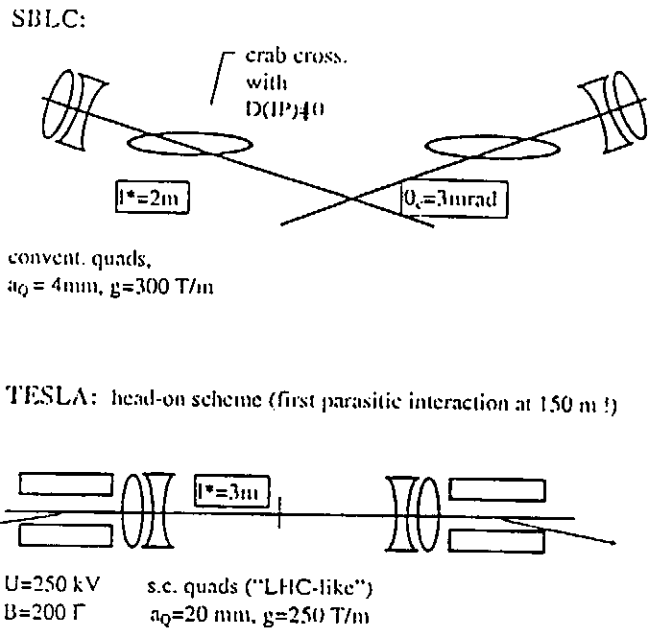

Fig. 1: Basic layouts of the interaction region

Table 2: results of beam-beam simulations for SBLC and TESLA [5,6,7]

	SBLC	TESLA	
$<\delta E/E>_{cm;rms}$	2.7	2.	%
Υ_o	.04	.021	
Disr. D_x/D_y	0.4/8.5	0.4/8.5	
angle $\hat{\theta}_{yx/y}$	1.28/0.55	1.07/0.64	mrad
N_{pair}/bunch	7	14	
N_{hadr}/bunch	0.2	0.3	

The momentum acceptance of the FFS for both designs is far in excess of the beam energy spread. For TESLA, a simple two sextupole family chromatic correction gives a bandwidth of ±0.6 % [5] ($\sigma_{E,beam}$=0.06%) and for SBLC with an optimized sextupole distribution a bandwidth of ±2.0 % is achieved ($\sigma_{E,beam}$=0.5%) [8].

The requirements for beam collimation are determined by the condition that synchrotron radiation generated in the doublet before the IP has to pass freely through the aperture of the final quad on the opposite side. This means that particle amplitudes have to be restricted to $6\sigma_x \times 8\sigma_y$ for SBLC and $12\sigma_x \times 35\sigma_y$ for TESLA. In the latter case, continuous

scraping of beam tails may not be necessary, since in the s.c. linac gas scattering is negligeable and wakefields are small so that particle betatron amplitudes should normally not reach the above defined limits. Following concepts developed at SLAC [9], a beam optics design for simultaneous collimation in x,y and dE/E has been worked out , the lattices for SBLC and TESLA being similar. However, an advantage of TESLA is that due to the large bunch spacing the beam can be stopped by a fast dump system, firing a kicker if from the first bunch(es) intolerable high loss rates are detected and sending the beam on an absorber block. The entire lattice from the linac to the IP will require approximately 1.1 km on either side of the IP.

4. MAIN LINAC

The SBLC and TESLA linacs consist of basic units as sketched in fig.2. For the conventional S-band machine, two 6m long travelling wave, constant gradient Cu-structures are powered by a 150 MW (peak power) klystron. For a 2μs flat top current pulse a modulator pulse width of 2.8μs is required. In total 2450 klystrons and modulators are required for the two 250 GeV linacs. A focussing scheme with scaling $\beta \propto \gamma^{1/2}$ and β=18m at the entrance of the linac (E=3 GeV) is foreseen.

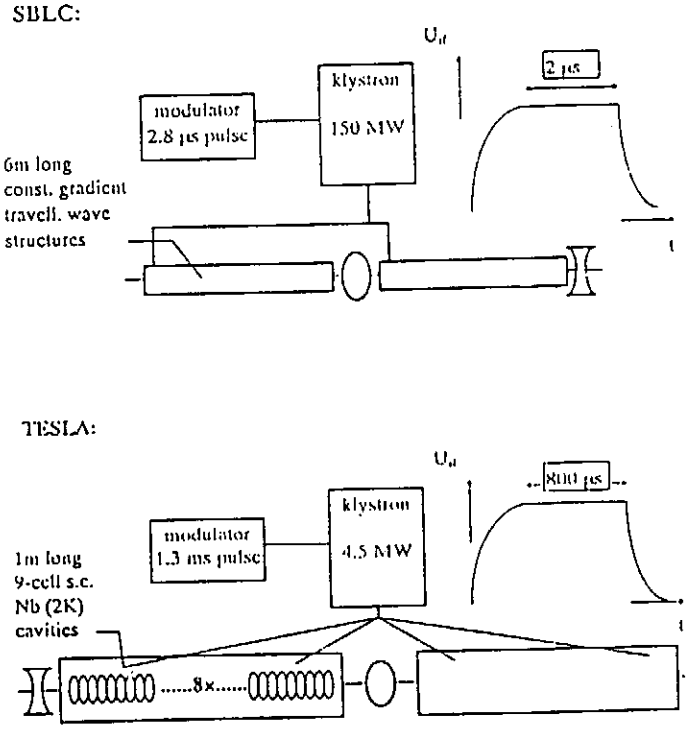

Fig.2: Basic units of the SBLC and TESLA main linac

In case of TESLA, a 4.5 MW klystron delivers rf-power to 16 9-cell 1.3 Ghz s.c. Nb cavities. There are 8 of these 1m long cavities in one kryostat. The modulator provides a 1.3 ms long pulse, yielding a 0.8 ms long accelerating gradient flat top. The two TESLA linacs require in total 1250 klystrons and 20,000 cavities. A focussing scheme using s.c. quadrupoles with constant β=66m is foreseen.

One of the most important accelerator physics issues in a linear collider concerns preservation of a small (especially vertical) emittance in the linac. Emittance dilution caused by chromatic effects (dispersion, filamentation) due to energy spread in the bunch, short range wakefields and long range deflecting modes are investigated for both designs considered here. Recent computer simulation results for SBLC [10] show that single bunch beam break-up can be well suppressed by applying BNS-damping only over the first 30% of the linac length (in the other part of the linac σ_E can be reduced to 0.3% by choosing an rf phase of -12 deg). With a coherent energy spread in this section of σ_E=0.9% the emittance growth due to injection oscillations can be kept small. Taking into account transverse position errors for quadrupoles, accelerating structures and beam position monitors (BPM's) of 0.1 mm (rms), it is shown that after applying different correction algorithms (wakefield-free (WF) orbit correction [11], bumps for dispersion and wakefield compensation), the dilution can be kept as small as $\Delta\varepsilon_y/\varepsilon_y$=3%. In addition to a BPM resolution of 5μm this requires 4 stations distributed along the linac where the emittance can be measured with an accuracy of 3%. The higher order modes (HOM's) induced when bunches pass off-axis through the accelerating structures cause oscillations growing over the entire bunch train (multibunch beam break-up). In order to keep this effect within limits, a frequency spread for the deflecting modes is introduced (the max. variation is assumed to be 40 Mhz). Furthermore, the quality factor of the modes with the strongest coupling to the beam has to be reduced by three HOM-couplers per 6m structure resulting in a Q-profile of typically $\sim 3\times10^3$ [12]. With these assumptions and tolerances as described above, computer simulations yield an effective multibunch emittance dilution of $\Delta\varepsilon_y/\varepsilon_y \sim 20\%$ [13]. This dilution can be further reduced by "beam-based alignment" of the cavities (measure HOM's and move the structures) and/or by using a fast kicker to put all bunches back on the same orbit [14].

Similar studies are performed for TESLA [15]. No BNS-damping is required and the emittance dilution from single bunch effects is small (~5%) even before optimization with bumps and with a relaxed tolerance of 0.5mm (rms) for cavity position errors. With HOM-damping provided by two couplers per 9-cell cavity ($Q<10^5$), multibunch BBU leads to an effective emittance growth of 22% (for this calculation 1mm rms cavity positon errors were assumed). A drastic reduction of this dilution by improving alignment of cavities with beam or applying the kicker-method should be easy for TESLA.

An important result concerning the stability of emittance with time has been obtained for SBLC [10] by assuming that the linac components are subject to diffusive ground motion following the ATL-rule. Using $A=4\times10^{-6}$ μm^2 m^{-1} s^{-1} as obtained from orbit motion observed at HERA [16], an emittance dilution of only 6% after 1 day is obtained if nothing but the simple one-to-one orbit correction is applied about once per hour. Concerning fast (>5 Hz) ground motion, active stabilization of magnet supports is investigated [17]. For TESLA, vibrations are not considered to be a problem since, thanks to the large bunch spacing, an orbit feedback can be applied within a bunchtrain (measure position of first bunch, correct for all others with a kicker).

5. INJECTION

The emittances required for the SBLC e^- and e^+ beams are provided by two damping rings of 650m circumference operating at 3.15 GeV. A beam optics layout with $\varepsilon_x=5\times10^{-6}$ m (50% of the design value at the IP) has been worked out [18]. The normalized dynamic aperture of 2.4×10^{-2} m is sufficient to accept the beam delivered from the e^+ source. Positrons are produced by converting γ's in a thin (0.4 radiation lengths) target. The required intense photon source is realised by passing the e^- beam after collision through a 30m long wiggler [19]. The method drastically reduces the heat load on the target and opens up the possibility to produce polarized positrons by using a helical undulator. The same scheme for e^+ production is foreseen for TESLA. Here, it is necessary to compress the 0.8ms long bunchtrain in order to fit into a damping ring of reasonable size. Two options are presently discussed: A conventional ring with ~6km circumference (like HERA-e) or a "dog-bone" shaped ring of ~20 km length [20] which fits almost entirely (except for the arcs at the end) into the linac tunnel. One advantage of the latter design is an increased bunch spacing (80 ns instead of 25 ns for the HERA-e like ring), which relaxes bandwidth requirements for the injection/extraction system [21] and the multibunch feedback . For TESLA also the possibility of of achieving the design emittance of the e^- beam by using a rf-photo-gun is being studied, which would allow to save one of the two damping rings.

6 UPGRADE POTENTIAL

With the relaxed tolerances of the low-frequency approach, SBLC and TESLA are very well suited designs if one aims to push the vertical emittance towards a smaller value. After gaining experience with correction and optimization procedures, operation of SBLC and TESLA with ε_y reduced by an order of magnitude seems conceivable. That would allow for higher luminosity and at the same time lower AC-power consumption (parameter sets for such a low emittance option at 500 GeV center-of-mass are given in table 3). A small ε_y becomes very important (if not inevitable) when an energy upgrade to 1TeV is considered. Whereas for TESLA a higher energy requires to increase the linac length, this upgrade could be made for SBLC within the same tunnel by doubling the number of klystrons and compressing the rf-pulse with a SLED system, thus doubling the accelerating gradient to 34 MV/m. Parameter sets for 1TeV are shown in table 4. Beamstrahlung is kept at a low level for both designs. The AC-power for TESLA is close to the 500 GeV version, whereas for SBLC the higher gradient leads to a loss in efficiency so that twice the AC power is required.

Table 3: modified parameters at 500 GeV (c.m.) with reduced vertical emittance

	SBLC	TESLA	
n_b/pulse	180	1200	
f_{rep}	25	5	Hz
N_e/bunch	2.0	3.4	10^{10}
$\varepsilon_x/\varepsilon_y$	5/0.05	10/0.1	10^{-6} m
σ_x^*/σ_y^*	632/6.3	775/12.6	nm
σ_z	0.25	0.5	mm
$<\Delta E/E>_{rad}$	3.0	3.3	%
P_{AC} (2 linacs)	57	70	MW
L (incl. H_D)	5.8	10	10^{33} cm^{-2} s^{-1}

Table 4: parameters at 1000 GeV (c.m.) with reduced vertical emittance

	SBLC	TESLA	
active leng.	29.4	40	km
n_b/pulse	50	4180	
t_{pulse}	0.6	830	μs
f_{rep}	50	5	Hz
N_e/bunch	2.9	0.91	10^{10}
$\varepsilon_x/\varepsilon_y$	5/0.05	5/0.063	10^{-6} m
σ_x^*/σ_y^*	742/6.3	325/8	nm
σ_z	0.50	0.5	mm
$<\Delta E/E>_{rad}$	4.3	2.7	%
P_{AC} (2 linacs)	230	153	MW
L (incl. H_D)	5.9	10.4	10^{33} cm^{-2} s^{-1}

7. R&D, TEST FACILITIES

The goal of the SBLC and TESLA test facilities under construction at DESY is to build and test the basic components required for the 2×250 GeV linear accelerators. For SBLC, the test linac consists of two 150 MW klystrons

(built at SLAC) which power two 6m long accelerating structures each. Recently the first klystron gun has reached its full design parameters in a diode test, while rf-tests with the complete device are in preparation at SLAC. Conventional line-type modulators are forseen for pulsing the klystrons. As an alternative, the possibility of using a switch tube modulator is also being studied [22]. The structure design includes symmetric rf-input couplers [23] and additional couplers for HOM damping [24]. Magnet and structure supports and precision movers as well as methods to compensate ground vibrations are investigated [17]. An injector is under construction to deliver the full design pulse current of 300 mA with the nominal bunch spacing of 16 ns for testing the setup with beam.

For TESLA the main objective of the test facility (TTF) is to process and test industrially fabricated Nb cavities and demonstrate that they can be operated with beam stably at a gradient of at least 15 MV/m [25]. The infrastructure includes facilities for high pressure rinsing, heat treatment and high peak power processing of the cavities [26]. The test linac consists of 32 9-cell cavities powered by two 4.5 MW klystrons. The klystron and the modulator (built at FNAL) have been tested successfully at full design parameters. The first cavities are on site and processing is in progress. Recently, with 5-cell 1.3 Ghz structures the g=25 MV/m goal has been reached at Cornell [27]. The injector for the TTF [28] is designed to deliver the full average pulse current, however with reduced bunch charge and higher bunch rep. frequency in its first stage. In a second stage, the bunch structure as designed for TESLA will be available. Furthermore, a low emittance rf-photo-gun for the injector is being investigated.

8. CONCLUSION

The low-frequency approach of SBLC and TESLA is well suited to achieve the performance goals of a next generation linear collider. Which of the two ways to go will have to be decided on the basis of results from the test facilities.

ACKNOWLEDGEMENT

The author would like to express his thanks to the colleagues of the S-band and TESLA collaborations for their support in collecting the information contained in this paper, and for many helpful discussions.

REFERENCES

[1] J. T. Seeman, "Lessons to be Learned from Operating the Stanford Linear Collider", contribution to this conference

[2] D. Burke, "Results from the Final Focus Test Beam Collaboration", contribution to this conference

[3] P. Chen "Disruption, Beamstrahlung and Beamstrahlung Pair Creation", SLAC-PUB-4822, 1988

[4] R. Brinkmann in: R. Settles (Ed.), Proc. LC92 workshop Garmisch-Partenkirchen, MPI-PhE/93-14, Vol. 2, p549-552

[5] O. Napoly, "A Large Aperture Final Focus Sytem for TESLA", TESLA report 93-23, 1993

[6] R. Brinkmann, presented at LC93, SLAC 1993

[7] D. Schulte, private communication, 1994

[8] R. Brinkmann, "Optimization of a Final Focus System for Large Momentum Bandwidth", DESY-M-90-14, 1990

[9] N. Merminga et al, "Collimation Systems in the Next Linear Collider", SLAC-PUB-5436, 1991

[10] M. Drevlak and R. Wanzenberg, "Single Bunch Tracking Calculations and Orbit Correction for the SBLC Study", contribution to this conference

[11] T. Raubenheimer "The Preservation of Low Emittance Flat Beams", SLAC-PUB-6117, 1993

[12] M. Dohlus and U. van Rienen, private communication , 1994

[13] M. Drevlak and R. Wanzenberg, "Multibunch Emittance Preservation in a Linear Collider", contribution to this conference

[14] This method was proposed independently by T. Raubenheimer and R. Brinkmann at LC93, SLAC-report 436, p. 301-303

[15] C. Magne and A. Mosnier, "Single .and Multi-bunch Wakefields Effects in the TESLA Linac", contribution to this conference

[16] R. Brinkmann and J. Roßbach, "Observation of Closed Orbit Drift at HERA Covering 8 Decades of Frequency", accepted for publication in Nucl. Instr. Meth., 1994

[17] M. Lomperski et al., "Studies of Measurement and Compensation Techniques of Magnet Motion for Linear Colliders", contribution to this conference

[18] R. Brinkmann, "A Study of Low-Emittance Damping Ring Lattices", DESY-M-90-09, 1990

[19] K. Flöttmann and J. Roßbach, "A High Intensity Positron Source for Linear Colliders", DESY-M-91-11, 1991

[20] K. Flöttmann and J. Roßbach, "Lattice Studies for a Large Dog-bone Damping Ring for TESLA", contribution to this conference

[21] J.P. Delahaye and J.P. Potier, "A Novel Injection/ Extraction Scheme for Short Bunch Separation in Accelerator Rings", contribution to this conference

[22] M. Bieler et al.,"Commissioning of the Hard Tube Pulser Experiment at DESY", contribution to this conference

[23] N.P. Sobenin et al.,"DESY Linear Collider Accelerating Section Coupler", contribution to this conference

[24] P. Hülsmann et al., "A New Technique for Quality Factor Measurements in Undamped and Damped Accelerator Cavities", contribution to this conference

[25] H. Weise, "The TESLA Test Facility (TTF)- A description of the Superconducting 500 MeV Linac", contribution to this conference

[26] M. Leenen, "The Infrastructure for the TESLA Test Facility (TTF)-A Status Report", contr. to this conf.

[27] T. Hays et al., "Achieving the TESLA gradient of 25 MV/m in Multicell Structures at 1.3 Ghz", contribution to this conference

[28] M. Bernard et al., "The TESLA Test Facility Linac Injector", contribution to this conference

Lattice Studies for a large Dog-bone Damping Ring for TESLA

Klaus Flöttmann, Jörg Roßbach
DESY
Notkestr.85, 22603 Hamburg, Germany

Abstract

A dog-bone shaped damping ring lattice is presented that meets all requirements of TESLA with respect to damping time, emittance, momentum compaction, bunch spacing and dynamic aperture. Due to its modular concept it exhibits large flexibility for future parameter modifications.

1. INTRODUCTION

A leading argument in the discussion of superconducting vs. normal conducting linear colliders is the efficiency of rf power conversion into beam power. With a highly efficient superconducting linear collider it is possible to obtain the desired luminosity at relaxed emittance tolerances or, alternatively, at moderate wall plug power consumption. Due to the long filling time of the rf sections, a very long bunch train will be characteristic for superconducting linear colliders (800 bunches, bunch spacing τ_b=1μs for TESLA; see ref.1). The production and damping of a huge number of particles leads, however, to some increased requirements for both the particle sources and the damping ring.

As far as damping rings are concerned there are three complications with such large intensities and long bunch trains:

1. The TESLA design foresees a bunch train of $800*10^{-6}\,s*c = 240km$ length. Obviously this bunch train can only be stored in a damping ring with a compressed bunch spacing and thus it must be expanded when extracted out of it. To this end very fast kickers will be required. Assuming a damping ring with circumference C and

$$\frac{240km}{C} = n \qquad (1)$$

we find the bunch spacing in the ring to be

$$\tau_{ring} = \frac{1}{n}\cdot\tau_b = \frac{1}{n}\cdot 1\mu s \qquad (2)$$

The ejection kicker has to operate with a rise time $\tau_r < \tau_{ring}$ at $\frac{1}{\tau_b} = 1MHz$ repetition rate.

2. Even if $\tau_r = 20ns$, $\tau_{ring} = 25ns$ is assumed, Eqs. 1,2 yield $n = 40$, $C = 6km$. Thus very large damping rings seem to be inevitable for TESLA.
3. Due to the bunch train compression, the mean current in the damping ring will be

$$I_{ring} = n*I_{linac} = n*8mA$$

With n of the order of 40, a broad band multi-bunch feedback system of $n/2$ MHz band width is required to store that large current.

2. THE DOG-BONE DAMPING STRUCTURE

In order to make the circumference of the damping ring very large and to reduce the tunnel cost, we have suggested a dog-bone design [2], with long straight sections within the tunnel of the main linac and two small rings connecting the straight sections at both ends (Fig. 1). The major part of emittance damping takes place in two 190m long wiggler sections [3,4].

The dog-bone shape offers a large flexibility concerning the circumference of the ring and the resulting requirements for the feedback system and the kickers but also with respect to emittance, damping time, energy and bunch length. In this paper we investigate the principle design features of a dog-bone structure.

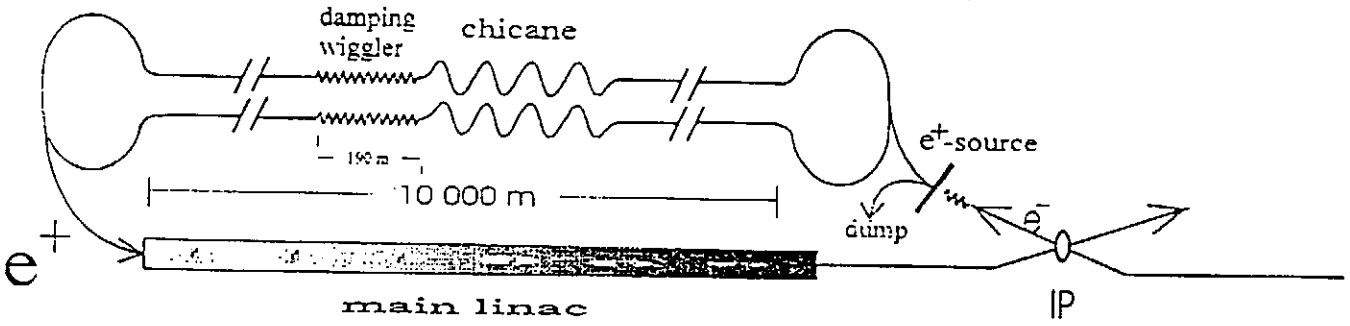

Fig.1 TESLA dog-bone damping ring scheme with circumference $C=20km$. The major part of emittance damping takes place in two 190m long wiggler sections. The chicanes provide momentum compaction without contributing too much of emittance growth.

For the arcs we use a modified lattice of R. Brinkmann's low emittance damping ring [5].

To find the optimum damping energy conflicting requirements have to be taken into consideration [2]:

* maximum energy is desired to reduce the length of the damping wiggler
* a higher energy increases instability limits
* minimum energy is favourable with respect to emittance generation in the chicane and bending sections, respectively.
* a lower energy simplifies the subsequent bunch compression.

We assume a circumference of the ring of $C=20km$ and an energy of $E=4GeV$ and get:

$$n = 12$$

$$\tau_{ring} = 83ns$$

$$I_{ring} = 96mA$$

band width of feedback system = $6MHz$

The straight sections of the ring consist of individual modules which can easily be combined to give maximum design flexibility. In addition we consider a twofold symmetry of the ring to increase the spacing of intrinsic resonances.

3. THE DAMPING WIGGLER MODULE

With the repetition frequency of the linac $\nu_{rep} = 10Hz$ a bunch can perform 1500 revolutions in the ring between successive rf pulses. Starting with a normalized beam emittance of $\varepsilon_x^N = 0.01\ \pi m$, as expected for the positron source [6], we need about 5 vertical damping times τ_D to reach the required vertical equilibrium emittance. In case of a low emittance electron source less damping times (i.e. a shorter damping wiggler) are sufficient.

With $\tau_D = 300 * T_0$ (T_0 = revolution time) and using:

$$\tau_D = 2\frac{E * T_0}{U_C} \qquad (3)$$

we obtain the energy loss per turn U_C to be:

$$U_C \geq \frac{E}{150} \qquad (4)$$

The energy loss per meter in a wiggler is given by:

$$\frac{\langle P_\gamma \rangle}{c}[GeV/m] = 3.3*10^{-13}\gamma^2 B[T]^2 \qquad (5)$$

Eqs. 4,5 can be combined into

$$B^2 L \geq \frac{1.03*10^7}{\gamma} T^2 m \qquad (6)$$

where L denotes the length of the wiggler section.

The condition for the emittance growth in the wiggler to be tolerable is [7,8]

$$\Delta\varepsilon_x\,(\text{per wiggler passage}) = \frac{1.05*10^{-15}}{m^3 T^5}\beta\lambda^2 B^5 L$$

$$< \frac{2T_0}{\tau_D}\frac{2*10^{-5} m}{\gamma} \qquad (7)$$

β = mean beta function in the wiggler section

λ = period of the wiggler

Note that the wiggler is traversed τ_D/T_0 times per damping time.

Using Eqs. 3 and 5 we get in addition to Eq. 6 the condition [9]

$$\beta\lambda^2 B^3 < 12 m^3 T^5 \qquad (8)$$

which is, remarkably, independent of energy.

Eqs. 8 shows that there is a large flexibility in choosing the wiggler parameter i.e. λ and B.

We have selected a high B version (yielding a minimum wiggler length) with $B=1.5T$, $\lambda = 0.4m$ because this might be the optimum with respect to cost and chromaticity contribution.

Fig. 2 shows the optical functions in one wiggler module of 15m length.

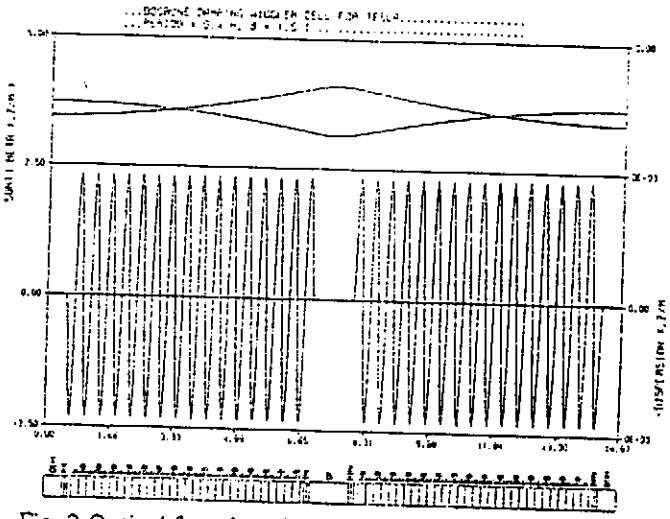

Fig. 2 Optical functions in the wiggler module.

4. THE CHICANE MODULE

In a dog-bone structure a momentum compaction factor α of -10^{-6} can be achieved. Thus a bunch length as small as 1mm would be possible. However, a larger bunch length (i.e. a larger α) will be required in the damping ring due to the microwave instability. A chicane can introduce a large, negative momentum compaction factor.

The longitudinal dynamic of a ring with negative momentum compaction factor has not been investigated in detail. According to experience with 'conventional' rings we assume that a momentum compaction of $\alpha = -2*10^{-4}$ is a reasonable number.

Neglecting the contributions of the arcs and the damping wiggler, α can be estimated at:

$$\alpha = -\frac{L}{2C}\left(\frac{ec}{2\pi E}\lambda B\right)^2 \qquad (9)$$

Combing Eq. 9 and Eq. 7 we get

$$\beta * B^3 < 0.29 m T^3 \qquad (10)$$

and with $\beta \approx 400m$

$$B < 0.09T$$

We select a field of $0.062T$ and set $L = \lambda * N$, where N denotes the number of periods, and get:

$$\lambda[m] = \left[14.6*10^6/N\right]^{1/3} \qquad (11)$$

We want to keep the geometric deviations from a straight line small enough to accommodate the chicane inside the standard size linac tunnel. Also we want to avoid excessively large dispersion values D_x to relax error tolerances which could affect emittance coupling. Therefore we choose $N=8$ and get:

$$\lambda = 122m$$

$$D_x < 2m$$

Fig. 3 shows the optical functions in one chicane module.

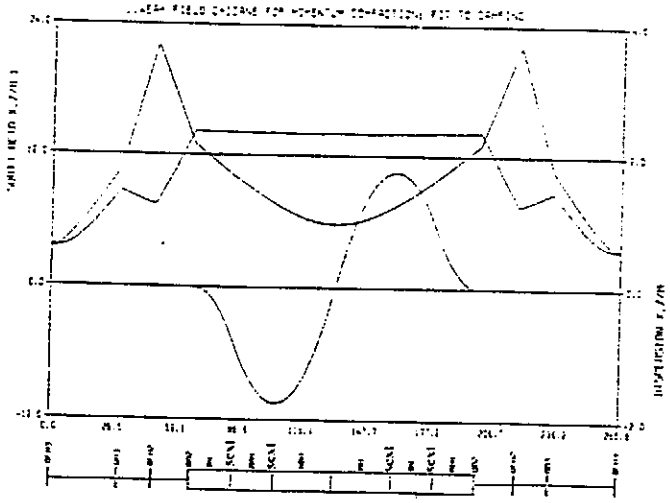

Fig.3 Optical functions in the chicane module.

5. COMPLETE DOG-BONE RING PARAMETER

The major part of the ring consists of long FODO cells which ensures a small chromaticity contribution of this long dispersion-free straight section and reduces costs.

As seen from Tab.1 the overall parameters meet the TESLA requirements.

Qx, Qy	106.30, 68.26
ξ_x, ξ_y	-159.0, -127.0
ε_x^N	$1.70*10^{-5}$ m
τ_D	18.9 ms
U_C	27 MV
σ_s at U_0=50 MV	7.0 mm
$\sigma P/P_0$	$1.2*10^{-3}$
α	$-2*10^{-4}$

Tab. 1 Parameters of the dog-bone ring.

The chromaticity of the long straight sections is compensated both by sextupoles in the chicane modules and in the arcs. It should be noted that the chromaticity of a ring with negative momentum compaction factor should also be negative in order to stabilize the first mode of the head-tail instability.

Four-dimensional tracking calculations including orbit errors have shown that the dynamic aperture exceeds the value required at injection within ± 1% energy width.

6. REFERENCES

[1] R. Brinkmann, "Low Frequency Linear Colliders", this conference

[2] K. Flöttmann, J. Roßbach, "Emittance Damping Considerations for TESLA", DESY 93-23, 1993

[3] K. Steffen, "The Wiggler Storage Ring, a device with Strong Radiation Damping and small Emittance", DESY-PET-79-05, 1979

[4] R. Palmer, "Exotic Damping Ring Lattices", SLAC-PUB-4329, 1987

[5] R. Brinkmann, "A Study of Low-Emittance Damping Ring Lattices", DESY M 90-09, 1990

[6] K. Flöttmann, "Investigations Toward the Development of Polarized and Unpolarized High Intensity Positron Sources for Linear Colliders", DESY 93-161, 1993

[7] J. Roßbach, "Positron recycling in high energy linear colliders", Nucl. Instr. Meth. A309, 25-36, 1991

[8] N. S. Dikanskii, A. A. Mikhailichenko, "Straight-line cooling system for obtaining high-energy beams e^+, e^- with minimal emittance ", INP-88-9 1988

[9] T. O. Raubenheimer, L. Z. Rivkin, R. D. Ruth, "Damping Ring Designs for a TeV Linear Collider", SLAC-PUB-4808 (1988)

The Infrastructure for the TESLA Test Facility (TTF) - A Status Report

M. Leenen, for the TESLA Collaboration

Deutsches Elektronen-Synchrotron DESY
Notkestr. 85, 22603 Hamburg, Germany

Abstract

The TESLA collaboration is preparing the installation of a 500 MeV superconducting linear test accelerator to establish the technical basis for a future 500 GeV e⁺e⁻ collider. The setup consists of 4 cryomodules, each containing 8 solid Niobium cavities with a frequency of 1.3 GHz. The infrastructure to process and test these cavities has been installed at DESY. The facility includes a complex of clean rooms, an ultraclean water plant and a chemical etching installation for cavity surface preparation and cavity assembly as clean as possible. To improve the cavity performance a firing procedure at 1500°C in an ultra-high vacuum furnace is foreseen. An existing cryogenic plant has been modified to cool down the cavities to 1.8K and measure them in vertical and horizontal test cryostats. The RF power will be provided by a 4.5 MW klystron (pulse length 2 ms) in connection with a modulator. This system will also be used for a high peak power RF treatment to further improve the cavity performance by eliminating potential sources of field emission. The components of the complete infrastructure for the TTF are described and their status is reported.

1. INTRODUCTION

The theoretical accelerating gradient in a Niobium superconducting cavity is limited to around 50 MV/m by the maximum value of the magnetic surface field occuring at the cavity equator. In praxis the gradient is limited to substantially lower values by field emission from localized regions of the cavity surface. In the past few years however there has been dramatic progress both in the understanding of field emission mechanism and in its cures. By means of ultrahigh vacuum baking at 1500°C under carefully controlled conditions or by high peak power RF processing (HPP) developped at Cornell multicell structures at S- and L-band frequencies have exhibited more than 20 MV/m accelerating gradients as demonstrated in fig.1 and fig.2.

To develop the surface treatment methods and the fabrication procedures required to produce high gradient multicell cavities on an industrial scale the TESLA collaboration first plans to construct and test forty 9-cell 1.3 GHz solid Niobium Cavities [1].

The necessary semiconductor standard clean rooms and the surface treatment facilities to process these cavities have been installed at DESY together with the equipment to test the cavity performance.

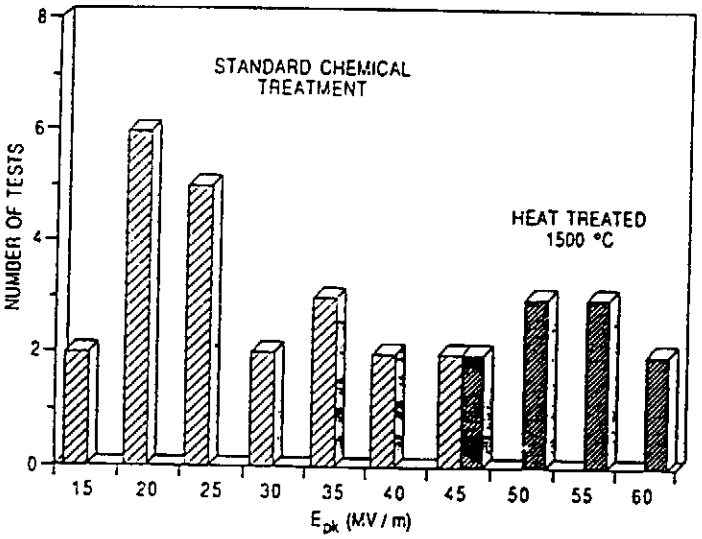

Fig.1. Improvement of cavity performance by heat treatment.

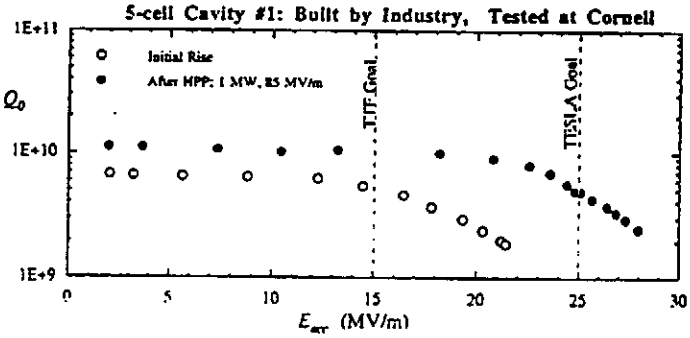

Fig.2. Improvement of cavity performance by HPP.

The most important components of this infrastructure are

- A complex of clean rooms (300m²) for dustfree cavity assembly and treatment, to avoid cavity contamination,
- A chemical etching facility complying with the purity standards of semiconductor industry,
- An ultraclean water supply for rinsing the inner cavity surface to remove potential sources of field emission,
- An UHV furnace to bake out the cavity at 1500°C to improve the Niobium material properties and to eliminate field emitters,
- A high peak power RF facility to process cavities for further reduction of field emission,
- Vertical and horizontal Helium cryostats to cool down and test the cavity performance at 1.8 K,
- A cryogenic plant to provide liquid Helium at 1.8 K and

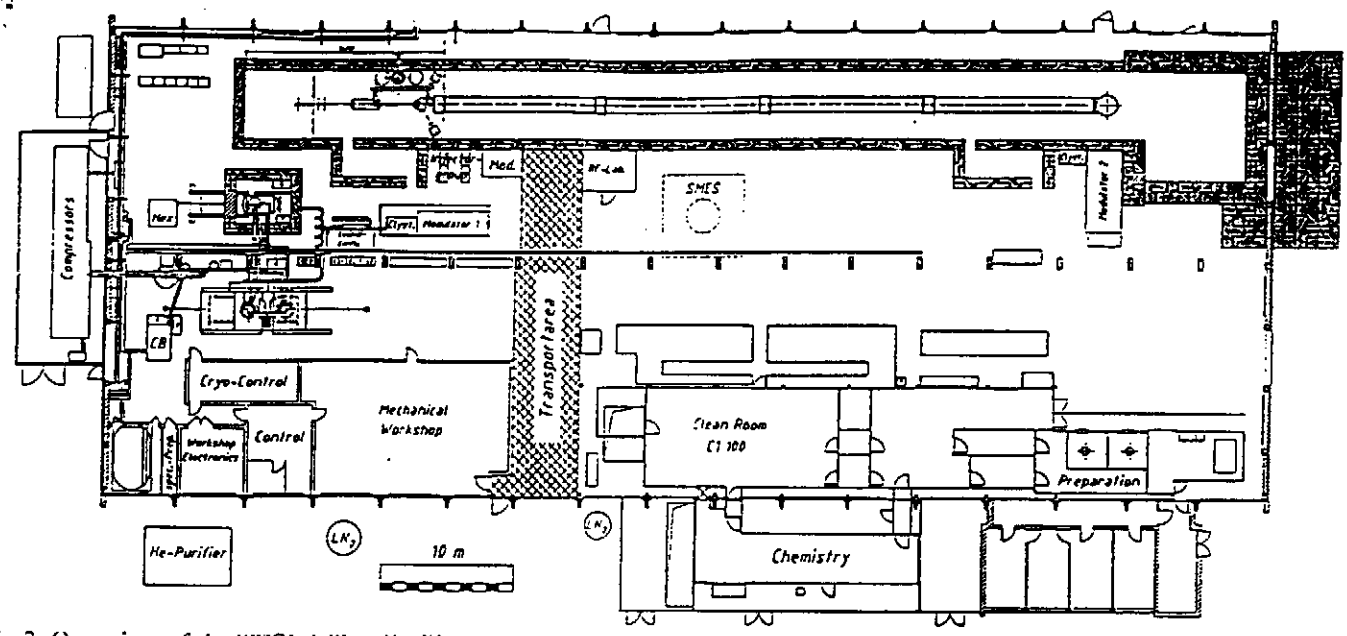

Fig.3. Overview of the TESLA Test Facility (TTF) at DESY.

4.5 K as well as Helium gas at 70 K for the cryostats and the planned test facility linear accelerator.

2. COMPONENT STATUS

The TESLA Test Facility (TTF) is located in an experimental hall of about 3000 m² surface area, which also houses the planned 500 MeV superconducting linear accelerator [2].

An overview of the TTF is shown in fig.3.

2.1 Clean room and assembly area

In order to avoid contamination of the cavity surface during processing and assembly a clean room has been built with an area of approx. 300m². The complex is divided into different classes, ranging from class 10000 down to class 10 (Federal standard 209), the last one being used for the most critical operations like connecting the cavities to a string for a cryomodule or mounting the input couplers to the cavity. Integrated in the clean room is the UHV furnace and the area for the chemical etching of the cavity surface. The clean room is operational since September 93.

2.2 Chemistry

Inside the chemistry area a cabinet for etching of the Niobium cavities is installed. The acid in use is a mixture of $HF/HNO_3/H_3PO_4$ of VLSI quality in a 1/1/2 ratio. The acid is circulating in a closed loop between the cavity and the storage tanks, which are located in a separate room outside the cleanroom. The pumps, tubes (made from PVDF) and filter elements (0.2µm size) of the chemical distribution system fulfill the standards of semiconductor industry.

Two different acid treatments are foreseen. The outside treatment removes the Niobium-Titanium surface layer after the postpurification in the furnace whereas the inside treatment with highest quality requirements is used for the preparation of the inner RF surface. The temperature of the acid can be set between 0° and 20°C with a mass flow of up to 20 ℓ/min. The process itself and the safety interlocks are controlled by a computer to reach high safety and reproducibility standards. After the etching process the cleaning procedure is finished by an ultrapure water rinse and a drying in an ultraclean hot nitrogen atmosphere.

Fig.4 shows the mounting of a cavity in the chemistry. The chemical facility has already been used for etching the first prototype TESLA cavities at DESY.

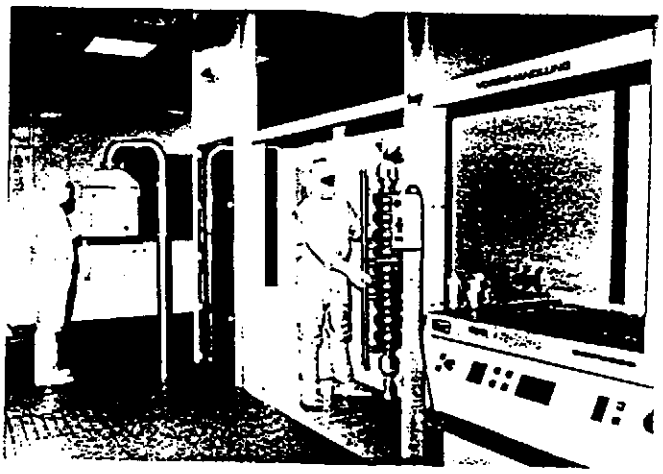

Fig.4. Cavity assembly in the clean room

2.3 Ultrapure water supply

An ultrapure water plant supplies the cavity cleaning facilities with water of 18.2 MΩ cm resistivity under (nearly) particle free conditions. Its first stage consists of a reverse osmosis unit (300 ℓ/h), the second stage is equipped with nuclear grade mixed bed ion exchangers, augmented by filters and an ultraviolet light source. The point of use filters have a mesh size of 0.04 µm. A storage tank of 4000 ℓ capability allows the use of large quantities of

ultrapure water for cavity surface rinsing and cleaning. This plant is a continuous operation since August 93.

Added to this facility is a high pressure rinsing station (up to 200 bar), which has been developped and built by CERN. This unit allows the ultimate cleaning of the inner cavity surface and is presently being commissioned (May 94).

2.4 UHV furnace

Heat treatment of the complete cavity reduces potential sources for field emission and improves the Niobium material properties like thermal conductivity (RRR) and homogeneity. During this process (at 1500°C and a vacuum of 10^{-7}mb) Titanium is evaporated and builts up as a film on the outer cavity surface. This effect leads to a solid-state gettering process for residual gases during high temperature annealing. The furnace for the TESLA cavities, which is shown in fig.5 has been delivered and will be commissioned with prototype cavities in August 94.

2.5 High power processing (HPP)

Besides heat treatment in an UHV furnace the application of high power RF pulses (≈MW) for a short time (≈ms) to the cold cavity has proven as very effective to remove potential field emitters from the inner cavity surface. To apply this method for the TESLA cavities an HPP test stand has been built. It consists of a modulator supplied by FNAL and a klystron with a peak power of 4.5 MW at a pulse length of 2ms. This setup (shown in fig.6) is connected through RF wave guides with the vertical and horizontal cryogenic cavity test stands. First HPP treatment of a TESLA cavity is expected in July 94.

2.6 Cryogenics

For cooldown and test of the TESLA cavities an existing liquid Helium plant has been extensively modified. By adding vacuum pumps and screw compressors a temperature of 1.8K can be reached, with a refrigeration power of 200W. The unit, which in addition provides Helium at 4.2K (400W) and 70K (2000W), is connected to two vertical cold test stands built by FNAL and a horizontal test cryostat provided by CE Saclay. The liquid Helium plant is operational since December 93.

3. SUMMARY

For the TESLA Test Facility (TTF) at DESY the complete infrastructure for superconducting cavity processing and testing has been built during the last 18 months. The components are in operation and commissioned with two prototype TESLA cavities. The arrival of the first series cavities for the test linac is expected in August 94.

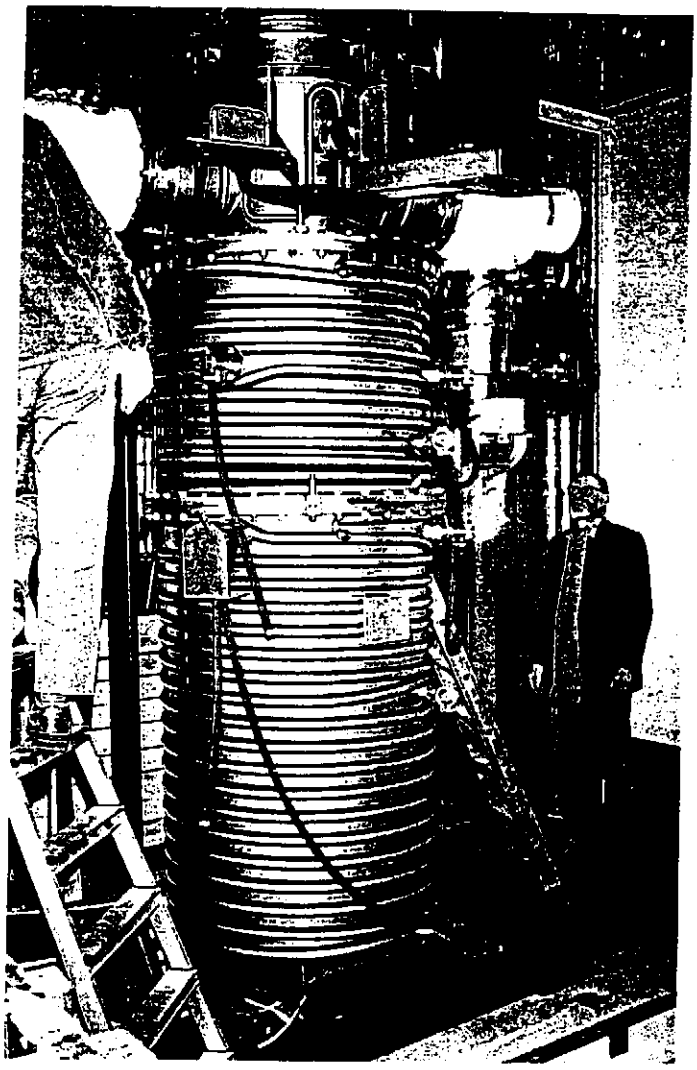

Fig. 5. UHV furnace for heat treatment.

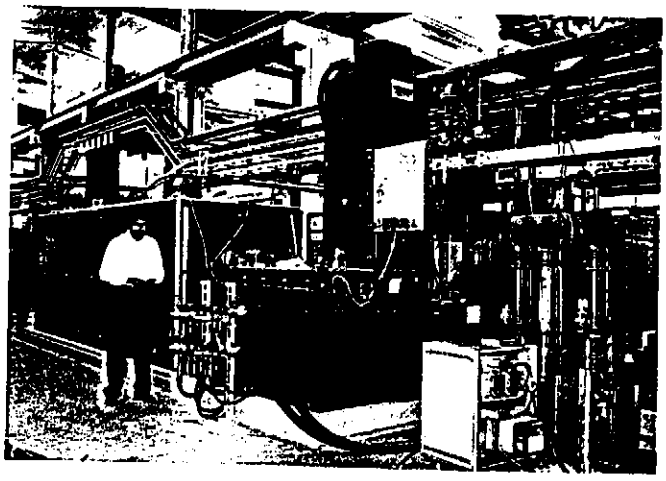

Fig.6. RF setup for HPP treatment.

4. REFERENCES

[1] Proposal of the TESLA collaboration. TESLA Report 93-01.

[2] H. Weise, DESY, for the TESLA collaboration. Contribution to this conference.

The TESLA Test Facility (TTF) - A Description of the Superconducting 500 MeV Linac

Hans Weise, for the TESLA collaboration
Deutsches Elektronen Synchrotron
Notkestraße 85
D-22603 Hamburg

Abstract

The energy range in e^+e^- collisions beyond LEP can only be explored by the use of linear colliders. Aiming for 500 GeV center of mass and luminosities in excess of $10^{33}cm^{-2}s^{-1}$, TESLA proposes to use superconducting (s.c.) standing wave RF structures at a gradient of 25 MV/m ($Q_0 = 5 \times 10^9$) and a frequency of 1.3 GHz. A total of 800 bunches each spaced 1 μs apart are accelerated. In order to establish a technical basis for such a s.c. linear collider the TTF is an essential part of the development of injectors, accelerating cavities, cryostats and new beam diagnostic techniques. The test of a string of 32 cavities with beam at an accelerating gradient of 15 MV/m and for different time structures of the injected beam is planned in an installation at DESY, Hamburg. Beam optics, alignment and high order mode (HOM) excitation have to be studied. The installation is described and the contributions of the different collaborators to the facility are reported.

1 INTRODUCTION

Worldwide, there are a number of groups pursuing different linear collider design efforts. The TESLA activity [1] is one of these R&D effords, differing from the others in its choice both of superconducting accelerating structures and of low frequency (L-band, 1.3 GHz; see also [2]). As one of these R&D groups, TESLA plans to have a working prototype test facility in the 1997 time scale which supports the development of a s.c. collider.

The TTF is to be located at DESY, with major components flowing in from the members of the TESLA collaboration. Although it is of highest priority to prove the feasibility of reliably achieving accelerating gradients of 15 MV/m or more, the TTF has also to show that the cavities can be assembled into a linac test string successfully operated with auxiliary systems to accelerate an electron beam to 500 MeV. Furthermore, different experiments to be carried out on the TTF linac have been defined and partly outlined in detail now so that the necessary diagnostics can be set up. This covers not only the more typical beam experiments but also the cryogenics and RF measurements that are needed in order to confirm the idea of a superconducting linear collider.

2 THE TTF LINAC PROGRAM

Although a full comparison of the TTF linac's parameter with a potential TESLA 500 linear collider [3] can not be carried out here, Tab. 1 lists the most important items.

Table 1: TESLA 500 - TTF linac parameter comparison.

Parameter	TESLA 500	TTF linac
Linac Energy	250 GeV	500 MeV
Accelerating Gradient	25 MV/m	15 MV/m
Quality Factor Q_0	5×10^9	3×10^9
No. of Cryo Modules	many	4
Single Bunch $\Delta E/E$	1.5×10^{-3}	$\approx 10^{-3}$
Bunch to Bunch $\Delta E/E$	10^{-3}	$\approx 5 \times 10^{-3}$
Beam Current	8 mA	8 mA
Macro Pulse Length	0.8 ms	0.8 ms
Injection Energy	10 GeV	10-15 MeV
Lattice β	66 m	12 m
Bunch Rep.Frequency	1 MHz	216 / 1 MHz
Bunch Population	5×10^{10}	$0.023/5 \times 10^{10}$
Bunch Length, rms	1 mm	1 mm
Emittances $\gamma\sigma^2/\beta$	20, 1 μm	3μm
Beam Size, Injection	60, 20 μm	1 mm
Beam Size, End of Linac	50, 12 μm	0.35 mm

The time structure of the beam, i.e. bunch frequency, bunch separation, and bunch length as well as the number of particles per bunch depends clearly on the injector. In a first step a design was chosen which is intended to be relatively straight forward (see Sect. 3). Both, the emittances and the the beam sizes are determined of the injection system intended for TESLA 500 (a 10 GeV system is foreseen) and therefore cannot be met by the TTF linac. Nevertheless, there are a number of respects in which TESLA 500 and the TTF linac are sufficiently similar, so that the TTF linac experience will feed directly into the TESLA 500 design. Some aspects of the full scale linear collider can be checked at the TTF linac, others may be difficult or even impossible to check. This fact is reflected by the following list.

What the TTF linac does check:

- Gradient achievable [4]
- Cavity construction and processing techniques [5]
- Input and HOM coupler designs [5]
- RF control of multi-cavity systems [5]
- Lorentz force detuning effects and control [6]
- High peak power processing [7]

Contributed Paper to the 4th European Particle Accelerator Conference,
London, 27 June to 1 July 1994.
TESLA-Report 1994-24

- Vacuum failure recovery potential
- cryostat design [5]
- Cryogenic operation
- Dark current [8]
- Energy and position feedback
- Alignment and its stability [8]
- BPM systems [9]
- First iteration on projected system costs

What may be difficult to check:

- Q_0 and HOM measurements are not easy
- Wake field measurements only far of axis
- Cavity alignment via wake fields hard (polarization)
- TESLA 500 bunch charge hard to achieve in time scale of TTF linac
- Accurate cost projection to mass production

What the TTF linac does not check:

- Emittance growth
- Vibration sensitivity
- Many features of an overall TESLA 500 facility

3 THE TTF LINAC

The TTF Linac, as it is shown in Fig. 1, consists of a 250 keV room temperature injection, a short superconducting linac followed by a 15 MeV beam analysis area and an optics matching system, the linac itself consisting of four cryomodules with eight cavities each, and the 500 MeV beam analysis area.

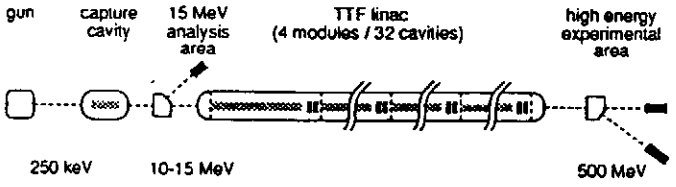

Figure 1: Schematic layout of the TTF linac. The overall length of the installation at DESY [10] amounts to ≈85 m; the drawing is not to scale.

3.1 Injector

Two injectors are planned for the TTF linac. The first, injector I, is intended to be relatively straight forward in design to provide the TESLA design current, but not the large bunch spacing of 1 μs and rather intense bunches (5 $\times 10^{10}$ electrons). In its initial form, injector I [11] will operate with the parameters as shown in Tab. 1, first column TTF linac. A later variant may operate at another subharmonic of the linac frequency and will provide higher charge per bunch. The second, injector II, is intended to provide the TESLA 500 bunch spacing and intensity. Here a design based on a laser driven photo cathode is considered and first designs are on the way. Nevertheless, neither of the two injectors will have the transverse emittance ratio of TESLA 500.

The warm part of injector I starts with a grid controlled thermionic gun as the source. The anode voltage of 40 kV accelerates the produced bunches ($2.3\text{-}10^8 e^-$ in 50 deg at 216.7 MHz) to an electron velocity of $\beta = 0.37$ with which the beam is injected into a 1 m long electrostatic preacceleration tube. Bunch compression is performed by means of a 6^{th} subharmonic buncher cavity (SHB) which is operated in the accelerating π-mode and causes a change in velocity along the injected bunch length. The converging bunch is then transported through the beam line down to the entrance of a superconducting 15 MeV injector linac which contains one standard 1 m long nine-cell TESLA cavity.

This accelerating structure has a crucial influence on the beam quality at the end of the injector. As a standing wave, $\beta = 1$ cavity it has three major impacts on the beam optics. At first, the large leakage field, which the injected electrons see in the beam tube in front of the first cell, acts as a decelerating field. Second, the low velocity of the 250 keV ($\beta = 0.74$) electrons results in a phase slippage in the first cell. The consequence is an energy modulation but fortunately also a further bunch compression. And third, the field of a standing wave cavity has a strong focusing influence on the transverse dimensions of the electron beam [12]. Although a rough estimate of some of the effects can be made analytically, a complete simulation has been carried out using the tracking code PARMELA. This calculation also takes the space charge effects into account.

The accelerated electron beam can be studied in the low energy beam analysis area behind the injection linac. Transverse and longitudinal phase space volume and orientation will be measured. Therefore several diagnostic stations are used together with a focusing quadrupole triplet. The influence of the accelerating gradient and its focusing effect in the transverse phase space will be seen. The energy stability within the 800 μs macro pulse has also to be detected.

3.2 Linac Beam Optics

The already above mentioned first quadrupole triplet will be used together with a second triplet to allow the matching of the beam to the optics lattice used along the linac. Although this matching strongly depends on the orientation of the injector beam in the transverse phase space, the chosen system is proper to handle injector output energies from 10 to 15 MeV.

The lattice along the TTF linac consists of four cells, each having a superconducting quadrupole doublet and a beam position monitor at the end of a string of 8 s.c. cavities. For beam optics calculation one cell is basically represented by a focusing element 'F', a short intermagnet drift 'I', a defocusing element 'D' and finally a long drift 'O'. The matching to this FIDO lattice is strongly disturbed by the already mentioned rf-focusing which has to be taken into account at least for the first main linac

cavities. Nevertheless, detailed beam optic calculations achieved a perfect matching with a β-function equal to the cell length of $\approx$12 m (module length).

Starting with this β–function, the accelerated electron beam (now 500 MeV) has to be transported through the high energy beam analysis area down to the end of the beam line, to the beam dump. It is planned to use one more quadrupole doublet together with the last superconducting one in order to measure again both beam emittance and in a dispersive section energy spread. Further quadrupole doublets will be used in the two straight sections behind the analyzing magnet to increase the β–function by at least two orders of magnitude before stopping the beam in two separate dumps. Thus the damage of the dump windows can be avoided.

3.3 The Linac Module

Each of the four linac modules houses 8 s.c. cavities of the TESLA type [5], which is an approx. 1 m long 9-cell stiffened π-mode standing wave structure operating at 1.3 GHz. The cavities are assembled as a string. They have an input coupler and a HOM coupler at one end and only a HOM coupler at the other end of each. This string is followed by a beam position monitor [9] and a s.c. quadrupole doublet whose beam tube acts as an additional HOM absorber. Each quadrupole has correction coils which can be used as steering coils and for the compensation of potential quadrupole vibrations.

Every s.c. cavity has its own helium vessel and the whole string is supported by a long helium gas return pipe. Operating temperature is 1.8 K; at an unloaded quality factor of $Q_0 = 3\times10^9$ the estimated heat load for the complete TTF linac is approximately 60/60/500 W at 2/4.5/70 K. The first module will be equipped with a large number of temperature sensors and two vibration detectors per cavity. Input and HOM couplers as well as rf windows will have rf pickups. Alignment during cool down will be monitored.

3.4 500 MeV Experimental Area

The high energy beam analysis area is located behind the last cryomodule and its terminating feed can. It serves as a room to measure the relevant beam parameters, i.e. beam position, beam size and emittance, beam energy and spread, beam current and transmission through the linac, bunch length and shape. Some parameters will be measured as a function of the bunch number in the 800 μs bunch train, others as an average over some part of it or for a series of trains. In a first step standard beam diagnostics (wire scanners, screens and striplines) will be used while commissioning the TTF linac. The extensive use of OTR screens is foreseen. Space for testing new diagnostic tools developed for TESLA also will be provided. Two beam dumps complete the whole TTF linac set up.

4 OUTLOOK

At present the commissioning of the TTF infrastructure is almost finished. Two prototype cavities have been used. The first six s.c. cavities will be at DESY this summer so that the processing of it can start soon. The assembly of 8 cavities as a string is scheduled for early 1995 and the first cold test for late spring. The injector assembly starts at Saclay in the beginning of next year. After successful tests it will be delivered to DESY to allow beam tests with the first cryomodule before end of 1995.

5 REFERENCES

[1] The TESLA R&D effort (TESLA = TeV Electron Superconducting Linear Accelerator) is being carried out by an international collaboration. A number of institutions have joined the collaboration and include IHEP Beijing, TU Berlin, CEN Saclay, CERN, Cornell, TH Darmstadt, DESY, Fermilab, Univ.Frankfurt, INFN Frascati-Milano, Univ.Karlsruhe, LAL Orsay, IPN Orsay, SEFT Finland, Univ.Wuppertal.

[2] R. Brinkmann, Low Frequency Linear Colliders, this conference

[3] H.T. Edwards, TESLA Parameter Update - A Progress Report on the TESLA Collider Design, 6^{th} RF Supercond.Workshop 1993, CEBAF; to be published in Part.Acc.

[4] T. Hays et al., Achieving the TESLA Gradient of 25 MV/m in Multicell Structures at 1.3 GHz, this conference.

[5] M. Champion, B. Dwersteg, A. Gamp, H. Kaiser, B. Petersen, D. Proch, J. Sekutovicz, S. Tazzari, diff. contributions to the 6^{th} RF Supercond.Workshop 1993, CEBAF; to be printed as workshop proc., ed. R. Sundelin.

[6] S. Chel et al., Field Stabilization in a Superconducting Cavity Powered in Pulsed Mode, this conference.

[7] H. Padamsee, Review of Various Approaches and Successes for High Gradients and Q's for TESLA, 6^{th} RF Supercond.Workshop 1993, CEBAF; to be published in Part.Acc.

[8] A. Mosnier, Proc. of the Linear Coll.Workshop LC92, Garmisch, ed. R. Settles, ECFA 93-154 (1993).

[9] R. Lorenz, Test Results on a Beam Position Monitor Prototype for the TTF, this conference.

[10] M. Leenen, The Infrastructure for the TESLA Test Facility (TTF) - A Status report, this conference.

[11] M. Bernard et al., The TESLA Test Facility Injector, this conference.

[12] J. Rosenzweig, L. Serafini, Transverse Particle Motion in Radio-Frequency Linear Accelerators, to be published in Phys.Rev.E.

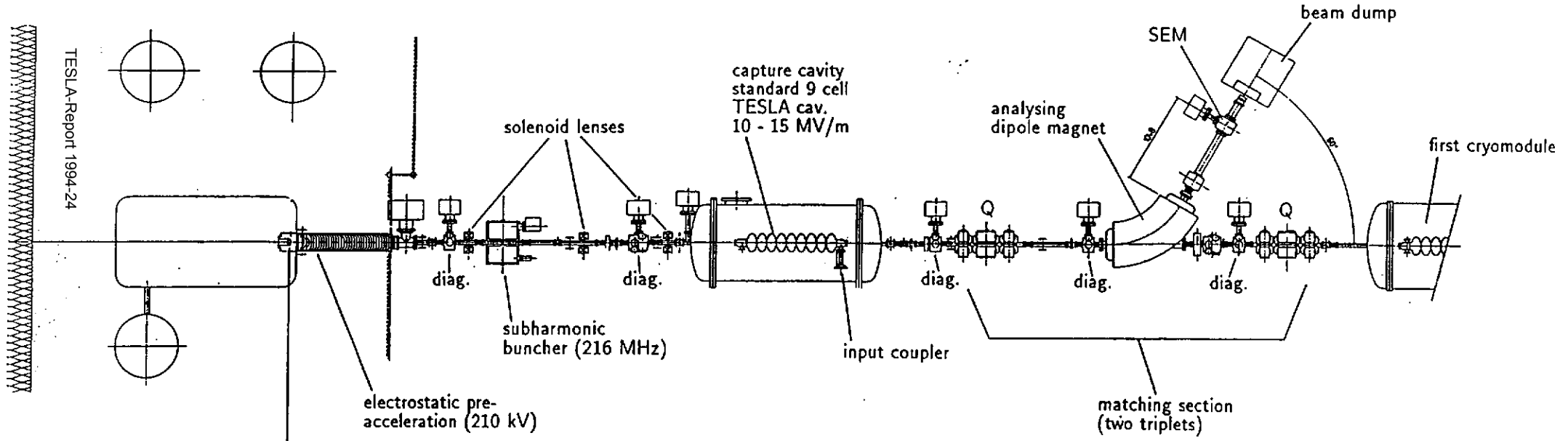

produced at gun

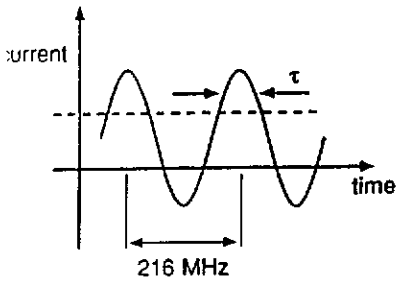

entrance of capture cavity

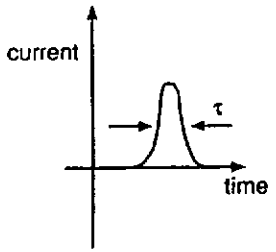

n_{e^-} = 2.3×10^8

τ = ±150 deg @ 1.3 GHz
±25 deg @ 216.7 MHz

β = 0.74

τ ≈ ±3 deg @ 1.3 GHz

time structure at entrance of first cryomodule

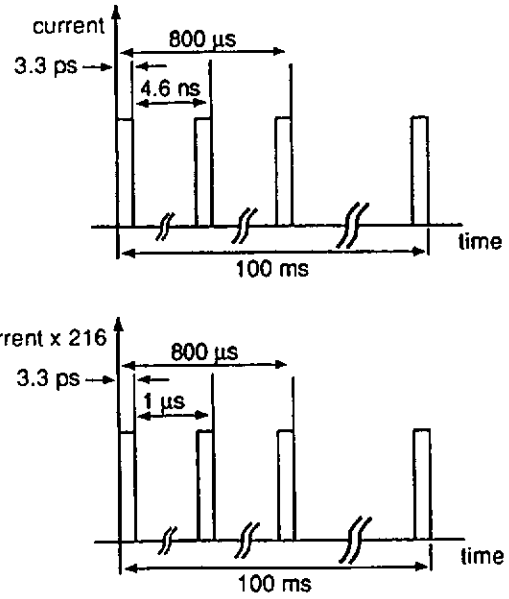

E = 10–15 MeV
$\bar{I}$ = 64 μA
$\bar{I}_{mp}$ = 8 mA
$\hat{I}$ = >10 A

TESLA
injector II

PARMELA results

E_0 = 9.9 MeV
σ_ϕ = 0.77 deg
σ_E = 78 keV
$\beta\gamma\varepsilon_{rms}$ = 4.2 mm mrad

see this conference

THP39B

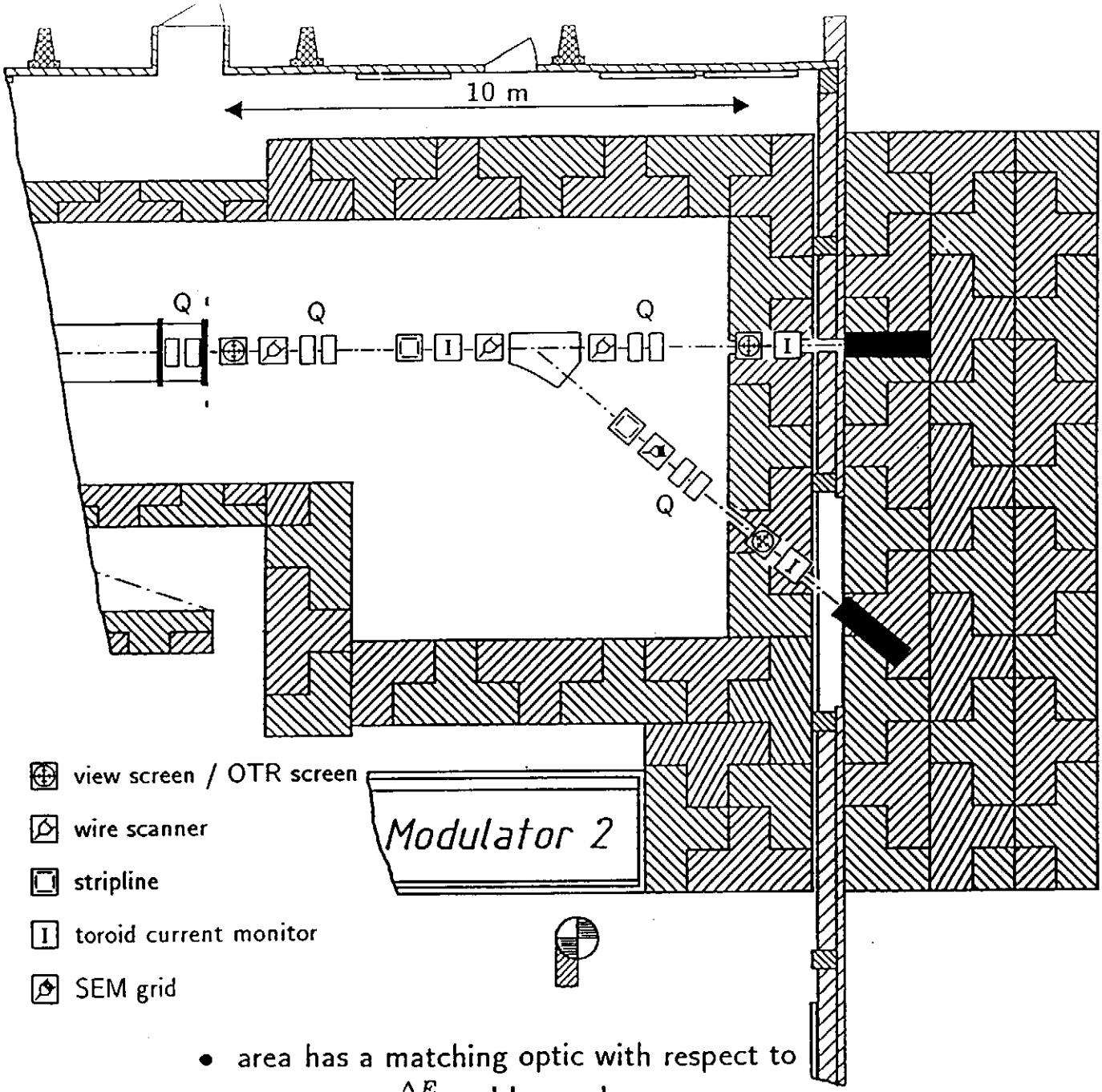

- area has a matching optic with respect to
  ε, $\frac{\Delta E}{E}$ and beam dump
- beam parameters will be measured as
  f(bunch) and/or
  f(bunch train) and/or
  f(time)
- f(bunch) means average measurements over
  1 μs (216 or 1 bunch(es))
- beam parameters to measure are
  position
  size, emittance
  current, transmission
  energy spread, energy stability
  bunch length
  dark currents

the FIDO lattice of the TTF linac

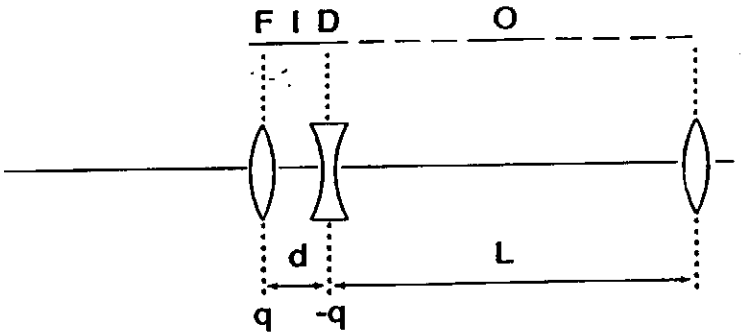

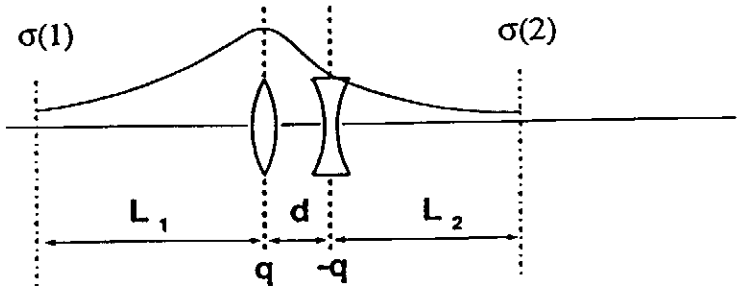

Results of the Transport Calculation for the TTF linac's FIDO Lattice

Input Parameters			
Intermagnet Drift	d	0.10	m
Quadrupole Length	l_q	0.15	m
FIDO Cell Length	L	12.2	m
Injection Energy	E_{inj}	14.0	MeV
Output Parameters			
Qudrupole Strength	q	0.287	T/m
x–Direction			
Maximum Beam Size	$\sqrt{\sigma_{11}^x}$	1.24	mm
Maximum Beam Divergence	$\sqrt{\sigma_{22}^x}$	0.176	mrad
Phase Space Orientation	r_{12}^x	-0.55	
y–Direction			
Maximum Beam Size	$\sqrt{\sigma_{11}^y}$	1.70	mm
Maximum Beam Divergence	$\sqrt{\sigma_{22}^y}$	0.176	mrad
Phase Space Orientation	r_{12}^y	-0.79	

The definition of the used FIDO cell and the geometrical constraints for finding a periodic solution. The lengths L_1 and L_2 sum up to the length L. The transverse beam ellipse is upright ($\sigma_{12}(1) = \sigma_{12}(2) = 0$) while the phase advance is $\pi/2$.

variables	fitting constraints
quadrupole strength q	$\sigma_{12}(1) = \sigma_{12}(2) = 0$
drift length L_1	$L_1 + L_2 = L$
	$\text{acos}\left(\frac{tr(R)}{2}\right) = \pi/2$

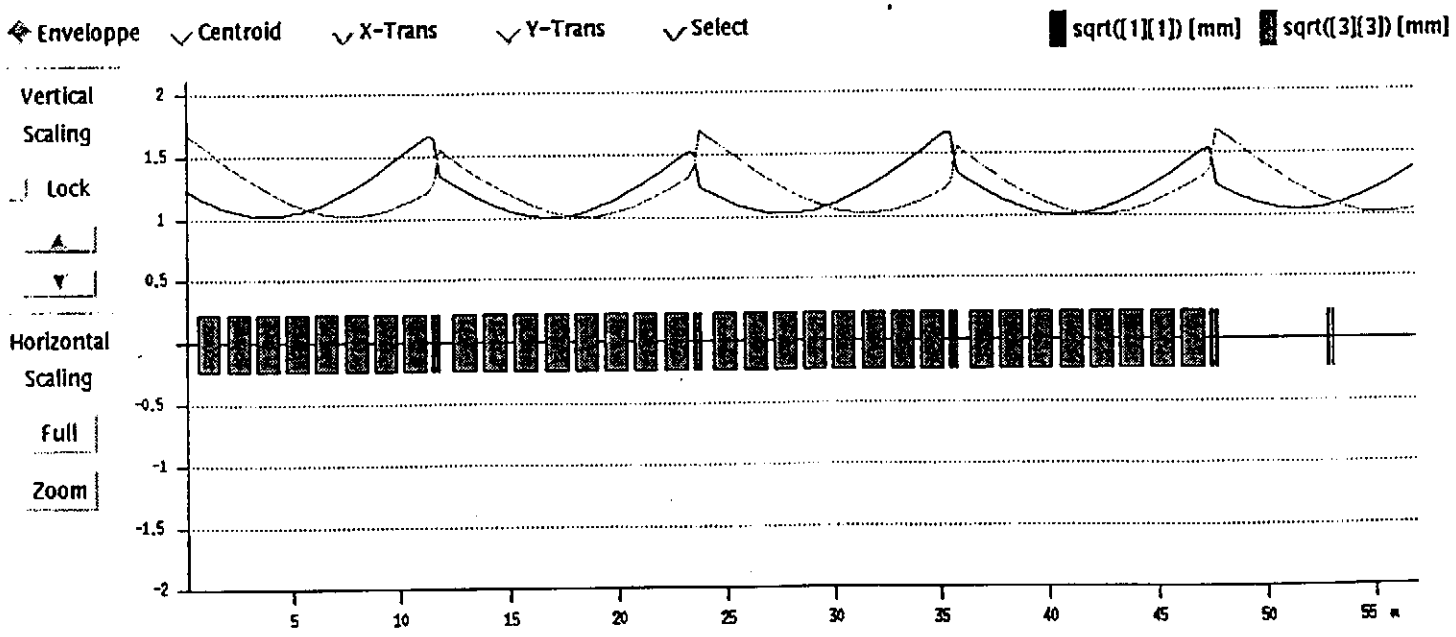

The periodic solution for the used FIDO lattice. The TTF accelerator's geometry is shown on axis and consists of four equal modules each containing eight superconducting cavities followed by a quadrupole dublet. Here the accelerating field in all 32 cavities is switched off in order to show the pure FIDO lattice. The graph gives the beam enveloppes $\sqrt{\sigma_{11}}$ (solid line) and $\sqrt{\sigma_{33}}$ (dotted line) in x-direction and y-direction respectively as they result from a first order beam transport calculation [Ref.XBEAM].

rf focusing of standing wave structures has to be taken into account!!!

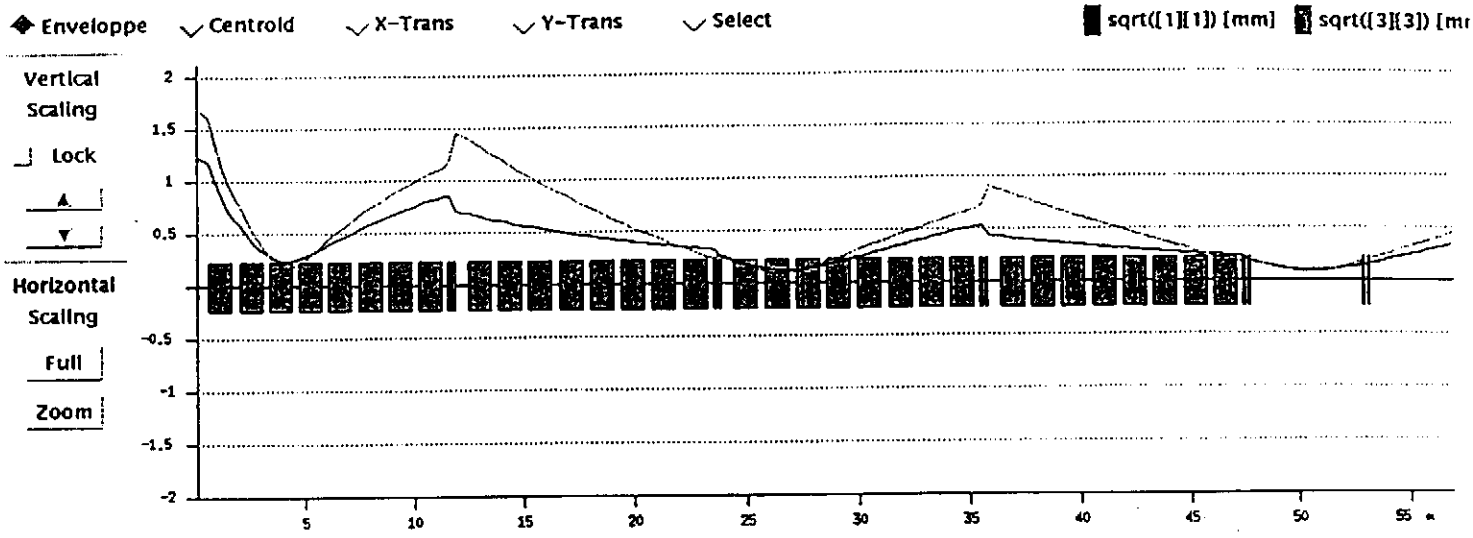

The effect of the accelerating field on the periodic solution for the used FIDO lattice. The graph gives the beam enveloppes $\sqrt{\sigma_{11}}$ (solid line) and $\sqrt{\sigma_{33}}$ (dotted line) in x-direction and y-direction respectively as they result from a first order beam transport calculation [Ref.XBEAM]. The accelerating gradient is 15 MV/m and the quadrupole strength is scaled with the beam energy. Although the injection energy was chosen to be 14 MeV, the focusing effect of the accelerating cavities is strong.

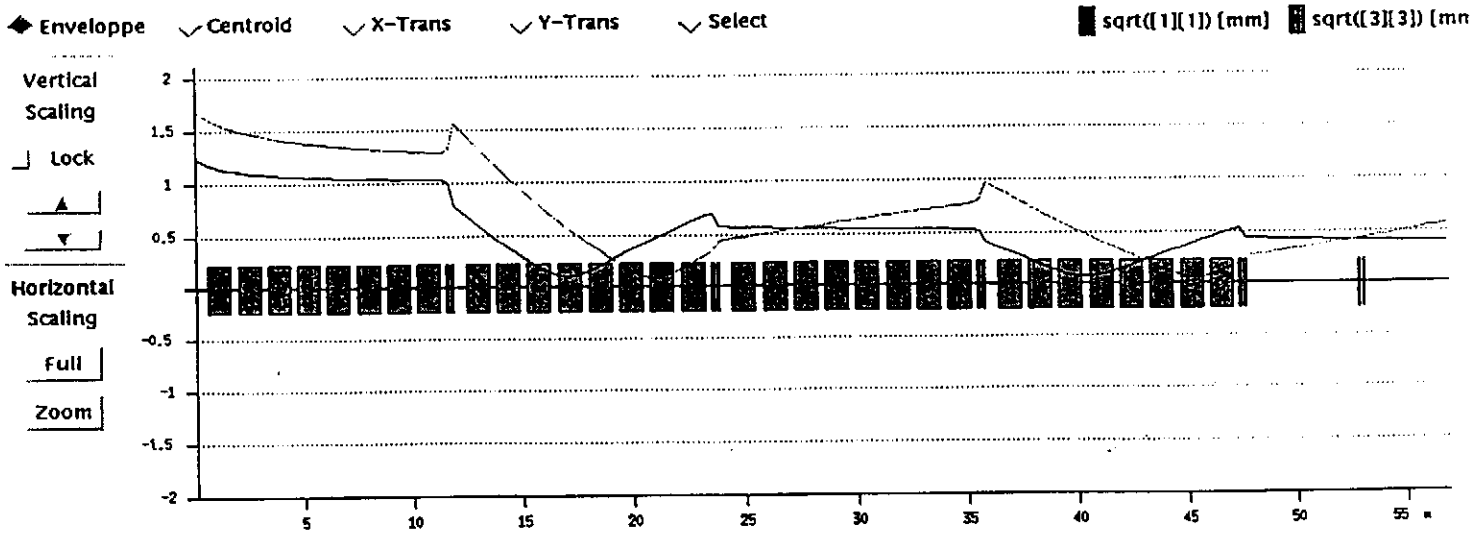

The effect of the accelerating field of a *travelling wave structure* on the periodic solution for the used FIDO lattice. The graph gives the beam enveloppes $\sqrt{\sigma_{11}}$ (solid line) and $\sqrt{\sigma_{33}}$ (dotted line) in x-direction and y-direction respectively as they result from a first order beam transport calculation [Ref.XBEAM]. Again the accelerating gradient is 15 MV/m and the quadrupole strength is scaled with the beam energy. The injection energy was chosen to be 14 MeV as in Fig.2. While the focusing of standing wave structures pulls the waist in the first module towards the linac entrance, the pure adiabatic damping in travelling wave structures pushes this waist downstream.

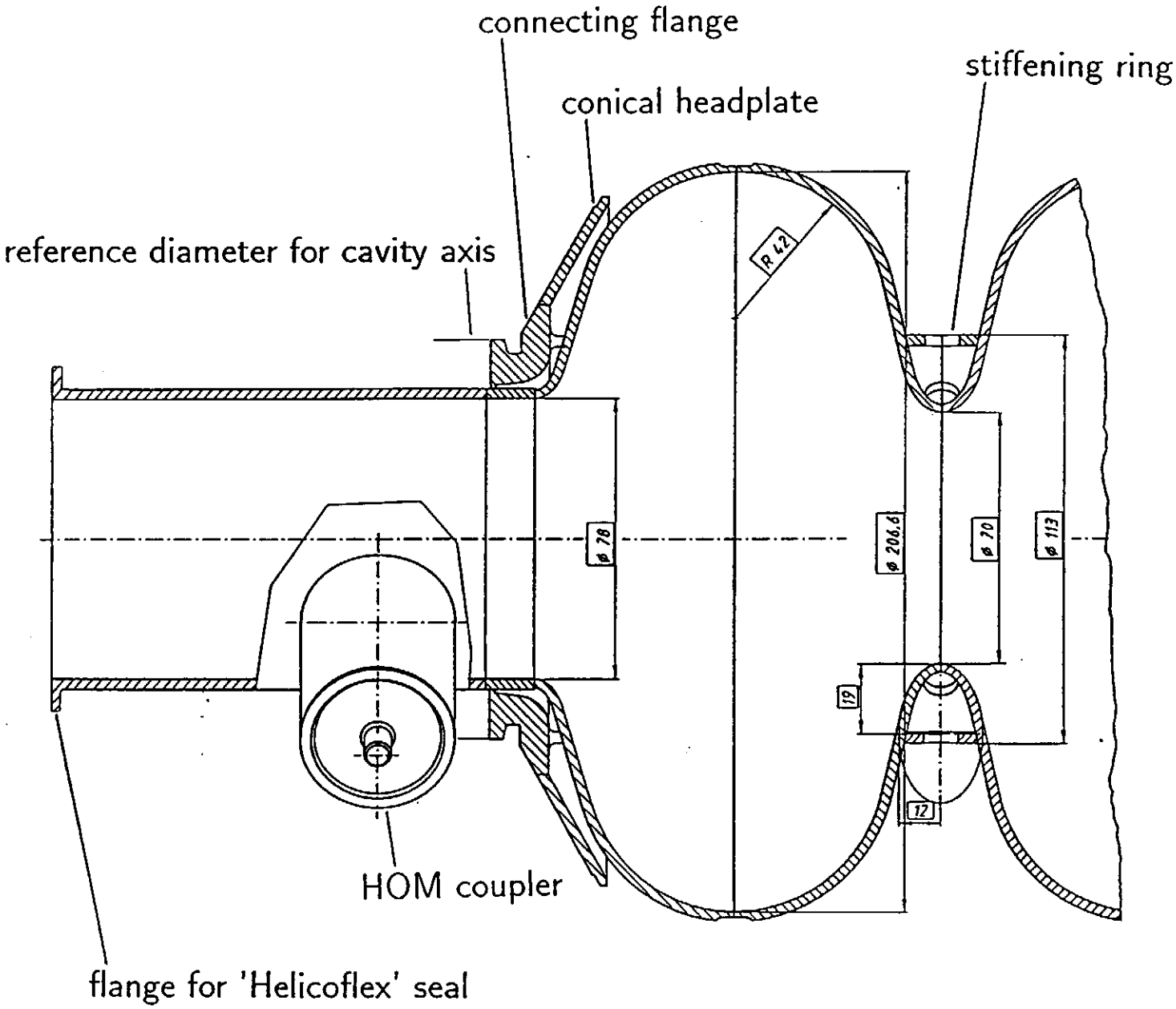

Cavity shape parameters, all dimensions in [mm]

cavity shape parameter	midcup	endcup 1	endcup 2
cavity radius R_o	103.3	103.3	103.3
external curv. radius R	42.0	40.34	42
iris radius R_i	35	39	39
horizontal half axis a	12	10	9
vertical half axis b	19	13.5	12.8
length L	57.692	56	57

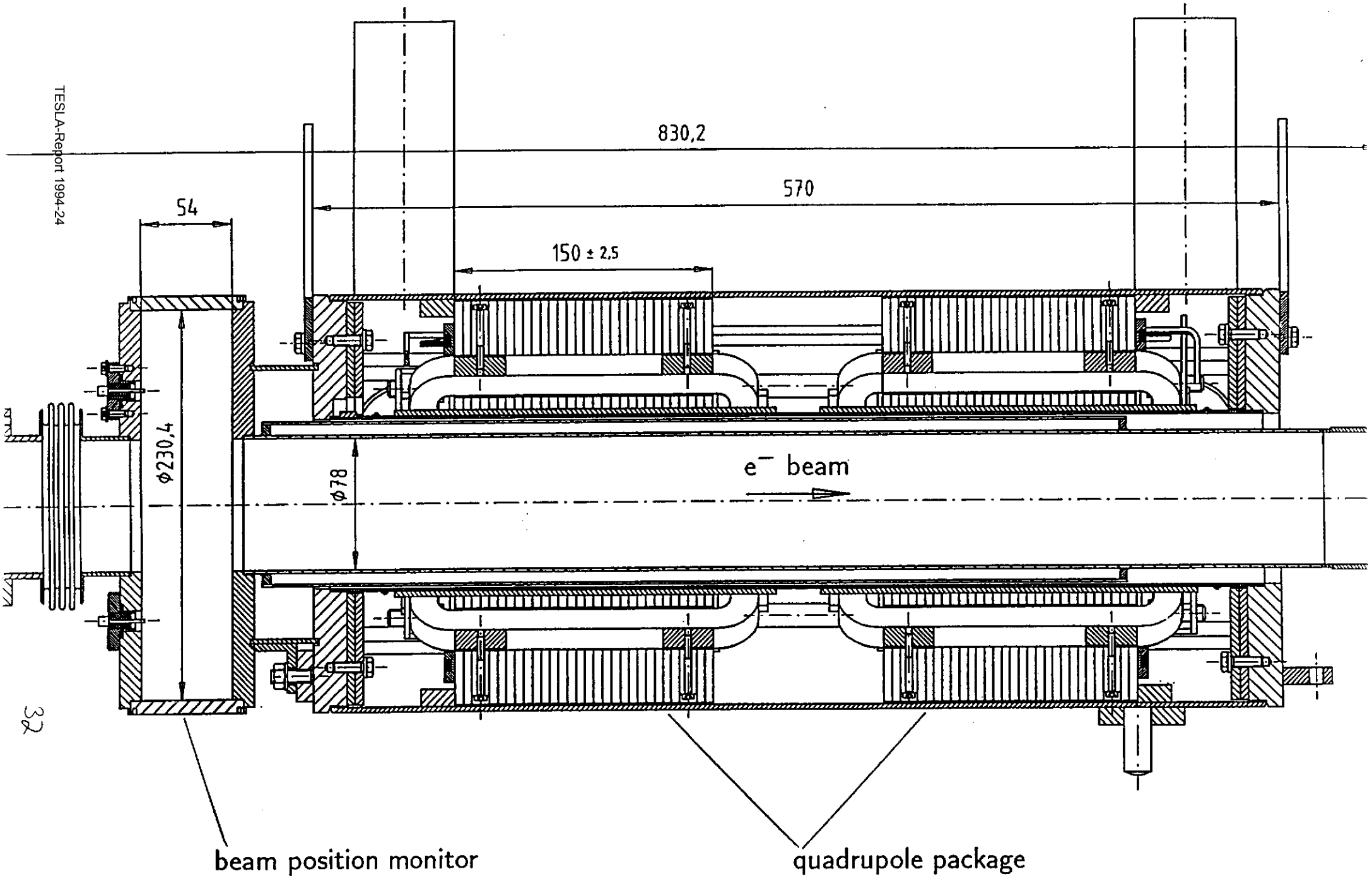
830,2
570
54
150 ± 2,5
ϕ230,4
ϕ78
e⁻ beam
beam position monitor
quadrupole package

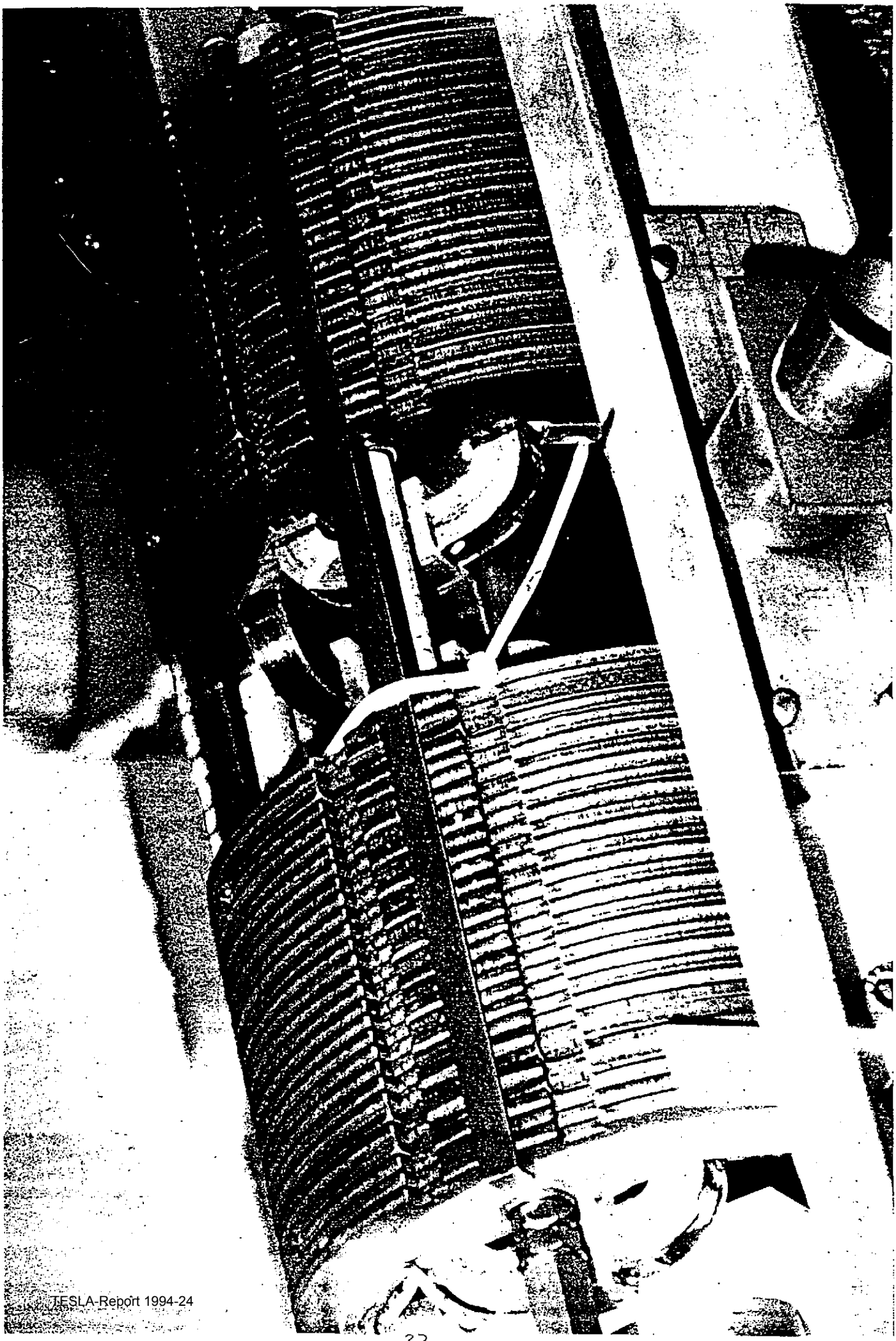

Quadrupole Lens				
quadrupole type	superferric			
pole radius	56	mm		
outer diameter of yoke	238	mm		
yoke length	150	mm		
distance of quad centers	250	mm		
no. of turns per pole	464			
field gradient	14	T/m	37.5	A
	17	T/m	46.1	A
	20	T/m	55.7	A
max. integrated gradient	~3	T	55.7	A
max. field at conductor	~2.23	T	55.7	A
integrated b6 at r = 10mm	7.4×10^{-4}		55.7	A
integrated b10 at r = 10mm	-0.2×10^{-4}		55.7	A
conductor wire	0.95× 0.5	mm^2		
conductor I_{ss} at 4.6 K	112	A	4.6	T
Dipole Correction Coil				
dipole type	single layer			
inner coil diameter	52.5	mm		
outer coil diameter	54.2	mm		
inner coil angle	15.85	deg		
outer coil angle	50.65	deg		
field strength	0.0639	T	100	A
integr. field strength	0.0096	Tm	100	A
conductor wire diameter	0.7	mm		
conductor I_{ss} at 4.6 K	>250	A	5.5	T

Beam Position Monitor			
type	pill box cavity		
material	stainless steel		
inner diameter	240	mm	
inner width	60	mm	
High Order Mode Absorber			
type	ann.space cooled with 70 K		
assumed heat load	20	W	
helium cooling	~0.4	g/s	60 K, dT = 10 K
heat input at 4 K	~1.5	W	
heat input at 2 K	~0.2	W	
material	stainless steel		
Current Leads			
type	gas cooled copper wires		
no. of pairs	4		
optimized cuurent	100	A	
assumed heat load	20	W	
helium cooling	~1.8	W	at 4 K and 0.1 g/s
Support System			
type	rings att.to He return tube		
no. of support planes	2		
accuracy of adjustment	0.1	mm	x- and y-plane
Instrumentation			
T-sensors at quadrupole	2		carbon, TSC
T-sensors at HOM absorb.	2		platinum, PT1000
accelerometers	2		helium vessel

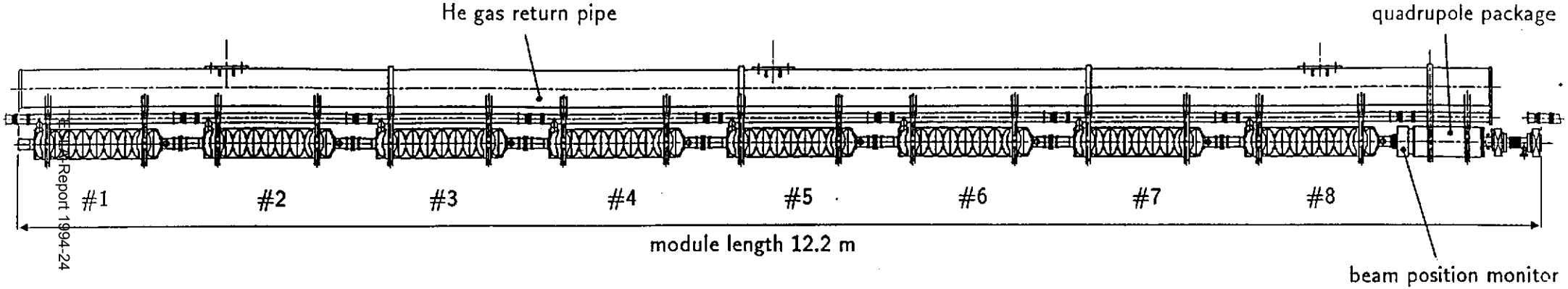

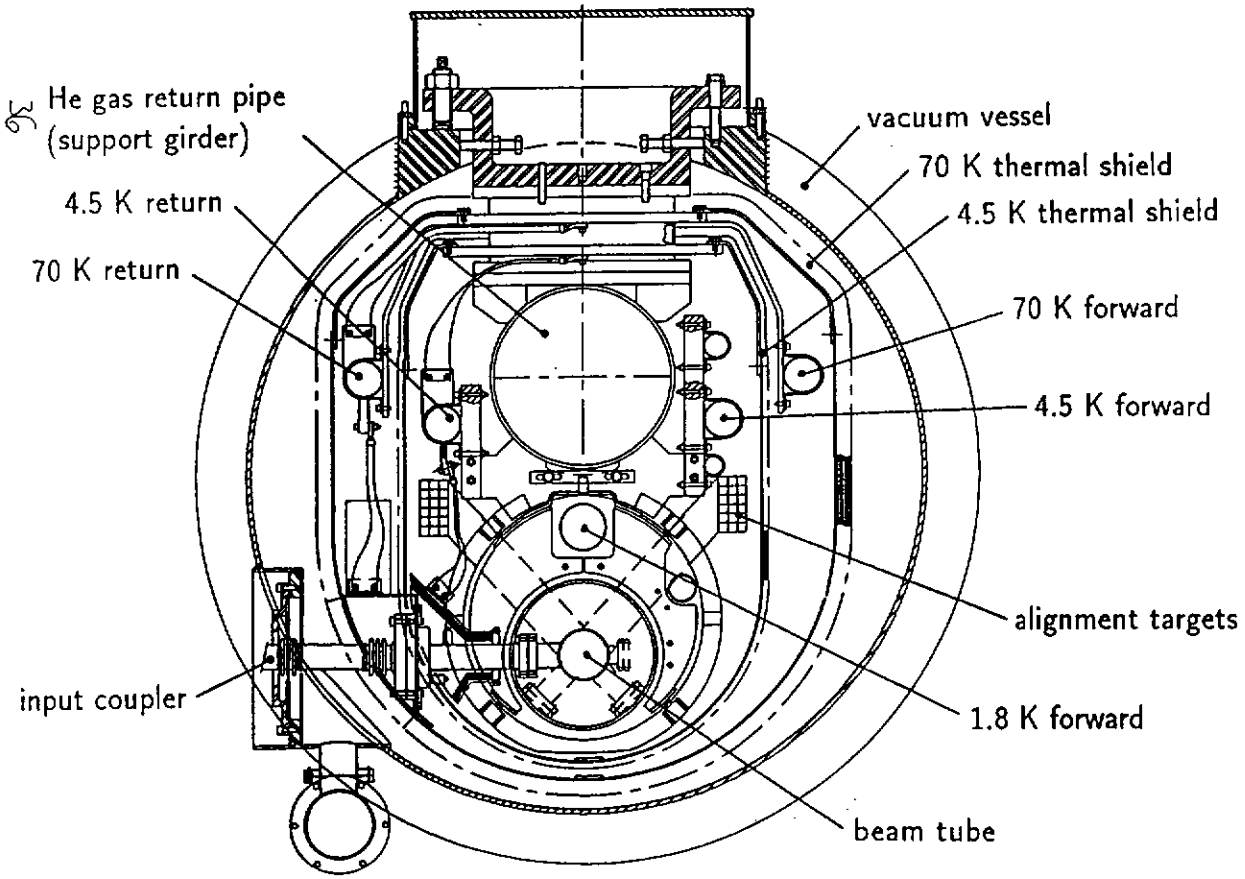

- He gas return pipe (HeGRP) is supported from above by three support posts (fiberglas pipe); it acts as a girder and is used for alignment
- the 8 cavities, the quadrupole package and aux.equipment are attached to the HeGRP by means of stainless steel collars
- two aluminium radiation shields are at intermediate nominal temperatures of 4.5 K and 70 K; they are cooled by means of flexible cooper braids connected to the centerline of the shield upper section
- the input coupler penetrate both shields and have special radiation shield 'cones'
- approx. 128 temperature sensors and 2 accelerometers are foreseen on the prototype cryomodule
- the anticipated static heat load budget for one cryomodule is

$$\leq 4\ \text{W} @ 1.8\ \text{K}$$
$$\approx 14\ \text{W} @ 4.5\ \text{K}$$
$$\approx 120\ \text{W} @ 70\ \text{K}$$

the matched FIDA lattice of the TTF linac

- using the PARMELA output data a matching between the injector and the first cryomodule is possible; two triplets are needed
- the rf focusing of standing wave cavities (for on- and also off-crest injection) has to be taken into account
- rf focusing is different from 'adiabatic damping'; in addition to this 'damping' a radial force exists which is a consequence of the forward/backward wave in standing wave structures
- perfect matching can be obtained by fitting the previously calculated waist (FIDO) in the middle of module #1

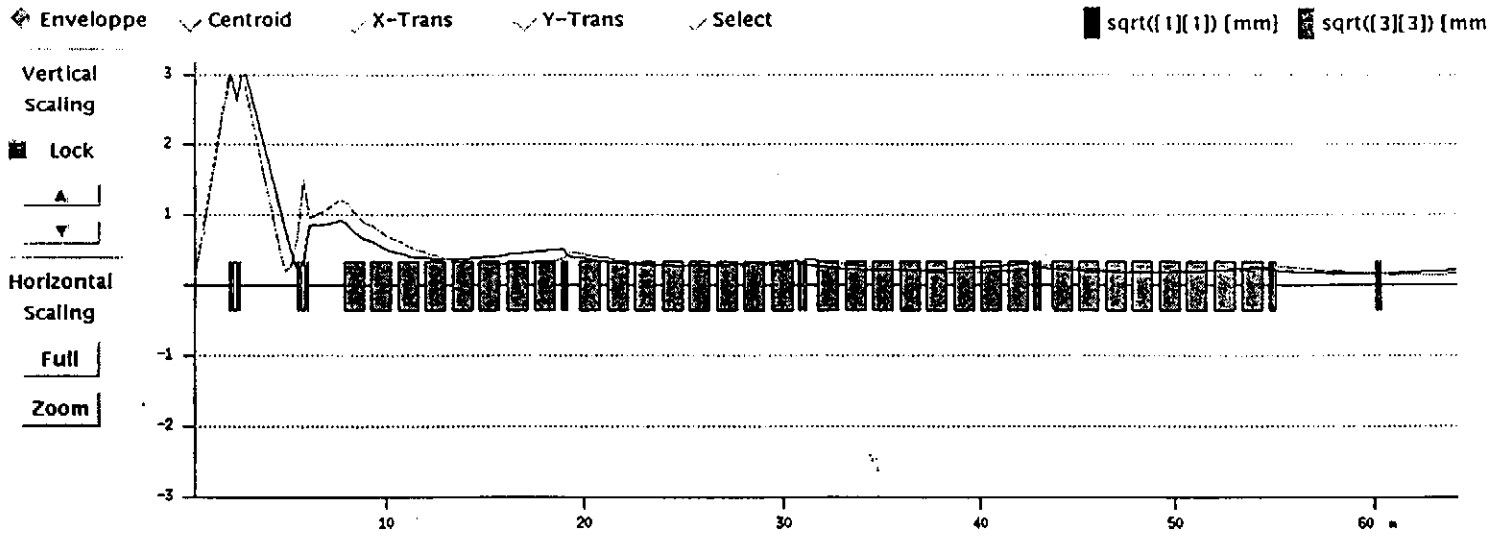

What the TTF linac does check:

- Gradient achievable
- Cavity construction and processing techniques
- Input and HOM coupler designs
- RF control of multi-cavity systems
- Lorentz force detuning effects and control
- High peak power processing
- Vacuum failure recovery potential
- cryostat design
- Cryogenic operation
- Dark current
- Energy and position feedback
- Alignment and its stability
- BPM systems
- First iteration on projected system costs

What may be difficult to check:

- Q_0 and HOM measurements are not easy
- Wake field measurements only far of axis
- Cavity alignment via wake fields hard (polarization)
- TESLA 500 bunch charge hard to achieve in time scale of TTF linac
- Accurate cost projection to mass production

What the TTF linac does not check:

- Emittance growth
- Vibration sensitivity
- Many features of an overall TESLA 500 facility

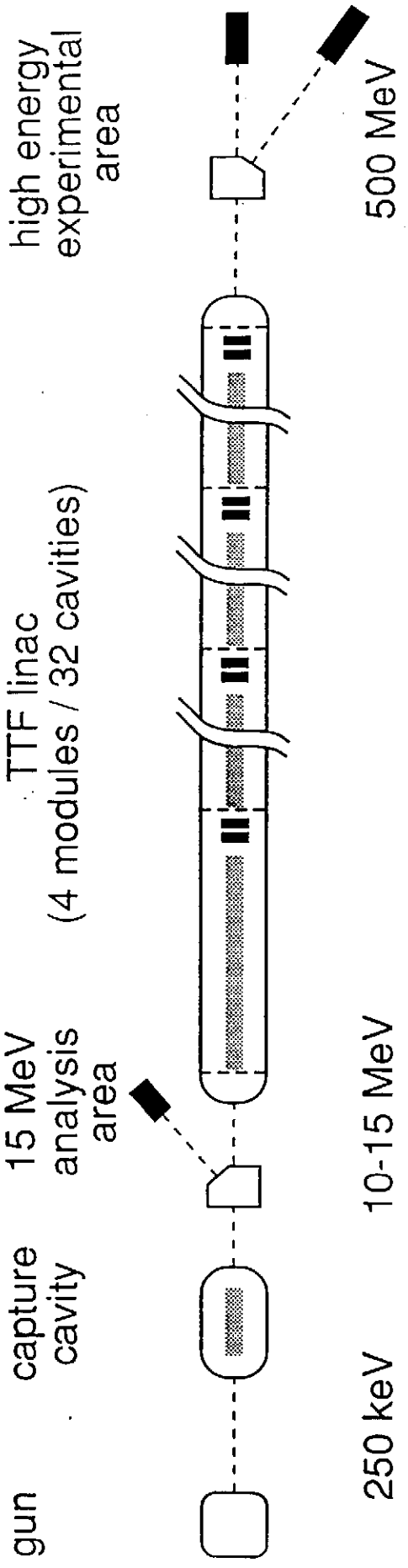
gun
capture cavity
15 MeV analysis area
TTF linac
(4 modules / 32 cavities)
high energy experimental area
250 keV
10-15 MeV
500 MeV

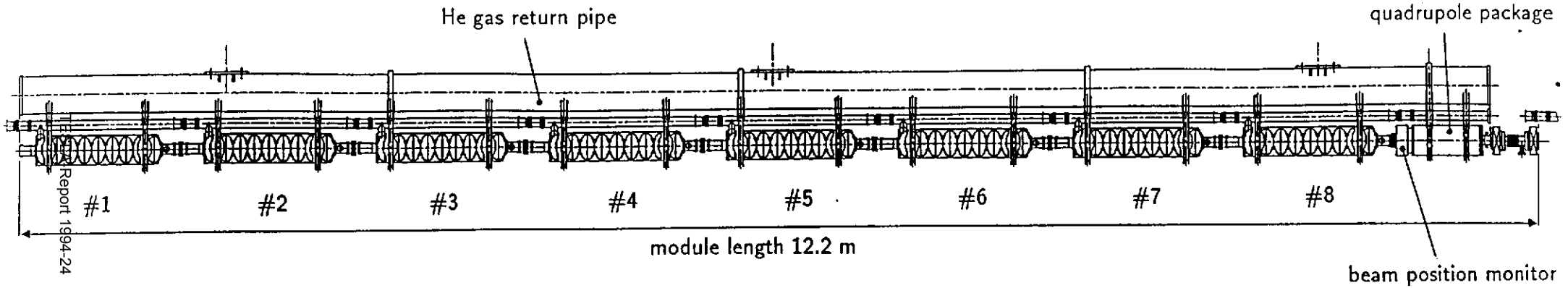

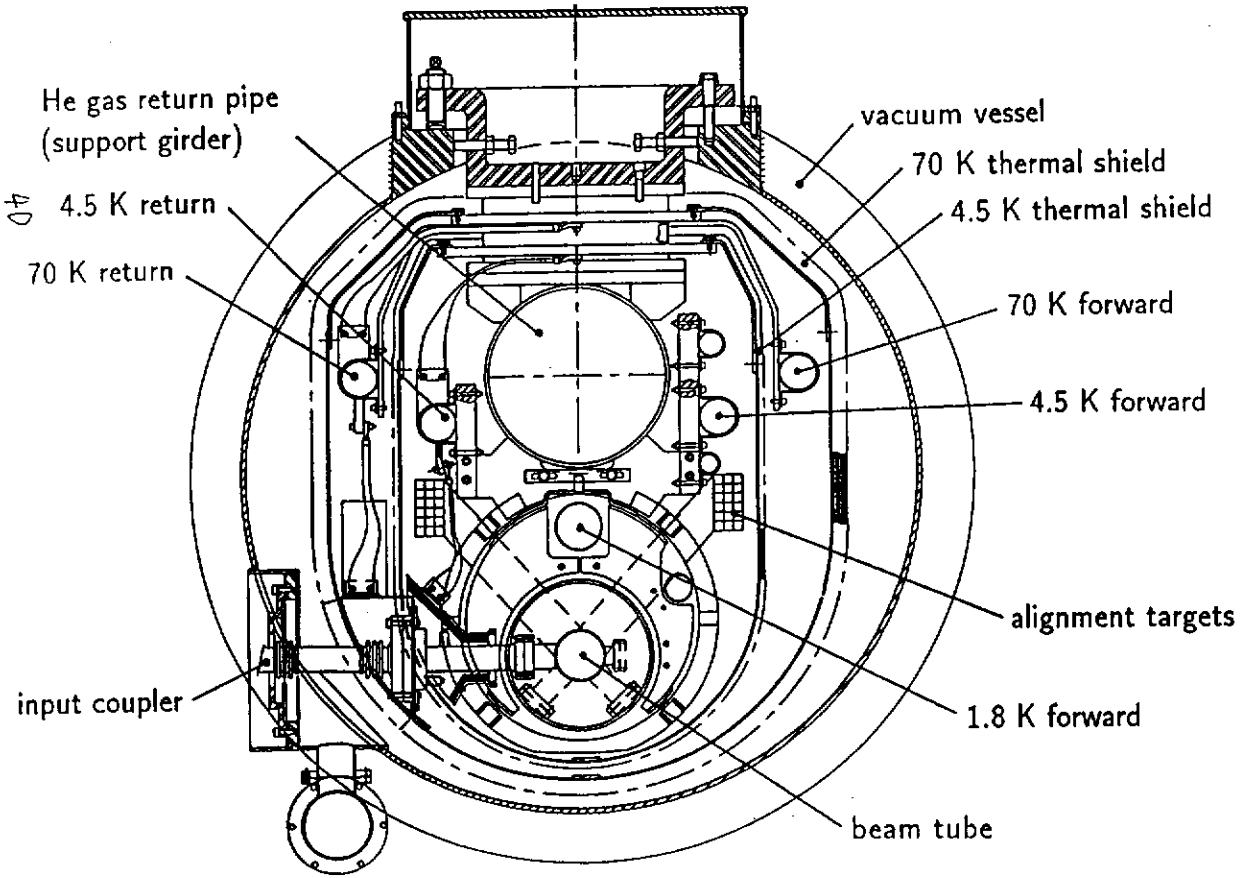

- He gas return pipe (HeGRP) is supported from above by three support posts (fiberglas pipe); it acts as a girder and is used for alignment
- the 8 cavities, the quadrupole package and aux.equipment are attached to the HeGRP by means of stainless steel collars
- two aluminium radiation shields are at intermediate nominal temperatures of 4.5 K and 70 K; they are cooled by means of flexible cooper braids connected to the centerline of the shield upper section
- the input coupler penetrate both shields and have special radiation shield 'cones'
- approx. 128 temperature sensors and 2 accelerometers are foreseen on the prototype cryomodule
- the anticipated static heat load budget for one cryomodule is

$\leq$	4 W	@	1.8 K
$\approx$	14 W	@	4.5 K
$\approx$	120 W	@	70 K

the matched FIDA lattice of the TTF linac

- using the PARMELA output data a matching between the injector and the first cryomodule is possible; two triplets are needed
- the rf focusing of standing wave cavities (for on- and also off-crest injection) has to be taken into account
- rf focusing is different from 'adiabatic damping'; in addition to this 'damping' a radial force exists which is a consequence of the forward/backward wave in standing wave structures
- perfect matching can be obtained by fitting the previously calculated waist (FIDO) in the middle of module #1

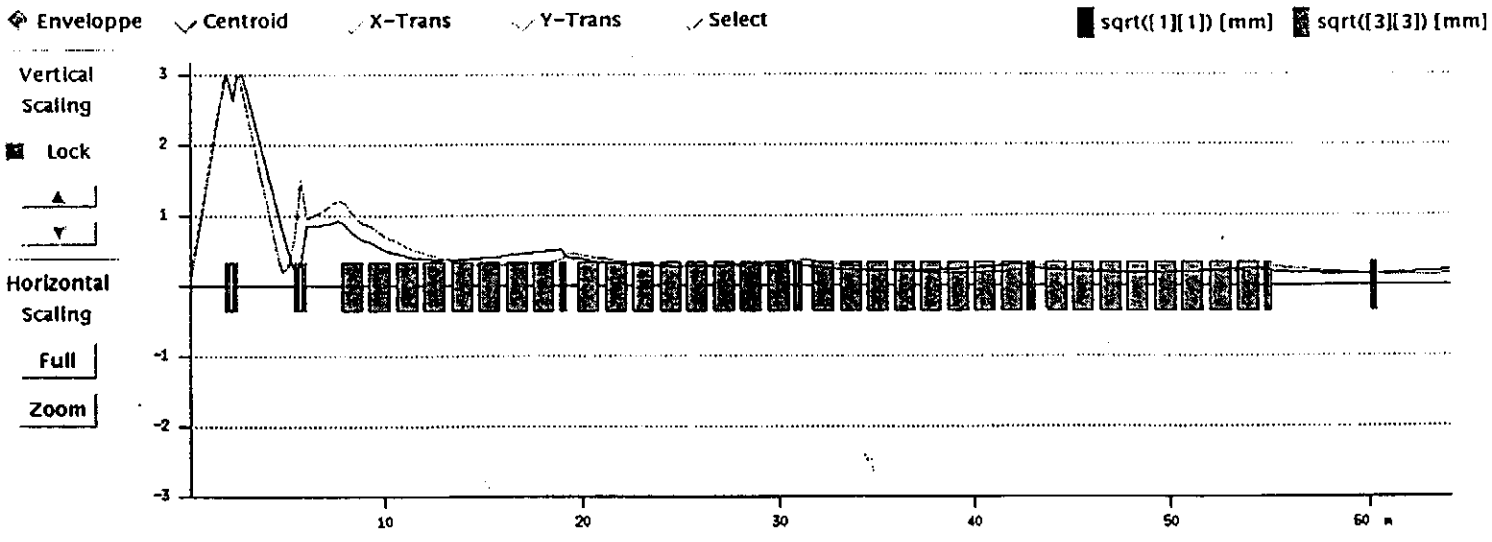

What the TTF linac does check:

- Gradient achievable
- Cavity construction and processing techniques
- Input and HOM coupler designs
- RF control of multi-cavity systems
- Lorentz force detuning effects and control
- High peak power processing
- Vacuum failure recovery potential
- cryostat design
- Cryogenic operation
- Dark current
- Energy and position feedback
- Alignment and its stability
- BPM systems
- First iteration on projected system costs

What may be difficult to check:

- Q_0 and HOM measurements are not easy
- Wake field measurements only far of axis
- Cavity alignment via wake fields hard (polarization)
- TESLA 500 bunch charge hard to achieve in time scale of TTF linac
- Accurate cost projection to mass production

What the TTF linac does not check:

- Emittance growth
- Vibration sensitivity
- Many features of an overall TESLA 500 facility

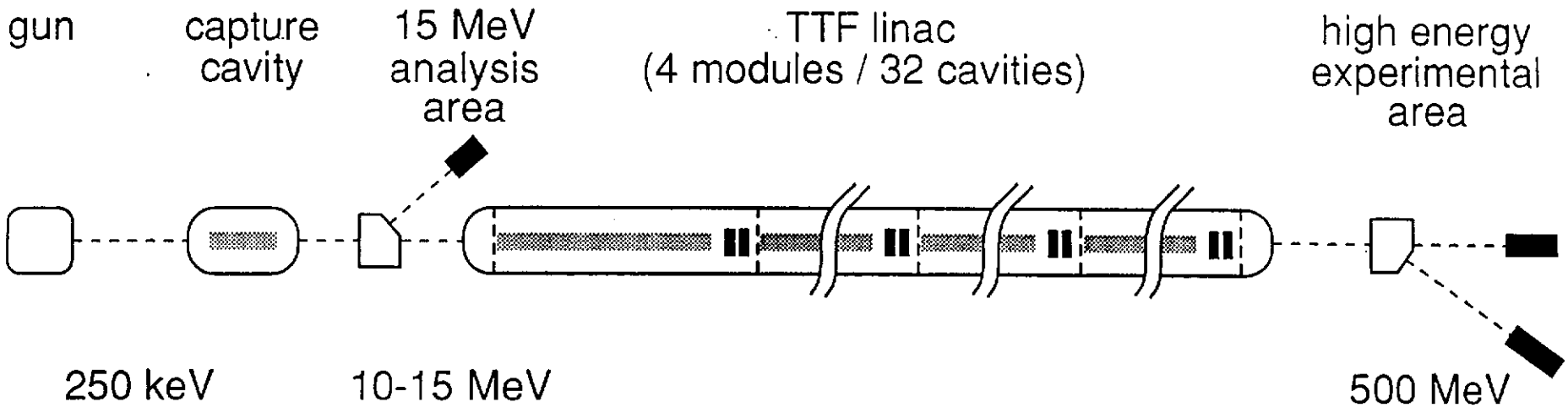
gun
capture cavity
15 MeV analysis area
TTF linac
(4 modules / 32 cavities)
high energy experimental area
250 keV
10-15 MeV
500 MeV

A Long Pulse Modulator for Reduced Size and Cost

H. Pfeffer, L. Bartelson, K. Bourkland, C. Jensen, Q. Kerns, P. Prieto, G. Saewert, D. Wolff
Fermi National Accelerator Laboratory
P.O. Box 500
Batavia IL 60510

Abstract

A novel modulator has been designed, built and tested for the TESLA test facility. This e^+ e^- accelerator concept uses superconducting RF cavities and requires 2 ms of RF power at 10 pps. As the final accelerator will require several hundred modulators, a cost effective, space saving and high efficiency design is desired. This modulator uses a modest size switched capacitor bank that droops approximately 20% during the pulse. This large droop is compensated for by the use of a resonant LC circuit. The capacitor bank is connected to the high side of a pulse transformer primary using a series GTO switch. The resonant circuit is connected to the low side of the pulse transformer primary. The output pulse is flat to within 1% for 1.9 ms during a 2.3 ms base pulse width. Measured efficiency, from breaker to klystron and including energy lost in the rise time, is approximately 85%.

Introduction

This paper is a description of the TESLA 5 MW modulator built at Fermilab and presently in use as a test stand at DESY. We examined several different modulator techniques and chose a new design suited to a long (2 ms) output pulse. The requirements for the modulator are:

Pulse Width (99% to 99%)	Output Voltage	Output Current	Repetition Rate	Operating Lifetime
2 ms	130 kV	95 A	10 pps	>10 years

Design Approach

Our initial approach to the modulator design was a line type PFN with a step-up transformer. Although we realized the 2 ms pulse length was rather long for this technique, a 24 section, 8.3 Ω PFN was designed to meet the specifications. Iron core inductors were used because of the long pulse length and the need to reduce physical size. The PFN that we designed was 2 m x 4 m x 2 m high and had a component cost of approximately 225 k$. The total modulator component cost estimate was 535 k$.

A modulating anode supply was then investigated. The estimated cost of this system is less than the PFN approach. However, no switch tube was available that would meet performance requirements. Additionally, the efficiency of the modulated anode approach is significantly lower than the PFN approach.

We next looked into a switched-capacitor design. Our main concern about this approach was the large amount of stored energy (1 MJ) that would be required. Then one of us, Q. Kerns, suggested an ingenious way to reduce stored energy and cost.

The classic text by Lebacqz and Glasoe shows how the output of hard tube modulator may be flattened by the use of a parallel L R circuit in series with the load [1]. This circuit has power loss; however the reduction in stored energy is impressive. Kerns' idea reduces the stored energy by adding low loss passive components to the modulator. A switched capacitor bank is used. However, it is allowed to discharge approximately 20% during the pulse. This large droop is then compensated for by the use of a low impedance resonant LC (" bouncer ") circuit. This greatly reduces the loss over the L R circuit but retains the benefit of lower stored energy. The estimated cost of this bouncer circuit was 20 k$, and its size was approximately 2m by 1m by 2m. The component cost estimate for this modulator was under 400 k$, and we decided to pursue this design.

Principles of Operation

The modulator topology is shown in Figure 1. The main capacitor bank, C1, is charged to approximately 10% higher than the required output voltage, while the bouncer, L3 & C2, is charged to 10% of the required output voltage. To produce an output pulse, the bouncer resonant circuit switch, S4, is closed, and the capacitor starts to ring with the inductor. At the *appropriate* time, the GTO switch, S1, connecting the main capacitor bank to the pulse transformer is closed. After the 2 ms output pulse length, the GTO switch is opened. The bouncer circuit then continues to ring through its full cycle. Figure 2 shows the bouncer voltage and main capacitor bank voltage. The bouncer waveform is subtracted from the main capacitor bank waveform, and Figure 3 shows the resultant output voltage in full size and expanded versions. The specifications are clearly met.

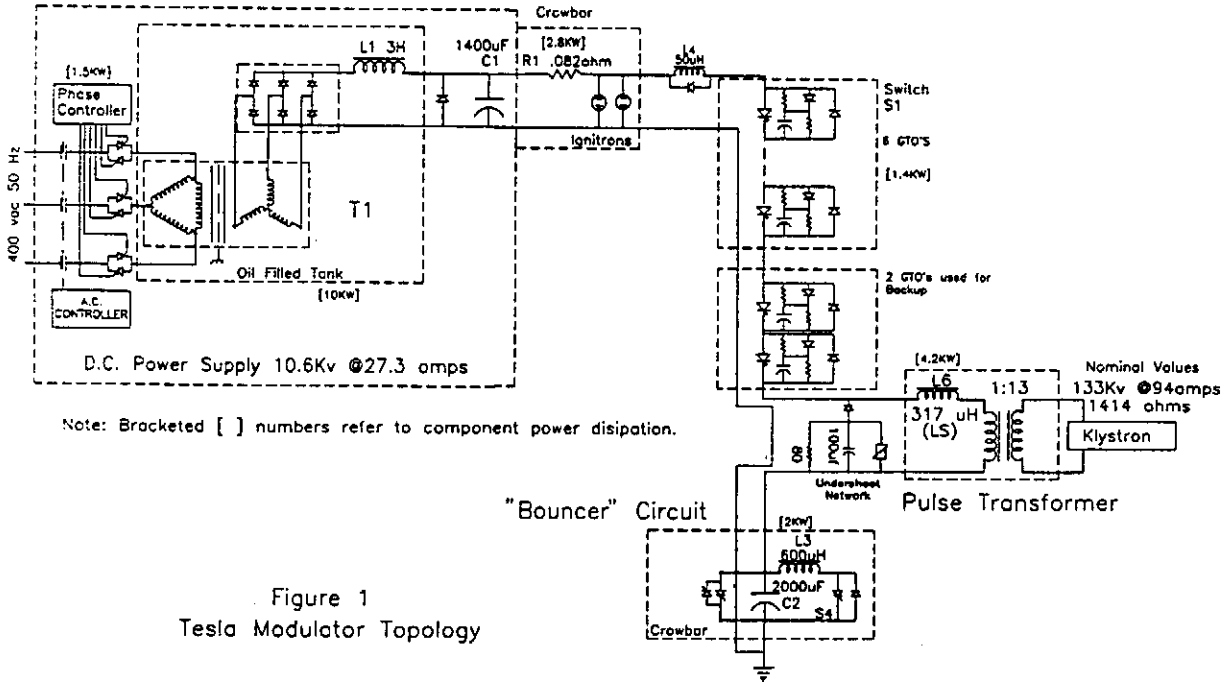

Figure 1
Tesla Modulator Topology

Work supported by the U. S. Department of Energy under contract No. DE-AC02-76CH03000

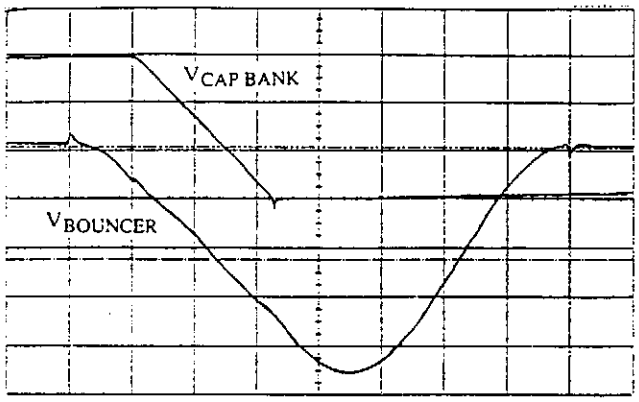

Figure 2. Main Capacitor Bank Voltage (Top) and Bouncer Voltage (500 V/div, 1 ms/div, Main Capacitor Bank Zero Suppressed)

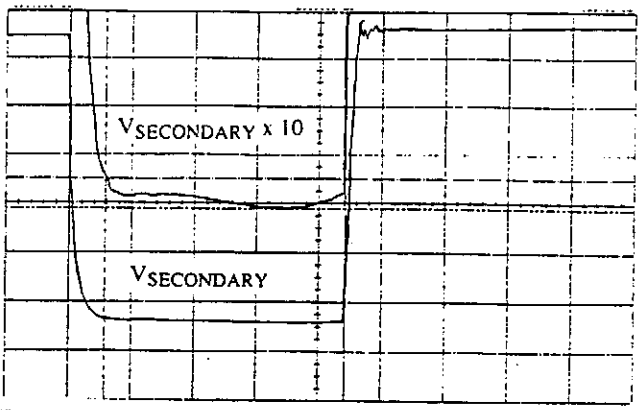

Figure 3, Expanded Secondary Voltage (Top) and Secondary Voltage (2 kV/div, 20 kV/div, 0.5 ms/div, Expanded Zero Suppressed)

Key Modulator Components

Several components are unique to this modulator. A reliable and robust closing and opening switch is required, so a series stack of six GTOs (Gate Turn Off thyristor) is used. The bouncer circuit must be designed with low loss and the maximum impedance consistent with effective output regulation. The main capacitor bank must be designed for crowbar operation and capacitor fault conditions. The bus bar must have low inductance between all major components and must be designed to tolerate the crowbar current between the main capacitor bank and the crowbar switch. The pulse transformer must have a very large volt second rating and a relatively low leakage inductance. Mechanical vibration from the system must be kept to a minimum because the RF superconducting cavities are nearby.

GTO Switch

The switch element in the transformer primary circuit must be rated to operate at 12 kV and switch 1200 Amps both on and off. We seriously considered the use of a series SCR switch with a forced commutation circuit to turn it off. The design effort revealed that the forced commutation circuitry was costly, dissipative and complex. A series GTO switch seemed like a natural choice for this application. We were hesitant to proceed due to the scarcity of documented series GTO applications. We decided to use the GTOs after studying their manuals and talking to the designer of a successful commercial application [2].

The switch is a series string of six devices as shown in Figure 4. Two more series GTOs are controlled independently and constitute a backup switch that operates in conjunction with the capacitor bank crowbar if the main switch fails to open properly. The GTOs we have used are GEC type DG758BX45. The key GTO ratings are listed below.

I_{tgqm}	3.0 kA	Maximum controllable current
V_{drm}	4.5 kV	Maximum repetitive off state voltage
T_{gs}	25.0 µs	Maximum turn off storage time

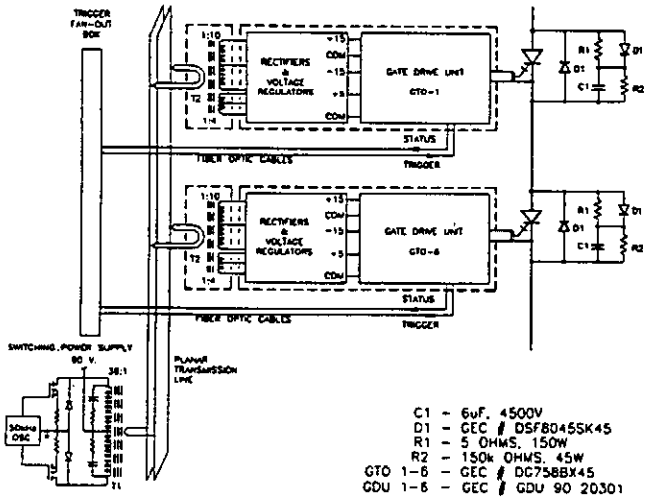

Figure 4, GTO Switch Schematic

The snubber circuits are those recommended by the vendor. The gate drive units are purchased from GEC/Plessey. They are controlled by fiber optic cables, but require isolated power.

We designed a high current, low voltage 50 kHz switcher supply capable of delivering 10 W of isolated power to each of the eight gate drive units. Power from the switcher supply is distributed using a planar transmission line connected to the secondary terminals of a ferrite (MN100) step–down transformer (T1, Figure 4). Eight one turn loops of the center conductor of RG–17 cable are connected in parallel across the planar transmission line. These are the primary windings of step–up transformers (T2) located at each gate drive unit. The RG–17 cable provides the voltage isolation between the switcher supply and the GTO gate-drive units. At the step–up transformers, power is converted to ±15V and +5V and used by the gate drive units. The step–up transformers are driven in parallel rather than in series. The series configuration suffers from unequal drive voltage sharing due to variations in loading of the individual gate drive units. The unequal sharing is exacerbated by the use of voltage regulators in the secondary circuits.

Although the nominal primary current is 1200 A, a klystron gun spark causes the current to rise to 1800 A. The extra current is generated because of the 20 µs storage time (T_{gs}) of high current GTOs. When a gun spark is detected, the switch is immediately gated off. During the storage time the switch current rises at a rate of 27 A/µs, as limited by the pulse transformer leakage inductance (320 µH) and the inductance of a 50 µH coil in the primary circuit. We chose 3 kA GTOs in order to have sufficient margin to be able to reliably turn off at 1800 A. Figure 5 shows the primary current rising to 1800 A before turning off in an actual gun spark.

The switch turn–off transients have been controlled in two ways. First, the turn–off voltage sharing has been balanced through the matching of device storage times to within 2.5 µs. Second, the turn–off voltage overshoot has been limited by the use of planar transmission line buswork to limit stray primary circuit inductance to less than 2 µH. In addition, the snubber network inductance has been limited to 140 nH.

In order to protect the switch from catastrophic failure, we added control circuits to monitor and react to such situations as lack of cooling water flow, excess heat sink temperature, malfunctioning gate drive units, or the failure of a single GTO.

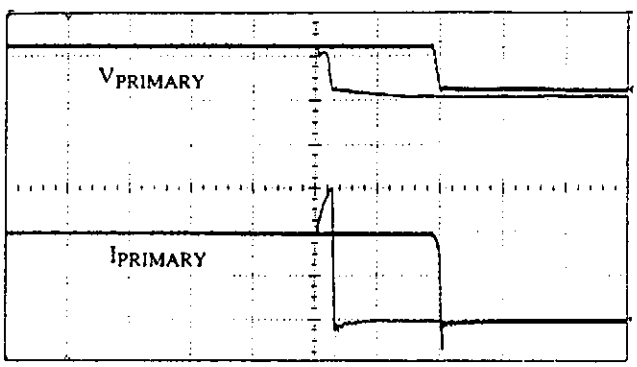

Figure 5, Primary Voltage (Top) and Current During a Gun Spark (10 kV/div, 600 A/div, 100 µs/div)

Bouncer Circuit

The bouncer circuit is a resonant LC circuit that is placed in series with the pulse transformer primary. The bouncer is triggered to ring through its single cycle sine wave just before the main pulse is started. As shown in Figure 6, the bouncer is in the linear part of its waveform as the output pulse goes through the bouncer circuit. The linear voltage is subtracted from the main capacitor bank voltage, and compensates for the capacitor bank 20% droop. The resultant output pulse is flat to within 1%.

Two ideas have been key for us in understanding the operation of the bouncer. The first concerns the bouncer impedance. If the bouncer were designed at an infinitesimally low impedance level, the presence of the pulse current going through it would make a negligible distortion of its sine wave, and the subtraction of the capacitor droop would be straightforward. Unfortunately, such a circuit would be infinitely large and expensive. On the other hand, the sine wave of a high impedance version would be drastically distorted if the pulse current were much larger than the bouncer resonant current. We started with a design in which the peak bouncer current was twice the pulse current. Our SPICE model showed that although the bouncer waveform was somewhat flattened during the current pulse, the droop compensation still worked at the 1% level once the bouncer starting voltage was raised to adjust for the flattening effect. If we doubled the impedance of the bouncer components, the model no longer worked at the 1% level. We therefore used our initial impedance choice.

The second key idea concerns the power flow into the bouncer circuit. Figure 6 shows that the bouncer capacitor voltage has equal positive and negative parts during the current pulse. During the first half of the pulse, the pulse current adds energy to the capacitor, and during the second half of the pulse it subtracts an equal amount. The only losses in the bouncer circuit are due to the dissipation factors of the bouncer components. The components were specified to dissipate less than 2 kW at full power operation.

It is interesting to note that if the pulse is shifted earlier in the bouncer waveform, a net positive energy is deposited in the bouncer capacitor. We make use of this feature by adjusting the relative timing of the bouncer and output pulse so that the bouncer is charged to the desired level. No bouncer capacitor charging supply is required! A closer look at Figure 6 reveals that the bouncer voltage zero crossing is slightly later than the midpoint of the current pulse since we were using this feature at that time.

We were surprised to find how stable this charging system turned out to be. For any timing relationship the bouncer voltage is stable. If the pulse timing is set too late, the bouncer capacitor charges to a lower stable operating voltage, and the output pulse has a negative slope. If the pulse timing is set too early, the bouncer capacitor charges to a higher stable operating voltage, and the output pulse has a positive slope. It is stable because as the bouncer charges to a higher voltage, the output pulse voltage and current are reduced. The linear portion of the sine wave therefore has a larger slope (less flattening), and the average bouncer capacitor voltage during the pulse is made more negative. The net power delivered to the bouncer capacitor is thus decreased until a stable balance point is reached.

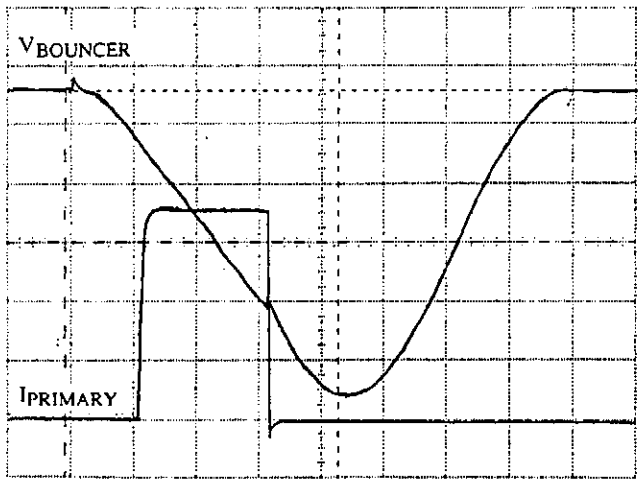

Figure 6. Bouncer Voltage (Top) and Modulator Primary Current (500 V/div, 300 A/div, 1 ms/div)

Main Capacitor Bank and Crowbar

The main capacitor bank has the standard concerns of a large stored energy application, and the additional concerns related to its high-speed crowbar. The crowbar circuit must remove the GTO switch input voltage within microseconds in order to protect the klystron from a switch failure. The crowbar resistive dump is in the main circuit path of the GTO switch. This enables the crowbar to remove the GTO switch input voltage in 4 μs while the capacitor bank is undergoing a 100 μs discharge. However, the resistance must be minimized to avoid excessive dissipation during normal operation. This minimal resistance causes large crowbar currents but has been chosen to critically damp the crowbar circuit.

The capacitor bank was divided into eight sections of 175 μF at 10 kJ each. Each section is connected to the main bus with a 0.1 Ω resistor to absorb the energy during a capacitor fault. Since a crowbar is a recoverable event and crowbar current and capacitor fault current are comparable, commercially available fuses could not be used.

The crowbar of the main capacitor bank is a back-up protection measure for the klystron, so we have made it redundant. The crowbar consists of two independent NL8900 Hg ignitron switches, each capable of the full discharge current (70 kA). Each ignitron is fired by an independent trigger circuit from independent fault detection logic.

The buswork between the main capacitor bank and the crowbar was designed as planar transmission line to minimize the inductance in the GTO circuit. This bus must also handle the forces during a crowbar, and be corona free at the 12 kV operating level. Lexan® (polycarbonate) was selected, because of its mechanical and electrical properties, both to insulate the bus conductors and to clamp them together. Extensive AC and DC hipotting of the buswork was done to insure a low partial discharge. Lexan's® corona threshold level was higher than either glass reinforced epoxy or fiber reinforced paper.

Pulse Transformer

The pulse transformer was also a challenging component . The primary leakage inductance was required to be less than 500 μH, and the primary magnetization was to be less than 12 A with at least 25 V•s before saturation. The transformer as delivered is large, approximately 1 m by 2 m by 1 m, with 320 μH of leakage inductance and 7 A magnetizing current at 27 V•s. The output voltage divider met specifications, however it had to be rebuilt to avoid excessive pickup during gun spark transients. There is very little acoustic noise from the transformer; the stiff core clamps and vibration isolation mounting of the core worked very effectively.

Klystron Protection

Klystron and modulator availability is a critical element of reliable linac operation. Protection of the klystron during gun sparks is an important element of the modulator design. The use of a pulse transformer makes possible an all solid state, and therefore more reliable and lower maintenance, modulator. However this same pulse transformer complicates the problem of protecting the klystron during a gun spark.

The klystron manufacturer has put a limit of 20 J on the amount of energy deposited into the klystron during a gun spark. During a normal pulse, 270 J is stored in the transformer leakage inductance. This energy must be removed from the transformer before it can be deposited into the sparking klystron. Crowbarring the primary circuit is not sufficient to remove this energy; the GTO switch must be opened so that the primary voltage can be inverted to at least 400 volts to rapidly reduce the leakage current.

The voltage inversion is controlled by an undershoot network installed across the transformer primary. The network is a parallel combination of a resistor, a capacitor, and a ZOV transient suppressor. The resistor absorbs the transformer magnetizing current and resets the core during normal operation. The capacitor absorbs the leakage inductance current during normal pulse turn-off, and limits the undershoot to 700 V. The ZOV clamps the undershoot to 1600 V following a gun spark. The capacitor would otherwise overcharge since the klystron does not share in absorbing the leakage inductance energy following a gun spark.

For the undershoot network to work at all, the GTO switch must first be opened. There is an alternate mechanism for opening the primary circuit if the GTO switch fails. If the primary current reaches

a threshold indicating that the GTO has not turned off, the backup system is used. The backup system crowbars the main capacitor bank and opens a pair of single GTOs in series with the main switch. Redundant control systems are used to monitor the current and control the crowbar and GTO switches to insure reliability.

Figure 7 shows the secondary current and voltage during an actual gun spark. Gun spark energy for this event is less than 4 J. The spark protection circuitry has functioned well through 40 gun sparks to date.

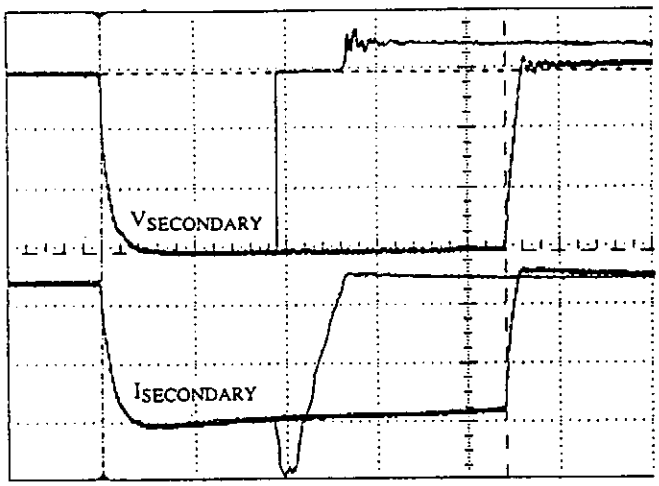

Figure 7. Secondary Voltage (Top) and Current During a Gun Spark (40 kV/div, 40 A/div, 0.5 ms/div)

Modulator Controls

The controls system used for this modulator is an in–house design rather than commercial equipment. Most of the electronics modules are copies or modifications of equipment designed for the recent Fermi LINAC upgrade. The controls consist of three functional blocks:

1. Signal transmission modules consisting of current drivers and receivers for transmission of analog signals from the high power section to the controls section, and fiber optic modules for the transmission of digital control signals to the high power section.

2. Analog circuit modules to generate the required signals for modulator operation and to compare the signals to references and generate error signals.

3. Digital modules which latch error signals and perform system control and timing correlation of the modulator switches.

There are two independent systems that monitor gun sparks. The first system monitors secondary voltage and current and responds to the rapid collapse of the gun voltage. The second system monitors the primary current with two independent current transformers. This system detects both gun sparks and failure of the system to respond to gun sparks. If the normal protection malfunctions, it initiates the backup protection system. In addition, all control circuits related to gun sparks have parallel redundancy.

Operational Results

The primary result is that the modulator works well and meets specifications. Operation at required voltage, pulse width and duty cycle were achieved. In addition, the complete modulator and klystron system has been installed at DESY in Hamburg Germany after commissioning at Fermilab. Recommissioning at DESY took only five weeks from unpacking to full RF power. A number of interesting problems occurred during the initial commissioning phase at Fermilab.

Various changes to the pulse transformer auxiliary circuits were made as a result of studies of spark related transients. These studies were done by using a triggered spark gap across a dummy load on the transformer secondary. The capacitor divider circuit needed modification to handle secondary transients, and high frequency bypass capacitors were added to suppress voltage transients on the transformer primary.

There was one GTO device failure during the commissioning phase. This occurred when the capacitor bank was crowbarred just as the GTO switch opened. The controls system also suffered a transient that caused erroneous status and the failure of a logic chip. We don't fully understand what happened, but we changed a crowbar threshold to prevent a recurrence and more carefully shielded some of the status monitoring cables in the modulator cabinet. No similar failure has happened since.

We have experienced some problems with the pulse transformer. On three occasions the waveforms associated with gun sparks looked strange, indicative of a turn–to–turn transformer short initiating after the gun spark. Upon turning the modulator back on after these events we experienced low voltage turn-to-turn transformer shorts which cleared up after two pulses. Inspection of the transformer was inconclusive and we decided to run at 115 kV rather than 122 kV in order to minimize gun sparks. The subsequent three gun sparks that we experienced at this new level showed no signs of turn-to-turn shorting. Since the klystron generates sufficient power for test stand operation at the 115 kV level, our operational approach for now is to run at this level and investigate transformer replacements.

The ability to vary the pulse length easily has been very useful, especially in conditioning the klystron. The klystron came to Fermilab conditioned with a 500 μs pulse. We lengthened the pulse over several days completing the conditioning process.

Power Efficiency

The power efficiency of this modulator is an important criterion. We measured the efficiency while running at 122 kV with a 2.2 ms pulse length and 10 pps. The 480 VAC power was 274 kW as measured by a Yokagawa power meter. The usable pulse power as defined by the output voltage between +1.0% and -5% of the nominal, was 236 kW, and the efficiency is 86%. Our calculated efficiency is 89% and Figure 1 shows the calculated dissipation in various modulator components. For future systems, tradeoffs between component cost and power efficiencies can be explored.

Costs

The cost of the modulator components was approximately 370 k$. This includes approximately 20 k$ for the bouncer circuit, 25 k$ for the controls, 50 k$ for the GTO switch, 75 k$ for the 400 VAC phase controller and power transformer, and 90 k$ for the pulse transformer. Fermilab labor costs are not included.

References

[1] Glasoe, G. N., Lebacqz, J. V., Pulse Generators, pp. 165 – 172, McGraw Hill, 1948, First Edition

[2] Espelage, Paul M., Symmetrical GTO Current Source Inverter..., IAS 1988, Vol. 1 pp. 302 – 306, 1988 IEEE Industry Applications Annual Meeting.

Test Results on a Beam Position Monitor Prototype for the TTF

R. Lorenz, K. Yezza
TU Berlin
Einsteinufer 17
10587 Berlin

Abstract

A beam position monitor using a cylindrical cavity excited by the beam in the TM_{110}-mode has been developed for the first modul of the TESLA Test Facility. The cavity design and the signal processing scheme are briefly described, the expected signals are estimated. A stainless steel prototype and the electronics were tested. Therefore, the cavity was excited by an antenna, fed by a network analyzer or a pulser. To achieve the measured resolution near the electrical center of better than 10 μm two symmetrical outputs were combined in a hybrid.

1 INTRODUCTION

Beam position monitors with a resolution of less than 10 μm near the electrical center are required for the alignment of the quadrupoles in the TESLA Test Facility TTF. This has to be achieved in a cold environment and for two different injectors with 800ms long macro pulses:

injector 1a charge/bunch 32 pC bunch spacing 4.6 ns
injector 2 charge/bunch 8 nC bunch spacing 1 μs

Because of the desired resolution and the limited longitudinal space, a single circular cavity was designed. These monitors are also under investigation for other linear collider studies ([2],[3],[4]). The amplitude of the TM_{110}-mode excited by an off-center beam is proportional to the beam displacement and the bunch charge. The phase relative to an external reference yields the sign of the displacement. Both polarizations have to be measured to get the displacement in x and y.

2 PROTOTYPE DESIGN

The cavity design parameters given in Table 1 were calculated with URMEL, and the measurements were performed on a stainless steel prototype (shown in Fig.1) at room temperature. To avoid interferences from the accelerating cavities, the cavity was designed for a resonant frequency of $f_{110} = 1.517$ GHz.

One of the main mechanical problems was to reduce asymmetries caused by welding. CrNi was chosen as the cavity material to measure individual bunches spaced 1 μs and to have a good thermal isolation between an accelerating cavity and a quadrupole. The antennas are replaceable, consisting of Kyocera-feedthroughs welded into a special flange. This allows a pre-tuning by adjusting the coupling at room temperature.

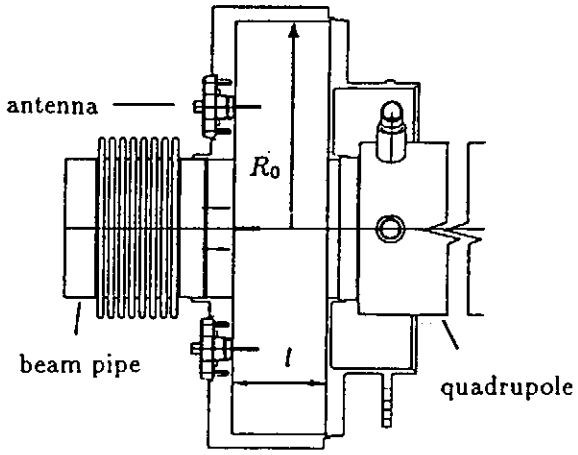

Figure 1: Design of the BPM-Prototype

dimension	at 290 K	target	sensitivity $\pm.1$ mm Δ
radius R_0	115.2 mm	114.77 mm	$\mp$1247 KHz
length l	52.0 mm	51.80 mm	$\pm$79 KHz
beam pipe $\emptyset$	78.0 mm	77.70 mm	$\mp$610 KHz
theoretical loss factor $[\frac{V}{pC}]$		$k_{110} = 0.242$, $k_{010} = 0.179$	
theoretical unloaded Q		$Q_{110} = 2965$	
measured frequency [GHz]		$f_{110} = 1.5133$, $f_{010} = 1.04$	
measured coupling		$\beta_{110} = 1.31$, $\beta_{010} = 0.1$	

Table 1: Cavity design and measured parameters

3 ESTIMATED SIGNALS

The resolution near the electrical center of the cavity is limited by the thermal noise of the electronics and the excitation of common modes. For a cavity without beam pipes, the voltage in the TM_{110} excited by a beam at a position δ_x can be estimated as

$$V_{110}(\delta_x) = V_{110}^{max}\frac{\delta_x \cdot a_{11}}{2J_1^{max}R_0} = \delta_x\frac{k'_{110}a_{11}q}{J_1^{max}R_0} \approx 0.417 \cdot \delta_x \frac{\text{mV}}{\mu\text{m}}$$

where a_{11} is the first root of the Bessel function J_1 and $k'_{110} = 0.228$ V/pC is the longitudinal lossfactor of the geometry in Table 1 (but without a beam pipe).

Assuming a noise figure of NF = 6 dB, the S/N-ratio in a bandwidth $B = 100$ MHz at $T = 290$ K is given by

$$\frac{V_{signal}}{V_{noise}} = \frac{0.417\text{ mV}}{\text{NF}\cdot\sqrt{Z_0\cdot k_0\cdot T\cdot B}}\frac{\delta_x}{\mu\text{m}} \approx 47\cdot\frac{\delta_x}{\mu\text{m}}$$

Since the field maximum of the common modes is on the cavity axis, they will be excited much stronger by a beam near the axis than the TM_{110}. The voltage of the TM_{010} with respect to the TM_{110} and the ratio of the spectral densities at ω_{110} ([1]) can be estimated as

$$S_1 = \frac{V_{010}(\omega_{010})}{V_{110}(\omega_{110})} = \frac{1}{\delta_x}\frac{\lambda_{110}}{5.4}\frac{k_{010}}{k_{110}} \approx \frac{0.027}{\delta_x}$$

$$S_2 = \frac{v_{110}}{v_{010}} \approx \delta_x \frac{1}{S_1}\frac{Q_{110}}{1+2\beta_{110}}\left(1-\frac{\omega_{010}^2}{\omega_{110}^2}\right) \approx 16000 \cdot \delta_x$$

S_1 gives the required frequency sensitive common-mode rejection - about 69 dB for a displacement of $\delta_x = 10\mu$m (for the parameters in Table 1). But the minimum detectable signal is still limited by residual signals at ω_{110}. For a single antenna, this can be estimated using $S_2 = 1$, which yields $\delta_x^{min} \approx 62$ μm. With a combination of two antennas in a hybrid one gets a field selective filter, which gives a rejection of unwanted common field components at ω_{110} of more than 20 dB. Hence, the theoretical resolution near the electrical center of the cavity is ≤ 6 μm.

4 SIGNAL PROCESSING

For signal processing, we adopted a synchronous detector scheme (Fig.2), where the amplitude of the TM_{110} and a reference are mixed down to DC. The phase of the reference signal can be adjusted to maximize the mixer output. When the beam is to the right, the system can be set up to give positive video polarity. The signal changes the phase by 180^0 when the beam moves to the left, and for a centered beam it becomes zero.

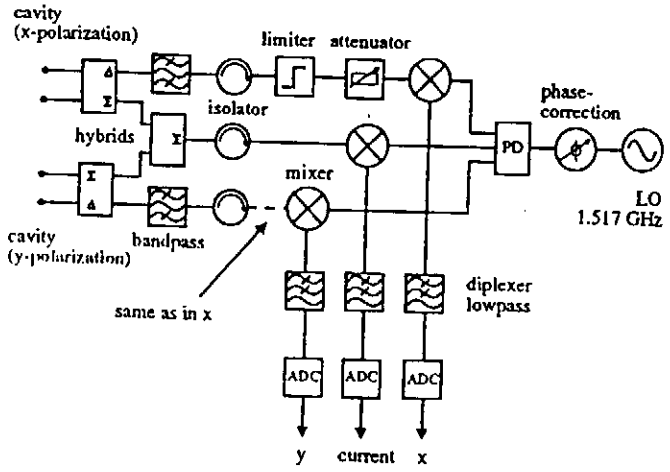

Figure 2: Signal processing scheme

Due to the limited space, the combination of two opposite antennas has to be realized outside the cryostat. The isolation of standard (broadband) hybrids is about 25dB, which limits the resolution. The tubular bandpass filter has a bandwidth of 100 MHz and a stopband attenuation of more than 80 dB, up to 8 GHz. Together with the hybrid and the different coupling factors this gives a common mode rejection of more than 100 dB.

Because of the finite isolation of the hybrid and between both polarisations the full aperture was divided into two measurement ranges:

$0 \cdots 300$ μm, normalization from the hybrid sum

$0.3 \cdots 39$ mm, normalization from current monitors

The LO-RF-isolation of the double-balanced mixer determines the dynamic range of the electronics. About 45dB is required, due to the displacement and differences in the bunch population. An isolator was inserted between the filter and the mixer to reduce reflections and error signals due to second-time mixing. A low-pass filter removes the residual LO-signal and the sum-signal of both mixer inputs. The signal passes through a bipolar video amplifier to the 12-bit flash ADC. Its trigger is generated by the sum-signal of the hybrid, with a delay of 85 ns. All data can be read out between two bunch trains and the normalization will be done in a computer.

We are planning to test a Quadrature IF Mixer, too. When its two outputs are applied to an oscilloscope, a polar display is produced. The vector radius is proportional to the amplitude of both signals and the angular displacement to the phase difference between both inputs. This system does not need an additional phase shifter for the reference signal, and a signal proportional to the phase difference might be usefull in a PLL.

5 MEASUREMENT RESULTS

Bench tests were carried out on a stainless steel prototype to measure the resolution near the center and to test the electronics. The cavity was excited by an antenna, fed by a network analyzer or a pulser.

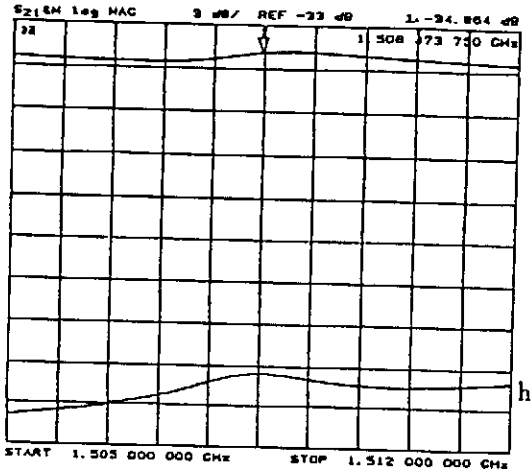

Figure 3: Measured common mode rejection

First, we measured the common-mode rejection due to the combination of two antennas in a 180^0 stripline hybrid. Therefore, the antenna was fed by a network analyzer and moved in x- and y-direction until a minimum was found. The upper trace in Fig.3 shows the output of one antenna and the lower trace the signal at the Δ-port of the hybrid. The difference between both traces corresponds to the isolation of the hybrid, about 23 dB.

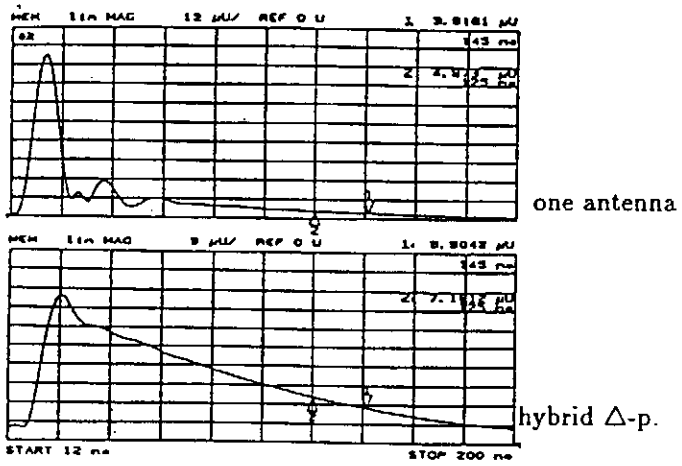

Figure 4: Impulse response of the cavity

To measure the impulse response of the cavity and the electronics, the frequency was swept over a wider range and the inverse Fourier transform was used (t-domain bandpass mode). The equivalent pulse width was about 350 ps. An amplifier was inserted to compensate for the high insertion losses. The upper trace in Fig.4 was measured using a single antenna, whereas the lower trace shows the response at the Δ-port of the hybrid. The oscillation on both traces corresponds to the impulse response of the bandpass filter (inserted after the antenna and the hybrid, respectively).

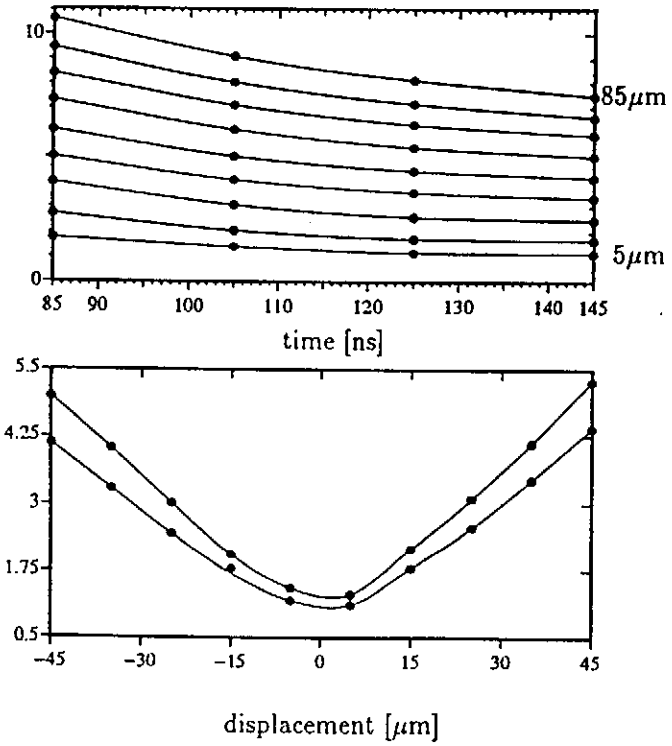

Figure 5: Resolution in the t-domain (impulse response)

Then, four markers spaced 20 ns were placed on the curve and the cavity was moved within 10 μm steps only in the x-plane. All marker-readouts are plotted in Fig.5a for different cavity positions. The shape of all curves shows the exponential envelope of the TM_{110}-amplitude, whereas the difference between two traces corresponds to a movement of 10 μm. The lowest trace gives the response for a position of about 5 μm from the electrical center of the cavity. Fig.5b shows the readout of two markers, plotted versus the relative position. We missed the center position since the cavity was moved only in one direction. Note that the magnitudes are given in relative units.

To get similar responses in a real time domain measurement and for testing the electronics, a pulser with a pulse width of 370 ps and a variable repetition rate (up to 5 MHz) was built to excite the cavity. The filtered Δ-port signal was mixed down to DC and displayed on an oscilloscope (upper trace in Fig.6). The oscilloscope was triggered by the sum-signal of the hybrid, similar to the scheme shown in Fig.2. Again, the oscillation on top of both signals corresponds to the filter impulse response. Since the pulser was not very stable with respect to its amplitude, it was impossible to measure the parameters mentioned above (resolution, min. detectable signal etc.).

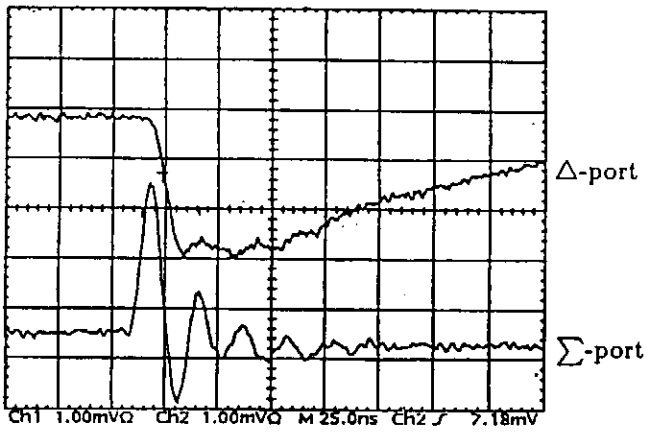

Figure 6: Cavity response to a pulser

6 ACKNOWLEDGEMENTS

The authors would like to thank DESY for supporting this work and building several prototypes. Special thanks are extended to R.Bandelmann and H.Luedecke for the mechanical design and to R.Schroeder for building some electronical subcomponents.

7 REFERENCES

[1] W. Schnell, "Common-mode rejection in resonant microwave position monitors for linear colliders", CLIC note 70, CERN-LEP-RF/88-41

[2] J.P.H. Sladen et. al., "Measurement of the precision of a CLIC Beam Position Monitor", CLIC note 189, March 1993

[3] Balakin et.al., "Beam Position Monitor with Nanometer Resolution for Linear Collider", These proceedings

[4] H. Hayano, T. Shintake, "Submicron Beam Position Monitor for the Japan Linear Collider", presented at LINAC 92, Ottawa, 1992

[5] R. Lorenz, K. Yezza, "Beam Position Monitors for the TESLA Test Facility", TESLA-Note 93-34, July 1993

Beam Position Monitor Developments for TESLA

K. Yezza, R. Lorenz, H. Henke
Technische Universitaet, Berlin, Germany

Abstract

A programme to develope beam position monitors for the TESLA 500 is under way. The goal is to design a low-impedance BPM with an accuracy of better than 50 μm and a resolution of less than 10 μm. Two different structures using resonant buttons and a ridged waveguide to combine two opposite buttons are briefly described. Brass models were built and measurement results will be discussed. The measured resolution is better than 30 μm.

1 INTRODUCTION

Beam position monitors with a resolution of about 10μm near the axis are required for the quadrupole alignement in the TESLA Linear Collider study. This has to be achieved in a cold environment, measuring single bunches with a charge of 8 nC spaced 1 μs. A TM_{110}-cylindrical cavity has been designed for the TESLA Test Facility and test results on a prototype will be discussed elsewhere ([1]). But due to the longrange wakefields monitors with a lower impedance might be required, having the same resolution and a reliable behaviour at lower temperatures ([3]). In this paper we discuss two different button monitors and present measurements on brass models. Another structure using two coupled cavities where the signal is superimposed as a modulation has been described previously ([2]). This structure can be machined within μm-tolerances and a reliable behaviour in a cold environment is expected.

2 RESONANT BUTTON PICKUPS

A button pickup usually consists of four round electrodes in the wall of the beam pipe. The response of such a capacitive pickup can be calculated for two opposite buttons using field theory. For small buttons at $y = \pm b$ and the geometry shown in Fig.1a this yields

$$V^{\pm}(\delta_x,\delta_y) \approx \frac{Z_0 k_0 a_1 d I_b \cos(\frac{\pi\delta_y}{2b})}{4b(1\mp\sin(\frac{\pi\delta_y}{2b}))} \cdot \left(\frac{\pi^2(a_1^2+4\delta_x^2)}{32b^2(1\mp\sin(\frac{\pi\delta_y}{2b}))}-1\right) \cdot \frac{H_0^{(1)}(\xi)+\rho H_0^{(2)}(\xi)}{H_1^{(1)}(k_0a_1)+\rho H_1^{(2)}(k_0a_1)} \quad (1)$$

with

$$\rho = \frac{j\frac{Z_s}{Z_0}H_1^{(1)}(\xi)-H_0^{(1)}(\xi)}{H_0^{(2)}(\xi)-j\frac{Z_s}{Z_0}H_1^{(2)}(\xi)} \qquad \frac{Z_s}{Z_0} = \frac{2\pi\cdot d_a\cdot ln\frac{d_a}{d_i}}{d(2\pi+j\omega C_e Z_0 ln\frac{d_a}{d_i})}$$

$H_{0,1}^{(1),(2)}$ are the Hankel functions, $\xi = k_0 d_a = \frac{2\pi d_a}{\lambda_0}$
C_e is the electrode capacitance, $Z_0 = 377\Omega$
δ_x is the horizontal and δ_y the vertical beam position

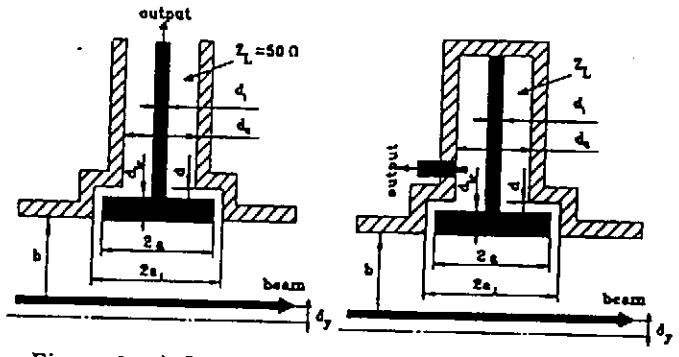

Figure 1: a) Capacitive button b) Resonant button

In Fig.2a, eqn.(1) is plotted for the parameters given in Table 1 and N=5 · 10^{10} particles/bunch.

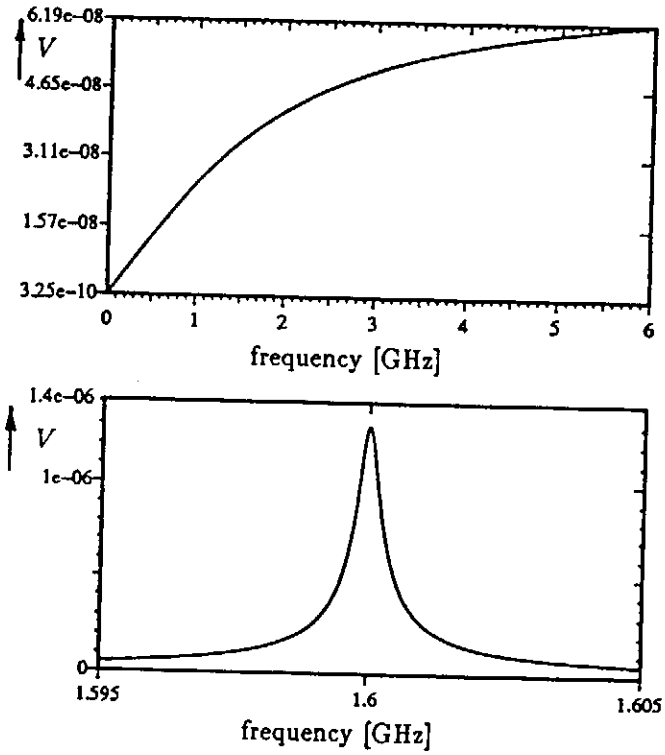

Figure 2: Response of a a) capacitive b) resonant button

The theoretical resolution limited by the thermal noise of the electronics can be estimated using eqn.(1)

$$\frac{\Delta}{\Sigma} = \frac{V^+ - V^-}{V^+ + V^-} \approx \frac{\pi}{2}\frac{\delta}{b} = \frac{V_{noise}}{V_{signal}} = \frac{1}{S/N}$$

This yields a S/N-ratio of ≥ 2500 to detect a displacement of $10\mu m$. Since the bandwidth of the electronics has to be $\geq$ 1MHz (to measure single bunches), one has to increase the signal voltage to get the required S/N-ratio.
Making the buttons resonant, one increases the detector output power density by a factor of $\frac{Q}{2}$ for the same displacement (Q is the quality factor of the resonant circuit, [4]). A simple realisation is a shorted button, as shown in Fig.1b. In the equivalent circuit, an inductor was placed in parallel with the capacitance. For this structure one gets similar results for $V^{\pm}$, but with a different impedance:

$$Z_s = \frac{2\pi d_a Z_L \tanh((\alpha + j\beta)l)}{d(1 + j\omega C_e Z_L \tanh((\alpha + j\beta)l))}$$

where α is the attenuation constant and β the phase constant of the 50Ω coax-cable. The voltage coupled out by a loop or a probe is plotted in Fig.2b, assuming a coupling factor of 1.

dimension	a	a_1	d	d_k	d_i	d_a	b	l
value [mm]	7	9	1	1	1.5	6.5	39	16.9

Table 1: Parameters for a resonant button brass model

2.1 Measurement Results

A brass model with two opposite resonant buttons was built and measured at room temperature using an antenna and a network analyzer. The mechanical parameters are given in Table 1. Fig.3 shows the resonant behaviour of the two buttons, with a measured Q-value of about 400 for both buttons. Hence, the required S/N-ratio (to detect 10 μm) decreases down to 13.

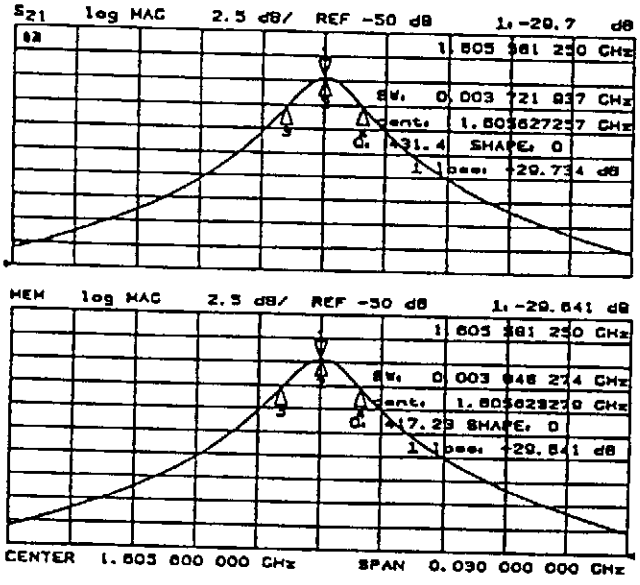

Figure 3: Measured response of two resonant buttons

Then, the structure was woved within 50 μm steps with respect to the antenna. The signals of both buttons were measured and the $\Delta/\sum$-ratio was calculated. Fig.4 shows

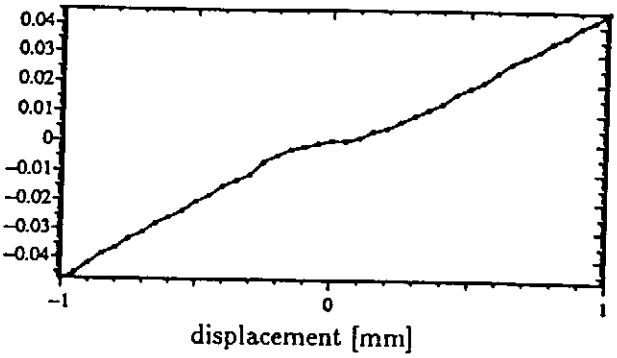

Figure 4: Response to a movement within ±1 mm

the results for a movement within ±1 mm from the center. Note that the magnitude is given in relative units.
The main problem is to build two identical buttons having the same resonant frequency and Q-value. Although it is possible to tune the buttons at room temperature, we expect problems to maintain this behaviour in a cold environment. Another important parameter is the coupling to the external load, which has to be almost identical for two opposite buttons. Therefore, other coupling structures than the tested probe are under investigation.

2.2 Signal Processing

For signal processing we adopted a narrowband technique, succesfully used in many accelerators for beam position monitoring ([5]). In this AM/PM method (shown in Fig.5), the amplitude ratio of two opposite electrodes is coverted in a $\frac{\pi}{2}$-hybrid into two signals having the same amplitude and a phase difference of

$$\psi = 2\arctan(\frac{V^+}{V^-}) - \frac{\pi}{2}.$$

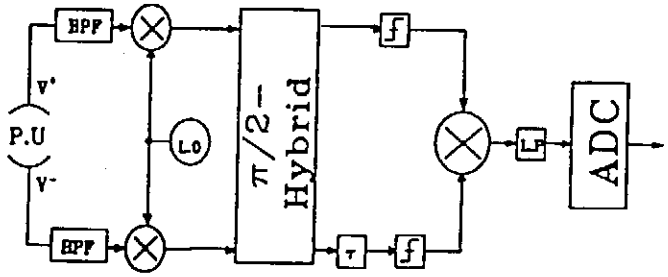

Figure 5: Signal processing scheme

The two signals coming out of the hybrid are clipped to a constant amplitude (hard-limiter) and the phase difference is measured in a phase detector. After the lowpass filter, the remaining dc-signal is proportional to

$$v_{out} = 2k_{pd} \cdot \arctan(\frac{V^+}{V^-}) \quad \Rightarrow \quad \delta_y \approx \frac{b}{\pi}\left(\frac{v_{out}}{k_{pd}} - \frac{\pi}{2}\right)$$

k_{pd} is the transfer characteristic of the phase detector.

This method avoids the problem of transmitting very tiny Δ-signals. Furthermore, it gives the normalized position and it allows a large dynamic range. The hard limiters usually restrict the system performance because of their high frequency limit, phase shift and dynamic range.

3 RIDGED WAVEGUIDE

Another processing method for deriving the normalized position signal is the difference-over-sum method ([5]). Therefore, in a narrowband system a hybrid is often used two combine the signals of two electrodes and to obtain the Δ and the $\sum$.

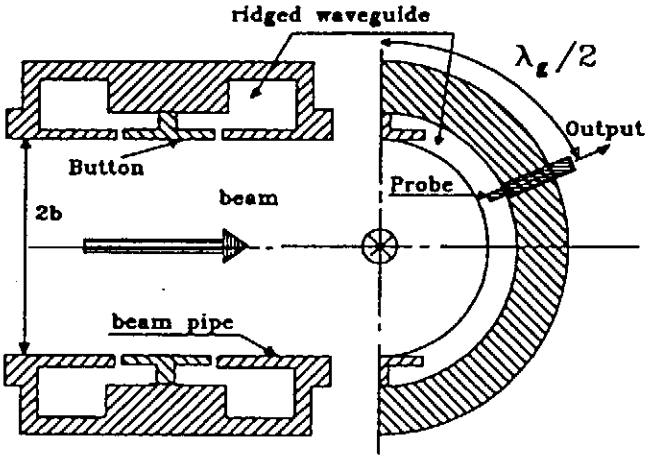

Figure 6: Ridged waveguide combining two buttons

Instead of using a standard hybrid, a ridged waveguide around the beam pipe was designed combining two opposite buttons (Fig.6). The signal is coupled out by a probe at a distance of $\frac{\lambda_g}{2}$ from the upper button. At that point, the signals coming from the upper and the lower button have the same amplitudes but opposite phases for the frequency

$$f_g = \frac{c_0}{\lambda_g} = \frac{c_0 \cdot 3}{2\pi a}$$

where λ_g is the wavelength in the ridged waveguide and a is the mean radius.
In principle, the field pattern is similar to that of the TE_{311}-mode in a coaxial resonator. Hence, the output signal is proportional to the beam position (difference between both signals) and the beam intensity.

A brass model was built and measured using an antenna and a network analyzer. Some of the results are shown in Fig.7. The difference between both traces corresponds to a movement of the structure with respect to the antenna of 50μm. A Q-value of about 400 has been measured. Hence, the S/N-ratio again has to be $\geq$ 13 to detect a displacement of 10μm (similar to the estimation described above). In Fig.8 the displacement is plotted versus the readout at $\frac{\lambda_g}{2}$. We missed the center position since the structure was moved only in one direction.

For signal processing it is forseen to use a homodyne system, where the signals and a reference are mixed down

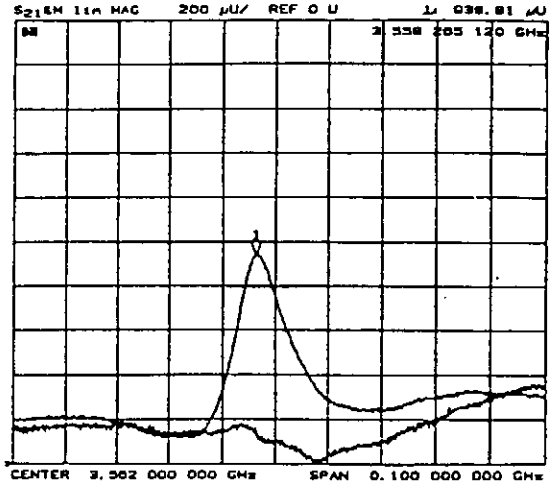

Figure 7: Measurements on a brass model

to DC to get the envelope. The beam current has to be measured elsewhere to normalize the signals in a computer. Unfortunately, this gives the beam position only for one plane. Hence, two such structures are required to detect the position in x and y.

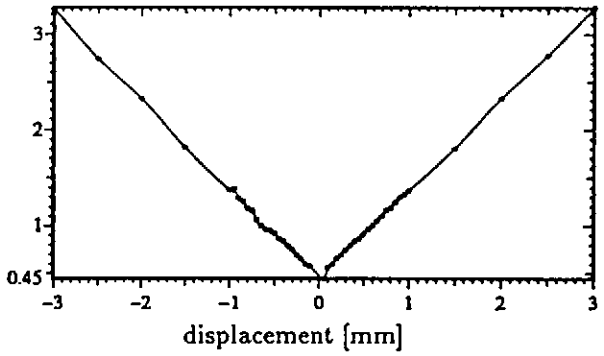

Figure 8: Response of a ridged waveguide structure

4 ACKNOWLEDGEMENTS

The authors would like to thank DESY for supporting this work.

5 REFERENCES

[1] R. Lorenz, K. Yezza, "Test Results on a Beam Position Monitor Prototype for the TTF", These proceedings

[2] R. Lorenz, "Beam Position Monitors for the TESLA Test Facility", in Proceedings of the DIPAC 93, Montreux, Switzerland, May 3-5 1993, pp. 161-165

[3] K.H. Mess, "Diagnostics for Superconducting Accelerators", in Proceedings of the DIPAC 93, Montreux, Switzerland, May 3-5 1993, pp. 64-73

[4] G. Lambertson, "Dynamic Devices - Pickups and Kickers", AIP Conference Proceedings No.153, Vol.2 (1985), pp. 1414-1442

[5] R.E. Shafer, "Beam Position Monitoring", AIP Conference Proceedings No.212, 1989, pp. 28-58

Single and Multi-bunch Wakefields Effects in the TESLA Linac

Alban Mosnier, Armen Zakharian†
CEA, DSM/DAPNIA/Service d'Etudes d'Accélérateurs
CE-SACLAY,F-91191 Gif/Yvette Cedex, France

Abstract

Once the tolerable emittance growth of a beam accelerated in the main linac of a linear collider, departing from a perfect transport line, is fixed, all the tolerances on the various errors, like injection jitter, magnets and structures misalignment, can be in principle determined. The maximum allowable magnitudes of the errors however are closely related to the correction schemes considered in the machine. Furthermore, one correction method, which is favourable for single bunch effects, may be disastrous for multi-bunch effects, and vice versa. This observation led us to develope a tracking code named DILEM, which combines simultaneously single and multi-bunch effects[1] and includes numerous correction techniques, from orbit steering to wakefields compensation methods. Thus, we are able to evaluate the emittance dilution reduction not only for the first bunch but also for the entire bunch train. After a brief description of the code, results of simulations applied on the TESLA linac parameters are presented. In addition to the beam orbit corrections, like "one-to-one", "Dispersion Free" or "Wake Free" [1], further correction methods of emittance dilution, like non dispersive bumps or fast kickers [2] are also tested. The discrepancies in the results depending on wether the short- and long range effects are separately or simultaneously taken into account, are then discussed.

1. TRACKING CODE DILEM DESCRIPTION

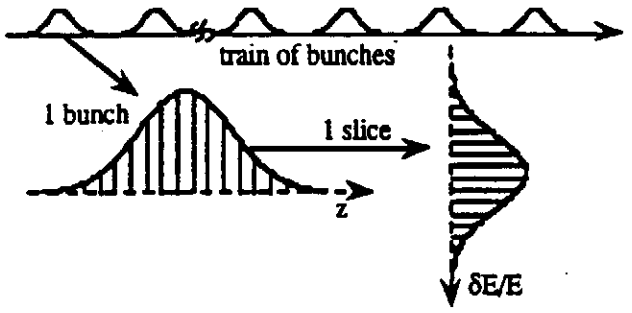

Figure 1 : The train is split into bunches, slices and subslices

Each bunch of the train (figure 1), as usual, is divided into N slices, typically 41, along the z-axis, with a gaussian charge distribution truncated at a couple of rms bunch lengths, in such a way that a slice in a bunch experiences the wakes induced by all the previous slices of this bunch but also by all the previous bunches of the train. Each slice itself is again divided into n subslices along the energy-axis, in order to take into account the chromatic effects of uncorrelated energy spread, which can be important at the beginning of the linac for injected beams of non-vanishing energy spread. All these macro-particles, defined by three indexes (bunch, slice, subslice) and associated to a charge, an energy, a centroid and a beam matrix, are tracked successively down the discrete focusing and accelerating elements forming the linac. The overall rms emittance and energy spread of the entire bunch train are computed along the machine and at the exit by a triple summation on the bunches, the slices and the subslices. For example, the kick angle imparted by a structure to a macroparticle i and belonging to the bunch m is given by

$$\Delta x_i' = \frac{e}{E_i}\left\{\sum_{j<i}^{N} Q_j x_j W_\perp^{s.r.}(z_j - z_i) + \sum_{k<m}^{M} Q_b x_k W_\perp^{l.r.}(z_k - z_m)\right\}$$

where $W_\perp^{s.r.}$, $W_\perp^{l.r.}$ are the short- and long-range point-like wakes; x_k, x_j are the bunch and slice (averaged on the subslices) offsets; Q_b, Q_j are the bunch and slice charges.

All the errors (quad, cavity and BPM offsets, cavity tilts, gradient-spread, frequency-spread of the dipole modes,...) are generated for the whole machine at the beginning of every new run and stored in scratch files. The accelerating field error, which induces the bunch-to-bunch energy spread, depends on the structure type and hence is read from a separate input file. For the TESLA cavity, the amplitude and phase errors during the beam pulse are caused mainly by the Lorentz forces. The net energy gain of the slice i belonging to bunch n is then

$$\Delta E_{i,n} = \Delta E_n \cos(\phi_n'' + \delta\phi_i) + e w_i$$

where ΔE_n and ϕ_n'' are the peak energy gain and phase for the bunch n, including the amplitude and phase errors, $\delta\phi_i$ is the phase of slice i with respect to the bunch center and w_i is the z-dependant longitudinal bunch wake.

The three orbit correction techniques, i.e. one-to-one, Dispersion Free (DF) and Wake Free (WF) [1], with the possibility of using multiple trajectories [2], are identical to the ones previously implemented in the distinct single-bunch (SB) and multi-bunch (MB) codes, except the bunch index, for which the trajectories are read by the BPMs, must be specified. In addition to these beam orbit corrections, further methods of correcting the emittance dilution heve been implemented, like the multiple non dispersive bumps [3] or the use of fast kickers [2] installed at a few judicious locations along the linac. The bumps are normally used to compensate globally the short-range wakefields induced in particular by cavity alignment errors. Once the bumps locations and the number of oscillations have been chosen by the user, the code looks for the amplitudes for each bumps pair, which

† On leave from Erevan Physics Institute, Armenia

[1] The first tracking code combining single and multi-bunch effects for emittance growth computation in linacs was presented by K. Kubo at the Fifth Intern. Workshop on Next-Generation Linear Colliders, SLAC, Oct 13-21, 1993.

minimize the beam emittance just before the next downstream bumps pair. Fast kickers are used for the re-alignment of multiple bunches, scattered by the long-range wakefields (beam breakup). In the same way, once the locations of fast kickers pairs have been chosen, the code adjusts the kick amplitudes imparted to each bunch of the train, to zero the measurement of the 90° phase-shifted, downstream BPM, except for a BPM error plus a kick error (figure 2).

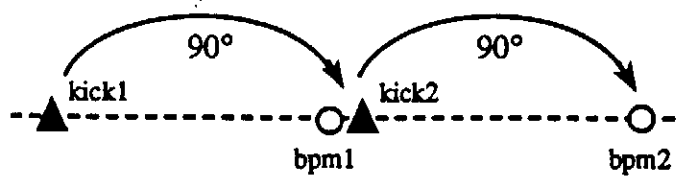

Figure 2 : Bunch re-alignment by fast kickers

2. TESLA LINAC

Since the s.c. cavities have low rf frequency and large iris aperture, short-range and long-range transverse wakefields effects and chromatic effects due to correlated bunch energy spread are low in the TESLA linac. The resulting tolerances were evaluated previously, see for example [4], by computing the emittance growth for SB and MB separately with the help of two distinct tracking codes. Table 1 shows the cavity, quadrupole and BPM alignment tolerances (assuming gaussian distributions truncated at $\pm 2\ \sigma$), which give a mean emittance growth lower than 10% among 50 different simulations, by using the optimal constant beta lattice (β=66m) and the classic one-to-one orbit correction.

cavity scatter	500 μm
quadrupole scatter	100 μm
BPM scatter	100 μm
BPM resolution	10 μm

Table 1 : Tolerances for the TESLA linac

More sophisticated correction algorithms, like DF or WF were also tested but without providing spectacular improvement because of the wakefield effects induced by the large cavity random offsets. When applying the orbit corrections for MB simulations, a first side-effect however was discovered [4], as soon as some bunch-to-bunch energy spread was introduced. This forced us into changing the correction method, which was only effective for the SB case. In fact, the trajectories of the different bunches in the train are strongly displaced from axis, leading to multi-bunch filamentation. Since the steady-state however is rapidly achieved, most of the bunches follow the same trajectory and this problem was solved by applying the static correction on the trailing instead of the leading bunches of the train.

3. ORBIT CORRECTIONS ALONE

The single-bunch rms energy spread can be reduced to 5.4 10^{-4} by running properly the bunch off the crest of the accelerating wave, while the rms bunch-to-bunch energy spread amounts to 2 10^{-4} in taking realistic fluctuations of cavity phase and amplitude during the beam pulse [5]. This results in an overall rms energy spread of about 6.9 10^{-4} for the entire bunch train. The orbit corrections gave the best results when the trajectory measurements are chosen for a bunch index larger than 150, when the steady-state is practically reached. The MB emittance growth is then much smaller than the SB emittance growth (more than 10 times), even in the presence of bunch-to-bunch energy spread. Therefore, we expect no big differences between pure SB simulations and combined simulations in TESLA. This was confirmed by DILEM, which gave emittance growths (average on 20 simulations) of 9.6 % with combined effects instead of 8.1 % with SB effects alone, by taking the simple "one-to-one" correction algorithm and the tolerances of table 1. Figure 3 shows an example of emittance dilution along the linac for MB alone (dashed line), SB alone (dotted line) and combined effects (solid line). The cavity, quadrupole and BPM errors are identical in the 3 simulations.

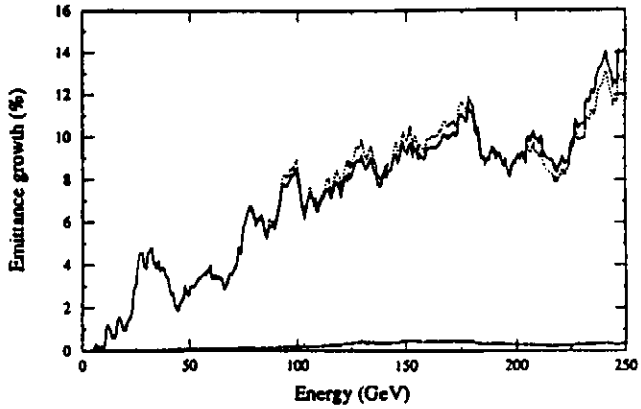

Figure 3 : Emittance growth for MB alone (dashed line), SB alone (dotted line) and combined effects (solid line) in the TESLA linac

Conversely, a linac with SB and MB emittance dilutions of the same order of magnitude, would have a net emittance dilution much larger than each of them. As an illustration, we assume that the damping of the dipole modes in TESLA are 10 times worse than the actual ones. Simulations of this fictitious linac show emittance growths of about 10% for SM or MB alone, but 3 times more (30%) with combined effects (see figure 4).

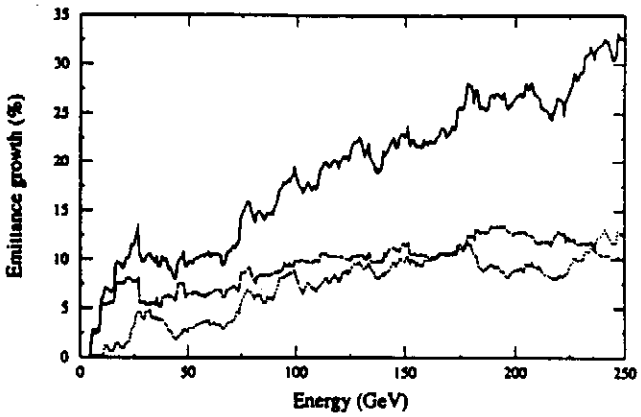

Figure 4 : Emittance growth for MB alone (dashed line), SB alone (dotted line) and combined effects (solid line) in a fictituous linac

4. ADDITIONAL ND BUMPS

In order to still more loosen the tolerances in TESLA, a global correction like non dispersive bumps [3] could be used. They might cancel the dilutions due to wakefields excited in particular in misaligned structures, where the other techniques fail. Three pairs of bumps, each with 3 oscillations, were distributed along the linac, at the beginning, at the middle and at 75%. The amplitudes of the bumps were first optimized by DILEM on a single bunch run. The largest emittance growth (30%) found among 20 different SB simulations was reduced by a factor of 6 (5%). The combined SB and MB simulation with the optimal bumps values gave about the same improvement (see figure 5).

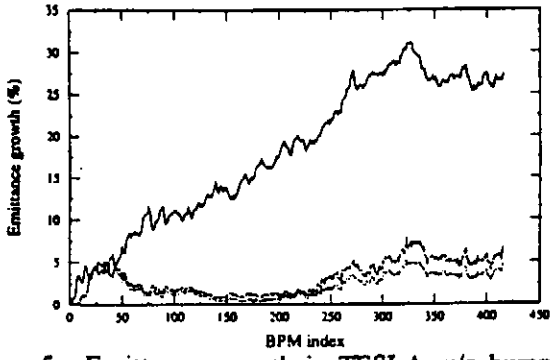

Figure 5 : Emittance growth in TESLA w/o bumps (solid line), with ND bumps for a single bunch (dotted line) and for a train of bunches (dashed line)

If we consider a linac with MB effects as strong as SB ones, this nice result cannot be repeated with simulations involving simultaneous SB and MB effects, because the bunches of the train have much larger trajectory differences. Degrading again the damping of the dipole modes in TESLA by a factor of 10, the overall emittance of the bunch train could be hardly improved (see figure 6).

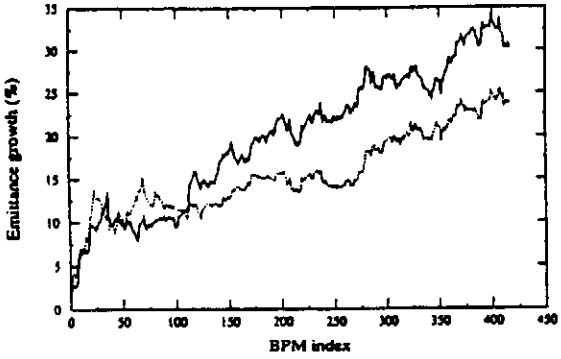

Figure 6 : Overall emittance growth with stronger MB effects w/o bumps (solid line), with ND bumps (dotted line)

5. ADDITIONAL FAST KICKERS

In a linac with a strong multibunch Beam Breakup, we could imagine to correct the individual orbits of the different bunches by means of fast kickers placed all along the linac [3]. Assuming a static orbit correction described in paragraph 2, based on the BPM readings of the last bunches, this dynamic bunch correction will not be very useful in TESLA because of the low MB dilution. The method was nevertheless tested by starting from the largest dilution caused by MB effects alone, among 20 simulations. Figure 7-a shows the reduction of the MB dilution after the adjustment by DILEM of the amplitudes of 2 kickers pairs located at the 100th and 300th half-cells. This improvement, however (7-b), disappears when the SB effects are added, as expected. If we now increase the MB effects, by lowering again the damping of the dipole modes, the efficiency of the method is evident even for 3 kickers pairs. Figure 7-c show the dilution reduction for MB alone (top-right) and combined simulations (7-d).

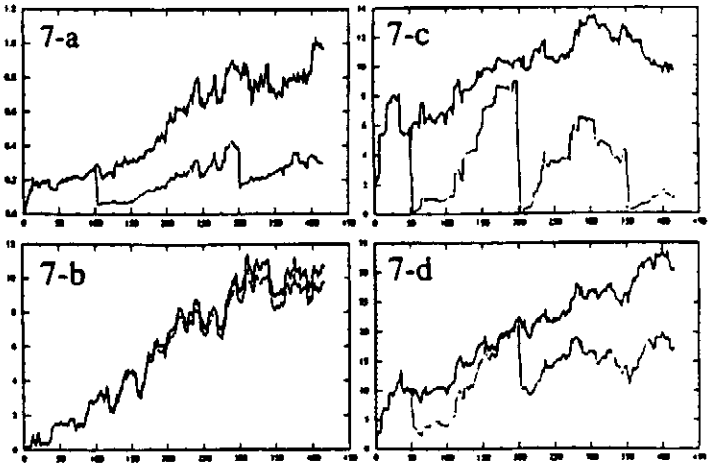

Figure 7 : Emittance growth with fast kickers correction before correction (solid line) and with kickers (dotted line)

6. CONCLUSION

A combined single and multi-bunch tracking code DILEM has been developed in merging two previous separate codes. The new correction techniques [3], like multi-trajectory DF and WF, non dispersive bumps for wakefields compensation or fast kickers for multiple bunches re-alignment have been implemented. The simulations demonstrate the necessity to take simultaneously into account the short- and long-range effects in the emittance growth evaluation, when both effects are of the same order of magnitude. Concerning the TESLA linac, since the multi-bunch dilution is much lower, the tolerances of table 1 given previously [4] are still valid and the use of a few bumps pairs would still more reduce the emittance growth (mean value of 10%).

7. REFERENCES

[1] T. Raubenheimer, "A new technique of correcting emittance dilutions in linear colliders", *Nucl. Inst. and Methods*, A306, 1991

[2] T. Raubenheimer in *Proc. of the Fith Intern. Workshop on Next-Generation Linear Colliders*, SLAC-436, 1993

[3] T. Raubenheimer, "The Generation and Acceleration of Low Emittance Flat Beams for Future Linear Colliders", SLAC-387, 1991

[4] A. Mosnier, "Beam Instabilities Related to Different Focusing Schemes in TESLA", *Proc. Part. Acc. Conf.*, Washington, 1993

[5] A. Mosnier and J.M. Tessier, "Field Stabilization in a Superconducting Cavity Powered in Pulsed Mode", these proceedings

Elaboration and characterization of Nb and NbTiN superconducting thin films for RF applications.

S. Cantacuzène, P. Bosland, J. Gobin, M. Juillard, J. Martignac
CEA, Direction des Sciences de la Matière, DAPNIA/SEA
CE Saclay, F-91191 Gif sur Yvette Cedex, France

Abstract

This paper presents the last results obtained at Saclay on Nb and NbTiN coatings prepared by magnetron sputtering for making 1.5 Ghz accelerating cavities. The optimisation of the sputtering parameters was made on small samples, and the surface resistance of the films deposited on Φ 12 cm copper disks was measured using a TE011 cavity. The results obtained (R_{res}=40 nΩ at T=1.4 K and F= 4 Ghz for the best NbTiN coating) encouraged us to deposit such films in 1.5 GHz copper cavities. One Nb/Cu and four NbTiN/Cu cavities have been prepared, the copper cavities being electrochemically polished before sputtering. The Nb/Cu cavity reached 12.5 MV/m with Q_0=10^{10} at low field. The NbTiN cavities could not be tested because of the blistering of the coatings.

1. INTRODUCTION

For the future accelerators, the technology of the sputter coated cavities appears as an interesting alternative to the bulk Nb superconducting cavities. Nevertheless , even if Nb sputtered cavities are already used for the 350 MHz cavities of the LEP project, important progress is still needed for the 1.5 GHz Nb and NbTiN sputtered cavities so as to become really competitive. That is why an intensive study started in 1986 at the C.E.Saclay was meant to develop and to optimize the technological process for making 1.5 GHz sputter coated copper cavities.

A magnetron sputtering setup, designed to prevent dust contamination of the cavity before sputtering was realized. In the mean time a new magnetron cathode designed so as to allow the variation of the atomic Nb/Ti ratio was also developed. Details on the setup and the cathode were previously reported elsewere [1],[2]. Several Nb sputtered monocells and pentacells cavities were prepared using this setup, and were tested at CERN. The good results obtained during this collaboration with CERN showed that the sputtering setup worked satisfactorily [2]. The selected material for the study was the NbTiN which, due to its higher critical temperature (between 16 K and 17 K), presents a lower BCS surface resistance at 4.2K than Nb [3],[4].

In this comunication we present the major results on NbTiN samples that helped to define the process parameters, the RF behavior of the NbTiN film measured using the TE011 cavity and some preliminary results on 1.5 GHz Nb/Cu and NbTiN/Cu cavities.

2. NbTiN SAMPLE RESULTS

NbTiN films deposited on polished SiO_2 substrates were used to measure the film critical temperature and its room temperature resistivity using a 4 points probe method. The film thickness was measured using a Taly-step device.The thickness of the sputtered NbTiN films was between 0.7 and 4 μm.

Chemical analysis were made for very thin films (<5000 Å deposited on polished graphit samples) using RBS and NRS technics [5], and for thicker films (1 μm to 15 μm deposited on copper samples) using GDS (Glow Discharge Spectroscopy).

All the NbTiN films have been prepared on the new sputtering setup (mentioned in the introduction) which had only been used for Nb coatings before. An exhaustive study of the sputtering parameters was thus necessary (as we did with our first setup in ref [1],[4]).

The curves on figure 1 show that there is an optimum value of the nitrogen flow for which the film has the highest critical temperature and the lowest resistivity at room temperature. Nevertheless this optimum value changes if we modify the parameters of the glow discharge.

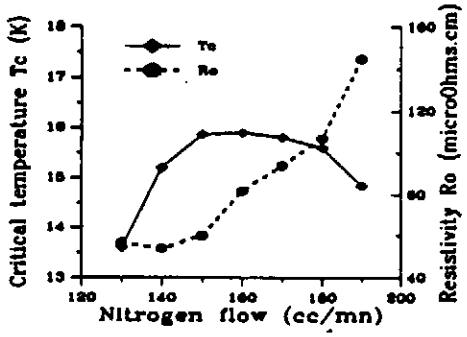

Figure 1: *typical variation of the film's critical temperature and resistivity at room temperature versus the nitrogen flow. For this example the argon flow was 250 cc/min (partial pressure of 7*10^{-3} mbar), the glow discharge power was P=600W, the film thickness was 1.7μm and the atomic Nb/Ti ratio was 0.52/0.48. The deposition speed is constant with the nitrogen flow (420±20 Å/min).*

We observed, like other authors [6], that the optimum value of the nitrogen flow is proportional to the power applied to the magnetron cathode. In addition we observed that the deposition speed (and thus, the metal atoms flow at the substrat's surface) is proportional to the magnetron power (figure 2). This confirms a result which is commonly observed in magnetron sputtering.

It is then clear that these two parameters, magnetron power and nitrogen flow (or nitrogen partial pressure), are the two main parameters controlling the reaction between the Nb or Ti atoms and the nitrogen ones. To obtain the good stoechiometric composition of the film (one nitrogen atom for one metal atom) the flows of metal and nitrogen atoms impinging the substrat's surface must be carefully adjusted.

Argon partial pressure, substrate temperature, magnetron cathode temperature, cathode-substrate distance

and pumping speed are also important, especially to minimize the film internal stress. The high rate of internal stress may cause the coating's blistering , when the adhesion with the substrat is poor (this will later be detailed for the NbTiN films sputtered inside some copper cavities). Therefore , all parameters have to be choosen carefully and their large number makes this optimization step quite complex.

One of the basic questions in reactive sputtering is to know whether the reaction takes place on the substrate surface, on the magnetron cathode surface, or during the transport of the metallic vapor between the two surfaces. The results described hereafter seem to show that the reaction might take place on the cathode surface.

Three samples have been deposited at the same time at different distances from the magnetron cathode: d=7, 8 and 12.5 cm. The range of the deposition speed of these films (and thus the sputtered metal atoms flow on the substrate surface) varies by a factor of 3.18 following a low in $1/d^2$, whereas the nitrogen flow depends only of the nitrogen partial pressure and is therefore the same for the three samples. The critical temperatures of these films are respectively 16.15, 16.04, and 15.95 K, whereas for films deposited with the same deposition speed a 20 % variation of the nitrogen flow leads to a drastic decrease of the Tc values (shown on figure 1).

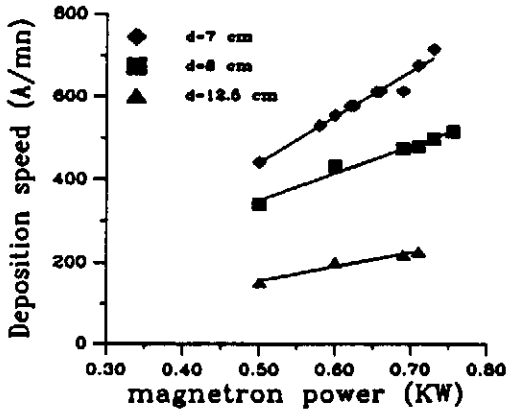

Figure 2: *the deposition speed versus the power of the glow discharge for three cathode-substrate distances (d). Argon and nitrogen partial pressures were kept constant (p_{Ar}=7*10^{-3}mbar and p_{N2}=2.5*10^{-3}mbar). A correction based on the cosine low was used each time a substrate was sputtered under an angle.*

We observed that for constant nitrogen flow, discharge power and substrate temperature, the film's critical temperature and resistivity were fairly constant regardless of the film's thickness (over 1μm).

The NbTiN films thinner than 1μm presented a lower critical temperature and a higher resistivity. This might be due to the fact that the samples reach a thermal equilibrium only after ~30min of deposition. An other possible explanation is the fact that at the begining of the sputter process the film is sligtly contaminated (O,H,C) by the adsorbed gases on the samples' surface and by the residual pressure of H_2O and CO_2. After the first micron is sputtered, the film plays a gettering role and the next microns of the layer contain less impurities.

3. RF CHARACTERIZATION USING THE TE011 CAVITY

In the next paragraphs we present the follow up of the RF characterizations made with the TE011 cavity developed at Saclay. This cavity and the method applied for the RF tests had already been described in detail previously [1]. In our last communication [1] we presented two main results:

- the first was the low residual surface resistance obtained (figure 3: R_{res}=40 nΩ for F= 4 Ghz and T=1.6 K) at low field level and the maximum RF field level B_{max}=34 mT.

- the second was the large spread of the R_{res} values measured on different NbTiN coatings: from 40 nΩ to 2000 nΩ at low field level.

We observed after the RF tests that the copper substrates had been deformed during mounting on the TE011 cavity. We increased the copper disk's thickness from 2 mm to 3 mm to diminish the deformations, and the spread of the RF results obtained on the next NbTiN coatings was considerably lowered as shown on figure 3.

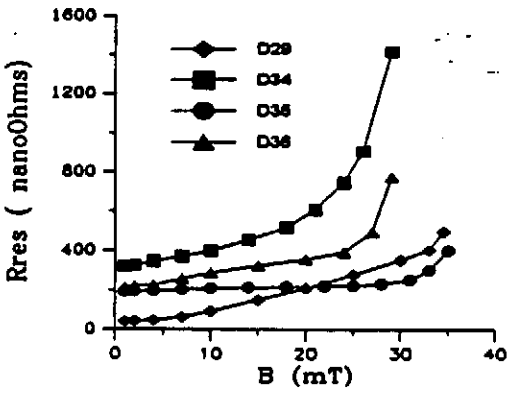

Figure 3: *Residual surface resistance of the last three NbTiN films deposited on 3 mm thick copper substrats compared to our best result previously obtained (D29)*

One hypothesis to explain the mechanical deformations' influence over the surface resistance could be the creation of micro-cracks on the NbTiN films surface. It is well known that the magnetron sputtered nitrides are brittle and cracks may appear under small deformations of the substrate. A great number of such micro-cracks could be the cause of RF dissipations. The confirmation of this hypothesis is of prime importance. It can be made by the analysis of the toughness of the films which we haven't done yet [7].

4. RESULTS ON 1.5 GHZ COPPER CAVITIES

Single cell copper cavities have been hydroformed at CERN [2]. Before sputtering, the copper cavities have been mechanically and then electrochemically polished. In figure 4 we describe the main elements of the electropolishing setup. The cavity is horizontaly placed (like on the KEK system for Nb polishing [8]), half filled with H_3PO_4 acid mixed with water and revolves around its axis at a speed of 3-5 turns per minute. The cathode, reproducing the cavity's shape, is fixed at a distance of 2-3

cm from the cavity's inner surface. A membrane, fixed all around the cathode, guides the H_2 bubbles to the upper half of the cavity. The current density is 5 A/dm^2. After the electrochemical treatment, the cavity is rinsed in ultra pure water, chemically treated with sulfamic acid and then rinsed again with utra pure water and dried in a class 100 clean air room. The film is afterwards prepared following the process described in ref [2].

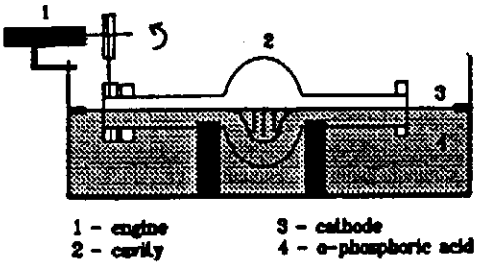

Figure 4: *electropolishing system*

4-1. Results on 1.5 GHz Nb/Cu cavities

Before sputtering any NbTiN coatings, we decided to prepare a Nb coated cavity so as to test the copper electrochemical treatment. After sputtering, the Nb coating was rinsed with ultra pure water and dried in a class 100 clean air room. The RF measurements are presented on figure 5. At T=1.6 K, $Q_0=10^{10}$ at low field level and decreases with the RF field down to 6.5 10^8 at E_{acc}=12.5 MV/m, limited by the amplifier. The cavity was not limited by Q-switches or by electrons. We will not discuss here the slope of the curve on figure 5, which is generaly observed with sputter coated cavities [9],[10] and interpreted in terms of granular superconductivity. This good result encouraged us to prepare NbTiN/Cu cavities using the copper's electrochemical polishing treatment.

4-2. Results on 1.5 GHz NbTiN/Cu cavities.

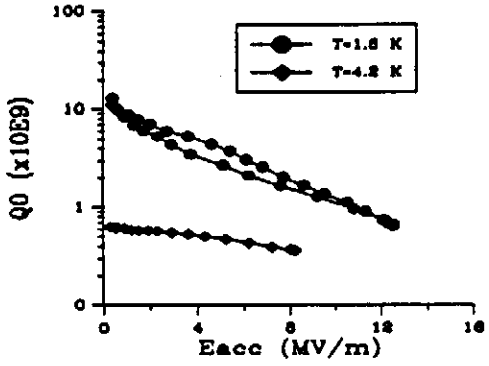

Figure 5: *RF measurements of S1-03 Nb/Cu cavity.*

Four NbTiN/Cu cavities were sputtered but unfortunately none could be tested. Indeed, the film's internal stress and probably the local poor adhesion caused the coating's blistering for all the cavities.

The process parameters were modified between the first and the last of the four cavities. External copper temperature was kept under 70°C during the process and argon partial pressure was incresed up to 10^{-2} mbars, which diminished the film's stress.

The sulfamic acid treatment was supressed and this seemed to somehow ameliorate adhesion.

Progress between the first and the last of the sputtered cavities is obvious but effort is still needed for process improvements.

5. CONCLUSION

Several sample studies have stressed the potential of NbTiN for RF applications. Process parameters were analysed and optimised working points were defined. Reproductibility of the RF surface resistance was studied on a TE011 cavity. The different sequences of the elaboration of 1.5 GHz sputter coated cavities (electrochemical polishing, rinsing, sputtering and final rinsing) were tested and work in a satisfactory manner.

We have obtained for the first Nb/Cu cavity a quality factor of $Q_0=10^{10}$ at low field level, and a maximum field of E_{acc}=12.5 MV/m without Q-switches or electron loading. The first series of NbTiN/Cu sputtered cavities could not be tested as the layer had several square milimeters blistering. Nevertheless, important progress is actualy being made.

Acknowledgements

The authors wish to thank A. Chevarier, N. Chevarier, and B. Wybourn (IPN Lyon) for ion beam analysis, H. Lengeler, C. Hauviller, E. Chiaveri and W. Weingarten (CERN) for the hydroformed copper cavities, J.P. Charrier, J. Gratadour, D. Roudier (CE Saclay) for performing the RF tests and B. Mahut, J.P. Poupeau (CE Saclay) for their help on the chemical treatment.

We have greatly appreciated the stimulating discussions and the encouragements of B. Aune and B. Bonin.

6. REFERENCES

[1] - P.Bosland et al , Proc. 6th Workshop on RF Supercond. 1993, CEBAF , Newport News V.A. (USA),ed. Sundelin.

[2] - Ph. Bernard et al , Proc. 6th Workshop on RF Supercond. 1993, CEBAF , Newport News V.A. (USA),ed. Sundelin.

[3] - R. Di Leo et al , J.Low Temp. Physics , vol 78 , n°1/2 , pp 41-50 ,1990.

[4] - F.Guemas , thesis , 1992 Paris XI - Orsay, (France)

[5] - B. Roux et al. Nucl.Instr.and Meth. in Ph. Reserch B64 pp184-188, 1992, (North-Holland)

[6] - J.Danroc et al , Int.Symp. on Trend. and new app. and Thin Films , Strasbourg , pp 16-20 , 1987

[7] - J.H. Selverian and al., Thin Solid Films vol 235 pp 120-128, 1993

[8] - K. Saito et al , Proc. 4th Workshop on RF Supercond., vol.2, 1989, KEK, Tsukuba (Japan)

[9] - B.Bonin et al. , Supercond. Science Technol. vol 4, pp 257-261, 1991

[10] - D.Bloess and al., this workshop.

Superconducting, hydroformed, niobium sputter coated copper cavities at 1.5 GHz

D. Bloess, E. Chiaveri, C. Durand, C. Hauviller and W. Weingarten
CERN - European Organisation for Nuclear Research
CH–1211 Geneva 23 (Switzerland)

P. Bosland, S. Cantacuzene
CEN Saclay
F-91191 Gif-sur-Yvette Cedex (France)

Abstract

Results from RF tests of five-cell niobium sputter coated cavities are presented. Accelerating gradients of 13 MV/m at low field Q-values of 10^{10} have been obtained. Experimental data on the decrease of the Q-value with accelerating gradient are explained in a model, in which weak superconducting spots are driven normal by the RF field.

1. INTRODUCTION

Superconducting (sc) technology in the 1.3 to 1.5 GHz range may be attractive for future linear colliders in the TeV energy range (TESLA), provided larger accelerating gradients (about 25 MV/m) at high Q-values ($5 \cdot 10^9$) can be obtained at moderate costs. Copper cavities with a thin sc coating of sputtered niobium (NbCu cavities) may offer an alternative to niobium cavities made from sheet, both with respect to costs and to performance. They can be formed in a monolithic piece from a single tube by hydroforming (with intermediate annealing steps), they do not exhibit "quenching" thanks to the high thermal conductivity of copper at low temperature, and the material costs of copper are substantially lower than those of niobium.

However, the RF loss increases more than quadratically with the accelerating gradient (non quadratic loss, NQL), and the copper niobium interface has to be extremely clean to guarantee good adhesion and sufficient cooling of the sputtered film. If not so, minute ($\varnothing \leq 1$ mm) spots of niobium loosely connected to the copper can switch to the normalconducting (nc) state (Q-switch) and even heat up sufficiently that electrons are emitted. This kind of "electron loading" cannot be reduced by "processing".

In what follows we will report on a common effort of CERN and CEN/Saclay to develop 1.5 GHz sc NbCu cavities for large gradients and low RF losses. Previous results have been presented elsewhere [1 - 3].

In particular, two lines of research and development work will be described. Firstly, we will report on results on the feasibility of multi-cell cavities, and secondly on the physics of sputtered layers with the ultimate goal to understand and eliminate NQL.

2. EXPERIMENTAL RESULTS

2.1 Sputtering parameters and reproducibility of results

The sequence of production of the cavity proper, the chemical cleaning and the coating set-up are described elsewhere [3]. Here we will only give information on the sputtering parameters which determine the coating process: anode voltage V, discharge current I, argon gas pressure p, and temperature of the substrate T. All these parameters are intimately connected. Generally speaking, one reduces V to avoid neutral gas resputtering of the film from recoil neutral atoms bouncing off the cathode, which are known to induce constraints in the film. One reduces p to create a dense, non-columnar film. Increasing the power P = IV of the plasma discharge reduces the probability of contamination of the film by gas impurities. It is difficult to take account of all these constraints simultaneously.

Since the new sputtering set-up is available [3], five one-cell cavities and three five-cell cavities have been coated and tested. The coating parameters were not varied significantly, because the reproducibility of the result was to be checked. Prior to coating, the cavities were baked between 100°C and 170°C for 30 minutes. The current I was controlled to about 1.5 A and p between 6 and $7 \cdot 10^{-3}$ mbar. V stabilised around 380 to 410 V and T between 135 and 153°C. Thirty minutes of plasma discharge were needed per cell to produce a layer thickness of 1.6 to 1.8 µm (near the equator and iris of the cavity, respectively), or one hour for twice the thickness.

Four of the one-cell cavities had low field Q-values (at 1.8 K) of $(1.0 \pm 0.2) \cdot 10^{10}$; in three of them the maximum gradient at Q = $1 \cdot 10^9$ exceeded 10 MV/m.

When applying rinsing with ultra pure water at high pressure (high pressure water rinsing HPWR at 90 bar, 12 l/ min mass flow for 75 minutes), some parts of the coating washed off, indicating poor adhesion.

2.2 Feasibility of five-cell NbCu cavities

After hydroforming, the dispersion of the mechanical dimensions was ±0.4‰, and that of the π mode frequencies was ±0.3‰ [3]. The field flatness (defined as the ratio of maximum to minimum field amplitude) was 1.25. After five iterations of inelastic deformations a field flatness of 1.08 could be obtained. Plastic deformation of the cavity was achieved for a longitudinal deformation of individual cells (with the force applied to the irises) corresponding to a change of 500 kHz for the π mode frequency. The measured sensitivity to the helium bath pressure was -40 kHz/mbar.

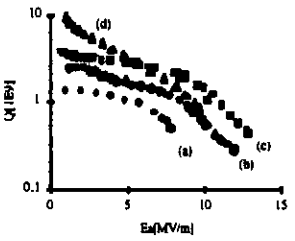

Fig. 1: Q-value vs. accelerating gradient in a five-cell cavity after various treatments: as received after coating (a), after rinsing with ultra pure water at low pressure (b) and high pressure (c, d).

Among the three five-cell cavities, two had poor results: the Q-value decreased steeply with accelerating gradient (due to Q-switches). The thickness of coating was 3.2 to 3.8 μm at the equator and the iris, respectively. The third cavity (thickness 1.6 to 1.8 μm at similar positions) had a Q-value at low field of $4 \cdot 10^9$ and a maximum accelerating gradient of 11 MV/m at $Q = 1 \cdot 10^9$ (Fig. 1), the field limitation being electron loading. No attempts have been made so far to decrease the electron activity, no thermal quench was observed. After a second HPWR the low field Q-value increased to more than 10^{10}, but the slope of the Q vs. E_a curve became somewhat steeper. A change of this slope after HPWR has already been observed before [1].

In conclusion, best RF results were similar to those of one-cell cavities, but the success rate (of producing a cavity without major surface flaw as for example a "Q-switch") was 33 %, compared 60 % for one-cell cavities.

2.3 Sample measurements

(a) Critical field B_{c2} and critical temperature T_c:

B_{c2} and T_c are measured inductively with a transformer consisting of two coplanar coils and the sample sheet in between [4]. A DC magnetic field (<3.5 T) parallel to the sample surface is superimposed. When the primary coil is driven AC in the kHz range, a significant voltage is induced in the secondary coil, when the sample is nc. This decreases substantially due to shielding when the sample becomes sc. The secondary voltage is measured vs. the temperature of the sample and vs. the DC magnetic field. A typical result (Fig. 2) shows smeared transitions, both in T_c and in B_{c2}, different from what was observed in bulk niobium. In addition, B_{c2} was significantly larger than for bulk niobium. The RRR of the samples were between 10 to 20.

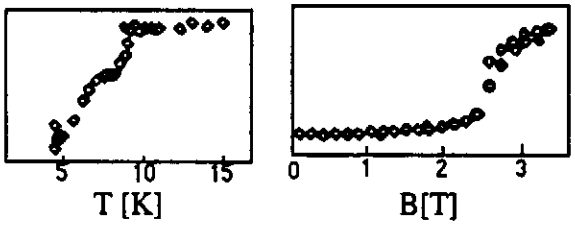

Fig. 2: Secondary coil voltage (arb. units) for measuring the critical temperature T_c (left) and the upper critical field B_{c2} (right) on a niobium layer sputter coated on a copper substrate. The RRR was 12 for this particular sample, and the temperature during coating was not controlled.

(b) Transmission electron microscope (TEM) analysis:

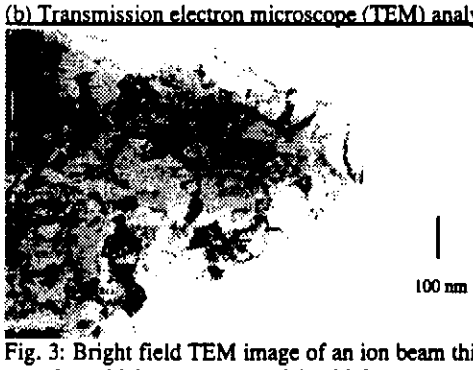

Fig. 3: Bright field TEM image of an ion beam thinned niobium sample, which was removed by high pressure water from a sputter coated one-cell cavity.

A sample which was removed from the cavity surface by a blast of HPWR was analysed in a TEM (Fig. 3).

Preliminary results are the following. A large number of grains per unit area are detected, of different size (5 to 200 nm). Within the grains, there are stacking faults and dislocations visible. In an analysis of elemental distribution neither oxygen nor sulphur contamination have been found. If the oxygen had been concentrated near the grain boundaries with a thickness of more than three monolayers, it would have been detected.

2.4 Measurements in conjunction with NQL:

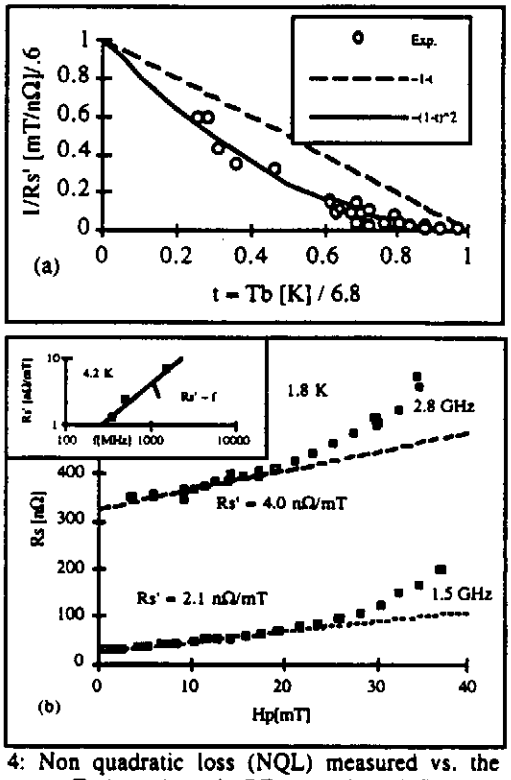

Fig. 4: Non quadratic loss (NQL) measured vs. the bath temperature T_b (a) and vs. the RF magnetic peak field amplitude H_p at 1.5 GHz and 2.8 GHz in the same cavity (b).

The losses P generated per m^2 by a RF magnetic field of amplitude H can be split into magnetic and non-magnetic losses:

$$P = R_s H^2 / 2 + \text{others}, \qquad (1)$$

where R_s is the surface resistance and "others" comprise dielectric loss, electron impact, nc spots, etc.. R_s can be separated into several terms, the BCS and the residual one, which are more or less well known, and another one, named R_s', which takes into account NQL:

$$R_s = R_{BCS} + R_{res} + R_s' \cdot H + \ldots. \qquad (2)$$

R_s' describes the physical mechanism which create the slope of the Q vs. E_a curve. In order to get more insight into the physics underneath, we have measured the temperature and frequency dependence of R_s' (Fig. 4).

The temperature of the cavity was determined by a calibrated germanium resistor (estimated precision < 0.1 K). The frequency dependence of NQL was measured by exciting not only the

fundamental mode at 1.5 GHz, but also a higher (quadrupole) modes at 2.8 GHz.

The temperature dependence of NQL can be represented by

$$R_s' \propto 1/\left(1 - T/T^*\right)^2, \qquad (3)$$

with $T^* = 6.8$ K.

The frequency dependence was linear, contrary to what was indicated in a previous paper [3]. However, evidence now is confirmed by data from NbCu cavities at 4.2 K and 352, 500 and 1500 MHz (inset Fig. 4, b).

3. DISCUSSION

As we have already proposed in a previous papers [5], NQL may be explained by weak sc spots. At that time, we hypothesised oxygen as contaminant, in the form of spots of weak sc phases with depressed T_c. In the TEM analysis we did not find up till now any confirmation for this hypothesis. So we conclude that these weak spots must have a different origin: What we found was a large density of metallurgical defects within grains and a large scatter in grain size. These features are characteristic of granular superconductors, which are composed of (nearly perfect) grains and weak links in between [6].

For those granular superconductors, when lowering the temperature, the grains become sc at the transition temperature of the bulk material. The sample nevertheless is not yet in a phase coherent sc state. This will only happen when the temperature is still lowered and the Josephson "phase locking" temperature T_{cJ} is passed. Then the coupling energy between the grains becomes of the order of the thermal energy kT, such that energy fluctuations can no longer destroy the phase coherence over the whole sample. T_{cJ} can be substantially lower than T_c. It is also known, that the critical field B_{c2} increases with decreasing grain size [7]. These ideas would naturally explain the B_{c2} and T_c measurements on samples at DC.

As to the RF measurements, we define f as that fraction of the surface which the RF magnetic field H has driven nc. We define f_0 that fraction of the surface composed of weak links if $H = 0$. We assume the weak links being nc contribute to the RF loss, and do not contribute at all being sc. By increasing H by a differential amount dH, f will increase by a differential amount df, which in first approximation for small H is proportional to f_0. Hence the relation:

$$df/f_0 = dH/H_c(T), \qquad (4)$$

where the critical magnetic field H_c (T) was introduced for normalisation reasons ($f(H_c) = f_0$). The surface resistance being proportional to the nc fraction f of weak links, $\alpha \cdot f$ (proportionality factor α), we obtain

$$dR_s/dH = R_s' = \alpha f_0/H_c(T). \qquad (5)$$

H_c (T) corresponds to the critical current j_c (T), by which the weak links are driven nc. Depending on their nature, $j_c(T) \sim T\text{-}T_c$ for weak links coupled by an insulator and $j_c(T) \sim (T\text{-}T_c)^2$ for weak links coupled by a metal [8]. The former temperature dependence was found elsewhere [3], the latter is found now (eq. 3). Hence we conclude,

$$R_s' = \alpha f_0/\left[H_{c0}\left(1 - T/T^*\right)^2\right]. \qquad (6)$$

It comes out naturally that T^* is identical with T_{cJ}.

As to the frequency dependence of R_s' it was suggested flux penetrates the intergranular medium in nanoseconds [9]. The energy needed to break the Cooper pairs is delivered by the electromagnetic field. This same energy can probably not coherently be delivered back to the electromagnetic field, when the nc electrons condense again into Cooper pairs. The RF loss is therefore proportional to the number of cycles per second, hence the RF frequency.

4. CONCLUSION

We have shown that maximum gradients of 13 MV/m and low field Q values of $Q > 10^{10}$ can be obtained in five-cell cavities. Thermal quenching was not observed, the limitation of the gradient was electron loading. These results are not significantly different from what has been obtained in one-cell cavities, despite the fact that in five-cell cavities the probability of having defects of poor adhesion is larger.

In the second part of the paper we have given an analysis of the decrease of the Q-value with the accelerating gradient in terms of weak links switching into the nc state by the action of the RF field.

ACKNOWLEDGEMENTS

We gratefully acknowledge the help of C. Dalmas for the co-ordination at CERN and the RF measurements, J. Williams for the B_c and T_c measurements, J. M. Rieubland for his effort to make us available the quantities of liquid helium needed, A. Insomby for rinsing and drying, and M. Taufer for chemical treatment.
We deeply thank Prof. Dr. M. Rühle from the Max-Planck-Institut für Metallforschung at Stuttgart and his collaborator Dr. J. Mayer for the TEM analysis of the samples.

REFERENCES

[1] Ph. Bernard et al., Proc. 5th Workshop RF Superconductivity, 19-23 August 1991, DESY, Hamburg (Germany), ed. D. Proch, 487.

[2] Ph. Bernard et al., Proc. 3rd European Part. Acc. Conf., Berlin (Germany), 24-28 March 1992, eds. H. Henke, H. Homeyer, Ch. Petit-Jean-Genaz, 1269.

[3] Ph. Bernard et al., Proc. 6th Workshop RF Superconductivity, 4-8 October 1993, CEBAF, Newport News VA (USA), ed. R. Sundelin, in press.

[4] W. Weingarten et al., CERN/EF/RF 87-2.

[5] G. Arnolds-Mayer and W. Weingarten, IEEE Trans. Magn. MAG-23 (1987)1620.

[6] J. Clem, Physica C 153 - 155 (1988) 50.

[7] M. Tinkham and C. J. Lobb, Solid State Physics 42 (1989) 91.

[8] P. G. de Gennes, Superconductivity of Metals and Alloys, New York 1966, 238.

[9] A. M. Portis, Proc. Earlier and Recent Aspects of Superconductivity, Erice (Sicily), Italy, 4-16 July 1989, ed. J. G. Bednorz and K. A. Müller.

RF processing of field emitting particles

J. Tan[a)], H. Safa[b)], B. Bonin[b)], J. Jodet[c)]

a) Thomson Tubes Electroniques, 78141 Vélizy Cedex, FRANCE

b) DAPNIA / SEA, & c) INSTN / SEPEM— Centre d'Etudes de Saclay, 91191 Gif sur Yvette Cedex, FRANCE

Abstract

In this paper, we describe the results obtained from RF field emission experiments on niobium samples polluted with metallic particles. In particular, the influence of the electromagnetic field, the RF pulse length as well as the total number of pulses applied is shown. The peculiar cumulative effect found could bring some new light on the so called high peak power (HPP) processing of cavities.

1. INTRODUCTION

It is now well established that field emission (FE) on broad area electrodes or in radiofrequency (RF) cavities is generally associated with local surface defects such as scratches or contamination particles [1], [2], [3]. Many theoretical models have been developed [4], [5] in order to explain the electron tunneling through the potential barrier at the metal–vacuum interface, for field range two orders of magnitude lower than the theoretical one predicted by Fowler and Nordheim [6]. Lately, FE studies at Saclay [3] showed that the local enhancement of the field can be explained by a modified "projection model"[4] at least for two categories of emitter sites : "intrinsic" sites (i.e. whose composition contains nothing but the substrate's element, e.g. scratches), and "extrinsic" sites (meaning dust particles composed with other foreign species) [2].

Actually a great research effort among the particle accelerators community is undergone to repel FE threshold field. Dealing with scratches, those can be easily removed by means of a "heavy" chemical etching, and one may assume a surface state free of such defects after this treatment.

It had been clearly shown [7], [8] that more cleanliness during the cavity mounting steps led to significant gain for accelerating field. However, the presence of dust particles either in chemical baths or even in cleanroom atmosphere make it more difficult to avoid them on the cavity walls. One proceeds finally to surface treatments *in situ* i.e. with closed cavities.

It is generally believed that RF processing reduces FE by inactivation of emitting sites via a mechanism of thermal instability followed by a microdischarge destroying the site. This mechanism is certainly at work to reduce FE, but we would like to show that HPP processing [9] is also effective to remove mechanically dust particles from the surface, thereby reducing the total FE from the surface.

In a previous paper [10], first experimental results with dust particles obtained with the reentrant 1.5 GHz cavity were reported. Nb samples were intentionally contaminated with iron particles (20–50 μm size) and submitted to an intense pulsed field : 45 MV/m peak with repetition rate $\simeq 1\,Hz$. We noticed incidentally at that time that the number of remaining particles on the surface after applying the RF power was related to the pulse length. Long pulses led to important thermal effects i.e. melting and welding of the particles on the substrate. After treatment, the proportion of particles remaining on the surface was as follows : 75% for long pulses (τ =10 ms) as compared to 30% for short pulses (τ =100 μs). Thus one might deduce that short pulses were more likely to remove dust particles and then "clean" the surfaces. These observations were consistent with Cornell's group who showed the efficiency of HPP processing for reducing FE in accelerating cavities [9].

Following these observations, we wished to undertake a more systematic study in order to lighten the basic mechanism of "cleaning" dust particles by RF pulses. Three parameters appear to be of major importance :

1. the maximum field level on the surface E_{max},
2. the RF pulse length τ,
3. the total number of RF pulses N.

2. EXPERIMENTAL SET UP

The core of the experimental set up is a re-entrant 1.5 GHz copper cavity working at room temperature. A 5 kW klystron permits application of 50 MV/m peak field on the 10 mm^2 hemispherical top of removable niobium samples. As the cavity is not cooled, the maximum allowed RF power duty cycle is 1 %. Electrons emitted hit a current probe placed 12 mm afar from the sample collecting an *integrated intensity*. Working pressure is better than 10^{-7}mb. The full description of the apparatus, cleaning and operating procedures has been detailed in a previous paper [11].

The purpose of this work is to study the mechanism of particle removal . Thus niobium samples chemically etched are sprinkled with hundreds of iron particles (20–50 μm size) and examined using a scanning electron microscope (SEM) before mounting in the cavity.

RF duty cycle is always kept equal to 1 %. The reference number of particles is arbitrarily taken to be 100 % after an initial low RF field test ($E_{max} \leq 5$ MV/m) — so as to get rid of uncertainties due to poorly adhering particles that can get lost during transportation between the SEM and the RF cavity. After each RF test, the sample is dismounted from the cavity and observed with the SEM where the number of remaining particles on the surface is counted.

3. EFFECT OF FIELD LEVEL

It has been shown that with a pulse length τ =10 ms and at a field level of 45 MV/m, particles can melt and weld to the sample surface [10]. Therefore, the study of the behavior of

particles as a function of field level should give informations about the optimum field to apply answering the following questions : i/ what is the minimum field required to remove a given particle ? ii/ what is the minimum field to cause an irreversible damage (either by welding the particles or by leaving craters on the surface)?

3.1. Experimental procedure

Four Nb samples were prepared following the procedure described in section 2.2, with different τ values for each, namely 10 ms, 1 ms, 100 μs and 10 μs.

All samples were RF processed at a low field level for 30 mn then removed for SEM observations before applying the higher RF field. Thus all samples experience *successively* 14 MV/m, 30 MV/m and 45 MV/m for 30 mn each time.

3.2. Experimental results

The results are summarized in figure 1. As one could expect, the stronger the field, the lower the number of remaining particles and consequently the more efficient is the "cleaning". More interesting is the fact that at a given field, the shorter the pulse length the better is the cleaning.

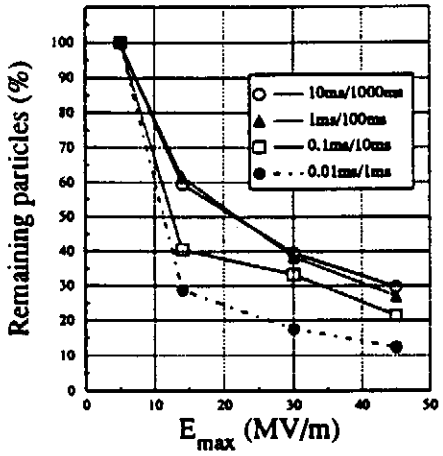

Figure 1. Effect of increasing electric field for different pulse lengths.

3.3. SEM observations

At 5 MV/m, some particles are seen to be lined up along the electric field. Almost all particles seemed in good electrical contact with the substrate as they did not charge under the SEM beam. As the field level was increased, more particles piled up. Below 30 MV/m, no craters were observed on all the samples surfaces with the exception of the sample having the longest pulse length (10 ms) where few craters (about typically 5 μm size) appeared at 30 MV/m. Craters' location was always associated with missing iron particles, and X-ray analysis revealed the presence of Fe element in craters. At 45 MV/m, the number of craters increased with τ.

3.4. FE measurements

Few reliable currents values had been obtained during RF processing. Until 14 MV/m no current signal exceeded the measurement noise (10 pA). For higher field levels, as the working duty cycle chosen was the upper limit for our experiment, microwave heating yielded an important degassing. This led to unstable positive ionization probably near the current probe which altered the current reading. At 30 MV/m the current was generally less than 4 μA whereas it increased to 15 μA at 45 MV/m.

After the last RF tests at 45 MV/m, FE measurements were performed once again at 30 MV/m : significant gain on FE was obtained as the final current did not exceed 1 μA for one sample, and 150 pA for another one.

4. TIME PROCESSING EFFECT

4.1. Experimental procedure

Four other Nb samples were prepared following the procedure described in section 2.2, with different τ values for each (10 ms, 1 ms, 100 μs and 10 μs). After one low field test, all RF tests were done keeping the field constant and equal to 30 MV/m.

We wish to observe whether the total number N of applied RF pulses can modify the number of remaining particles. In other words, is there a cumulative effect of the RF field due to the successively applied pulses and to what extent ? To do so, we apply different time durations t on the same sample, counting after each test, with the help of the SEM, the percentage of the remaining particles. As the effective RF time is $t_{eff} = C \times t$ (C is the duty cycle, here 1 %), the total number of pulses can be evaluated by $N = \frac{t_{eff}}{\tau} = \frac{C \times t}{\tau}$.

4.2. Experimental results

They first confirm the importance of the pulse length that has been already pointed out in the previous section. Short RF pulses are far more efficient than long ones. Moreover, one sees from figure 2 that there is a very strong cumulative effect (at any pulse length) which seems to show no saturation limit : the cleaning of the surface continues as long as the RF power is applied. The longer the time of exposure to RF power, the better will be the processing.

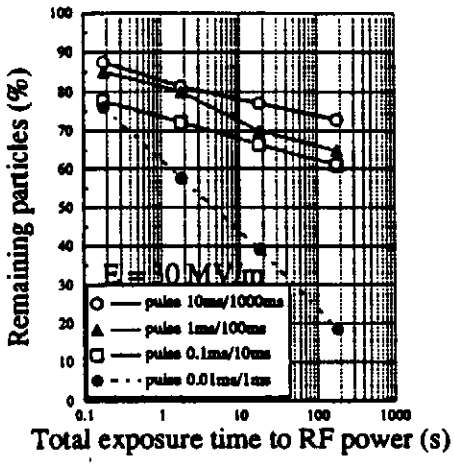

Figure 2. Effect of RF time duration for different pulse lengths.

4.3. SEM observations

Figures 3.a and 3.c show the samples before RF tests. In figure 3.b the first sample has undergone 18 s of RF power with a pulse length τ =10 ms, whereas the second sample is shown in figure 3.d after 5 hours of RF power at τ =10 μs. Although the field level was the same for both samples (30 MV/m), one notices that nearly all particles were still lying on the first sample while very few remained on the second one. This clearly proves the efficiency of cleaning with time using very short pulses.

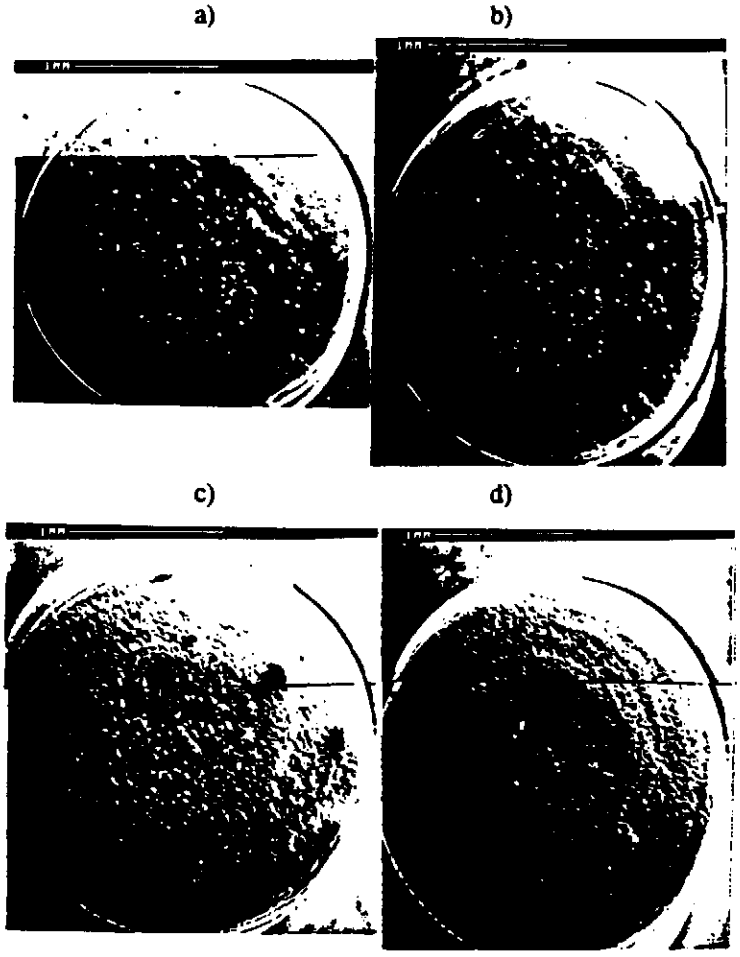

Figure 3. An effective RF processing needs short pulse length and long time : in 3b, the sample shown in 3a before test, has undergone 18s of RF power with τ=10ms. While on another sample (3c before test), 5 hours of processing with 10μs pulses at the same field have nearly clean all particles from its surface (3d after test).

It should also be noted that the surface is much more damaged (craters and molten particles) by long pulses than by short ones, even at the same field and for equal number of RF pulses.

5. DISCUSSION

A first series of experiments confirms the need for high electric field levels to throw away dust particles. Besides, they demonstrate that short RF pulses are also necessary to avoid strong thermal effects that may lead to melting and consequently welding particles onto the surface (generally the contact particle-substrate is very poor). The associated constant time may be easily evaluated and model calculations provides values close to 1 ms [12]. In that view, continuous RF processing for example is expected to be far less effective than pulsed treatments to remove particulate contaminants and to reduce FE.

The second series of experiments suggests that the removal of particulate contaminants by pulsed RF power occurs via a *cumulative mechanism*, and that many pulses of short duration are more effective than a few long ones to clean the surface. In view of this, we predict that medium power pulsed (MPP) processing should be effective to reduce FE, provided the pulse duration and the total processing time are properly chosen.

6. CONCLUSION

This work shows that pulsed RF processing can remove particulate contamination. For that purpose three conditions are required :

- A large number of pulses to obtain cumulative effect,
- Processing with short pulse lengths to avoid welding particles on the surface,
- Applying a high enough peak field to remove particulate.

These new effects contribute to the reduction of FE usually observed after application of "high peak power processing". They should be taken into account in the choice of HPP parameters, favoring (if possible) shorter pulses.

REFERENCES

[1] Niedermann Ph., Ph. D, thesis no 2197, University of Geneva (1986)

[2] Moffat D. et al., Particle Acc., 40, (1992),85–126

[3] Jimenez M. et al., J. Appl. Phys. D, 27, (1994), 1038–1045

[4] Noer R.J., Appl. Phys. A, A28, (1982) 1–24

[5] Latham R.V., IEEE Trans. Elec. Insul., EI23, no 5 (1988), 881–894

[6] Fowler R.H., Nordheim L., Proc. Roy. Soc London, A119,(1928), 173–181

[7] Proceedings of the 2nd Workshop on RF Superconductivity, Geneva, Switzerland (1984)

[8] Proceedings of the 3rd Workshop on RF Superconductivity, New York, USA (1986)

[9] J. Graber, Ph. D, Thesis, Cornell University (1993)

[10] Tan J. et al., Field emission measurements in a radiofrequency field, to be published in J. Phys. D

[11] Tan J. et al., A microwave cavity for field emission studies, to be published in J. Phys. D

[12] Junquera T. et al., Studies on field emission in RF cavities using an optical system, this conference EPAC, London, U.K. (1994)

Status and applications of superconducting cavities

B. Bonin

CEA DAPNIA SEA

Saclay F-91191 Gif sur Yvette, France

Abstract

This paper sketches the most recent trends of the R&D and applications of RF superconductivity to accelerators.

1. INTRODUCTION

Superconducting cavities have now been used in many accelerators, eg heavy ion linacs, large storage rings at CERN, KEK and DESY, electron linacs at Stanford, Darmstadt, Saclay-Orsay and CEBAF, or free electron laser drivers. Experience gained during the building of these machines strongly suggests that RF superconductivity is already a mature technology, even if it is still far from its limits. New applications are now being envisaged, both at the high luminosity and at the high energy frontiers of the accelerator technology.

The physics and accelerator applications of RF superconductivity have been excellently reviewed by many authors [1–5]. The present paper will concentrate only on the highlights and on the most recent developments in the field. Included topics are large scale fabrication, thin films, surface preparation and cavity performance level. Despite its importance and its close connection to cavities, the problem of RF couplers and windows has been deliberately omitted in this article. The most important issues of the R&D on superconducting cavities, ie the quest for high gradients and reduced RF dissipation, will be reviewed.

2. HIGH GRADIENTS

The accelerating gradients available in accelerating superconducting structures have been in considerable progress recently, increasing by as much as 50% during the last two years. This progress may be ascribed to the conjunction of at least four factors: improved cleanliness standards [6], the development of RF processing techniques like High Peak Power Processing [7–9], the availability of higher purity niobium [10], and the generalization of the heat treatment of the cavities [11,12].

Accelerating gradients are still limited by two phenomena: quenches and field emission. The impression gathered from a systematic compilation of the results worldwide is that roughly 50% of the gradient limitations are due to quenches, while the remaining 50% come from electron emission.

The maximum electric field that can be obtained without field emission depends on the area exposed to the field. Surface fields higher than 100 MV/m have been obtained without electron emission on areas of the order of 1 cm^2 [13]; superconducting radio-frequency quadrupoles (RFQ) have reached a peak electric field of 128 MV/m [14]; surface fields of 50 MV/m have been reached often at about 1 GHz on single cell accelerating cavities, and 35 MV/m on 3– or 5–cell cavities. The largest data base comes from CEBAF (5 cell, 1.5 GHz, T = 2K), [15], (fig. 1). The results are very encouraging, since nearly all the CEBAF cavities tested so far exceed by large amounts the design value: the average surface field obtained is close to 20 MV/m. Moreover, there is no significant degradation of usable gradient of the CEBAF cavities between their test in a vertical cryostat and their use in the accelerator. Similar gradients have been achieved in a much smaller test series on 9–cell cavities at Cornell and Wuppertal (3 GHz, 1.8 K). There is much confidence that surface fields as high as 30 MV/m can be obtained reliably, without electron emission, in 9–cell structures at 1.3 GHz. With the ratio $E_{surface}/E_{acc} = 2$ currently obtained in present day "β=1" cavity designs, this corresponds to accelerating gradients of 15 MV/m.

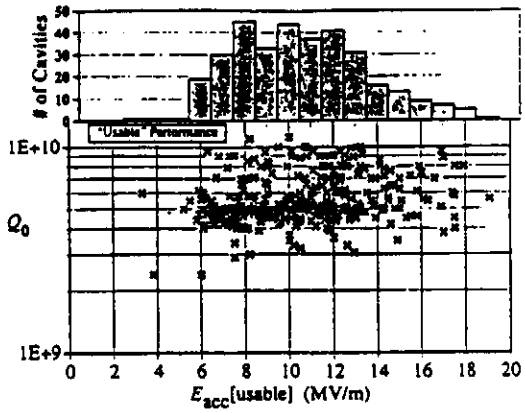

Figure 1 Systematics of the 1.5 GHz, 5–cell cavities from CEBAF (from ref. 15).

2.1 Field emission

It is now recognized that field emission in cavities is due to surface defects of micrometer size, causing electron emission from the surface and subsequent loading of the cavity [16]. Recent systematic studies have confirmed that deliberate contamination of the cavity surface by conducting, micrometer sized particles results in heavy field emission [17]. Insulating particles seem to be much less dangerous. The relevance of this information for the case of SC cavities may be discussed, but a rigorous cleanliness of the cavity surface seems to be an indispensable prerequisite to avoid field emission. So far, efforts have concentrated on the prevention of particulate contamination during the chemical treatment of the cavity,

and during the subsequent rinsings. Among the advanced cleaning techniques presently under investigation, high pressure rinsing seems to be most promising [18,19]. Its idea is to use the mechanical action of a high speed water jet to remove micron sized particles adhering on the surface.

Particulate contamination also arises during assembly and pumping of the cavities. The assembly steps involve unavoidable contact and abrasion of metal parts, liable to generate metallic dust particles and field emission. Despite its considerable potential of improvement, this problem has received much less systematic attention than the problem of cleanliness during the wet process.

2.2 RF processing

High peak power processing (HPP) is another possible recipe for suppressing field emission in superconducting cavities. It consists basically in sending a RF pulse intense enough to "burn" the electron emitters, during a time short enough to prevent a quench [7–9]. A two-cell, 3 GHz cavity reached a maximum surface field of 100 MV/m at Cornell after such a high peak power processing. This is certainly a very promising technique, but its applicability to the real case of an accelerator is not demonstrated yet. If HPP is to be applied on a cavity already installed in an accelerator, the coupling line will have to withstand the power necessary for the treatment (of the order of 1 MW/m). This requirement cannot be met in most accelerators. However, "moderate power processing" (a few kW/m) is much more readily applicable in situ, has proven its validity [20], and is used, for example at CEBAF and on MACSE. On the other hand, the usefulness of HPP as an "ex situ" treatment is not yet fully established, because it remains to be seen to what extent the benefit of the treatment is kept after a dismounting of the cavity and a new exposure to air.

2.3 Quenches, and the problem of niobium purity

The limitation of gradients by quenches (ie thermal instabilities of the cavity initiated by heating defects) has been a severe one in the past. Improved fabrication techniques and the use of high purity niobium already restrict the occurrence of quenches to about 20% for Nb single cell accelerating cavities in the GHz range with gradients smaller than 15 MV/m. High temperature vacuum annealing of the cavity gives the possibility of increasing the wall thermal conductivity, and the cavity quench threshold. It is striking to see that in all laboratories, the highest gradients have been obtained with fired cavities. For example, accelerating gradients as high as 30 MV/m have been reached at Cornell on single cell cavities at 1.5 GHz after heating the cavity to 1300°–1500° C (fig. 2). Unfortunately, the heat treatment has many drawbacks: it is expensive and difficult to integrate in a large scale production process. Moreover, it severely degrades the mechanical properties of the cavities. Despite these shortcomings, heat treatment seems to be an obliged detour on the road to high gradients.

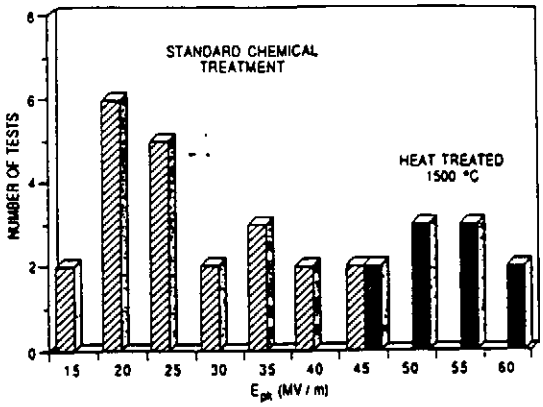

Figure 2 Benefits of the heat treatment on single cell niobium cavities at Cornell (from ref. 1).

A significant proportion of the CEBAF cavities are still limited by quenches. This probably means that the cavity chemical treatment and handling are done in very clean conditions, thus preventing field emission. Another consequence is that these cavities might reach higher gradients after a purification improving their thermal conductivity. Definitely, a niobium purity of RRR 200, which has been the "state of the art" during the last five years, is not sufficient for high gradient applications!

In the far future, it is probable that the purification of Niobium will be achieved at the stage of the Nb sheet production. A high purity Nb sheet of RRR 350 with adequate formability can already be ordered from industry. Prospects of further improvement are good, since very high purity Niobium (RRR > 600) is in principle available from russian industry [21]. However, it is known that the forming of niobium sheet introduces a large density of dislocations in the material, thereby reducing its RRR and thermal conductivity. This might reduce somewhat the advantage of using very high purity Nb sheet as a starting material. This problem has been largely overlooked in the past, due to the difficulty of measuring the RRR of a cavity already formed into shape. In this context, heat treatment of the material at the stage of the half cell production remains an interesting option.

3. PROGRESS IN Q-VALUE

It is essential for the success of many kinds of superconducting accelerators to minimize the RF power dissipated in the cavities. Substantial progress has been made during the past two years. The main cause of non-reproducibility of the cavity Q value, i.e. hydrogen contamination, has been understood [22] and eradicated to a large extent. In all laboratories, this effort yielded cavities with reproducible residual surface resistance, between 10 and 20 nΩ. Surface resistance as low as a few nΩ have indeed been observed, for example at Wuppertal ([23], fig. 3) or at Saclay. This corresponds to Q_{res} = 5–6 10^{10}, a value now routinely obtained in vertical test cryostat at Saclay, even with non heat-treated accelerating cavities. This result, obtained thanks to an especially careful magnetic shielding of the cavities, and a minimization of the losses in the cutoff tubes, has considerably clarified

the list of possible causes of residual dissipation in superconducting cavities. Putting aside the two major causes already mentioned, this list featured [24] dielectric losses in the Nb_2O_5 oxide layer and in the adsorbed species, normal conducting inclusions, oxide-induced surface serrations, geometrical defects like cracks, crevices or delaminations, losses in the disordered layer at the Nb-oxide interface, losses in the grain boundaries,..... The order of magnitude of each contribution was poorly known : we now know from experiment that their sum amounts to less than a few nΩ for state-of-the art, non heat-treated cavities. This value can and should become a standard for vertically tested cavities. It remains to be seen to what extent the benefits of this improvement in Q value are kept in a real accelerator environment, where the demands on magnetic shielding, cavity design, and cooling speed are met less easily. If significant improvement in Q values can be obtained in real accelerators, the cost of CW accelerators could be reduced by reduction of the needed cryogenic power. This might also permit operation of pulsed accelerators like TESLA with duty cycles larger than the ones envisaged now.

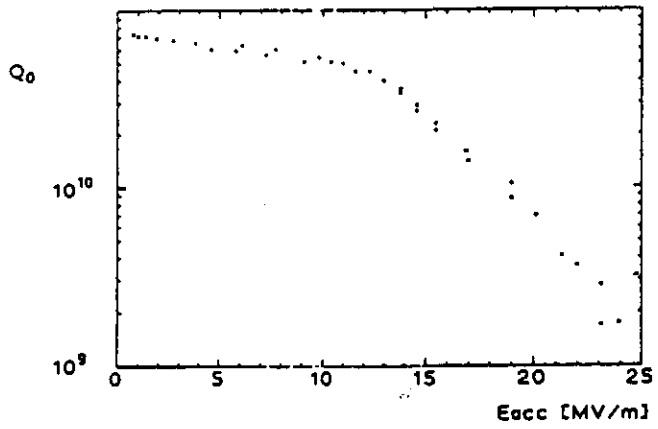

Figure 3 Very high Q-value obtained in a 3 GHz single-cell niobium cavity at Wuppertal (from ref. 23).

4. CAVITY FABRICATION

In most cases, low-beta structures are produced in limited number. Their fabrication poses problems which can be solved at the laboratory level. The situation is very different for β=1 cavities, which are often to be produced in large quantities for a given accelerator project. Here, the fabrication cost and quality of the product become industrial problems.

Presently, most β=1 accelerating cavities are made from Nb sheet, and their fabrication includes forming of half cells from sheet material, and electron beam welding of the half cells. This "EB welding method" is very delicate because of the requirements it imposes on the degree of cleanliness of the surfaces to be welded. It is also time consuming and poorly suited to large scale production in industry. It involves many operations, especially for cavities with a large number of cells. Besides, even with a good vacuum in the EB welder, the preservation of the niobium purity at the welds becomes increasingly difficult to guarantee, if very high purity niobium is used.

Alternative approaches based either on spinning a single niobium sheet [26] or hydroforming a tube [27] to produce seamless cavities are under investigation. The drawability of niobium seems to be sufficient for this purpose, but forming of refractory metals is a very delicate process, especially if high purity material is used. These new methods will probably involve intermediate annealings of the cavity during fabrication. It remains to be seen whether the number of annealings and the purity of the material can be maintained at an acceptable level. In case of success, these techniques might result in a very significant reduction of costs for a large scale cavity production.

4.1 Thin superconducting films

In RF superconducting structures, the superconducting current flows in a very shallow skin depth, of the order of 100 nm. This suggests the use of a thin superconducting film deposited inside the cavity. The expected gain is threefold: a metal with good thermal conductivity can be chosen as substrate, with a subsequent enhancement of the cavity thermal stability ; the substrate (eg OFHC copper) is cheaper than niobium sheet ; the thin film may have improved superconducting properties as compared to niobium. Investigations have been made mainly with Nb, NbN, NbTiN and Nb_3Sn thin films.

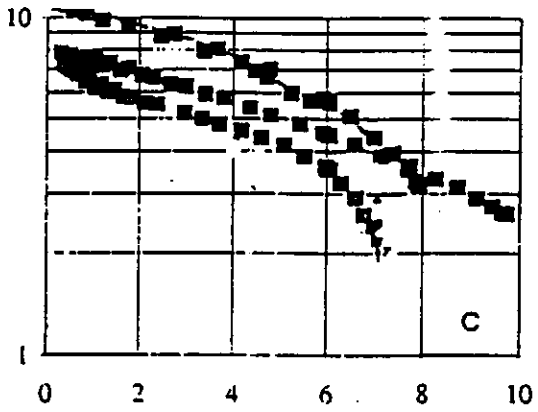

Figure 4 Typical Q (10^9) vs E_{acc} (MV/m) of accepted Nb/Cu cavities for LEP, as measured in vertical test cryostat (from ref. 28).

CERN has developed with success the technique of Nb thin film deposition on copper for the LEP200 cavities [28,29]. The transfer of this new technology to industry has met some difficulties. The chemical treatment of the copper substrate turned out to be a most crucial point, determining the adherence of the Nb film. Local lacks of adherence resulted in "blisters", causing abrupt degradations of the cavity Q value. An appropriate chemical treatment, combined with a dust-free handling of

the Cu substrate brought this problem under control. All three companies involved in the LEP cavity fabrication now deliver cavities with Q values and gradients above the specifications (E_{acc} =6 MV/m, Q_0= 4 10^9 at 4.5 K). These Nb/Cu cavities behave as well, if not better, than massive niobium ones of the same design. Full scale production of the cavities has now started, and the first assembled cryomodules arrive for qualification at CERN.

Thin film samples of the intermetallic compounds NbN, NbTiN and Nb_3Sn are being elaborated in a few laboratories, e.g CERN, Wuppertal or Saclay [30]. Unfortunately, the residual surface resistance of these films is rather high (a few hundreds of nΩ at GHz frequencies), and increases with increasing RF field. Moreover, the gradients obtained (of the order of 35 mT) are still too low for most applications. The present limitations of performance are probably curable. They are thought to be due to imperfections in the thin film morphology, causing granular superconductivity [31].

Overall, thin films other than Nb/Cu have promising results on samples, but no convincing high-performance cavity has been fabricated yet using these films. The preferred applications of thin film cavities will be focussed on accelerators requiring large duty cycle and small RF dissipation, for which the criterion of high gradient is not a very high priority. Here, thin films open perspectives of simplified cryogenics, since operation of the cavity at high temperatures will be allowed by the very small BCS contribution to the surface resistance.

5. PERSPECTIVES FOR SUPERCONDUCTING CAVITIES

SC cavity technology is now applied to a wide variety of accelerators, taking advantage of the low RF losses in the cavities. This feature can be exploited in different ways, depending on the particular application under consideration (Table 1). We shall only deal here with the most recent trends and results.

Until recently, the only "low beta" application of RF superconductivity has been for heavy ion linacs. The increasing number of such accelerators indicates that this will continue to be a dominant application. The development of new resonator shapes like superconducting radiofrequency quadrupoles and spoke resonators might open the field: new applications such as high intensity CW ion beams or high duty cycle proton beams for neutron spallation sources are forthcoming.

The advantages of superconducting cavities for accelerators of high luminosity are well known and well documented [1–5]. β = 1 superconducting cavities have been successful in storage rings, and in large duty cycle electron linacs. With the years, these applications are spreading, and becoming more and more convincing. The good news from these last two years is the superb behaviour of the CEBAF cavities. Nearly all cavities tested so far exceed by large amounts the design value (fig. 1).

Accelerator type	Required cavity characteristics
Heavy-ion linacs	Mechanical stability, high gradients
e-linacs with large duty cycle: - for Nucl. Phys. (CEBAF, Darmstadt, ELFE) - for free electron lasers (LISA, HEPL, JAERI...)	Low RF dissipation
High energy hadron rings (LHC, SSC, RHIC)	
High intensity accelerators: - Storage rings (KEK, HERA, LEP200) - Hadron linacs (ESS, AWT...)	Large diameter iris; Couplers with large power handling capabilities
e+ e- linear collider (TESLA)	High accelerating gradient

Table 1 Main applications of SC accelerating cavities

Now, other domains of application are opening, exploiting the advantages of RF superconductivity in other ways:

The idea that RF superconductivity could also be applied to accelerators at the high energy frontier is not new [32], but is gaining strength. The future high energy e+ e- collider might use superconducting cavities. The TESLA collaboration [33], which promotes this idea, has grown considerably during the last two years. Here, the reduced RF dissipation of superconductors is still exploited, but the large diameter beam holes permitted by SC cavities (and the machine parameters which derive from this feature) is probably the most convincing argument in favor of the TESLA project. Altogether, TESLA has already emerged as a credible option for an e+ e- collider in the TeV range. The main challenge of the TESLA cavities will be to reach accelerating gradient of the order of 25 MV/m in 9 cell, 1.3 GHz cavities. The gradients obtained recently in Cornell, Saclay, Wuppertal, CEBAF or KEK suggest that this goal can be reached, but an important amount of R&D will certainly be required to obtain it in a reproducible manner and at low cost.

There is also a new and powerful interest in high intensity hadron linacs, eg for spallation sources. The idea that these accelerators could use superconducting cavities [34] is new and exciting. Here again, the large diameter irises of superconducting cavities are exploited, but this time, the main interest seems to be the reduced activation by the beam halo. These accelerators will necessarily operate at rather low frequency, similar to the

LEP frequency (350 MHz). For the same reasons than at LEP, thin film cavities (maybe niobium nitride ?) could be an interesting option for these accelerators.

RF superconductivity is a reliable technology. Some heavy ion linacs or electron rings like Tristan at KEK have already used it for a long time. No long term degradation of the cavity performance have been observed [35]; the essentials of the physical phenomena underlying the behaviour of SC cavities now seem to be understood at the laboratory level. But RF superconductivity is still far from its theoretical limits. The remaining problems are probably of technological order. There is still ample room for improvement, if the present limitations imposed by cleanliness and preservation of the surface quality can be pushed further.

RF superconductivity has reached a stage of validation at the industrial level. One of the main obstacles to the development of this technology is its cost. An important challenge for the future years will be to cut it down.

As far as one can see, the main R&D topics which should be addressed to improve cavities could thus be as follows :

i) field emission, in connection with improved techniques to achieve a good cleanliness of the cavity surface;

ii) thin superconducting films;

iii) improved fabrication techniques, in connection with the metallurgical aspects of Nb elaboration and purification;

Acknowledgements.

The author wishes to thank his colleagues from CEBAF, CERN, Cornell, DESY, KEK, Wuppertal, Los Alamos for kindly supplying information for this review.

6. REFERENCES

1. H. Padamsee, K.W. Shepard and R. Sundelin, Ann. Rev. Nucl. Part. Sci. 43 (1993) 635

2. P. Kneisel, J. Vac. Sci. Technol. A11 (1993) 1575

3. W. Weingarten, Particle World 1 (1990) 93

4. D. Proch, Proc of the 1993 Particle Accelerator Conference, Washington (1993) 758

5. H. F Dylla, L. R. Doolittle and J. F. Benesch, Proc of the 1993 Particle Accelerator Conference, Washington (1993) 748

6. C. Z. Antoine et al. Proc. Vth Workshop on RF Superconductivity, D. Proch, ed., Hamburg (1991) 456

7. J. Kirchgessner et al., Proc of the 1989 Particle Accelerator Conference, Chicago (1989) 482

8. J. Graber, PhD Thesis, Cornell University, Ithaca (1993)

9. H. Padamsee et al., Proc. Vth Workshop on RF Superconductivity, D. Proch, ed., Hamburg (1991) 37

10. M. Hörmann, J. Less Common Metals 139 (1988) 1

11. Q. S. Shu et al., NIM A 278 (1989) 329

12. P. Kneisel, J. Less Comm. Metals 139 (1988) 173

13. D. Moffat et al. Cornell report CLNS 89934, Cornell University, Ithaca, NY (1989)

14. J. Delayen and K.W. Shepard, Appl. Phys. Lett. 57 (1990) 514

15. C. Reece et al. Proc of the 1993 Particle Accelerator Conference, Washington (1993) 1016

16. P. Niedermann, "Experiments on enhanced Field Emission", PhD dissertation, Université de Genève (1986)

17. M. Jimenez et al., J. Phys. D: Appl. Phys. 26 (1993) 1503

18. P. Bernard, D. Bloess et al., Proc. of the IIIrd European Particle Accelerator Conference, Berlin (1992) 1269

19. B. Rusnak et al. Proc. of the 1992 Lin. Acc. Conf., Ottawa, C. R. Hoffmann, ed. (1992) 728

20. I. Campisi, IEEE Trans. Mag. 21 (1985) 134

21. A. V. Eliutin et al., Proc. Vth Workshop on RF Superconductivity, D. Proch, ed., Hamburg (1991) 426

22. B. Bonin and R. Röth, Part. Accelerators, 50 (1992) 59

23. D. Reschke, private communication

24. J. M. Pierce et al. Proc. IXth Int. Conf. Low Temp. Phys. (Plenum press, NY (1965) 396

25. J. Kirchgessner, Proc of the IIIrd Workshop on RF superconductivity (Argonne Ntl Lab. 1988) Report ANL. Phys. 88–1 (1988) p 533

26. V. Palmieri et al., contribution to this conference, and article to be published in NIM (1994)

27. C. Hauviller, private communication.

28. G. Cavallari et al., Proc of the 1993 Particle Accelerator Conference, Washington (1993) 806 and refs. therein.

29. C. Benvenuti et al. XX Int. Conf. on Low Temp. Phys., Eugene, Oregon, USA (1993)

30. P. Bosland et al., Proc. of the Third European Particle Accelerator Conference, Berlin (1992) 1316

31. B. Bonin, H. Safa, Supercond. Sci. Technol. 4 (1991) 257

32. M. Tigner, Nuovo Cimento 37 (1965) 1228

33. H. Padamsee, editor. Proc. of the 1st TESLA Workshop, CLNS report 90–1029 (1990)

34. H. Lengeler, VIth Workshop on RF Superconductivity, ed . R. Sundelin, CEBAF (1993)

35. K. Kubo et al. Proc. XVth Int. Conf. on High Energy Accelerators HEACC 92, ed. J. Rossbach, Hamburg (1992) 691

Thermal Tests of HOM Couplers for Superconducting Cavities

S.Chel, A.Mosnier
CEA,DSM/DAPNIA/Service d'Etudes d'Accélérateurs
CE-Saclay, F-91191 Gif-sur-Yvette, France

M.Fouaidy, T.Junquera
Institut de Physique Nucléaire (CNRS-IN2P3)
F-91406 Orsay, France

Abstract

In order to restrict the multi-bunch phenomena due to long-range wakefields in the TESLA linac, the higher order modes of the cavity must be damped down to the 10^4-10^5 level. For this purpose, HOM-couplers, mounted at both ends of the cavity, must couple strongly to the most dangerous modes, while rejecting by means of a filter the accelerating mode. Two versions have been developed [1], one is welded to the beam tube and the other one is demountable thanks to an intermediate flange. In this paper, we present the results of high power tests performed on the demountable version with a special test stand, including a single-cell cavity, a 5kW klystron and the coupler itself, as well as thermal simulations, which were initiated previously [2] with the help of a finite elements code. Accelerating field of 21 MV/m in cw mode, limited by cavity quenches and not by the coupler, was achieved, giving a confortable safety margin if one keeps in mind that the duty cycle of the TESLA pulsed mode is lower than 2 %. Moreover, by intentional detuning of the filter, the coupler was capable to transmit a peak power of 1.75 kW for the TESLA beam pulse duration, higher than the maximum HOM power which could be resonantly excited by the beam.

1. INTRODUCTION

The key component of the demountable coupler is a loop whose plane is orthogonal to the beam axis (see figure 1), which couples mainly to magnetic field for the dipole modes and mainly to electrical field for the longitudinal modes. The rejection filter of the fundamental mode is simply formed by the inductance of the loop itself and the capacity between the loop end and the outer conductor [3]. No stringent fabrication tolerances are required and the final tuning of the filter can be performed outside the clean room, once the coupler is mounted and the cavity is closed, with the help of the small bellow located above the Helicoflex gasket. The present design of the LHe-vessel of the TESLA cavity prevents from a direct cooling of the coupler by LHe. The loop is then simply cooled by conduction through the upper stub, which can be however linked to the LHe bath through a thermal shunt. Since the integrated filter has to a sustain very high reactive power (the external Q of the coupler without filter with respect to the accelerating mode is only a few 10^6), the thermal behaviour of the device under high RF power must be carefully studied. We present and discuss the results of RF tests and calculations obtained with different couplers mounted on the beam tube, which was not in direct contact with the LHe bath, of a single-cell cavity.

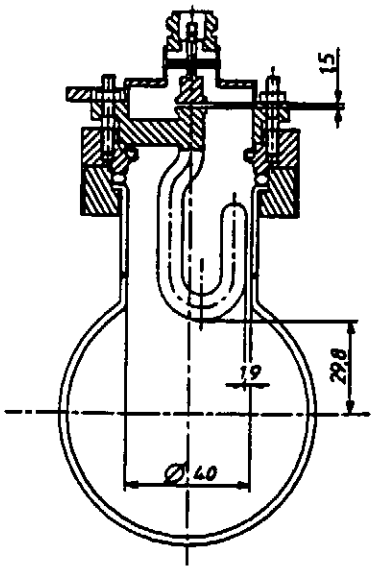

Fig. 1 : Drawing of the demountable HOM coupler

2. TEST STAND AND CALIBRATION

For the power tests, we used the existing 1497 MHz RF equipment. The cavity and coupler dimensions were then scaled from the 1300 MHz TESLA frequency to 1497 MHz. However, in order to push away limitations due to cavity quenches, the coupling of the scaled version to the accelerating mode was made on purpose five times higher than the final 1300 MHz TESLA version. The distance between the cavity iris and the HOM coupler was decreased, while the loop penetration in the beam tube was increased. With this test arrangement, the surface magnetic field at the filter location is about 3 Gauss/MV/m. We also used calibrated thermometers fixed around the coupler and the beam tube for temperature measurements. On the other hand, the important parameters which can be only deduced from experimental data, such as the thermal contact resistance at the sealings, were determined by means of a special arrangement using a heater. This arrangement looks like the real coupler (Fig. 2) and was also used to check the thermal simulations. A manganin wire heater, attached to the end of the loop, is used to simulate the RF losses and the resulting temperature distribution around the coupler and the uncooled beam tube is measured as function of the heater power (Pheater).

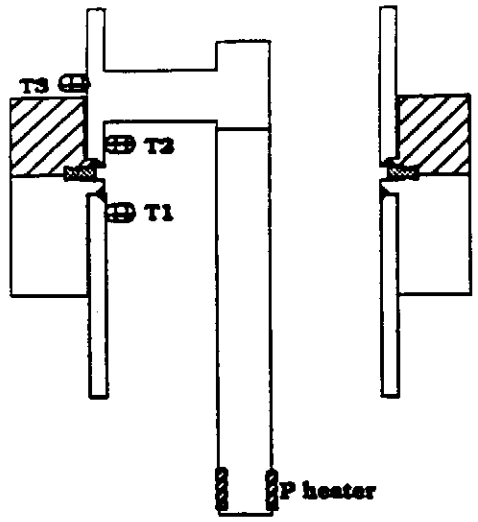

Fig. 2 : calibration test assembly

The results showed an important thermal contact resistance across the flanges. An overall equivalent thermal conductivity k_{eq} to this assembly can then be defined by :

$$\int_{T_1}^{T_2} k_{eq}(T)\,dT = P_{heater}\frac{L}{S}$$

where L and S are geometrical parameters. The value of this equivalent thermal conductivity at 4.2K is 720 times lower than that of the Nb used for the tests (RRR=270).

Furthermore, by introducing k_{eq} in the simulation model, the resulting temperature distribution is very close to the measured values (Fig. 3). Moreover, the Nb critical temperature is reached at the extremity of the inner conductor for a heater power of 60mW inducing a temperature difference across the flanges of 6.2K.

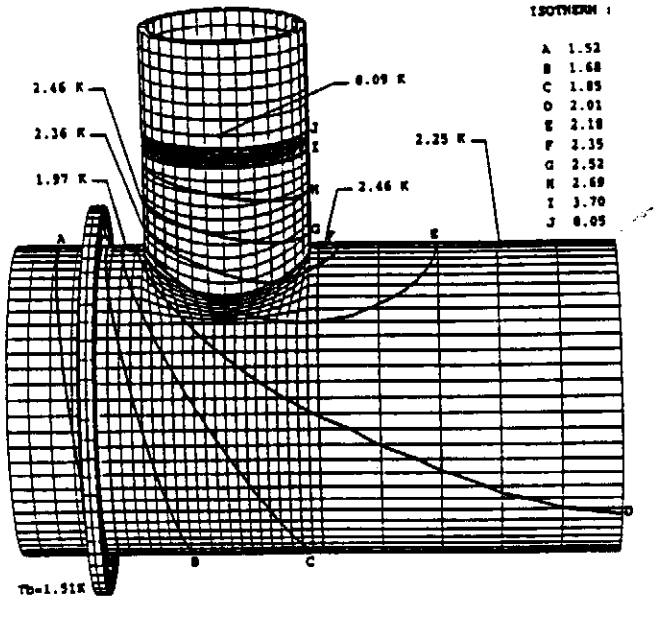

Fig. 3 : measured and computed temperature distributions for a heater power of 46mW

Consequently the thermal breakdown of the coupler will be mainly controlled by this thermal contact resistance, and only a small gain on power capability (<10%) is obtained by using a loop made of sputtered niobium onto a copper substrate.

3. RESULTS OF THE RF TESTS

A. Without thermal shunt

Preliminary tests were performed without any thermal shunt in cw mode. Various configurations were used : different loop geometries (cylindrical and bean shaped capacitor), different construction materials (bulk Nb, Nb/Cu) and/or different tunings ($2.10^{10}<Qex_{fund.}<6.10^{12}$). For all these tests, the quench of the coupler occured for cw accelerating fields in the range 11-14 MV/m and was always characterized by the same phenomena (Fig. 4) : Eacc jumps from the maximum field to ~2MV/m at the same incident power, the quality factor drops from $\sim 10^{10}$ to $\sim 10^{9}$, the $Qex_{fund.}$ of the coupler decreases by ~30%, the maximum temperature measured during the RF test reaches values higher than 20K.

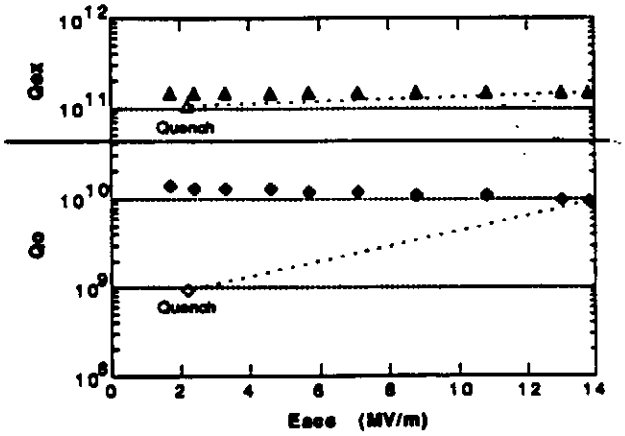

Fig. 4 : Qo and Qex versus Eacc for a Nb HOM coupler without thermal shunt.
(Solid symbols : values before the coupler quench
Open symbols : values after the coupler quench).

From the test corresponding to Fig. 4, it is possible to evaluate the dissipated power of the HOM after the quench. Before the quench at a field of 2.1 MV/m the Qo value gives a dissipated power in the cavity of 31mW (all the other dissipations are neglected at this very low field). After the quench of the HOM coupler and for the same field, the Qo value is about ten times lower, leading to a dissipated power in the coupler of 430mW. The dissipating area is the region where the magnetic field is highest, *i.e.* the extremity of the loop. At this location, from the dissipated power and the value of the magnetic field, one can deduce a surface resistance of 5.3mΩ which is consistent with the measured temperature of 26K. Once the quench of the coupler is reached (Tmax ~ 25K), about 3 minutes are needed for recovering the s.c. state with a maximum temperature lower than 4K. It is worthwhile noting that even without thermal shunt, the quench of the coupler, which occurs at 14 MV/m in cw mode, will occur at a much higher field for the TESLA pulsed mode (2% d.c.). For example, the thermal breakdown was observed at 20.7 MV/m for a duty cycle of 40 %. However, since the coupler could be

exposed to intense field conditions if the cavity has to be processed in-situ with pulsed peak power, and in order to increase the safety margin in normal operation, a thermal shunt linking the upper stub to the LHe-vessel was added.

B. With thermal shunt

In order to by-pass the gasket, the stub of the HOM coupler was connected to the LHe tank by a thermal shunt (standard braided copper wires). The test with this arrangement was limited by a quench of the cavity at 21 MV/m, but up to this value the coupler did not show any anormal behaviour (Fig. 5).

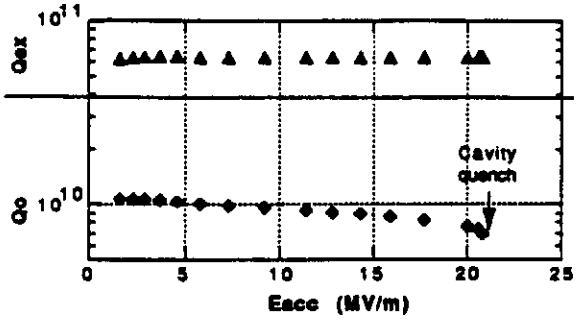

Fig. 5 : Qo=f(Eacc) (Nb HOM with thermal shunt)

With a LHe bath temperature of 1.65K, the maximum temperature measured around the coupler (Fig. 6) is 4.06 K at the maximum field level. A test in pulsed mode with 18.6% duty cycle at the same field level (21 MV/m) showed oscillations of the maximum temperature between 1.94K and 2.22K, consistent with the curve of Fig. 6 obtained in cw mode if one considers the average squared field ($= E_{acc}^2 \cdot d.c.$). Using the calibration test assembly, the heater power needed to reach the Nb critical temperature was 285mW (as compared to 60mW without the thermal shunt).

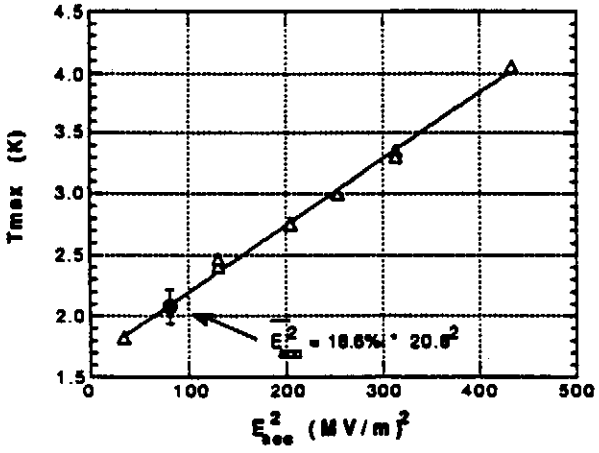

Fig. 6 : Maximum temperature measured in cw mode (triangles) and in pulsed mode (dot).
(Linear fit : $T_{max} = 1.65 + 5.47\,10^{-3}\,E_{acc}^2$)

In addition, the coupler was tested with the TESLA beam pulse (10Hz, 0.8ms) and a detuned filter to simulate the peak power which could be induced by resonantly excited HOMs. A peak power of 1.75 kW, higher than the expected HOM power which could be extracted in the worst case, was transmitted before reaching the anormal heating of the coupler. The hotest point during this test was located close to the N-SMA transition at the RF output of the coupler.

4. MULTIPACTOR AND FIELD EMISSION

No multipactor was detected with the final coupler whose filter capacitor is made of the end of the straight cylindrical inner conductor and the outer conductor. However, the multipactor was clearly identified with a coupler whose capacitor IC is bean shaped. Taking into account the capacitor gap variation due to a concentricity default between the bean shaped IC and the outer conductor, multipactor is expected to occur theoretically in the Eacc range 1.6-2.2MV/m. This is consistent with our observations among which : the high temperature values for Eacc = 1.8MV/m, the random strong and fast temperature increases in the vicinity of the capacitor during the field rise or fall of some pulses for 13.2MV/m (the maximum temperature is measured at this location while it is measured in front of the stub without multipactor), and the electronic current measured at the RF output of the coupler.

For each test, the computed and measured temperature distributions are in good agreement for all the thermometers excepted those located on the uncooled beam tube (systematically higher than the computed values by 0.3 K to 1.0K depending on Eacc). The emitted electrons from the cavity could dissipate a power of up to 1 W on the beam tube if we assume typical values for the involved parameters (electron kinetic energy, e$^-$ current, ...). This additional heat load could explain the observed discrepancy.

5. CONCLUSION

The thermal behaviour of the demountable coupler has been still enhanced thanks to a thermal shunt. A cw accelerating field of 21 MV/m, limited by a cavity quench, was then reached. The maximum temperature measured in front of the stub is 4.0 K at this field level, and decreases to 2.1 K with a duty cycle of 18.6 %. The coupler should then operate with an important safety margin with TESLA parameters (1.4% d.c. and 25 MV/m). Moreover, the test with a detuned filter and the TESLA beam pulse showed that the coupler could handle a RF power of 1.75kW, higher than the maximum power extracted from HOMs when they are resonantly excited by the beam.

6. REFERENCES

[1] Sekutowitcz, "HOM coupler for TESLA ", 6th Workshop on RF Suprconductivity, CEBAF, 1993

[2] M. Fouaidy et al., "Thermal study of HOM couplers for s.c. RF cavities". IEEE Part. Acc. Conf., Washington D.C., 05/1993.

[3] A. Mosnier, "Developments of HOM couplers for superconducting cavities", 4th Workshop on RF Superconductivity, Tsukuba, 1989.

A High Charge Injector for the TESLA Test Facility

B. M. Dunham* and M. Jablonka
DAPNIA/SEA, CE Saclay
91191 Gif/Yvette Cedex, France

Abstract

Several possible models for a high charge injector for the TESLA Test Facility (TTF) have been studied. The injector is required to produce 5×10^{10} e$^-$/bunch with a pulse length of σ_z = 1 mm during a macropulse length of 800 μs and a duty cycle of 1%. Two possible schemes are discussed, one starting with a 250 kV thermionic gun and a second starting with a 500 kV DC photocathode gun. The thermionic case requires initial bunching using two subharmonic cavities, while the photocathode gun solution does not. It is demonstrated that a short, normal conducting buncher operating a ~5 MV/m can then efficiently preaccelerate the beam. It is finally accelerated through a 9-cell superconducting capture cavity and compressed to the required bunch length using a chicane-type magnetic buncher. Simulations of the entire injector for both cases show that the needed bunch length can be obtained with a final emittance of $\sim 50\ \pi$ mm mrad.

1 INTRODUCTION

The Tesla Test Facility (TTF), presently under construction at DESY, requires an injector able to produce not only very high charge (5×10^{10} e$^-$), but also very short bunches (σ_z = 1 mm). A number of such injectors are already in existence or in the planning stages [2, 3]. Direct application of one of these injectors for the TTF injector would be difficult, however, as TTF requires a requires a long macropulse (1 ms) and a high duty cycle (1%). For this reason a simpler injector (injector #1) has been built first [1], delivering the same macropulse current (8 mA) but in 216 MHz bunches instead of the 1 MHz bunches for the high charge injector. It will consist of a 250 kV gun and a 216 MHz buncher injecting directly into a 9-cell superconducting (SC) cavity powered by a separate 250 kW klystron. The high charge specification will only be achieved by injector #2.

*present address: CEBAF, 12000 Jefferson Ave, Newport News, VA 23606

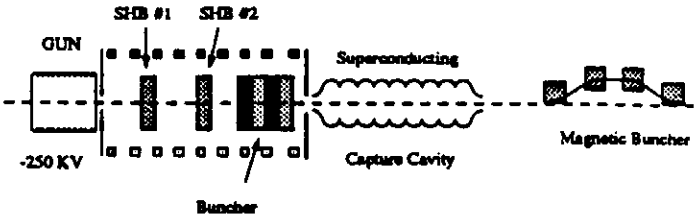

Figure 1: A schematic of the injector model using a thermionic gun.

An RF gun is a possible solution for injector #2, but the required photocathode, laser system and rf cavity would be pushing the limits of the present state of the art due to the high duty cycle and long pulse length. We have proposed to study a conventional scheme, using also a thermoionic gun and 2 subharmonic prebunchers, which is the topic of this paper. A model using a DC photocathode gun has also been studied. Simulations with PARMELA [4] are presented and the use of PARMELA is discussed.

2 INJECTOR MODELS

2.1 *Thermionic Gun Model*

A schematic diagram of the injector is shown in figure 1. A model for using a thermionic gun was inspired by a design for the NLC injector described by R. Miller [5]. The gun is assumed to operate at 250 kV and emit 5×10^{10} e^- in a rectangular pulse 350 ps wide. A gun with similar properties, 170 kV and 2×10^{10} e^- in 350 ps FWHM (700 ps FW), has been reported [6]. Initial bunching is performed by two 650 MHz subharmonic bunchers (separated by ~50 cm).

For high charge injectors it is necessary to immerse the beam (from the gun on) in a continuous solenoidal field to counteract the huge space charge forces. As this is not possible to do with a SC capture cavity, it is proposed to pre-accelerate and bunch the beam using a 4-cell, $\beta = 1$ normal conducting (NC) buncher. Assuming a shunt impedance of 50 MΩ/m and a total length of ~50 cm, 250 kW of power is required to ob-

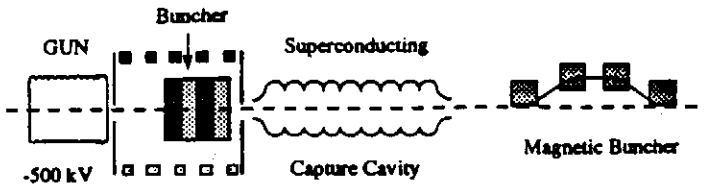

Figure 2: A schematic of the injector model using a photocathode gun.

tain an accelerating field of 5 MV/m. This is the same value as is required to power the SC capture cavity for the low charge injector for TTF, so an identical klystron and modulator could be used. This buncher is located 25 cm after the second subharmonic cavity.

After the NC buncher, it is planned to use the 9-cell SC capture cavity of the low charge injector to boost the beam energy. The distance between the NC and SC cavities should be as short as possible, and the length surrounded by a solenoidal field. To obtain the desired final bunch length, the accelerated beam is further compressed using a chicane-type magnetic buncher (MB).

A basic chicane-type magnetic buncher is a relatively simple achromatic system, requiring only four identical rectangular bending magnets. The path length variation of the MB can be adjusted by changing the bend angle to match the phase-energy correlation of the beam from the RF bunching system. The MB in these simulations uses dipole magnets 15 cm long with bend angles of $\sim 30°$ for an overall length of ~1.2 m and a resulting $R_{56} = -.17$ cm/%.

2.2 *Photocathode Gun Model*

Figure 2 shows an alternative model using a high-voltage DC photocathode gun as an electron source. This is not exactly an off-the-shelf item, but it has properties which are interesting enough to warrant an investigation. Such a gun is now under construction at CEBAF [7] for use as an injector for their FEL project, and is designed to produce 0.12 nC, 100 ps bunches at 500 keV using a GaAs photocathode. Simulations show [8] that it is capable of producing the 8 nC bunches needed here with an emittance of 30 π (all emittances are normalized, rms values with units of mm–mr) and a beam radius (diverging) of 2.6 cm.

The ability to generate 100 ps bunches obviates the need for subharmonic bunching, and allows direct injection into the NC capture section. This feature makes the injector much more compact and reduces the number of components in the beamline. In addition, since the gun needs only a 500 kV DC power supply (commercially available) for operation, a complicated and space consuming modulator is not required. Some disadvantages are the need for semiconductor photocathode processing techniques, as well as an expensive laser system.

3 BEAM DYNAMICS

3.1 *Introduction*

The space charge forces on the macroparticles in PARMELA are calculated in the usual fashion by superimposing a 2-D cylindrically symmetric mesh over the particle distribution in the rest frame of the bunch and determining the fields due to the particles in the bins. This method has the advantage of running quickly, but there are many free parameters to set so one must carefully check output variations with changes in these parameters.

Since the bunch length changes dramatically during the bunching process, it is important to vary the total mesh length in the longitudinal direction as the bunch compresses. We have introduced a routine in PARMELA to automatically do this. Using this adaptive meshing method gives convergent results for the final emittance using the smallest number of bins (25) compared to requiring over 50 bins for convergence when the initial mesh length is not varied (see [9] for complete details of this and of all the simulations described in this report). This is important to know as one wants to use as few bins as possible in order to speed up execution. The meshing in the radial direction is not as important as the radial beam dimensions do not vary so dramatically.

In these simulations, PARMELA hard edge solenoids are used to model the magnetic field along the beamline and the subharmonic bunchers are represented using a zero-length, ideal buncher with a sinusoidal field. The normal-conducting buncher is described using the internal field values provided in PARMELA for a 1300 MHz Los Alamos side-coupled structure. The accelerating field for the entire 9-cell SC cavity is calculated using URMEL and a Fourier transform of the fields is included in a separate subroutine.

3.2 *Thermionic Model Results*

Figure 3 shows the radial and phase variation and emittance growth of the beam for the thermoionic injector model. The bunch is compressed by a factor of $\sim$ 30 to reach a final bunch length of $\sigma_z = 1.4°$

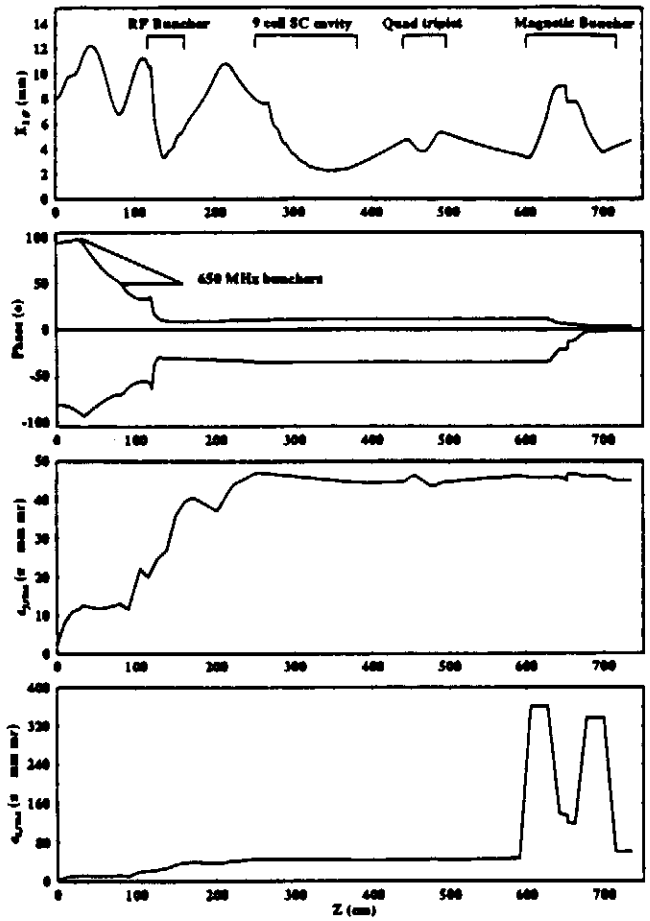

Figure 3: The top figure shows the 2-σ beam envelop for the horizontal plane and the second figure shows the phase compression envelop. The bottom two figures show the emittance growth in the vertical and horizontal planes.

at an energy of 16 MeV. The emittance grows by a factor of 12 to 45 π in the vertical plane, and to 65 π in the horizontal plane after passing through the MB. Without space charge the horizontal emittance explodes in the bending region, but cancels out at the end of the achromatic magnetic buncher system. With space charge the dispersion is no longer suppressed and a net emittance growth results. All of the parameters were optimized to keep the emittance growth as small as possible while obtaining a good phase compression.

3.3 Photocathode Gun Model Results

The plots for the photocathode gun model are similar to those for the thermionic model and are not shown here (see [9]). In this case, it was possible to reach a final bunch length $\sigma_z = 2.2°$ without using a MB by phasing both the NC buncher and the SC cavity off crest. The resulting emittance is high (75 π), though, and the energy is low (13 MeV). By varying the phases, it is possible to obtain a beam with an energy of 16 MeV and an emittance of 60 π, but a MB is required.

4 CONCLUSION

From the simulations performed here, one can conclude that an injector can be built that will fulfill the requirements for a high charge injector for the TESLA Test Facility. Such an injector would consist of an electron gun (either thermionic of photocathode), two subharmonic bunchers (not necessary for the photocathode gun), a 4-cell, normal conducting buncher, a 9-cell superconducting structure, and a magnetic buncher. The exact details of the models depend very strongly on the actual properties of the electron gun to be used. For future simulations, the model should include the measured parameters of an existing gun, as well as more realistic characterizations of the the elements of the injector. Effects such as wakefields, beam loading, and instabilities have not been included.

5 REFERENCES

[1] "The TESLA Test Facility Linac Injector", these conference proceedings.

[2] A. Yeremian *et al.*, Proc. 1989 Particle Accelerator Conference, 657 (1989).

[3] S. Takeda *et al.*, IEEE Trans. Nucl. Sci., **NS-32**, 3219 (1985).

[4] K. Crandall and L. Young, private communication.

[5] R.H. Miller, presented at the TESLA collaboration meeting, Fermilab, 1993.

[6] H. Matsumoto *et al.*, Proc. 1992 Linear Accelerator Conference, 296 (1992).

[7] C.K. Sinclair, Nucl. Instr. and Meth. **A318**, 410 (1992).

[8] D. Engwall, private communication.

[9] B.M. Dunham and M. Jablonka, Technical Note CE-Saclay, DAPNIA/SEA 94-05.

Beam performances of MACSE, the Saclay superconducting test accelerator

M. Jablonka, J.M. Joly, M. Boloré, J.P. Charrier, B. Dunham[1], J. Fusellier, M. Juillard, D. Roudier
CEA,DSM/DAPNIA/Service d'Etudes des Accélérateurs
CE SACLAY, F- 91191 Gif/Yvette Cedex, France

Abstract

MACSE is a short superconducting electron linac operated at Saclay[1], to study the problems of acceleration with S.C. cavities. Main beam characteristics like transverse and longitudinal emittances have been measured after the injection line, after the capture cavity and after the main cryomodule. Results are given, discussed and compared to predicted values. Measurement apparatus and methods are described.

1. INTRODUCTION

Over the past 3 years, most of MACSE operationnal time has been devoted to RF experiments with the S.C. cavities, that constituted the main part of its goal. Producing and measuring an electron beam was also, of course, an aspect of the projected experimental program. Beam specifications had been oriented to study the problems of a future machine for nuclear physics : Main nominal parameters are 100 μA and 100% duty cycle. The program of the beam experiments therefore consisted, first to demonstrate the capability of delivering such a beam, in reproducible and stable conditions, then to measure its main characteristics.

2. BEAM MONITORING OVERVIEW

From the beam monitoring point of view, MACSE presents 3 regions : the 100 keV injection beam forming line that precedes the capture cavity; the 2 MeV transfer and analyzing beamline between the capture cavity and the main cryomodule; the high energy (capable of 20 MeV) transport and analyzing beamline. The latter is a long line (~20m), comprising 4 triplets, which transports the beam in a separate room (to avoid radioactivity near the accelerator) where the dipole and the beam dump are located.

These energy variations do not justify different design of the monitoring devices.

For setting up the beam, a pulsed regime has been defined : The pulse length (3 μs) is much shorter than the cavities filling time, so that low level RF loops do not see it, and the repetition rate (25 Hz) is low enough so that the beam can hit any place, as long as necessary, without damage. 25 Hz being half the network frequency, it permits to measure beam parameters free of residual ripple. A synchronous but non 50 Hz submultiple frequency (24.39 Hz) is also available to allow observation of residual ripple at low beam power.

The beam intensity monitoring is performed by toroids transformers. In D.C. beam regime, they still can be used thanks to 3 μs, 3000 Hz "notches" that are made in the beam intensity control signal of the electron gun. These toroids also are in charge of the beam loss monitoring by mean of differential measurement between the begining and the end of the operated beam line.

Beam centering is performed in using viewing screens (made of Cr doped Al_2O3). In the injector beamline, isolated collimators also give a convenient information. At the entrance and the exit of the cryomodules we have installed non isolated collimators that can produce a centering signal thanks to X-ray sensitive photodiodes [2] placed outside the beam tube. This device permitted an ultimate centering of the beam when D.C tests were carried out.

Beam profiles are made with wire scanners that translate an L shaped, 30 μm carbon wire across the beam. They are driven by a stepping motor, at low speed if the pulsed regime is used and at higher speed (40 mm/s) in D.C regime. The control is made through a dedicated VME crate and the signals can be displayed and interpreted on the screen of the control room work station (Fig 1).

These monitors are installed both on straight beam lines for emittance measurements and on deviated ones for energy spread measurement.

3. D.C BEAM TESTS

We have obtained hours of stable run at 100 μA after careful centering of the beam and also careful setting of the beam loss monitoring and interlocking. One injector collimator had to be redesigned to improve its cooling : We had observed a slow evolution of the intercepted current that was attributed to a local dilatation under the beam impact.

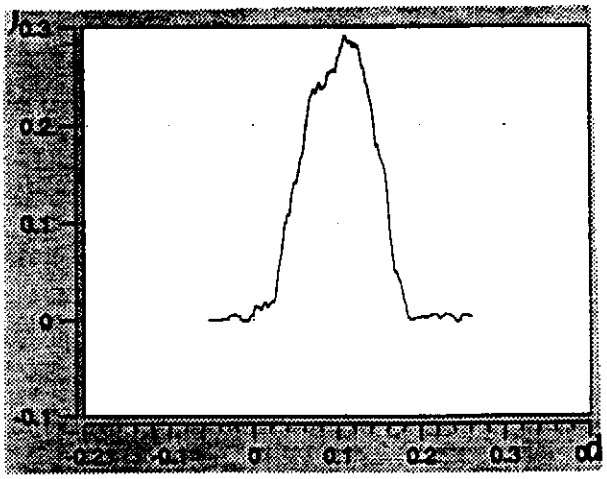

Figure 1 Beam energy spectrum at 12.2 MeV, (σE=7 keV) obtained from a wire scanner (horizontal scale in %)

1- Present adress : CEBAF, Newport News, VA, USA.

4. EMITTANCE MEASUREMENTS

In all emittance measurements we have used a multigradient method, i.e. a lens or a triplet force was varied and the beam size measured some distance away in correlation. The calculation then is made in using the method described in [3] when a solenoidal was used (fig. 2). As a D.C. beam could easily burn a hole, only a 40 μA peak, pulsed current has been measured.

Following results give the quantity $4\beta\gamma\varepsilon_{rms}$.

100 keV station : The measurement has been made on the chopped beam. We have found 1.1 π.mm.mrad. The maximum emittance is defined upstream by 2 collimators at 1.3. We can therefore say that the cancellation of transverse deflections by the 2 cavities of the chopping system, following the scheme developped for the NIST micrtron [4] worked quite well.

2 MeV station : We have found an emittance of 2.4 π.mm.mrad, i.e rougily twice the input emittance This is a disappointing result with respect to the 20% maximum increase predicted by Parmela simulations [5]. New and careful measurements should permit to understand this difference that we can for now share between beam misalignment and measurement errors.

High energy station: Measurements have been made with a beam energy of 12.2 MeV. We have found 4.7 π.mm.mrad, i.e., again, a doubling between the input and the output of the 4 cavity cryomodule,.that may have the same causes.

5.ENERGY SPREAD

After the capture cavity, the energy is about 2 MeV. Energy spread (Fig. 2) is optimized by RF phases and amplitudes of the prebunching and capture cavities. Typical measured σE is 7 keV i.e. twice the predicted value.

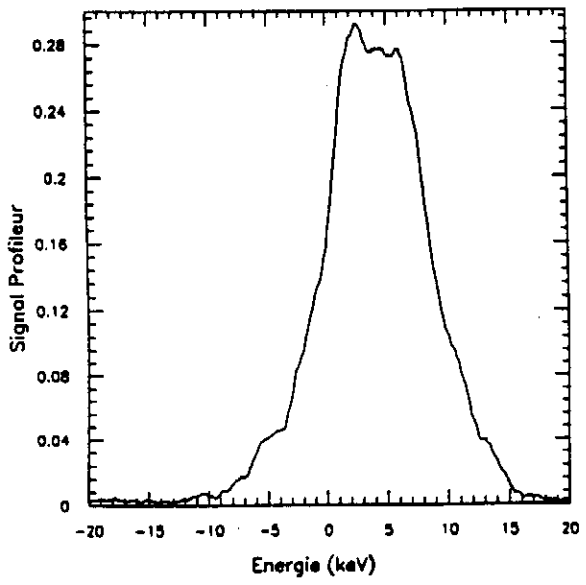

Figure 2 Energy spectrum after the capture cavity. Beam energy is 1.94 MeV. σE=7 keV.

At the high energy station, measurements at 12 MeV, in pulsed regime, for a 40 mA peak current, gave also σE= 7 keV. Increase of energy dispersion due to a finite bunch length is in fact negligible.

6. BUNCH LENGTH

We have not installed any direct bunch length monitor. Instead we have used the very classical "backphasing" method [6]. For the experiment, the 3 first cavities of the main cryomodule (out of 4) were used. The capture cavity and the 2 first cavities accelerated the beam to 8.31 MeV. The 3rd cavity was attenuated to contribute by only 0.46 Mev when phased. Its phase was then shifted by +90° and -90°. Both corresponding energy profiles were recorded. The bunch angular length can then be calculated by :

$$\Theta_{bunch} = \left| \frac{\Delta E_{+90} - \Delta E_{-90}}{2 E_{cav3}} \right|$$

where $\Delta E_{+/-90}$ are the total energy spreads, E_{cav3} is the energy contribution of cavity 3.

We have measured ΔE_{+90}=30.1keV and ΔE_{-90}=10.9keV, hence Θ = 1.2° which is close enough to the expected 1°. The measurement was made very unpractical because of the necessary retuning of the long transport line to the analyzing magnet whenever phases were shifted by a large amount.

7. OTR BEAM PROFILE

Using optical transition radiation for analyzing electron beams profile is a very promissive technique. We have demonstrated its suitability for our low energy, low intensity beam : The radiator was made of a polished stainless steel plate. The pulsed beam frequency was pushed up to 250 Hz. In using a 10^{-4} lux S.I.T. camera, built by Sofretec (France) we have obtained quite satisfactory images. Beam profiles were very conveniently extracted in using the image processing software Laserlab, on a P.C.(fig. 3)

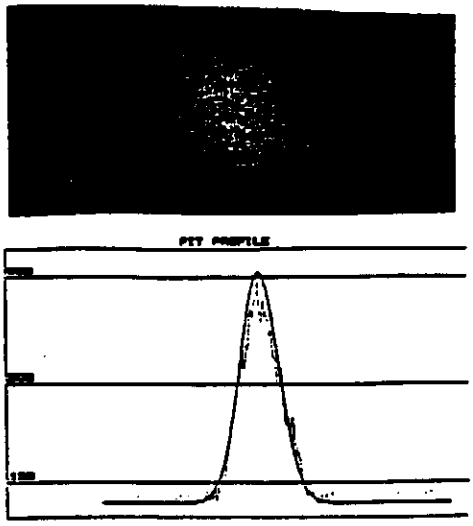

Figure 3 Beam image from optical transition radiation. Below, gaussian fit of the tranverse horizontal profile.

8. NEXT PROGRAM

Our group is now involved in the TESLA collaboration and participates in the construction of TTF (Tesla Test Facility) at DESY. MACSE has permitted to test schemes of pulsed feeding of the cavities under Lorentz forces detuning [7] : A 8 MV/m gradient in a MACSE cavity causes the same relative detuning (with respect to its bandwidth) as will be experienced by the 9-cell TTF cavities at 15 MV/m.

To complete this work, experiments with beam will be soon undertaken : In removing the emittance limiting collimators of the 100 keV line, beam intensity can be raised to 2 mA. 1 ms pulses will be generated. The goal is to reach 100% beam loading, as in TTF design, and to test it.

9. CONCLUSION

Though too few operationnal sessions have been available for these experiments, we conclude that MACSE beam specifications have been achieved. Beam monitors and the computer control system have proven quite a good efficiency. If energy spread and bunch length measurements have been found in sufficient agreement with computer predictions, too a big emittance growth has been observed. MACSE has also proven to be a useful tool for various experiments that were not in its initial program.

8. REFERENCES

[1] "MACSE: Accelerating Electrons at Saclay with Superconducting Cavities", Ph. Leconte, B. Aune et al., Proc. of the 1990 Lin. Acc. Conf..

"First Operation of MACSE the Saclay Pilot Superconducting Electron Linac", B. Aune et al., Proc. of the 1991 P. A. C., 2393.

[2] "Le rayonnement X-gamma dans les cavités supraconductrices", J. Arianer, J. Fusellier, J.M. Joly, G. Lagarde, M. Poitevin, NOTE SFEC T-38, (1989)

[3] "A device for electron gun emittance measurement", B.Aune, M. Jablonka, J.M. Joly, 1985 P.A.C proc., 1896.

[4] "NBS-LANL RTM Injector installation", M.A. Wilson et al., IEEE Trans. Nucl. Sc., NS-30, (1983), 3021.

[5] "The MACSE Injector", B. Aune, M. Jablonka, E. Klein, Proc. of 2nd EPAC (1990), 1246.

[6] "Measurements of the SLAC injector emittance", R.H. Miller, Proc. 1966 Linac Conf., 65.

[7] "Field Stabilization in a Superconducting Cavity Powered in Pulsed Mode", A. Mosnier, J.M. Tessier, These proceedings.

Achieving the TESLA Gradient of 25 MV/m in Multicell Structures at 1.3 Ghz[1]

C. Crawford[2], J. Graber[3], T. Hays, J. Kirchgessner, A. Matheissen[3], W-D. Moller[3], H. Padamsee, M. Pekeler[3], P. Schmuser and M. Tigner.

Laboratory of Nuclear Studies, Cornell University, Ithaca, NY 14853

Abstract

The challenges for the SRF approach to linear colliders are to achieve gradients of 25 MV/m or higher, and to reduce the cost of the structures, cryostats and peripheral devices, like couplers. We present here a breakthrough in the gradient goal. Using advanced preparation and processing techinques, three half-meter long units at the TESLA RF frequency of 1.3 GHz have achieved accelerating gradients between 25 - 28 MV/m.

1. INTRODUCTION

The present state of the art in superconducting cavities as well as the technological aspects of RF superconductivity discussed here are reviewed in Ref. [1]. There are two major field limiting mechanisms operative: thermal breakdown and field emission. A proven approach to avoid thermal breakdown is to raise the thermal conductivity of Nb by purification, which involves removal of interstitially dissolved impurities: oxygen, nitrogen, carbon and hydrogen. A convenient way to characterize the purity and thermal conductivity is the residual resistivity ratio (RRR). The RRR of sheet Nb delivered by industry today is about 300 and can be further improved by a factor of two (or more) by solid state gettering removal of the major impurity, oxygen.

Microparticle contaminants, most often micron and submicron size foreign particles of a conductive nature, are the culprits responsible for field emission. Increased vigilance in cleanliness during chemical etching, rinsing and assembly procedures has kept field emission under control up to the level Eacc = 10 MV/m. There are several new efforts underway to further improve cleanliness, such as UHV heat treatment[2], high pressure water rinsing[3] etc. There is evidence to show that with these clean treatments, emitter density is reduced[2].

While these efforts at supercleanliness have the potential to improve cavity performance, there are areas of concern. As is often observed, a single field emission site in an accelerating unit can limit the maximum field level, if this emitter will not "process" away. There is always some probability, high for large area cavities, that one or more such emitters will find their way on to the cavity surface. This shortcoming is especially clear in the light of the experience of all laboratories that there is a 20 - 25% decrease in the performance between the acceptance (or vertical cryostat) tests and the in-tunnel test results. It is also clear that due to the random nature of contamination, cavities with a large surface area show field emission limitation at lower fields.

Therefore a technique that processes (eliminates) emitters in-situ is highly desirable. Besides increasing the performance of a cavity prepared by existing cleaning techniques, such a technique would be effective against accidental contamination of the cavity in an accelerator, or during assembly of couplers and other components into a pre-cleaned cavity. Such a technique would also help to reduce the large spread typical in the performance of cavities.

A technique with just these desirable features has recently been demonstrated[4]. By applying High Pulsed RF Power (HPP) to 3 GHz superconducting cavities, emitters have been processed and operating field levels raised. With power levels between 5 and 150 kwatts, and pulse lengths between 5 msec and 1 msec, the CW operating field levels for several 1-cell, 2-cell and 9-cell cavities were raised consistently over a series of 25 separate tests. For example, in the 8 separate tests on 9-cell cavities, CW accelerating field levels improved from 8 - 16 MV/m before HPP to 15-20 MV/m after HPP. The HPP technique was also demonstrated to recover high gradient performance after delibertately introducing field emitting contaminants through cold and warm vacuum accidents.

The present level of understanding that has emerged from these studies is that, as the field is raised, the strongest emitters put out so much field emission current that a micro-discharge (RF spark) takes place, and the ensuing explosive event destroys (processes) the field limiting emitter. When the field level is raised further, the next strong emitters process, and so on. The essential idea of using high power pulses is to raise the surface field as high as possible. The processing is effective even if the fields reach high values for times as short as μsecs, because spark formation times are < μsec[5].

The goal of the present study is apply the HPP technique to multi-cell cavities at the TESLA RF frequency of 1.3 GHz.

2. NIOBIUM ACCELERATING STRUCTURES

Two 5-cell, 1.3 GHz cavities were purchased from industry (Cavities #1 and #2) and two 5-cell cavities were built at Cornell (Cavities #3 and #4). The important properties of the accelerating mode are listed in Table 1. During construction, one of the Cornell-built cavities (#4) had a weld hole which had to be repaired, but the repair was not very successful as judged from the premature thermal breakdown field. Results from this cavity will be omitted. Figure 1 shows one of the 5-cell cavities as it is set up for chemical treatment.

Table 1
Accelerating Mode Properties of the 5-cell, 1.3 GHz Cavities

Property	Industry Built	Cornell Built
R/Q(Ohm/m)	1012	1088
Epk/Eacc	2.5	2.0
Hpk/Eacc	41	43

[1] Supported by the NSF with Supplementary Support from the U.S.-Japan Co-Operative Agreement.

[2] Visiting scientist for Fermilab, Batavia, Illinois

[3] Visiting scientist from DESY, Hamburg, Germany

Presented at EPAC LONDON - 1994

Figure 1: 5-cell niobium accelerating section set up for HPP

The starting sheet material for all cavities had a RRR = 250 - 300. After prelimnary RF tests, during which thermal breakdown limited the performance at Eacc < 14 MV/m, cavities #1 and #3 were further purified by solid state gettering. Both the inside and outside surfaces were exposed to Ti vapors at 1400 C. After RRR improvement, both the inside and outside surfaces were chemically etched to remove the Ti rich layers. Previous tests with samples treated in the same way have shown that the RRR improves to 500 - 600. The titanium diffuses into the bulk to the order of 100 μm, requiring removal of a comparable thickness of material by chemical etching, which was carried out.

3. HIGH POWER SOURCE AND TEST STAND

The high power klystron and modulator system available were capable of providing a maximum of 1 Mwatt of power at a pulse length of 150 μsec. The design of the high power test set-up is shown in Figure 2 We had to overcome several difficulties with the high power test stand before we could transmit 1 Mwatt of incident power to the cavity. After diagnosing and remedying these problems we could raise the power to 1.2 Mwatt without significant delays associated with the conditioning of the coupler.

5. FIVE-CELL TEST RESULTS

As mentioned, two of the cavities (#1 and #3) had their RRR improved by solid state gettering. Before RRR improvement,these cavities were limited by thermal breakdown

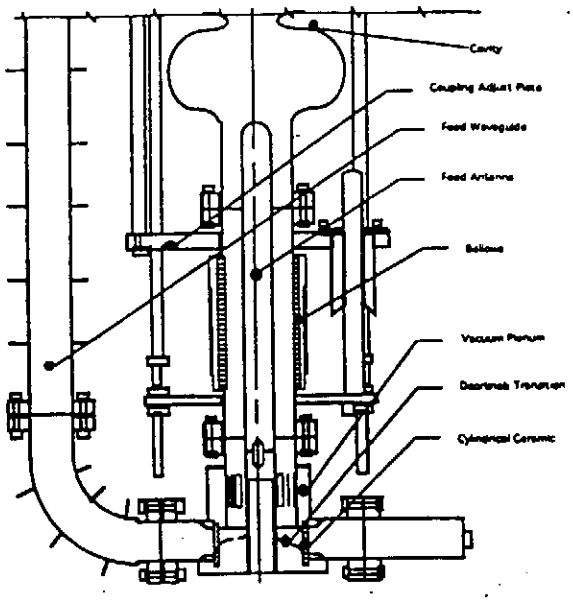

Figure 2: Schematic of High Pulsed Power RF test stand for 1.3 GHz cavities.

during CW operation at Eacc =14 MV/m (#1) and Eacc = 12.5 MV/m (#3). Cavity #2 did not show a low field breakdown and its RRR has therefore not yet been enhanced. As we shall discuss below, after RRR improvement the maximum CW field in our cavities improved to Eacc = 28 MV/m (#1, limited by field emission) and Eacc = 27 MV/m (#3, limited by thermal breakdown). Therefore the RRR improvement increased the field by a factor of 2 or more.

Figures 3 a-c show the performance of each of the three five cell cavities before and after HPP to process field emission. In these tests, before the application of HPP, the CW gradient for all three cavities was limited by field emission. In two cases the Q_0 had dropped substantially at Eacc = 10 MV/m, and in one case at Eacc = 22 MV/m. The spread in field emission limited performance is typical for the etching, rinsing and preparation techniques now in vogue.

In all three cavities, after HPP with 1 Mwatt of power, the field emission was substantially suppressed, so the maximum CW accelerating gradients reached were 27, 28 and 28 MV/m, all above the TESLA goal of 25 MV/m. During the pulsed processing stage, the surface electric fields reached were between 85 - 90 MV/m. After HPP at 1 Mwatt, the CW performances of cavities #1 and #2 were ultimately limited by field emission. Because of field emission loading, cavity #1 was limited by available CW RF power, and cavity #2 was limited by the radiation level safety trip point. The CW performance of cavity #3 was finally limited by thermal breakdown.

Our results show that the RRR improvement was effective in removing the thermal breakdown limitation of 12-14 MV/m level. Even if cavities are limited by field emission to CW Eacc =10 MV/m, they can be improved to Eacc = 28 MV/m with HPP. Therefore the HPP technique provides a way to reduce the spread in performance typical of field emission limited cavities.

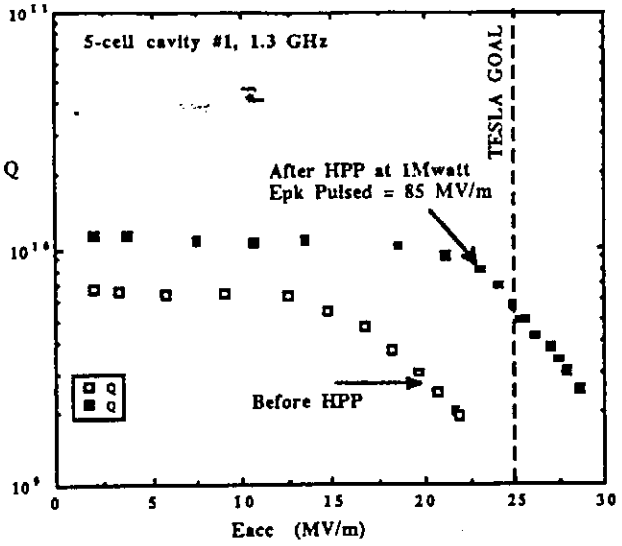

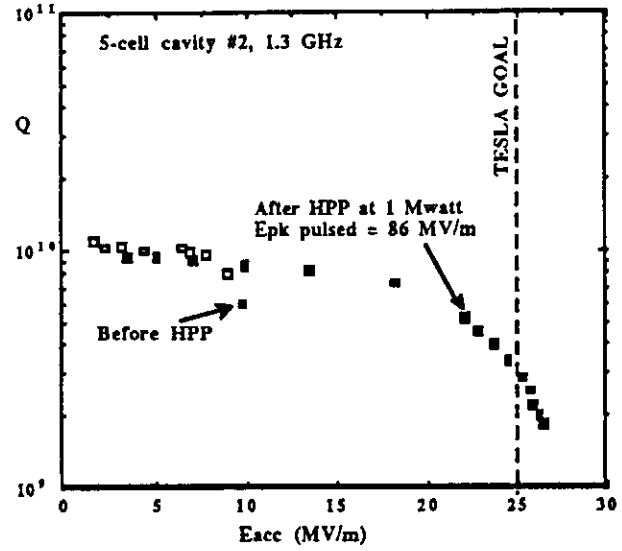

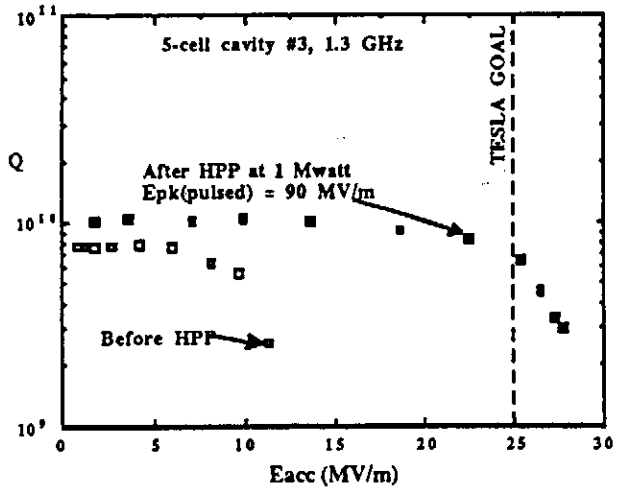

Figure 3: RF test results on 5-cell, 1.3 GHz cavities before (open squares) and after (filled squares) HPP.

Our results for the effectiveness of HPP are very consistent with 3 GHz HPP experiments. We find as before [4] that the most important parameter for successful processing of field emission is the value of the surface field reached during the pulsed conditioning stage. To demonstrate this we plot in Figure 4 the results from 5-cell 1.3 GHz cavities as the maximum CW surface field reached versus the pulsed conditioning field imposed on the RF surface. For both 1.3 GHz as well as for 3 GHz cavities we observe that

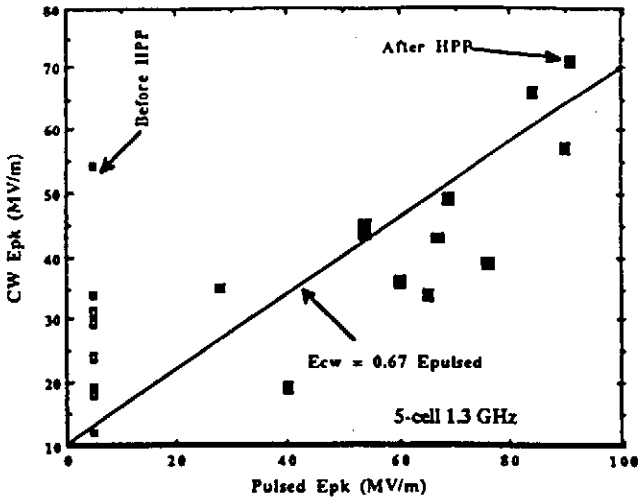

Figure 4: A summary of the benefits of HPP on 1.3 GHz cavities. The open squares are the CW results before HPP and filled squares are results after HPP.

Epk (CW) = (0.6-0.7) x Epk (pulsed).

ACKNOWLEDGEMENTS

We would like to thank our colleagues P. Barnes, D. Moffat and J. Sears for valuable assistance in many stages of this work. We are grateful to Robert Snead, U.S. Army, and to D. Shoffstall, J. Adamski and P. Johnson from Boeing for the loan of the Thompson Klystron. The following Fermilab persons helped in setting up the klystron at Cornell: L. Bartelson and H. Pfeffer. The following Fermilab persons helped with the design and construction of the high power test stand: M. Champion, H. Edwards, K. Koepke, M. Kuchnir, T. Nichols, D. Peterson, and M. Rushman. We also wish to thank Babcock and Wilcox, Lynchburg, Virginia for their excellent effort in building two 5-cell niobium cavities.

REFERENCES

[1] H. Padamsee, K. Shepard and R. Sundelin , Ann. Rev. Nucl. Part. Sci., 43, p.635 (1993).
[2] H. Padamsee et al, Proc. of the 1991 Particle Accelerator Conference, San Francisco, IEEE Cat. No. 91CH 3038-7, p. 2420 (1993).
[3] D. Proch, Proc. of the 1993 Particle Accelerator Conference, Washington, DC, IEEE Cat. No. 3279-7, p. 758 (1993).
[4] J. Graber et al, Proc. of the 1993 Particle Accelerator Conference, Washington, DC, IEEE Cat. No. 3279-7, p. 886 (1993).
[5] G.A. Mesyats, IEEE Trans. Electrical Insulation, EI-18, 218 (1983) and B. Juttner, IEEE Trans. Plasma Science, PS-15,474 (1987)

THE TESLA TEST FACILITY STATUS REPORT

R. Bacher, H. Edwards and H. Weise
for the TESLA Collaboration
Deutsches Elektronen-Synchrotron DESY
Notkestraße 85, 22603 Hamburg, Germany

Abstract

The TESLA Test Facility and Linac, under construction at DESY by an international collaboration is an R&D test bed for the superconducting cavity variant of the TeV scale future linear colliders. The TTF will include capability for processing and measurement of 1.3 GHz superconducting accelerating structures, the cryogenics, power, diagnostics, injector, and other support system appropriate to implementing a 500 MeV test Linac. The main body of the TTF Linac will consist of four cryomodules, each containing eight 1 meter nine-cell cavities. The base accelerating goal is 15 MV/m. Two injectors are planned, both with an average pulse current of 8 mA. The first (less demanding) will provide the 8 mA with a 216 MHz structure; the second which will be necessary for HOM measurements will need to operate with a bunch charge of 5×10^{10} at 1 MHz for 800 bunches. Beam analysis areas will be provided for study of both injected and high energy output beams. Overview and status of the facility, Linac design, and proposed experiments will be given.

Introduction

Worldwide, there are a number of groups pursuing different linear collider design efforts. The TESLA activity [1] is one of these R&D effords, differing from the others in its choice both of superconducting accelerating structures and of low frequency (L-band, 1.3 GHz; see also [2]). As one of these R&D groups, TESLA plans to have a working prototype test facility in the 1997 time scale which supports the development of an s.c. collider.

The TTF is to be located at DESY, with major components flowing in from the members of the TESLA collaboration. Although it is of highest priority to prove the feasibility of reliably achieving accelerating gradients of 15 MV/m or more, the TTF has also to show that the cavities can be assembled into a Linac test string successfully operated with auxiliary systems to accelerate an electron beam to 500 MeV. Furthermore, different experiments to be carried out on the TTF Linac have been defined and partly outlined in detail now so that the necessary diagnostics can be set up. This covers not only the more typical beam experiments but also the cryogenics and RF measurements that are needed in order to confirm the idea of a superconducting linear collider.

The TTF Linac Program

Although a full comparison of the TTF Linac's parameter with a potential TESLA 500 linear collider [3] can not be carried out here, Tab. 1 lists the most important items.

TABLE 1
TESLA 500 - TTF Linac Parameter Comparison.

Parameter	TESLA 500	TTF Linac
Linac Energy	250 GeV	500 MeV
Accelerating Gradient	25 MV/m	15 MV/m
Quality Factor Q_0	5×10^9	3×10^9
No. of Cryo Modules	many	4
Single Bunch $\Delta E/E$	1.5×10^{-3}	$\approx 10^{-3}$
Bunch to Bunch $\Delta E/E$	10^{-3}	$\approx 5 \times 10^{-3}$
Beam Current	8 mA	8 mA
Macro Pulse Length	0.8 ms	0.8 ms
Injection Energy	10 GeV	10-15 MeV
Lattice β	66 m	12 m
Bunch Rep. Frequency	1 MHz	216 / 1 MHz
Bunch Population	5×10^{10}	$0.023 / 5 \times 10^{10}$
Bunch Length, rms	1 mm	1 mm
Emittances $\gamma \sigma^2/\beta$	20, 1 µm	5 µm
Beam Size, Injection	260, 60 µm	1.7 mm
Beam Size, End of Linac	50, 12 µm	0.25 mm

The time structure of the beam, i. e. bunch frequency, bunch separation, and bunch length as well as the number of particles per bunch depends on the injector. The two injectors planned for the TTF will provide the macro pulse current, length and repetition rate planned for TESLA 500; one will provide the design bunch charge. Beam sizes intended for TESLA 500 with 10 GeV injection will not be realized in the TTF Linac.

Nevertheless, there are a number of respects in which TESLA 500 and the TTF Linac are sufficiently similar, so that the TTF Linac experience will feed directly into the TESLA 500 design. Some aspects of the full scale linear collider can be checked at the TTF Linac, others may be difficult or impossible to check.

What the TTF Linac does check is the achieved gradient [4] including High Peak Power processing [5], the cavity construction and processing techniques [6], and the design of input and HOM couplers. The RF control of multi-cavity systems will be developed and tested under real conditions (Lorentz force detuning, microphonics) [7]. The vacuum failure recovery potential can be studied and a cryostat design [6,8] can be tested under cryogenic operation. The possibility of dark current is of interest as well as an energy and position feedback system. Alignment and its stability [9] can be checked using position monitors and BPM systems [10]. A first iteration on projected system costs should be possible.

Measurements of Q_0 and HOM (both by calorimetric method) are not easy but appear possible. HOM and wake field

measurements require the high bunch charge of injector II. Transverse wake measurements are possible with the beam far of axis [11]. Cavity alignment measurements via wake fields will be attempted but may prove difficult. The schedule for injector II will be critical for much of this program. The TTF Linac program will not check out the sensitivity needed for TESLA 500 such as vibration sensitivity and emittance growth.

The TTF Linac

The TTF Linac, as it is shown in Fig. 1 with injector I, consists of a 250 keV room temperature injection, a short superconducting Linac followed by a 15 MeV beam analysis area and an optics matching system, the Linac itself consisting of four cryomodules with eight cavities each, and the 500 MeV beam analysis area.

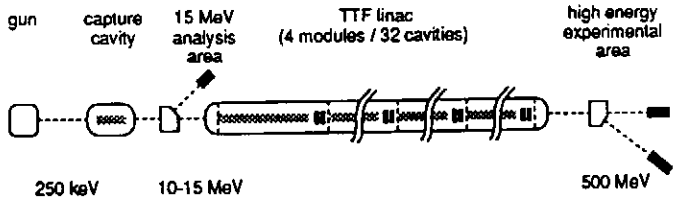

Fig. 1: Schematic layout of the TTF Linac. The overall length of the installation at DESY amounts to ≈85 m; the drawing is not to scale.

Injector

Two injectors are planned for the TTF Linac. The first, injector I, is intended to be relatively straight forward in design to provide the TESLA design current, but not the large bunch spacing of 1 μs and rather intense bunches (5×10^{10} electrons). In its initial form, injector I [12] will operate with the parameters as shown in Tab. 1, first column TTF Linac. The second, injector II, is intended to provide the TESLA 500 bunch spacing and intensity. Here a design based on a laser driven photo cathode is considered and first designs are on the way. Nevertheless, neither of the two injectors will have the transverse emittance ratio of TESLA 500 which is not required for the TTF program.

The warm part of injector I starts with a grid controlled thermionic gun as the source; the anode voltage is 40 kV. The produced bunches ($2.3 \times 10^8 e^-$ in 50 deg at 216.7 MHz) are injected into a 1 m long electrostatic preacceleration tube and accelerated to 250 keV. Bunch compression is performed by means of a 6th subharmonic buncher cavity (SHB). From the 250 keV energy then one standard 1 m long nine-cell TESLA cavity finally increases the electron beam energy to above 10 MeV.

This accelerating structure has a crucial influence on the beam quality at the end of the injector. As a standing wave, $\beta = 1$ cavity it has three major impacts on the beam optics. At first, the large leakage field, which the injected electrons see in the beam tube in front of the first cell, acts as a decelerating field. Second, the low velocity of the 250 keV ($\beta = 0.74$) electrons results in a phase slippage in the first cell. The consequence is an energy modulation but fortunately also a further bunch compression. And third, the field of a standing wave cavity has a strong focusing influence on the transverse dimensions of the electron beam [13]. A complete simulation has been carried out using the tracking code PARMELA. This calculation also takes the space charge effects into account. The accelerated electron beam can be studied in the low energy beam analysis area behind the injection Linac. Transverse and longitudinal phase space volume and orientation will be measured. Therefore several diagnostic stations are used together with a focusing quadrupole triplet and an energy analyzing dipole magnet.

Linac Beam Optics

The already above mentioned first quadrupole triplet will be used together with a second triplet to allow the matching of the beam to the optics lattice along the Linac. This lattice along the TTF Linac consists of four cells, each having a superconducting quadrupole doublet and a beam position monitor at the end of a string of 8 s.c. cavities. Due to the mentioned rf-focusing the matching to the first cell of the lattice is strongly disturbed. Nevertheless, detailed beam optic calculations achieved a perfect matching with a β-function equal to the cell length of ≈12 m (module length) and provide 90 deg phase advance per cell.

Starting with this β-function at the end of the Linac, the acceleratedd electron beam (now 500 MeV) has to be transported through the high energy beam analysis area to the beam dumps. One more quadrupole doublet will be used together with the last superconducting one in order to optimize both beam emittance and in a dispersive section energy spread measurements. Further quadrupole doublets in the two straight sections behind the analyzing magnet increase the β-function by at least two orders of magnitude before stopping the beam in two separate dumps.

The Linac Module

Each of the four Linac modules houses 8 s.c. cavities of the TESLA type [6], which is an approx. 1 m long 9-cell stiffened π-mode standing wave structure operating at 1.3 GHz. The cavities are assembled as a string. They have an input coupler and a HOM coupler at one end and only a HOM coupler at the other end of each. This string is followed by a beam position monitor [10] and a s.c. quadrupole doublet whose beam tube acts as an additional HOM absorber. Each quadrupole has correction coils which can be used as steering

coils and for the compensation of potential quadrupole vibrations.

Every s.c. cavity has its own helium vessel and the whole string is supported by a long helium gas return pipe. Operating temperature is 1.8 K; at an unloaded quality factor of $Q_0 = 3 \times 10^9$ the estimated heat load for the four TTF Linac modules is approximately 60/60/500 W at 2/4.5/70 K. The first module will be equipped with a large number of temperature sensors and two vibration detectors per cavity. Input and HOM couplers as well as rf windows will have rf pickups. Alignment during cool down will be monitored.

The rf power source, one 5 MW klystron for 16 s.c. cavities and therefore one half of the TTF Linac, has been already commissioned [14]. The necessary macro pulse repetition rate of 10 Hz at pulse lengths of 2 ms is available at the desired power. At present, tests of warm components of the rf distribution such as rf windows and circulators are made.

500 MeV Experimental Area

The high energy beam analysis area is located behind the last crymodule and its terminating end cap. It serves as a room to measure the relevant beam parameters, i.e. beam position, beam size and emittance, beam energy and spread, beam current and transmission through the Linac, bunch length and shape. Some parameters will be measured as a function of the bunch number in the 800 μs bunch train, others as an average over some part of it or for a series of trains. In a first step standard beam diagnostics (wire scanners, screens and striplines) will be used while commissioning the TTF Linac. The extensive use of OTR screens is foreseen. Space fo[7] testing new diagnostic tools developed for TESLA also will beco provided. Two beam dumps complete the whole TTF Linac scLo up.

First Results and Outlook

At present the commissioning of the TTF infrastructure i. e. a chemical etching facility, a high pressure rinsing station and a preparation area / clean room [15] is almost finished. Two prototype test cavities have been used to commission the cavity processing. After a chemical etching and a high pressure rinsing (≈100 bar) both cavities (RRR = 250) had excellent quality factors at low fields ($Q_0 = 3 - 5 \times 10^{10}$). In preliminary results one cavity reached a cw field gradient of 16 MV/m (at $Q_0 = 2 \times 10^{10}$) while the other one was limited close to 10 MV/m (at a clearly reduced $Q_0 \approx 3 \times 10^9$). Both cavities are limited by quench events. High peak power processing could flaten out the Q_0 vs. E behaviour of one of the two cavities.

The first six s.c. cavities, planned for TTF cryomodules and equipped with real input and HOM couplers, will be at DESY this summer so that the processing of it can start soon. The assembly of 8 cavities as a string is scheduled for early 1995 and the first cold test for late spring. The injector I assembly starts at Saclay in the beginning of next year. After successful tests it will be delivered to DESY to allow beam tests with the first cryomodule before the end of 1995.

References

[1] The Tesla R&D effort (TESLA = TeV Energy Superconducting Linear Accelerator) is being carried out by an international collaboration. A number of institutions have joined the collaboration and include IHEP Beijing, TU Berlin, CEN Saclay, CERN, Cornell, TH Darmstadt, DESY, TU Dresden, Fermilab, Univ. Frankfurt, INFN Frascati-Milano-Rom, KFK Karlsruhe, LAL Orsay, IPN Orsay, SEFT Finland, UCLA, Univ. Wuppertal.

[2] R. Brinkmann, Low Frequency Linear Colliders, invited talk, EPAC 1994, London, to be printed.

[3] H. T. Edwards, TESLA Parameter Update - A Progress Report on the TESLA Collider Design, 6th RF Supercond. Workshop 1993, CEBAF; to be published in Part. Acc.

[4] T. Hays et al., Achieving the TESLA Gradient of 25 MV/m in Multicell Structures at 1.3 GHz, EPAC 1994, London, to be printed.

[5] H. Padamsee, Review of Various Approaches and Successes for High Gradients and Q's for TESLA, 6th RF Supercond. Workshop 1993, CEBAF; to be published in Part. Acc.

[6] M. Champion, B. Dwersteg, A. Gamp, H. Kaiser, B. Petersen, D. Proch, J. Sekutowicz, S.Tazzari, diff. contributions to the 6th RF Supercond. Workshop 1993, CEBAF; to be printed as workshop proc., ed R. Sundelin.

[7] S. Chel et al., Field Stabilization in a Superconducting Cavity Powered in Pulsed Mode, EPAC 1994, London, to be printed.

[8] G. Horlitz et al., A 1.8 k Test Facility for Superconducting RF cavities, to be published in Adv. in Cryogen. Eng., Plenum Press, Vol. 39, New York, 1993.

[9] A. Mosnier, Proc. of the Linear Coll. Workshop LC92, Garmisch, ed. R. Settles, ECFA 93-154 (1993).

[10] R. Lorenz, Test Results on a Beam Position Monitor Prototype for the TTF, EPAC 1994, London, to be printed.

[11] B. Aune, A. Mosnier, Experimental Program with Beam in the TESLA Test Facility, this conference.

[12] M. Bernard et al., The TESLA Test Facility Injector, EPAC 1994, London, to be printed.

[13] J. Rosenzweig, L. Serafini, Transverse Particle Motion in Radio-Frequency Linear Accelerators, to be published in Phys. Rev. E.

[14] H. Pfeffer et al., A Long Pulse Modulator for Reduced Size and Cost, to be printed in Proc. 21st Intern. Power Modulator Symposium, June 27-30, 1994, Costa Mesa, CA, USA

[15] M. Leenen, The Infrastructure for the TESLA Test Facility (TTF) - A Status Report, EPAC 1994, London, to be printed.

Experimental Program with Beam in TESLA Test Facility

Alban Mosnier, Bernard Aune
CEA, DSM/DAPNIA/Service d'Etudes d'Accélérateurs
CE-SACLAY, 91191 Gif/Yvette , France

Abstract

In order to establish a technical basis for a high energy e^+e^- collider using the superconducting RF technology, the test of a string of 32 cavities with beam at an accelerating gradient of 15 MV/m is planned in an installation at DESY [1]. Several experiments with beam in TTF will be performed, first with a low charge injector (40 pC, 216 MHz) then with a full charge one (8 nC, 1 MHz). The dissipated HOM power at helium temperature is a key issue for TESLA, its estimation requires careful calorimetric measurements and the full charge injector. Bunch wake potentials can be estimated with bunch charges of at least 1 to 2 nC. Multibunch measurements require a beam of a few hundreds of these bunches. The beam will be injected either on axis or off axis. RF steering due to couplers will be estimated by measuring the beam displacement for different RF phase settings. The expected resolution is well below the TESLA specification. The acceleration of dark currents will be observed for different settings of the focusing elements.

1. RF to beam power transfer

The beam energy stability will be carefully studied, along a beam pulse and from pulse to pulse. The bunch to bunch chromatic effects in the TESLA linac must be less important than the single-bunch ones. Lorentz forces detuning and microphonics [2] are the main sources of energy spread along the bunch train. An RF feedback system should guarantee a constant acceleration during the 800 μs beam pulse. The monitoring of energy and energy spread during the pulse, at time intervals of 1 μs, will be performed using a BPM and a profile monitor in the analyzing station. All these informations can be collected with the low charge injector.

2. Beam power deposition at 2 K

The loss factor due to the longitudinal higher modes has been evaluted to about 8.5 V/pC/cavity for a bunchlength of σ_z=1mm. For the TESLA bunch charge of 8 nC and the bunch rep rate of 8 kHz, the HOM power deposited by the beam is then 4.35 W per cavity. The low frequency part (up to 5 GHz) of this HOM power will be mainly extracted by the HOM couplers and has been estimated to about 30 %. In order to limit the cryogenic load, special HOM absorbers (at 70 K) are located at the end of each 8-cavity module. They are expected to dissipate 90% of the remaining power. The table 1 below gives the distribution of HOM power, together with the static and dynamic heat load at 2 K, for comparison.

A correct evaluation of the 2 K power deposition requires a high charge beam and a resolution of a few tenths of a watt in the cryogenic heat measurement.

HOM-couplers	10.4
70 K absorbers	22
HOM at 2 K	2.4
Static load at 2 K	2.8
RF load at 2 K	11.6

Table 1 : Heat loads (W) for one 8-cavity module

3. Cavity offset

The alignment tolerances on the quadrupoles (0.1 mm) and cavities (0.5 mm) in TESLA are not too tight in comparison with other room-temperature linear collider proposals. The final components displacements in the real cryostat environment will be carefully checked in the TTF linac. It is planned to monitor the motion of the inner components during cool-down, operation and warm-up by means of optical targets. In addition, the individual cavity offsets of one module can be measured by detecting with a spectrum analyser the dipole HOM power, excited by the beam assumed on-axis, coming from the HOM couplers. Due to the large bunch spacing, an harmonic of the beam spectrum is always close enough to a dipole mode frequency to give rise to resonant build-up of fields. Taking the TM_{110} mode (1875 MHz) of highest impedance and assuming the beam can be steered close enough to the centerline, cavity offset measurements with resolution better than 10 μm, would be possible. A beam of about one hundred full charge bunches is sufficient to make this measurement. The power induced on the longitudinal modes, including the fundamental, is harmless.

4. Bunch wake potentials

The knowledge of the short-range wakefields is of outstanding importance for the estimation of the emittance growth in the TESLA linac. These quantities are not easily computable for short bunches and will be carefully studied with the high charge injector. The beam will be observed either after the first module, with all 8 cavities non powered, or after the entire TTF linac operating at low gradient (about 5 MV/m). The former alternative assumes that the next modules have been removed to give way to beam monitors.

The longitudinal wake will be estimated by measuring the energy profiles for different bunch charges. Simulations show an energy spread of 0.5% for a charge of 1.6 nC after the first module and 0.7% for 8 nC after the entire linac. The plot 1 shows the correlated energy profile for 8 nC and acceleration through the linac at 5 MV/m.

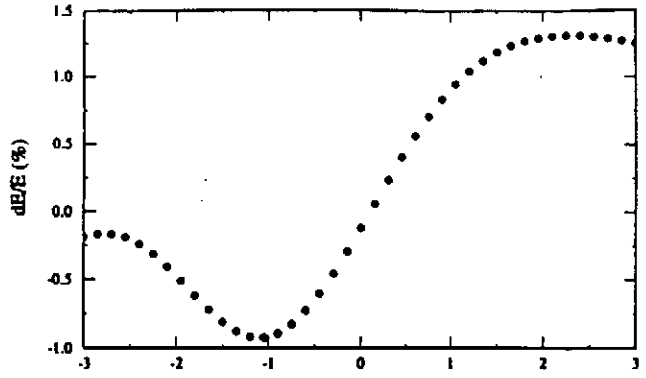

Figure 1 : Correlated energy profile at the exit of the linac (N=5.10^{10})

The dipole wakefield will be studied by injecting the beam 10 mm off-axis. When the beam is observed at the exit of the whole linac, the planned focusing scheme with quadrupole doublets providing a phase advance of 90° per module cancels out the wakefields effects. A weaker focusing with a phase advance of 30° per module is much more convenient in this case. Figure 2 shows the head (dotted line) and the tail (solid line) of a bunch injected 10 mm off-axis through the TTF linac with an accelerating gradient of 5 MV/m. The trajectory of the head is kept constant by means of steerers located at the quadrupoles. Owing to this weak focusing, both trajectories diverge clearly, almost 5 mm, at the exit of the linac. The focusing effect of the SW structures can be seen in the low energy part. The plot 3 shows the corresponding transverse profile of the bunch.

After the traversal of first idle module, a head-tail displacement of 5 mm is obtained with a bunch centroid displacement of 1.5 mm, which can be measured by means of the BPM located at the end of the module.

The energy profile and the transverse profile of the bunch will be best measured by means of a streak-camera associated with OTR located on the spectrometer and straight-ahead beam lines.

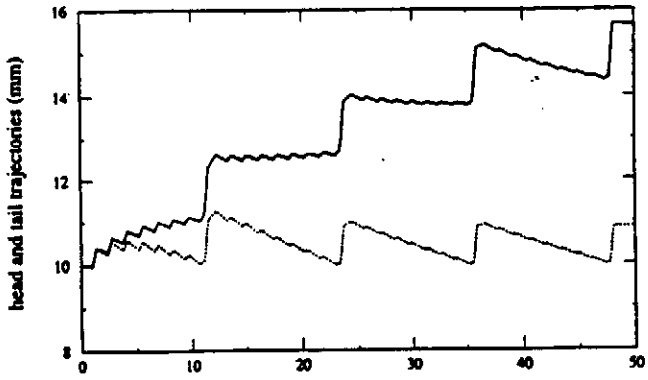

Figure 2 : Head and tail trajectories with 10 mm offset and weak focusing (N=10^{10})

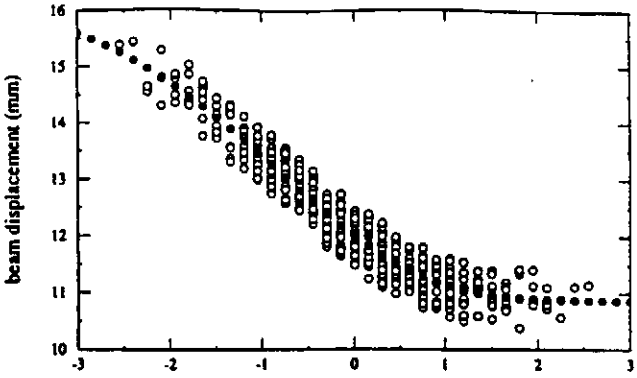

Figure 3 : Transverse profile with 10 mm offset at the exit of the TTF linac (N=10^{10})

5. Multi-bunch Beam Breakup

The Beam Breakup phenomenon, caused by the long-range wakefields, is controlled in the TESLA linac through a mode damping combined with a large bunch spacing on the one hand and the natural cavity to cavity mode detuning on the other hand. The multi-bunch effects in the TTF linac will be however very weak, even with a beam travelling through all the cavities operating at low field level. The beam will be injected 10 mm off-axis into the first non-powered 8-cavity module and the position of the bunches will be observed at the BPM located at the end of the module. The bottom curve of the figure 4 shows a weak bunch displacement, once the steady-state is achieved. Ten dipole modes were used with an rms frequency spread of 1 MHz. A rms cavity offset of 0.5 mm was assumed. Each mode can be then studied individually by tuning the cavities to the resonant excitation $F_{res} = nF_b(1 \pm 1/2Q)$. The tuning system can be actuated because the cavities are not powered. The middle and the upper curves show the bunch displacements when two and four cavities, respectively, are tuned to the resonant condition for a TM_{110} mode, giving final relative displacements of 2.5 and 5 mm for the bunch population of 10^{10}. Due to the rapid build up of the steady-state, a beam of about two hundred bunches per pulse with a bunch charge of 1 to 2 nC is sufficient for this experiment.

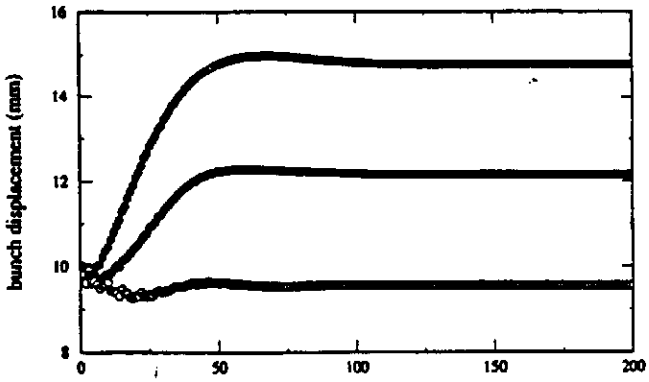

Figure 4 : Bunch displacement with 10 mm offset at the 8-cavity module exit (N=10^{10})

6. RF steering

Radial asymmetries in the rf fields in the accelerating structures deflect the beam transversely. The static deflections of the beam centroid and the variations in the deflections due to field jitters from pulse to pulse can be compensated for by the dipole magnets and the fast kickers in the linac. Their contribution to emittance dilution through wakefield and chromatic effects will be small. Due to the finite bunch length, however, the rf kicks vary during the passage of a bunch, causing a tilt to the beam, driven by the out-of-phase rf component [3]. The main sources of rf deflections in TESLA are the input and HOM couplers. By varying the rf phase of one TTF module and monitoring the change in the beam position before the focusing magnets at the end of the module, the strength and the phase of the rf deflection can be inferred with a resolution below the TESLA tolerance (0.1 mrad). These experiments can be carried out with the low charge injector Figure 5 shows the expected BPM reading when the rf phase of the third module is varied, assuming a rf kick of 10 keV/c per cavity, without (solid circles) and with (empty circles) the effect of a random cavity tilt of 1 mrad.

The effect will be more sensitive at the low energy end of the TTF linac, but the rf focusing effects of the accelerating structures are stronger and must be taken into account.

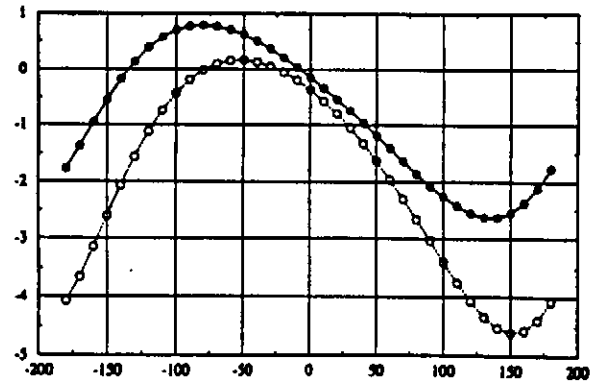

Figure 5 : Beam displacement (mm) for a rf phase variation (deg) of the 3rd module

7. Dark current

Field emission currents can be easily captured in the TESLA linac operating at 25 MV/m and 1.3 GHz. Instead of being accelerated over the full length of the linac, forming a halo to the beam and finally causing a significant backgroung problem to the interaction region, this dark current will be intercepted along the machine by the low energy acceptance of the focusing optics. Figure 6 plots the field emitted beam in transverse phase space after acceleration through a second cavity. The potential emitters were disclosed by a sweeping of the first cavity surface and of the rf phase.

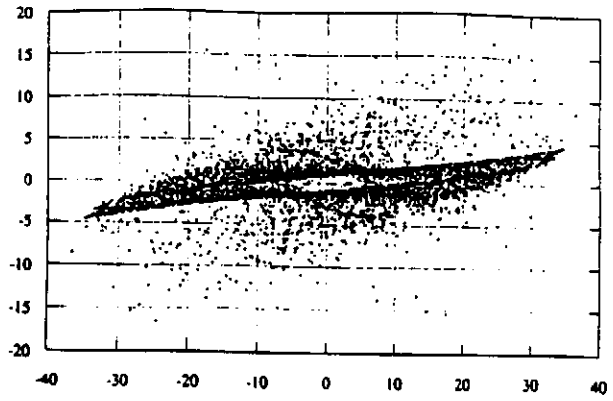

Figure 6: Field emission beam in transverse phase space (mm*mrad) after a 2nd cavity

This dark current has then be tracked through the TESLA linac,with usual components misalignments, the one-to-one correction, and induced wakes from the main bunches. The figure 7 shows the amount of particles lost along the machine, assuming that the current, formed by 10000 particles, was emitted from the first cavity of the linac after the DR (worst case). Most of the particles are lost in the first quadrupoles and the last particle after five FODO cells. In the TTF linac, 40% to 70% of the current emitted by the first cavity can be transmitted, depending on the quadrupole setting. These transmitted field emission currents will be measured at the end-station and scintillation counters will be placed at the critical points to measure the expelled current.

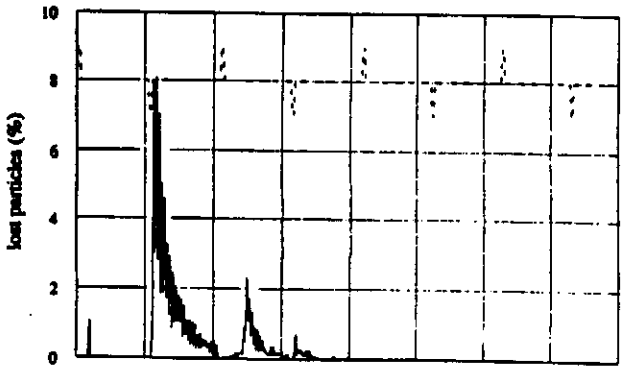

Figure 7 : Amount of particles in % lost along the TESLA linac

8. References

[1] H. Weise, for the TESLA collaboration, "The TESLA Test Facility (TTF)", *Proc. of 4th European Part. Accel. Conf., London, 1994.*

[2] A. Mosnier and J.-M. Tessier, "Field Stabilization in a Superconducting Cavity Powered in Pulsed Mode", *Proc. of 4th European Part. Accel. Conf., London, 1994.*

[3] J. T. Seeman, "Effects of RF deflections on Beam Dynamics in Linear Colliders", *Part. Accel., 1990, Vol. 30, pp. 73-78.*

Final Focus System with Superconducting Magnets in the Interaction Region of the TESLA Linear Collider

Etienne KLEIN, Olivier NAPOLY and Jean Michel RIFFLET
CEA, DSM/DAPNIA
CE-Saclay, F-91191 Gif-sur-Yvette Cedex, France

Abstract

The TESLA final focus system is presented for a center of mass energy of 500 GeV. The effect of magnets misalignment and field errors is analyzed for this system using the recently available program FFADA. A design for the last doublet superconducting quadrupoles, based on the LHC quadrupoles, is proposed. Tolerances to higher multipole components in the last doublet have been analyzed as well as the effect of the detector solenoid.

1 INTRODUCTION

The basic idea of the TESLA design for 500 GeVcenter of mass energy is that the high luminosity is obtained with moderate beam spot sizes, 1μm×64nm, at the interaction point (IP), as compared with other linear collider designs, and with a very high beam current. Hence the beta-functions at the IP are larger than in any other designs. This, together with the expected relative energy definition of the beam, eases the design of the final focus optics. This advantage is balanced by the difficulty to clear the spent beam power and the secondary background (synchrotron radiation and beamstrahlung photons, e^+-e^- pairs and hadronic jets). It is also used to offer a 6 meter long free space around the IP to design the detector and the interaction region (IR).

Another specific property of TESLA is the large 1μs separation of the bunches. It offers the possibility to collide the beams head-on and to separate them outside of the detector. In order to clear all the debris of the collision on axis through the IR, it is necessary to use superconducting magnets with a large enough aperture and gradient. If iron-free, these magnets need not be shielded by compensating solenoids to operate in the field of the detector solenoid. This allows a significant reduction in transverse dimension and weigth of the last doublets.

We present a version of the TESLA final focus system (FFS) adapted to the latest set of beam parameters for 500 GeVcenter of mass energy. This new version obeys the same general principles as the preceding one [1] but has been reduced in length down to 370 m. The total bandwidth of the order of 1.8% has been obtained by optimizing the beam demagnifications achieved in the first and final telescopes. The properties of this new system have been investigated by using the program FFADA [2]. In particular, the beam collimation requirements are calculated, the effect of magnet misalignment and field errors are analyzed and tolerances derived. A design for the superconducting magnets of the last doublet is proposed. It is based on the LHC magnet prototypes [3] which recently achieved 250 T/m with a physical aperture diameter of 48 mm [4]. Their higher multipole components are tolerable and a superimposed detector solenoid field requires a skew-quad correction.

2 BEAM AND OPTICS PARAMETERS

The beam parameters for the 500 GeVcm energy version of TESLA are as follows :

Energy	[GeV]	:	250.
Horizontal RMS at the IP	[nm]	:	1000.
Vertical RMS at the IP	[nm]	:	64.
Horizontal normalized emittance	[m]	:	2.0e-5
Vertical normalized emittance	[m]	:	1.0e-6
Longitudinal RMS	[mm]	:	1.0
Bunch population		:	5.0e+10
Repetition rate	[Hz]	:	8.0e+3

With these parameters, the values of the beta-functions at the IP are $\beta_x^* = 24.5$ mm and $\beta_y^* = 2.0$ mm.

The main optics and hardware parameters for the upgraded version of the TESLA FFS are given below :

Total length of the FFS	[m]	:	370.
Total horizontal demagnification		:	68.1
Total vertical demagnification		:	98.6
Parameters of Final Telescope			
Horizontal FT demagnification	XM = -R22	:	8.
Vertical FT demagnification	YM = -R44	:	30.
Length of last drift	[m]	:	3.0
Length of last but one drift	[m]	:	0.35
Polarity of last quadrupole		:	D
Pole-tip field of last doublet quads	[T]	:	6.
Aperture diam. of last doublet quads	[mm]	:	48.

These parameters have been input in the program FFADA [2] to derive the optics of the FFS and analyzed its properties.

3 THE LARGE APERTURE OPTICS

The lattice layout, the beta-functions and the dispersion, calculated with MAD [5], are presented in Fig.1. The momentum bandwidth estimated from the doubling of the beta-functions is ±0.9%. Fig.2 completes the chromatic analysis of the FFS by plotting, from tracking simulation results, the relative dependence of the spot sizes and luminosity on the rms energy spread of bunches with Gaussian energy distributions. It shows that the energy acceptance is limited by the blow-up of the horizontal spot size.

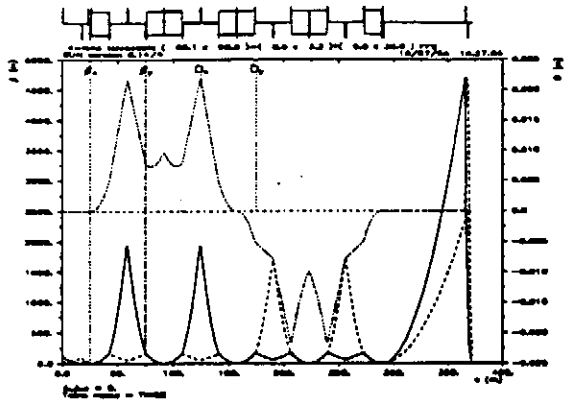

Figure 1: Lattice layout and orbit functions of the FFS.

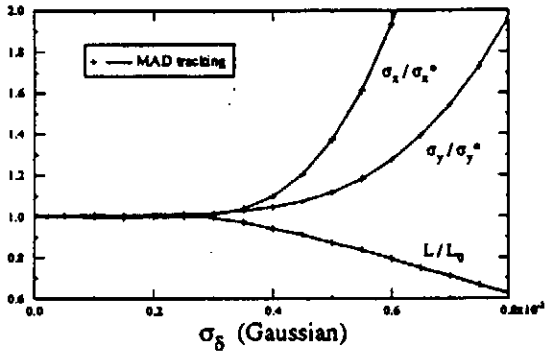

Figure 2: Dependence of the spot sizes and luminosity on the Gaussian rms relative energy spread.

3.1 *Beam collimation*

The main constraint on beam collimation comes from the synchrotron radiation emitted by the incoming beam in the last quadrupole doublet. Requiring that no photon hits the 48 mm circular exit aperture of the opposing doublet leads to the transverse collimation of the beam at $12\sigma_x \times 38\sigma_y$. With these requirements, a 3 cm diameter vertex detector located at the IP is safe from synchrotron radiation.

3.2 *Error analysis and alignment tolerances*

The effect of the 6-D displacements and gradient error of each quadrupole and sextupole of the FFS has been calculated with FFADA [2] in terms of the transverse (position and angular) offsets and dispersions, the longitudinal waist shift, the xy-coupling of the beam at the IP and of the resulting luminosity loss. Figs.3 and 4 show for instance the effect of the transverse displacement of each magnet on the IP beam offset and on the luminosity loss.

The tolerances on the uncorrelated vibrations of both the e^+ and e^- FFS magnets, except the last doublets, are 190 nm horizontal and 48 nm vertical rms, for 2% luminosity loss without beam steering correction (fast vibrations). If the beam relative offset at the IP is corrected (slow vibrations), the luminosity loss is dominated by the spot size growth induced by dispersion, and the tolerances go up to

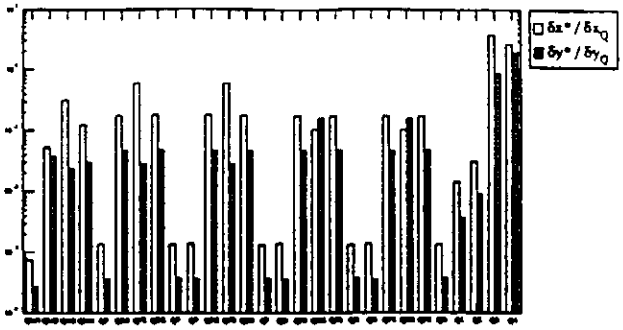

Figure 3: Ratio of IP offset to quadrupole transverse displacement.

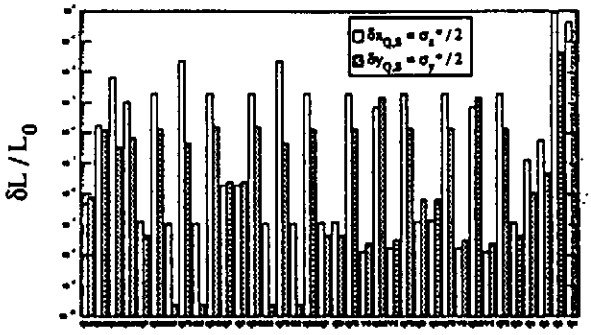

Figure 4: Relative luminosity loss for fixed quadrupole and sextupole displacements.

21 μm hor. and 400 nm vert. rms for a beam with 0.1% relative energy spread.

Tolerances on the transverse displacements of last doublet quadrupoles are essentially unchanged with respect to [1]. Finally, a 2% luminosity loss is induced by the displacement of a common support for the two doublets of about 100 μm horizontally and 20 μm vertically.

4 DESIGN OF THE SC QUADRUPOLE

The required characteristics of the quadrupoles (see Table 1) and the possibility to use superfluid helium lead to consider the prototype of the LHC lattice quadrupole [3] as the basic concept.

Gradient	250 T/m
Inner coil aperture	56 mm
Magnetic length	1.920 m and 1.274 m
Overall current density	560 A/mm^2
Peak field in conductor	7.8 T (Quad alone)
Peak field in conductor	8.4 T (with 3T-Solenoid)
Current	15900 A
inner coil diameter	56 mm
outer coil diameter	108 mm

Table 1: Superconducting Quadrupole Parameters

4.1 *Description*

The cross-section of the quadrupole and cryostat is shown in Fig.5. As compared to the LHC prototype, the iron core is removed to avoid saturation in the 3 T magnetic field of the detector solenoid. Even without the iron core, the transverse stray fields decrease fast enough not to perturb the physics (e.g. $B_y(y=0) = 0.005$ T at $x = 60$ cm).

The conductor is a keystone cable whose bare dimensions are approximately $13.05 \times (1.7 \div 2.16)$. The coils are made of two shells without splice between them. The stainless steel collars are strong enough to cancel the electromagnetic forces. The collaring process consists of setting subsequent pairs of collars in direction perpendicular to each other along the entire coil length. The prestress needed to avoid any motion in the coils during excitation is given by the insertion of eight tapered keys at the outside of the collars. The collared coil is then centered in the helium vessel by mean of four keys. The coil mechanical center is defined by the intersection of the two perpendicular planes of two opposite keys. The helium vessel is a rough tube, machined precisely ($\sim 25\mu$m) to give the correct position of the centering keys. Its thickness is enough to withstand the pressure drop in case of quench and to give the axial rigidity necessary to reduce the magnet sag. Two screens at 4.2 K and 70 K are necessary to intercept the radiations coming from the room temperature vacuum tank. The distances between parts at different temperatures are chosen to be 40 mm. This leads to a weight of about 305 Kg/m.

4.2 *Field Quality*

The magnet harmonic content is parametrized by the coefficients of the relative multipole expansion

$$B_y + iB_x = B(r_0) \sum_{n \geq 2} (b_n + ia_n)(x + iy/r_0)^{n-1}$$

at the reference radius r_0. The beam spot size at the IP is mostly sensitive to the normal and skew sextupolar coefficients b_3 and a_3. Using $r_0 = 1$ cm, a 2% spot size growth is induced by a sextupole error $a_3 = 6.7 \times 10^{-4}$ or $b_3 = 1.8 \times 10^{-3}$, or over 10^{-2} for the higher multipoles. In practice, all b_n and a_n coefficients can easily be made smaller than 7×10^{-4}.

4.3 *Alternative*

Using Nb_3Sn instead of NbTi as superconducting material would lead to one of the following changes:

1. use of 4.2 K helium instead of 1.8 K superfluid helium. This option would permit to remove one screen and to decrease the outer diameter by about 80 mm;
2. work at 1.8 K with the same gradient and increase the magnet aperture since the superconductor can stand at a higher magnetic field;
3. work at 1.8 K with the same aperture and increase the gradient.

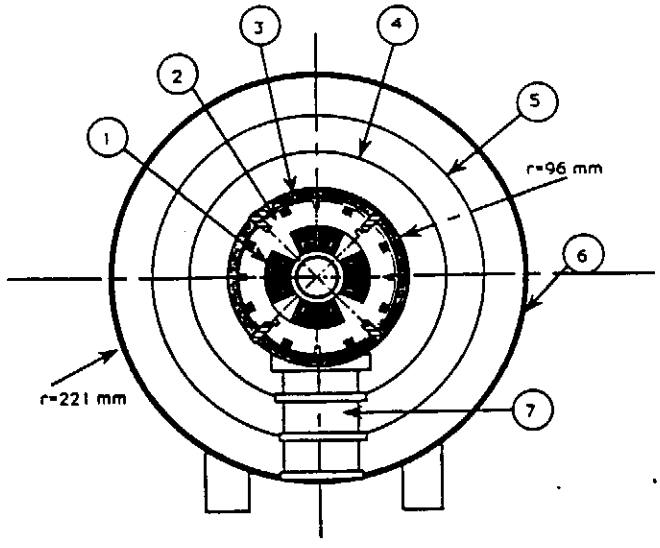

1 Coils, 2 Stainless steel collars, 3 Inertia tube, 4 Screen @ 4.2 K, 5 Screen @ 70 K, 6 vacuum tank, 7 Support

Figure 5: Quadrupole cross-section.

Although these options are attractive, the Nb_3Sn technology is not yet well mastered: it would lead to challenging R&D work and to a modified design since the mechanics and the quench protection in particular would be more constraining.

4.4 *Effect of the Main Solenoid*

Operating the iron-free quadrupole in a longitudinal solenoid field of 3 T shifts the operating point to about 90% of the critical field. Increasing the safety margin can be achieved either by progress to come on the maximum current sustained in SC cables or by reducing the focusing gradient of about 10%. Opticswise, the detector solenoid field is harmless as long as it does not extend, even partially, over the last doublet and superimposes over the quadrupole field. It then induces a blow up of the horizontal and vertical beam spot sizes at the IP. However this effect can be compensated completely with one skew quadrupole in front of the solenoid [6].

5 REFERENCES

[1] O. Napoly, Proc.of XIVth PAC, Washington DC (1993).

[2] B. Dunham and O. Napoly, "FFADA, Final Focus Automatic Design and Analysis", Saclay Preprint DAPNIA/SEA 94-06.

[3] J.M. Rifflet et al., "Status of the Fabrication and test of the Prototype LHC Lattice Quadrupole Magnets", MT13 Conf. Victoria, Canada, 1993.

[4] J.M. Rifflet et al., "Cryogenic and Mechanical Measurements of the first two LHC Lattice Quadrupoles Prototypes", EPAC94 Conf., London, Great Britain, 1994.

[5] H. Grote and F.C. Iselin, "The MAD Program", CERN/SL/90-13 (AP) Rev.3 (Jan.1993).

[6] R. Brinkmann and O. Napoly, unpublished.

Presented at the 1994 21st International Power Modulator Symposium, June 27-30, 1994, Costa Mesa, CA., USA

Generation of High Power Pulses Using a SMES

H. Salbert, K.P. Jüngst

Kernforschungszentrum Karlsruhe GmbH
Institut für Technische Physik, D-76021 Karlsruhe, Germany

Abstract

A model of a power modulator for linear accelerators that uses a SMES (Superconducting Magnetic Energy Storage) is being developed. It will generate 2 ms long, 3 kV / 300 A power pulses with a repetition rate of 10 Hz. For this device a fast IGBT-power-switch and a SMES are under development. The IGBT-power-switch consists of IGBT in parallel and in serial connection. The SMES is designed for ramping operations of more than 30 T/s.

Introduction

For the next generation of supercolliders linear concepts are being discussed, e.g. the TESLA collider at DESY Hamburg. A main part of a linear accelerator system is the power modulator that supplies the klystrons with high power pulses. For TESLA roughly 1000 klystrons are to be fed with 10 MW pulses of 2 ms duration at a repetition rate of 10 Hz. Drawing such power pulses directly from the electrical grid would cause a going unstable of the supply grid. Therefore, the modulator needs an intermediate storage of electrical energy. We developed a SMES-based model of a modulator that can smooth the power consumption of pulsed loads. The paper will present a description of the basic function of the modulator circuit. Moreover, the requirements of the construction of the superconducting magnet system are discussed. A fast IGBT based power semiconductor switch which is an essential part of our modulator is also described.

Power Modulator

Figure 1 shows the elementary SMES based power modulator circuit. The operation of this system can be divided into two modes. During the conduction time of the IGBT switch the voltage source charges the SMES and the SMES current increases. After opening of the switch the SMES current commutates into the load and provides it with energy. Across the load the voltage $V_p(t)$ will be generated.

$$V_p(t) = V_{source} + R_{KL}\, I_{SM}(0)\, e^{-\frac{R}{L}t} \qquad (1)$$

The shape of a pulse depends only on the turn on/off times of the switch and the ratio of L_{SMES} to R_{LOAD} . The decay of V_p during a pulse is given by the time constant L/R of the circuit if we neglect the supply voltage. Since the width of a pulse and the repetition rate are only depending on the switch operation this concept makes it possible to generate varying pulse sequences.
Our model modulator is scaled down and designed to generate 300 A and 3 kV pulses. As required for the big

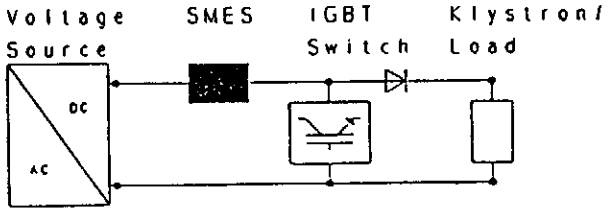

Figure 1
Basic circuit diagram

machine the pulse width is 2 ms with a repetition rate of 10 Hz. The voltage drop during a pulse is limited to 2 %. Therefore, we need a SMES inductance of L_{SMES} = 1 H at least. Since the supply voltage must satisfy equation (2) it is to be V_{SOURCE} = 60 V.

$$V_p = V_{source}\left(1+\frac{t_{on}}{t_{off}}\right) \qquad (2)$$

In the device with L_{SMES} = 1 H there is much more energy stored E_s = 45 kJ than needed for a pulse. One pulse dissipates an energy of about 1.8 kJ with an average power of about 900 kW. Figure 2 shows the SPICE simulation of the voltage across the load. The circuit parameters are: L_{SMES} = 1 H, I_{SMES} = 300 A, R_{LOAD} = 10 Ω, V_{SOURCE} = 60 V. The values used for this simulation reflect the current status of our work.
A step-up transformer may be used if higher pulse voltages are needed and longer pulse risetime caused by the leakage reactances of the windings can be accepted. Due to the voltage across the leakage inductances a protection of the

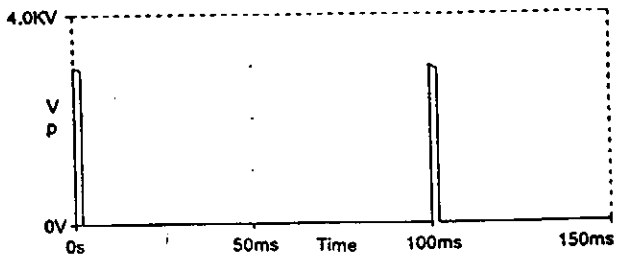

Figure 2
Simulation of the output voltage

overcurrent or by an insufficient gate voltage the faulty stage will be turned off. At the same time a fault signal will be transmitted to the central control unit. That immediately turns off all four stages. During the time delay of this process there will appear the total dV/dt across the defective stage because this stage was turned off at a time the other stages were conductive. Therefore, the snubber capacity must be large enough to keep the voltage uncritical until the other stages are turned off.

An overvoltage detection is also placed directly on the gate-unit. If a dangerous blocking voltage is detected the switch will be turned on at once. At the same time a fault will be reported to the central unit. That generates a switch off command for the complete device. This command has priority over the simple turn on/off signal and it cannot be removed by the gate-units. During the delay time the faulty stage can recover. In an emergency case when a stage will definitively break the circuit a crowbar short-circuits the switch and protects the modulator from overvoltage of the SMES. The basic switch control is shown in Fig. 4. and a picture of the switch in Figure 5.

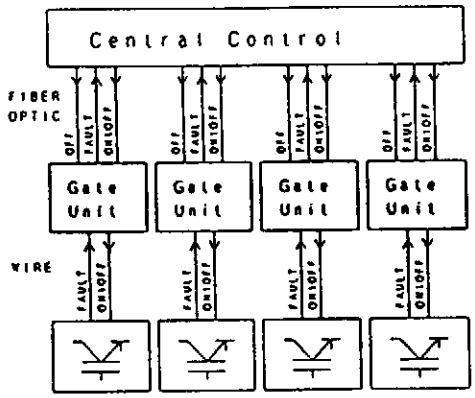

Figure 4
Switch control

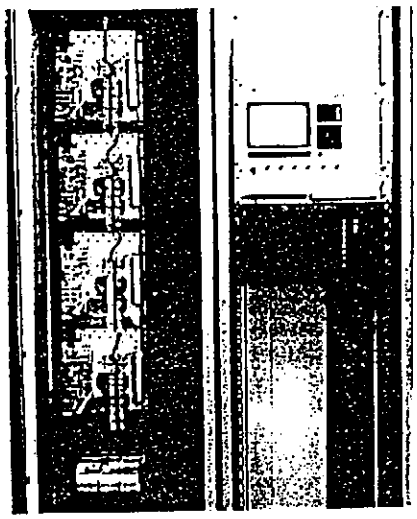

Figure 5
IGBT switch

The tension between the gate units depends on the status of the switch. During turn off the potential difference is about 800 V. To achieve a voltage insulation between the gate units and the central unit we link them with fiber optic cables. These assure insulation and fast signal transfer.

SMES

One important aspect with respect to our interest in the modulator is the analysis of the potential of a SMES for supplying pulsed loads. These applications require fast ramping (more than 30 T/s) of the coil system. Due to the fast change of the magnetic field AC losses are generated in the superconductor. By using different wires we intend to investigate the best suited wire for pulser applications. We further want to find out the limits in using mixed matrix conductors instead of more expensive net frequency wires.

Our SMES is designed as a twelve coil torus which is being composed step by step. First we are completing a 100 kJ four coil solenoid. For this solenoid we employ two types of multifilament superconductors. Their most interesting data are listed in Tab. 2.

Due to the requirement of effective cooling and mechanical stability the coils have a complicate composition. The simplified cross section of a coil is shown in Fig. 6.

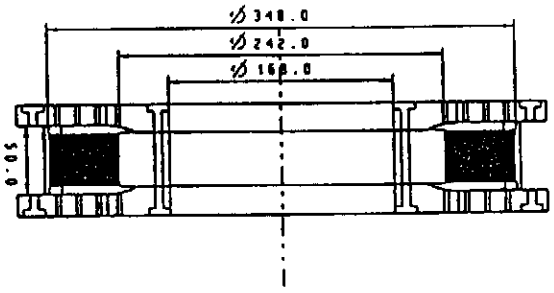

Figure 6
Cross section of a coil

Type	NbTi/Cu/CuNi	NbTi/Cu/CuNi
bare diameter	1.2 mm	1.2 mm
twist pitch	13.5 mm	19 mm
min. crit. current	530 A / 5T	492 A/ 5T
filament dia.	7 µm	2.4 µm
material ratio	1/1.55/0.77	1/1.5/2.9
insulation	0.1 mm	0.1 mm

Table 2: Superconductor data

The first coil consists of 30 layers and 30 windings a layer. Between two layers 140 spacers each 0.5 mm thick are placed. These are forming cooling channels which carry the evaporated helium to radial channels in the endplates. The stucture material must not be conductive because of the high rates of change of the magnetic field. Hence we apply fiber glass-epoxy which is matched with respect to the thermal contraction of the winding. Fiber glass-epoxy also has a satisfying mechanical strength.
The maximum field of the four coil SMES is 4.6 T. It causes a radial magnetic pressure of about 200 MPa and an axial attraction of 180 kN of the outer coils. To avoid wire movements we wound the coils with a prestress of 65 N/mm^2. The coils have an inner diameter of 240 mm, a cross section of 40 x 54 mm, and a total length of 80 mm. This results in an inductivity of approximately 300 mH per coil. Recently we have completed the third coil of the SMES. To date first DC tests on one coil were performed up to 360 A. Fig. 7 shows two coils that are prepared for a test.

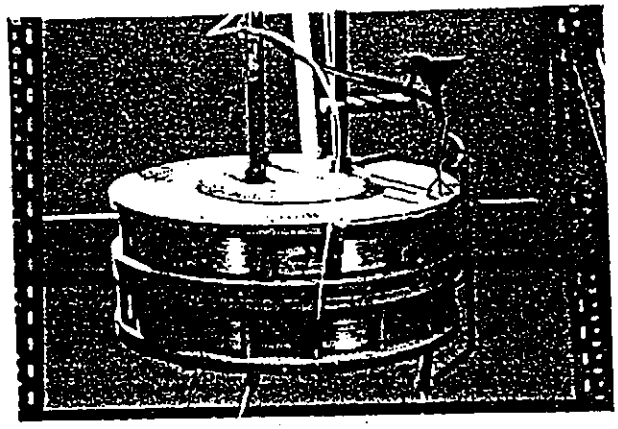

Figure 7
Two coil solenoid

References

[1] H. Steinhart, K.P. Jüngst, "Einsatz von SMES für dieVersorgung von Hochleistungs-Klystrons", Kernforschungszentrum Karlsruhe, March 93, internal report, unpublished

[2] Romeo Letor, IEEE Transactions on Industry Applications, Vol. 28, No. 2, March/April 92

[3] Eupec, Data sheet, Power Semiconductors, 92

[4] Semikron, Data book, Power Semiconductors, 92/93